Optomechanical Coupling between Ultracold Atoms and a Membrane Oscillator

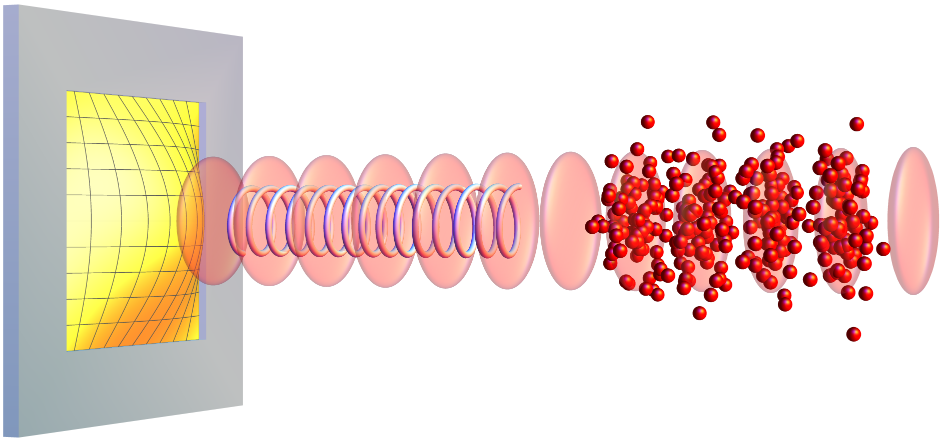

Maria Korppi

Optomechanical Coupling between Ultracold Atoms and a Membrane Oscillator

Inauguraldissertation

zur
Erlangung der Würde eines Doktors der Philosophie
vorgelegt der
Philosophisch-Naturwissenschaftlichen Fakultät
der Universität Basel

von

Maria Korppi
aus Finnland

Basel, 2014

Creative Commons License Deed

Attribution-NonCommercial-NoDerivatives 4.0 International

This is a human-readable summary of (and not a substitute for) the license.

You are free to:

Share — copy and redistribute the material in any medium or format

The licensor cannot revoke these freedoms as long as you follow the license terms.

Under the following terms:

Attribution — You must give appropriate credit, provide a link to the license, and indicate if changes were made. You may do so in any reasonable manner, but not in any way that suggests the licensor endorses you or your use.

NonCommercial — You may not use the material for commercial purposes.

NoDerivatives — If you remix, transform, or build upon the material, you may not distribute the modified material.

No additional restrictions — You may not apply legal terms or technological measures that legally restrict others from doing anything the license permits.

Notices:

You do not have to comply with the license for elements of the material in the public domain or where your use is permitted by an applicable exception or limitation.

No warranties are given. The license may not give you all of the permissions necessary for your intended use. For example, other rights such as publicity, privacy, or moral rights may limit how you use the material.

Source: `http://creativecommons.org/licenses/by-nc-nd/4.0/`

Genehmigt von der Philosophisch-Naturwissenschaftlichen Fakultät
auf Antrag von
Prof. Dr. P. Treutlein
Prof. Dr. A. Heidmann

Basel, den 10. Dezember 2013

Prof. Dr. Jörg Schibler
Dekan

Abstract

In this thesis, I report on the realization of a hybrid optomechanical system in which ultracold atoms are coupled to a micromechanical membrane. The atoms are trapped in the intensity maxima of an optical standing wave formed by retroreflection of a laser beam from the membrane surface. Vibrations of the membrane displace the standing wave, thus coupling to the center-of-mass motion of the atomic ensemble. Conversely, atoms imprint their motion onto the laser light, thereby modulating the radiation pressure force on the membrane. In this way, the laser light mediates a long-distance, coherent coupling between the two systems.

When the trap frequency of the atoms is matched to the membrane frequency, we observe resonant energy transfer. In addition, by applying simultaneous laser cooling to the atoms, we can dissipate energy from the coupled system leading to sympathetic cooling of the membrane mode. The experimental data follows the theoretical estimations that predict the coupling to scale with the number of trapped atoms. Furthermore, by including the finite temperature of the atoms and their spatially inhomogeneous trapping potential in the theoretical model of the optomechanical coupling, we can accurately describe the width and shape of the resonance.

In an improved experimental setup, the membrane is enclosed in a cavity while the atoms are trapped in the standing wave lattice outside the cavity. The presence of the cavity results in a considerable enhancement of the coupling strength in proportion to the cavity finesse. So far we have observed sympathetic cooling of the membrane mode by a factor of 32 starting from room temperature. Theoretical estimates show that in such a setup ground-state cooling of the membrane mode should be possible, allowing one to access the quantum coherent coupling regime.

Contents

1

Introduction

1.1 Hybrid Quantum Systems with Cold Atoms

Laser light can exert a mechanical force on material objects through radiation pressure and through the optical dipole force [1, 2]. These forces have been used for decades to achieve extraordinary control over the quantum states of atoms, molecules, and ions. A diverse toolbox [1, 3] exploiting tailored optical and magnetic fields provides control and detection of the internal and motional states of atoms on the level of single quanta. Furthermore, the possibilities to tune interactions between atoms and ions have made it possible to study exotic quantum matter [4] and generate entanglement in these systems [5, 6].

Recently, solid-state physicists have started to achieve similar control over individual vibrational modes of high-quality fabricated mechanical structures. In the very active field of optomechanics [7, 8, 9, 10, 11], light forces are exploited for cooling and control of the vibrations of mechanical oscillators ranging from macroscopic mirrors to micro-membranes and nanoscale cantilevers. Notably, the ground-state of a single mechanical mode of an optomechanical crystal was reached by laser-cooling [12]. Experiments with other types of mechanical oscillators have also reached phonon occupation numbers very close to the ground state using laser-cooling [13, 14]. In addition, very high-frequency oscillators have been cooled to their ground state by simply placing them in a dilution fridge [15], and by using additional radiation pressure cooling in the microwave domain [16].

Beyond cooling, a subsequent goal is to coherently control these mechanical devices on the quantum level, analogously to what can be achieved with atomic systems. A necessary prerequisite for this is the quantum coherent coupling regime, which has been reached in experiments [14, 17, 15]. This would allow one to study quantum physics on a macroscopic scale [18, 19], possibly revealing yet unobserved quantum decoherence mechanisms [20, 19, 21, 22]. From a more applied physics perspective, such devices could provide quantum-limited force-sensing in precision measurements [23].

Combining the aforementioned advancements in atomic and solid-state physics, a number of recent theoretical articles have proposed that light forces could be used to couple the motion of atoms in a trap to the vibrations of a single mode of a mechanical oscillator [24, 25, 26, 27, 28, 29, 30, 31, 32, 33, 34]. In the resulting hybrid optomechanical system, the well-established toolbox of atomic physics could be used to control the vibrations of an engineered mechanical device. Atoms could be used to read out the motion of the oscillator, to manipulate its dissipation, and ultimately to perform quantum information tasks such as coherently exchanging the quantum state of the two systems. Moreover, the oscillator could serve as a new tool in atomic physics experiments. By functionalizing the oscillator with an electric charge or magnetic moment, it could serve as a universal transducer between otherwise incompatible systems, for example coupling atomic and molecular degrees of freedom. This could facilitate the construction of more advanced quantum networks, where quantum signals are shuttled between different type of elements performing quantum operations.

Atomic systems and solid-state oscillators are complementary in their benefits, while they can compensate each others disadvantages. Atomic quantum systems live in an ultra-high vacuum environment, whereas solid state systems are integrable and scalable [35]. Exceptionally long coherence times up to several seconds can be achieved in atomic systems as compared to mechanical oscillators whose coherence time can reach about a hundred microseconds. The coherence of the mechanical oscillator is limited by coupling to the support. A special case in this context are levitated mechanical oscillators, where a direct connection to the bath is missing similarly to atoms [22, 36].

The challenging prerequisite for any quantum hybrid experiment is the creation of a coherent, quantum interface between the atoms and the mechanical oscillator. Our group has studied different interfaces between atoms and mechanical oscillator based on magnetic [37], van der Waals [38], and optical forces [39, 40, 33, 31, 41, 32]. A graphical summary of these experiments and proposals is illustrated in Fig. 1.1. In the pioneering interface-experiments atoms were used to detect vibrations of micromechanical oscillators using magnetic forces in the J. Kitching's group [42], and surface-force coupling in our group [38] (Fig. 1.1a+b). However, the backaction of the atoms onto the oscillator's motion, which is required for cooling and manipulating the oscillator with the atoms, could not yet be observed. Furthermore, both of these coupling mechanisms rely on short-distance interactions, requiring the atoms to be in close vicinity of the oscillator. A qualitatively different setting can be created by using optical fields, which can provide coupling over long distances. In this thesis, a novel type of an optical interface is described [39, 40] (see also [43]), as illustrated in Fig. 1.1c. Using the optical interface we have demonstrated the backaction of an ensemble of atoms onto a mechanical oscillator for the first time.

Beyond atomic-mechanical oscillator systems, a variety of other types of quantum hybrid systems have been proposed, where a mechanical oscillator is coupled

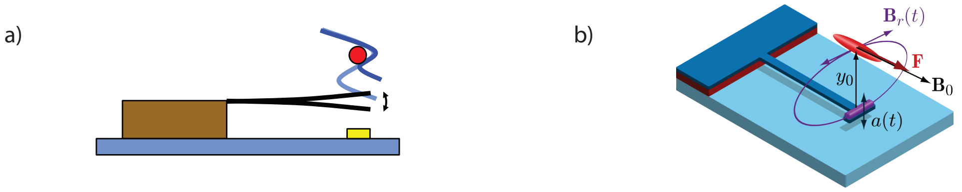

coupling via atom-surface forces

magnetic coupling to atomic spin

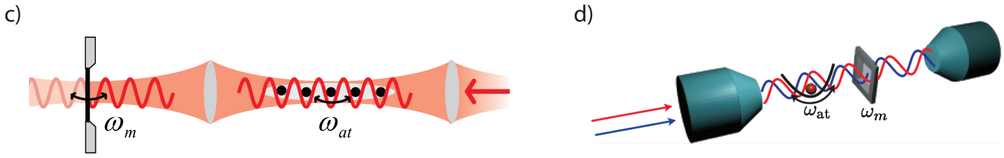

coupling via optical lattice

cavity-mediated coupling

Figure 1.1: Different types of interfaces between atoms and a mechanical oscillator studied in our group. a) Experiment: Coupling of a Bose-Einstein condensate and an AFM tip via van der Waals surfaces forces [38]. b) Proposal: Coupling of Zeeman-states of atoms and a magnetized cantilever [37]. A related experiment has been done in the group of J. Kitching [42]. c) Experiment: Coupling of atoms and a membrane oscillator via an optical lattice [39, 40]. See theory in [33, 41]. d) Proposal: Cavity-mediated coupling between a single atom and a partially reflecting membrane [31].

to a microscopic solid-state quantum system. Examples include coupling of a mechanical resonator to NV centers, quantum dots, charge or spin qubits [44]. In addition, there are also hybrid quantum systems that involve for example superconducting resonators instead of a mechanical oscillator [35]. All in all, the diversity of atomic and solid-state quantum systems in the context of quantum hybrid-systems has led to interdisciplinary sub-fields in both theory and experiment within quantum information science, condensed matter physics, and many-body physics.

1.2 This Thesis

In the hybrid optomechanical system described in this thesis, an ultracold ensemble of a few million atoms is coupled via laser light to a mechanical oscillator as illustrated in Fig. 1.1c. The atoms are trapped in free-space in the intensity maxima of a standing wave that is formed by retro-reflecting a laser beam from the mechanical oscillator. This trap configuration is commonly known as a one dimensional *optical lattice*. The optical lattice creates both the trap for the atoms and simultaneously mediates *long-distance* coupling between the two systems. The mechanical oscillator is a silicon nitride membrane on top of a silicon frame and it has dimensions of $0.5\,\mathrm{mm} \times 0.5\,\mathrm{mm} \times 50\,\mathrm{nm}$. We chose silicon nitride membranes as they exhibit surprisingly low dissipation [45], but also have a reasonable reflectivity at infrared frequencies. The membrane resides in a separate vacuum chamber from the atoms. This type of *modular setup* is experimentally advantageous as the membrane properties can be studied independently of the atoms, and the membranes can be exchanged relatively quickly without breaking the ultra high vacuum necessary for the atom preparation.

The membrane motion couples to the *center of mass-mode* of the atomic ensemble. As the membrane is displaced, the lattice potential minima shift spatially by the same amount. Consequently, the atoms feel a restoring optical dipole force towards their equilibrium position. This force mediates the direct action of the membrane onto the atoms. On the other hand, the dipole force results in redistribution of photons between the two running-wave components that form the standing wave. This leads to a power modulation of the laser beam that has passed trough the atoms and travels towards the membrane. As a result, the radiation pressure force on the membrane becomes also modulated. This gives rise to the backaction of the atoms onto the membrane. If optical losses in the beam path and the finite transmission of the membrane are neglected, the forces experienced by the atoms and the membrane are equal in magnitude, but opposite in sign - in accordance to the *action-reaction principle.* However, in our experimental realization the losses lead to a unique situation of *asymmetric coupling*, which in the quantum regime is described in terms of a *cascaded quantum system.*

In a simplified picture, where all of the atoms move in a common mode in an ideal harmonic trapping potential, the atomic and the membrane motion form a pair of coupled harmonic oscillators. The coupling constant scales with the mass ratio of the atoms and the membrane and is thus *collectively enhanced by the atom number.* Furthermore, continuous laser-cooling of the atoms during the coupling results in *sympathetic cooling* of the membrane mode. A propitious feature of our setup is that the atomic cooling rate is *tunable* and can be switched off at will.

In a *proof-of-principle experiment*, we detect the coupling by measuring the damping induced upon the membrane by the atoms [39, 40]. The atoms are continuously damped at a rate of $2\pi \cdot 130\,\mathrm{kHz}$. The trap frequency of the atoms can be tuned by changing the laser power of the lattice beam. When the atoms are tuned to resonance we observe an increased damping by a few percent of the oscillations of the membrane. This damping scales linearly with the atom number in the trap as predicted by the theory. The observed shape of the resonance differs considerably from what is expected for coupled and damped, simple harmonic oscillators, but it can be accurately explained with a theoretical model that takes into account the finite temperature of the atoms and the *spread in the vibrational frequencies of the atoms* in the trapping potential. This is the *first demonstration of backaction* of ultra cold atoms on a mechanical oscillator.

In a second experiment, we switch the laser cooling of the atoms off and excite the membrane with a piezoelectric transducer. We observe resonant heating of the center of mass mode which confirms that the coupling is indeed *bi-directional.* At the same time, the narrow membrane excitation serves as a probe for the distribution of vibrational frequencies in the lattice.

One route to considerably enhance the coupling is to enclose the membrane inside an optical cavity, which results in an enhancement of the coupling proportional to the cavity finesse. The atoms remain trapped outside the cavity in the standing light-wave that is formed in reflection from the cavity. The theory for this system shows that the optimal cavity finesse is restricted to relatively low values in the non-resolved sideband regime [41]. By implementing the cavity to the experimental setup, we have been able to cool the membrane mode starting from room temperature to a steady-state temperature of 9 K. With the significant improvements that are underway in the new cavity-enhanced setup, observation of normal mode splitting and sympathetic ground state cooling of the oscillator seems a feasible goal [41].

Organization of the Chapters

- The **second Chapter** provides an introduction to mechanical oscillators in the classical and quantum regimes. The description of optomechanical systems can often be reduced to that of two coupled harmonic oscillators. This is briefly introduced from the viewpoint of coupling atoms to mechanical oscillators. The latest significant advancements in optomechanics are reviewed, and finally a harmonic oscillator formed by an ensemble of ultra cold atoms in an optical lattice potential is discussed. The optical lattice theory is derived for the case of a partially reflecting mirror.

- A semiclassical model captures the essential features of the original free-space and the cavity-enhanced atom-membrane coupling schemes, as discussed in the **third Chapter**. The model is used to derive the coupling constant, sympathetic damping rate of the membrane and the normal modes of the system. In order to analyze the fundamental quantum limits of the system performance, a quantized description of the system is briefly introduced. The theory was developed in collaboration with P. Zoller's group [41].

- The **fourth Chapter** describes characterization measurements on the commercial, low and high-stress silicon nitride (SiN) membranes used in the experiment. The mechanical quality factors of the membranes depend strongly on the mounting of the membranes to a supporting structure. By optimizing the mounting, ultrahigh ($> 10^6$) quality factors are obtained. The absorbance of the low-stress stress membranes is found to be considerably higher ($1.5 \cdot 10^{-3}$) than that of the high-stress ones ($\lesssim 2 \cdot 10^{-5}$) at 780 nm. Absorption related heating in the membrane results in a decrease of the eigenfrequency via a reduction in its tensile stress. At discrete eigenfrequencies, the membrane mode couples to a mode of the frame, which manifests itself as a dramatic drop in the quality factor of the membrane mode.

- The experimental setup for the free-space experiment and the optomechanical coupling results are presented in the **fifth Chapter**. The optomechanical coupling is observed both as a resonant temperature increase of the atoms and as a resonant enhancement in the damping of the membrane. A theoretical model is developed to accurately describe the shape of the observed resonance. The model takes into account experimental details of the inhomogeneous lattice beam profile and the finite temperature of the atoms. The results presented in this Chapter demonstrate a proof-of-principle and are used for optimizing the experimental parameters. The Chapter concludes with proposals of direct improvements that can be applied to the setup to boost up the coupling.
- **Chapter six** focuses on the theory and implementation of the new membrane module, where a membrane is placed in the middle of a cavity. The basic principles of optical cavities are first covered and then the optomechanical coupling between the membrane and the cavity is explained. It is found out that fine-positioning a low-loss membrane inside an asymmetric cavity can increase the cavity finesse beyond its free-space value due to classical interference effects inside the cavity. After the theoretical part, the new experimental membrane module is described in detail. By using the cavity-enhanced module in a new series of atom-membrane coupling experiments, we have so far been able to sympathetically cool the membrane using the atoms from room temperature to a steady-state temperature of 9 K, which is a considerable improvement compared to the original free-space setup.
- **Chapter seven** summarizes the work and presents an outlook on the short and long term goals of the main experiment. Improvements to the current setup are suggested to enhance the coupling further towards the coherent coupling regime.

Publications

- *Sympathetic cooling of a membrane oscillator in a hybrid mechanical-atomic system*
  in preparation (2013)

- *Hybrid Atom-Membrane Optomechanics* [40]
  M. Korppi, A. Jöckel, M. T. Rakher, S. Camerer, D. Hunger, T. W. Hänsch, and P. Treutlein
  EPJ Web of Conferences **57**, 03006 (2013).

- *Cavity-Enhanced Long-Distance Coupling of an Atomic Ensemble to a Micromechanical Membrane* [41]
  B. Vogell, K. Stanningel, P. Zoller, K. Hammerer, M. T. Rakher, M. Korppi, A. Jöckel, and P. Treutlein
  Phys. Rev. A **87**, 023816, (2013).

- *Spectroscopy of Mechanical Dissipation in Micro-Mechanical Membranes* [46]
  A. Jöckel, M. T. Rakher, M. Korppi, S. Camerer, D. Hunger, M. Mader, and P. Treutlein
  Appl. Phys. Lett. **99**, 143109 (2011).

- *Realization of an Optomechanical Interface between Ultracold Atoms and a Membrane* [39]
  S. Camerer*, M. Korppi*, A. Jöckel, D. Hunger, T. W. Hänsch, and P. Treutlein
  Phys. Rev. Lett. **107**, 223001 (2011).
  (*) These authors contributed equally to the paper.

- *Coupling Ultracold Atoms to Mechanical Oscillators* [34]
  D. Hunger, S. Camerer, M. Korppi, A. Jöckel, T. W. Hänsch, and P. Treutlein
  C. R. Physique 12, **871** (2011).

2

Background

This Chapter introduces the basic concepts related to our atom-membrane coupling experiment, namely a mechanical oscillator, ultra cold atoms and the light field which mediates the coupling between the two.

Section 2.1 introduces the concept of a mechanical harmonic oscillator both in the classical and quantum regimes. It also gives a general description of two harmonic oscillators coupled via a distance-dependent force from the viewpoint of coupling atoms to mechanical oscillators. The quantum regime of a mechanical oscillator has become relevant in optomechanical experiments, where the mechanical mode is coupled to a light field. A brief overview of optomechanical coupling is given in Sec. 2.2.

Section 2.3 describes the properties of ultra-cold atoms in an optical lattice potential. The center of mass mode of a cold atom cloud in an optical lattice can be described with a harmonic oscillator. The atoms can be readily ground-state cooled and manipulated on a quantum level with laser fields, making them an attractive system to couple to.

2.1 Mechanical Oscillator

2.1.1 Mode Function and Effective Mass

Continuum mechanics gives an accurate description of long-wavelength vibrations and allows to calculate the eigenmodes of bulky geometries. The mechanical modes of different type of geometries may be solved via the elastic wave equation [47],

$$\rho \frac{\partial^2 \mathbf{u}\left(\mathbf{r}, t\right)}{\partial t^2} = \nabla \cdot T + \mathbf{f}\left(\mathbf{r}, t\right), \tag{2.1}$$

where $\mathbf{u}\left(\mathbf{r}, t\right)$ is a displacement field as a response to some externally applied force $\mathbf{f}\left(\mathbf{r}, t\right)$, ρ is the density of the material, and T is an elastic stress tensor. For more complex geometries one often needs to resort to numerical solutions, especially in cases where material inhomogeneity or anisotropy is present [47]. Furthermore, for large deflections from equilibrium, non-linear effects start taking place, and Eq. 2.1 must be adapted to include these.

In a few simple cases, the equations of motion can be readily derived from first principles. Here we take as an example a thin, square, homogeneous membrane that has displacement along x within the linear-response regime. The membrane has a side length of l_{m}. Let us consider a situation, where the membrane is released from some initial deflection x_0. In this case, the wave equation (Eq. 2.1) reduces to

$$\rho \frac{\partial^2 u\left(y, z, t\right)}{\partial t^2} = S \left(\frac{\partial^2 u\left(y, z, t\right)}{\partial y^2} + \frac{\partial^2 u\left(y, z, t\right)}{\partial z^2} \right), \tag{2.2}$$

where S is the tensile stress in the membrane. The eigenfrequencies of the membrane are [48]

$$\omega_{ij} = \frac{\pi}{l_{\mathrm{m}}} \sqrt{\frac{S}{\rho} \left(i^2 + j^2\right)}, \tag{2.3}$$

and the corresponding mode functions are harmonic

$$u_{ij}\left(y, z, t\right) = x_{ij}\left(t\right) \sin\left(i \frac{\pi}{l_{\mathrm{m}}} y\right) \sin\left(j \frac{\pi}{l_{\mathrm{m}}} z\right) \tag{2.4}$$

$$x_{ij}\left(t\right) = x_0 \sin\left(\omega_{ij} t + \phi\right), \tag{2.5}$$

where $i, j = (1, 2, 3..)$. Figure 2.1 shows the lowest order eigenmodes for a square membrane.

In the following description, we will treat a mechanical mode of any type of oscillator as a simple harmonic oscillator with a single position coordinate and a single momentum coordinate. For this purpose we define an effective mass for the oscillator, M, so that that the potential energy of the oscillator system is $E_{\mathrm{pot}}\left(t\right) = \frac{1}{2} M \omega_{\mathrm{m}}^2 x_{\mathrm{m}}(t)^2$, where $x_{\mathrm{m}}(t)$ and ω_{m} correspond to the peak displacement and eigenfrequency of the system. For a square membrane the potential

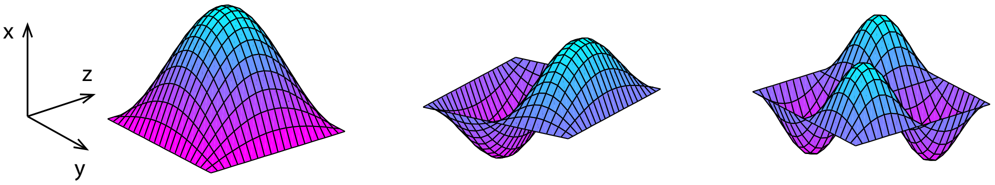

Figure 2.1: An example of the lowest order modes $(i, j) = (1,1); (2,1); (2,2)$ for a square membrane.

energy of the vibrational mode is

$$E_{\text{pot}}(t) = \frac{1}{2}\int_{l_{\text{m}}}\int_{l_{\text{m}}}\int_{d_{\text{m}}} u_{ij}^2 \omega_{\text{m}}^2 \rho dydzdx = \frac{1}{2}\omega_{\text{m}}^2 \frac{l_{\text{m}}^2 d_{\text{m}} \rho}{4} x_{\text{m}}(t)^2, \tag{2.6}$$

where d_{m} is the thickness of the membrane. From this we can identify the effective mass to be 1/4 of its physical mass and equal for all the modes of the membrane:

$$M = \frac{1}{4}\rho d_{\text{m}} l_{\text{m}}^2. \tag{2.7}$$

2.1.2 Damped and Driven Harmonic Oscillator

The equation of motion for a velocity-damped oscillator is given by [49]

$$M\ddot{x}_{\text{m}}(t) + M\gamma_{\text{m}}\dot{x}_{\text{m}}(t) + M\omega_{\text{m}}^2 x_{\text{m}}(t) = F(t), \tag{2.8}$$

where γ_{m} is the energy damping rate of the oscillator in angular units, ω_{m} is the mechanical resonance frequency in angular units, M is the effective mass, and F is an external driving force. The equation can be conveniently solved in the frequency domain. By applying the Fourier transform of the form

$$f(\omega) = \int_{-\infty}^{\infty} f(t) e^{-i\omega t} dt, \quad f(t) = \int_{-\infty}^{\infty} \frac{1}{2\pi} f(\omega) e^{+i\omega t} d\omega \tag{2.9}$$

to both sides of the equation Eq. 2.8 we get

$$-M\omega^2 x_{\text{m}}(\omega) + iM\omega\gamma_{\text{m}} x_{\text{m}}(\omega) + M\omega_{\text{m}}^2 x_{\text{m}}(\omega) = F(\omega). \tag{2.10}$$

The linear response of the oscillator to an external force can be expressed in terms of the mechanical susceptibility as

$$\chi(\omega) \equiv x_{\text{m}}(\omega)/F(\omega) = \frac{1/M}{\omega_{\text{m}}^2 - \omega^2 - i\gamma_{\text{m}}\omega}. \tag{2.11}$$

In the case, where the driving force is harmonic, $F(t) = F_0 \sin(\omega t)$, the oscillator has a solution on the time-domain $x_\mathrm{m}(t) = x_0 \sin(\omega t - \phi)$ with an amplitude and phase lag

$$x_0 = \frac{F_0/M}{\sqrt{\left(\omega_\mathrm{m}^2 - \omega^2\right)^2 + \omega^2\gamma_\mathrm{m}^2}} \tag{2.12}$$

$$\phi = \tan^{-1}\left(\frac{\gamma_\mathrm{m}\omega}{\omega_\mathrm{m}^2 - \omega^2}\right). \tag{2.13}$$

If the excitation vanishes abruptly, $F(t > 0) = 0$, the amplitude of a weakly damped oscillator ($\gamma_\mathrm{m} \ll \omega_\mathrm{m}$) will decay in time from an initial value x_0 as

$$x_\mathrm{m}(t) = x_0 e^{-\frac{\gamma_\mathrm{m}}{2}t} \sin\left[t\sqrt{\omega_\mathrm{m}^2 - \frac{\gamma_\mathrm{m}^2}{4}} - \phi\right]. \tag{2.14}$$

A useful quantity to characterize mechanical oscillators is the quality-factor Q

$$Q = \frac{\omega_\mathrm{m}}{\gamma_\mathrm{m}}, \tag{2.15}$$

which describes how many oscillations the oscillator experiences before its energy has decreased by a factor of e. In other words, a high Q means that the oscillator is well decoupled from its environment. Figure 2.2a shows an example of a ringdown for an oscillator that has $Q = 10$.

In the absence of external driving, Eq. 2.14 suggests that the amplitude of the oscillator will decay to zero. In reality, the oscillator is always coupled to an environment at some finite temperature T_bath, or in other words, to a thermal bath. The bath can be described as an infinite sum of harmonic oscillators exerting a force of equal amplitude but different frequency, which gives rise to a noise power spectral density given by the fluctuation-dissipation theorem [50, 11]

$$S_\mathrm{F}(\omega) = 4k_B T_\mathrm{bath}\gamma_\mathrm{m} M. \tag{2.16}$$

In order to avoid confusions with factors of two, it is noted that Eq. 2.16 is the single-sided power spectral density in the domain of positive angular frequencies $\omega > 0$. Fluctuations of F drive the fluctuations of x_m via the susceptibility as [51]

$$\begin{aligned} S_x(\omega) = |\chi(\omega)|^2 S_\mathrm{F}(\omega) &= \frac{4k_B T_\mathrm{bath}\gamma_\mathrm{m}}{M} \cdot \frac{1}{\left(\omega_\mathrm{m}^2 - \omega^2\right)^2 + \omega^2\gamma_\mathrm{m}^2} && (2.17) \\ &\approx \frac{4k_B T_\mathrm{bath}}{M\omega_\mathrm{m}^2\gamma_\mathrm{m}} \cdot \frac{1}{1 + 4\left(\omega_\mathrm{m} - \omega\right)^2/\gamma_\mathrm{m}^2}, && (2.18) \end{aligned}$$

where the last approximation holds when the oscillator is weakly damped, i.e., $\gamma_\mathrm{m} \ll \omega_\mathrm{m}$. The thermal vibration amplitude is related to the power spectral density by

$$\langle x_\mathrm{m}^2(t)\rangle_\mathrm{th} = \int_0^\infty S_x(\omega)d\omega/2\pi = \frac{k_B T_\mathrm{bath}}{M\omega_\mathrm{m}^2}, \tag{2.19}$$

resulting in a r.m.s thermal amplitude of the oscillator

$$x_{\mathrm{th}} = \sqrt{\langle x_{\mathrm{m}}^2(t)\rangle_{\mathrm{th}}} = \sqrt{\frac{k_B T_{\mathrm{bath}}}{M\omega_{\mathrm{m}}^2}}. \tag{2.20}$$

For example, we use a thin SiN membrane in our experiment which has dimensions $(0.5\,\mathrm{mm})^2 \times 50\,\mathrm{nm}$, tensile stress $S = 98\,\mathrm{MPa}$ [46], and density $\rho = 2.9\,\mathrm{g/cm^3}$ [46]. These result in a fundamental eigenfrequency $\omega_{\mathrm{m}} = 2\pi \cdot 270\,\mathrm{kHz}$, effective mass $M = 8\,\mathrm{ng}$ and a thermal amplitude of $x_{\mathrm{th}} = 13\,\mathrm{pm}$ at room temperature. Such an amplitude can be easily detected with interferometric means. Figure 2.2b shows the power spectral density of the membrane in room temperature.

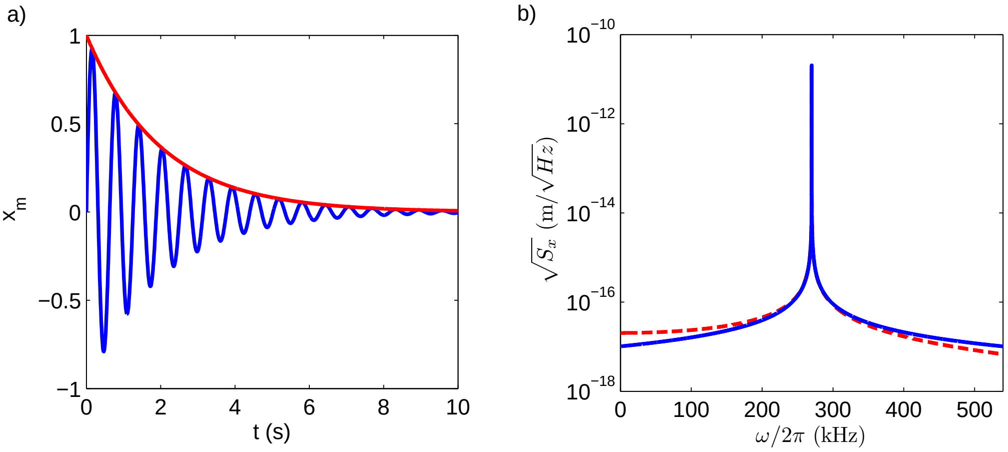

Figure 2.2: a) An example of a ringdown of an initially excited oscillator of $\omega_{\mathrm{m}} = 10$, $Q = 10$. b) Power spectral density in room temperature, $T_{\mathrm{bath}} = 293\,\mathrm{K}$, for a SiN membrane that has $\omega_{\mathrm{m}} = 2\pi \cdot 270\,\mathrm{kHz}$, $M = 8\,\mathrm{ng}$, $Q = 10^6$. Dashed line corresponds to Eq. 2.17 and solid line to Eq. 2.18.

2.1.3 Quantum Mechanical Harmonic Oscillator

In non-relativistic quantum mechanics, the evolution of a state $\Psi(x,t)$ is governed by the Schrödinger equation [52]

$$i\hbar\dot{\Psi}(x,t) = H\Psi(x,t) = \left(\frac{p^2}{2M} + V(x)\right)\Psi(x,t), \tag{2.21}$$

where H is the Hamiltonian operator of the system, p is the momentum operator, and $V(x)$ is the potential. In the coordinate representation

$$p = -i\hbar\frac{\partial}{\partial x}, \tag{2.22}$$

we obtain the corresponding Hamiltonian for a harmonic oscillator,

$$H = -\frac{\hbar^2}{2M}\frac{\partial^2}{\partial x^2} + \frac{1}{2}M\omega_{\mathrm{m}}^2 x^2. \tag{2.23}$$

It is useful to introduce new operators b and $b^\dagger$ and define the position and momentum in terms of these as

$$x = \sqrt{\frac{\hbar}{2M\omega_{\mathrm{m}}}}(b + b^\dagger) = x_{\mathrm{zp}}(b + b^\dagger) \tag{2.24}$$

and

$$p = iM\omega_{\mathrm{m}}\sqrt{\frac{\hbar}{2M\omega_{\mathrm{m}}}}(b^\dagger - b) = iM\omega_{\mathrm{m}}x_{\mathrm{zp}}(b^\dagger - b). \tag{2.25}$$

As x and p obey the commutation relation $[x, p] = i\hbar$, it follows that b and $b^\dagger$ will obey the bosonic commutation relation $[b, b^\dagger] = 1$. Substituting Eqs. 2.24 and 2.25 into Eq. 2.23 the Hamiltonian can be written in terms of b and $b^\dagger$ as

$$H = \hbar\omega_{\mathrm{m}}(b^\dagger b + \frac{1}{2}). \tag{2.26}$$

The Schrödinger equation has been transformed into an eigenvalue problem for the so-called number operator $N = b^\dagger b$ as $N|n\rangle = n|n\rangle$. The infinite set of eigenvectors for each eigenvalue of $n = 0, 1, 2...$ is the so-called **Fock-states** [53]

$$|n\rangle = \frac{1}{\sqrt{n!}}(b^\dagger)^n|0\rangle, \tag{2.27}$$

where the ground-state of the harmonic oscillator, $|0\rangle$, corresponds to the lowest eigenvector $n = 0$. The Fock states are orthogonal, $\langle n|m\rangle = \delta_{nm}$, and complete, $\sum_{n=0}^{\infty}|n\rangle\langle n| = 1$. The eigenenergies corresponding to the Fock-states are each spaced by discrete quanta of $\hbar\omega_{\mathrm{m}}$ and given by

$$E_n = \hbar\omega_{\mathrm{m}}(n + \frac{1}{2}), \tag{2.28}$$

where n defines the quanta of excitation of the harmonic oscillator. From Eq. 2.28 we see that the oscillator has a non-zero ground-state energy, so called zero-point energy, which has the value

$$E_0 = \frac{1}{2}\hbar\omega_{\mathrm{m}}. \tag{2.29}$$

In the coordinate representation, the ground-state wave function is given by [53]

$$\Psi_0(x) = \langle 0|x\rangle = \left(\frac{M\omega_{\mathrm{m}}}{\pi\hbar}\right)^{1/4}\exp\left(-\frac{M\omega_{\mathrm{m}}}{2\hbar}x^2\right). \tag{2.30}$$

By using the expectation values of the position operator and its square

$$\begin{aligned} \langle x \rangle_n &= \langle \Psi_n | x | \Psi_n \rangle = 0 & (2.31) \\ \left\langle x^2 \right\rangle_n &= \left\langle \Psi_n | x^2 | \Psi_n \right\rangle = \frac{\hbar}{M\omega_\mathrm{m}} \left(n + \frac{1}{2} \right), & (2.32) \end{aligned}$$

we find the ground-state amplitude to be

$$\sqrt{\langle x^2 \rangle_0 - \langle x \rangle_0^2} = \sqrt{\frac{\hbar}{2M\omega_\mathrm{m}}} \equiv x_\mathrm{zp}. \tag{2.33}$$

Another peculiar set of states are the eigenstates of the annihilation operator b, known as **coherent states**. A coherent quantum state resembles most closely a classical harmonic oscillator and is defined as [52, 54]

$$|\alpha\rangle = \exp\left(-\frac{|\alpha|^2}{2}\right) \sum_{n=0}^{\infty} \frac{\alpha^n}{\sqrt{n!}} |n\rangle. \tag{2.34}$$

Unlike the Fock-states that are characterized with discrete excitation quanta n (Eq. 2.28), coherent states are minimum uncertainty states, such that

$$(\Delta x)_\alpha^2 (\Delta p)_\alpha^2 = \frac{\hbar^2}{4}. \tag{2.35}$$

Furthermore, coherent states are not orthogonal and form an over-complete basis, i.e., $\int d^2\alpha |\alpha\rangle\langle\alpha| = \pi$.

The probability of finding n excitations in a coherent state follows Poisson statistics

$$P_n = \exp(-|\alpha|^2) \frac{|\alpha|^{2n}}{n!}, \tag{2.36}$$

with an average excitation number and variance

$$\langle n \rangle = |\alpha|^2, \tag{2.37}$$

$$\langle n^2 \rangle = |\alpha|^2 + |\alpha|^4, \tag{2.38}$$

such that $(\Delta n)^2 = \langle n^2 \rangle - \langle n \rangle^2 = \langle n \rangle$. The probability function for a coherent state is plotted in Fig. 2.3a. An example of a coherent state is light emitted from an ideal laser source. If the photon number distribution of a laser is dominated by a coherent-state distribution, the laser is said to be shot noise limited.

So far, we considered only pure states of the harmonic oscillator. If the system is in contact with the environment, it can be described by a **mixed state**, which is a statistical mixture of pure states. A harmonic oscillator in thermal equilibrium with a bath at temperature T_bath is an example of such a state, also generally known as a **thermal state**. A thermal state can be written in terms of the density matrix as [54]

$$\rho = \sum_n \frac{\bar{n}_\mathrm{th}^n}{(1 + \bar{n}_\mathrm{th})^{n+1}} |n\rangle\langle n|, \tag{2.39}$$

where the mean phonon number follows the Bose-Einstein statistics

$$\bar{n}_{\mathrm{th}} = \frac{1}{\exp\left(\frac{\hbar\omega_{\mathrm{m}}}{k_B T_{\mathrm{bath}}}\right) - 1}. \tag{2.40}$$

In high temperature, $k_B T_{\mathrm{bath}} \gg \hbar\omega_{\mathrm{m}}$

$$\bar{n}_{\mathrm{th}} \approx \frac{k_B T_{\mathrm{bath}}}{\hbar\omega_{\mathrm{m}}}. \tag{2.41}$$

The probability distribution for a thermal state (Eq. 2.39) is plotted in Fig. 2.3b.

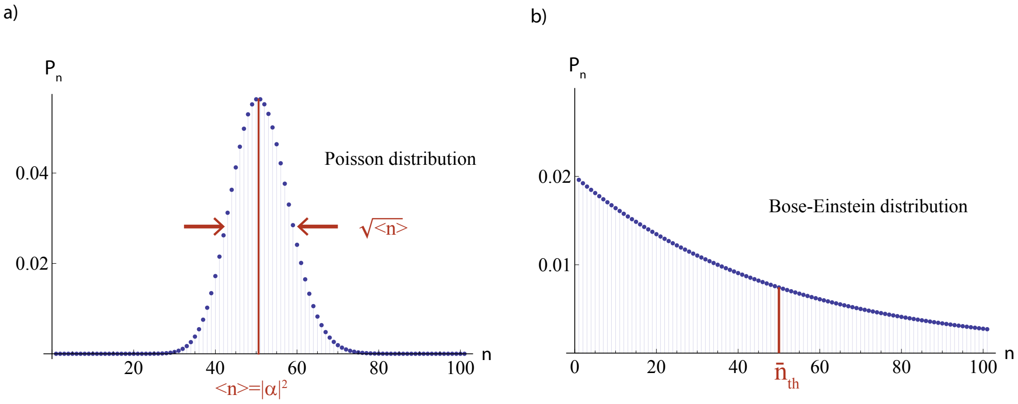

Figure 2.3: Probability to find n phonons in a) a coherent state, b) thermal state.

In general, the larger the zero-point uncertainty given by Eq. 2.33, the easier it is to experimentally detect the quantum fluctuations of the resonator. For this one would prefer to have small M and ω_{m}. In practice, a more stringent condition is set by the coupling of the oscillator to its bath, Eq. 2.41. In the absence of auxiliary cooling mechanisms the oscillator mode thermalizes with the bath temperature. To reach the ground-state we must require

$$\hbar\omega_{\mathrm{m}} \gg k_B T_{\mathrm{bath}}. \tag{2.42}$$

This is a stringent condition for practical, bulky mechanical oscillators. For example, at $T_{\mathrm{bath}} = 300\,\mathrm{K}$ and for an oscillator with $\omega_{\mathrm{m}} = 2\pi \cdot 1\,\mathrm{MHz}$ we get $\bar{n}_{\mathrm{th}} = 6 \cdot 10^6$ phonons, whereas at $T_{\mathrm{bath}} < 50\,\mu\mathrm{K}$, $\bar{n}_{\mathrm{th}} < 1$. Hence, in order to explore macroscopic mechanical oscillator in the quantum regime, low mass and high frequency oscillators are required. Quite remarkably, in the experiment reported in Ref. [15], bulk refrigeration of a 6 GHz mechanical oscillator in a dilution fridge was sufficient to reach phonon occupation of $\bar{n}_{\mathrm{th}} = 0.07$. In general, however, auxiliary cooling mechanisms are needed to enter the quantum regime.

Dissipation via Thermal Bath

To treat dissipation and noise in a mechanical system quantum mechanically, an open quantum system approach is required [55]. The mechanical oscillator is coupled to a large number of degrees of freedom of the environment which leads to an irreversible decay of the oscillator state. During this process the bath remains approximately in thermal equilibrium. This can be described in terms of the master equation formalism [52, 55], which is briefly reviewed here.

The time evolution of the density operator is governed by the master equation

$$\dot{\rho} = -\frac{i}{\hbar}\left[H, \rho\right] + \mathcal{L}\rho, \tag{2.43}$$

where H is the Hamiltonian of the system, and the Liouvillian $\mathcal{L}\rho$ describes the coupling to a Markovian reservoir. A reservoir is called Markovian when it has no short-term memory, i.e., the bath correlations decay faster than any other time-scale of interest in the problem. In general, $\mathcal{L}\rho$ can be expressed in the Lindblad form

$$\mathcal{L}\rho = \frac{\gamma_{\mathrm{m}}}{2}\left(\bar{n}_{\mathrm{th}} + 1\right)\mathcal{D}(b)\rho + \frac{\gamma_{\mathrm{m}}}{2}\bar{n}_{\mathrm{th}}\mathcal{D}(b^\dagger)\rho, \tag{2.44}$$

where we use the shorthand notation

$$\mathcal{D}(b)\rho = 2b\rho b^\dagger - b^\dagger b\rho - \rho b^\dagger b. \tag{2.45}$$

The term γ_{m} is the decay or relaxation rate of interest.

Importantly, the master equation can be used to determine the evolution of the expectation of system operators. For example, the average phonon number in the oscillator

$$\langle b^\dagger b\rangle = \mathrm{tr}\left(\rho b^\dagger b\right) \tag{2.46}$$

evolves as

$$\frac{d\langle b^\dagger b\rangle}{dt} = -\gamma_{\mathrm{m}}\langle b^\dagger b\rangle + \gamma_{\mathrm{m}}\bar{n}_{\mathrm{th}}. \tag{2.47}$$

For large times, the average number of phonons in the oscillator equilibrates to that of the bath, i.e., $\langle b^\dagger b\rangle = \bar{n}_{\mathrm{th}}$. Another insight into the above equation is obtained by re-expressing it as

$$\frac{d\langle b^\dagger b\rangle}{dt} = -\gamma_{\mathrm{m}}\langle b^\dagger b\rangle\left(\bar{n}_{\mathrm{th}} + 1\right) + \gamma_{\mathrm{m}}\bar{n}_{\mathrm{th}}\left(\langle b^\dagger b\rangle + 1\right), \tag{2.48}$$

where we see that there is an imbalance between the leakage (emission) of phonons from the system to the bath and from the bath into the system. In both terms the +1 is the contribution of spontaneous emission and has no classical counterpart. When the bath is at zero temperature, only spontaneous decay from the system to the reservoir is left. On the other hand, if the bath has a finite temperature T_{bath}, phonons enter the system at a thermal decoherence rate

$$\gamma_{\mathrm{th}} = \gamma_{\mathrm{m}}\bar{n}_{\mathrm{th}} = \frac{k_B T_{\mathrm{bath}}}{\hbar Q}. \tag{2.49}$$

The asymmetry predicted by Eq. 2.48 has been observed in an experiment, where a mechanical oscillator is operated close to its quantum ground-state [56].

2.1.4 Coupled Harmonic Oscillators

The description of harmonic oscillators coupled by a spring is a simple, but general description of many mechanical hybrid-systems operating at the quantum regime. The model of two coupled harmonic oscillators is covered in many textbooks, see for example Ref. [49]. Here the coupled oscillator model is described from the general perspective of direct coupling of the motion of an atom or ion in a harmonic potential to the vibrations of a mechanical oscillator via a distance-dependent force. The goal is to derive an expression for the coupling constant. The description follows the in-depth discussion in Ref. [34].

Let us consider an atom with a mass m in a harmonic potential with trap frequency $\omega_{\mathrm{at},0}$ and a mechanical oscillator of mass M and eigenfrequency $\omega_{\mathrm{m},0}$

$$H = \frac{p_{\mathrm{m}}^2}{2M} + \frac{1}{2}M\omega_{\mathrm{m},0}^2 x_{\mathrm{m}}^2 + \frac{p_{\mathrm{at}}^2}{2m} + \frac{1}{2}m\omega_{\mathrm{at},0}^2 x_{\mathrm{at}}^2 + U_{\mathrm{c}}\left[d + x_{\mathrm{at}} - x_{\mathrm{m}}\right]. \tag{2.50}$$

The constant d is the absolute distance between the two oscillators, and x_{m}, x_{at} describe amplitude of the oscillators around their equilibrium. The coupling potential U_{c} depends only on the relative distance $x_{\mathrm{m}} - x_{\mathrm{at}}$ between the two oscillators. For small oscillation amplitudes ($x_{\mathrm{m}}, x_{\mathrm{at}} \ll d$), the coupling potential can be expanded

$$U_{\mathrm{c}}\left[d + x_{\mathrm{at}} - x_{\mathrm{m}}\right] \approx U_{\mathrm{c}}\left[d\right] + U_{\mathrm{c}}'\left[d\right]\left(x_{\mathrm{at}} - x_{\mathrm{m}}\right) + \frac{1}{2}U_{\mathrm{c}}''\left[d\right]\left(x_{\mathrm{at}} - x_{\mathrm{m}}\right)^2. \tag{2.51}$$

The first term in the expansion is a constant and does not influence the oscillator dynamics. The second term proportional to U_{c}' results in a shift of the equilibrium positions of the oscillators. The third, quadratic term gives rise to the mechanical coupling. By expanding it, $\frac{1}{2}U_{\mathrm{c}}''\left[d\right]\left(x_{\mathrm{at}} - x_{\mathrm{m}}\right)^2 = \frac{1}{2}U_{\mathrm{c}}''\left[d\right]\left(x_{\mathrm{at}}^2 - 2x_{\mathrm{at}}x_{\mathrm{m}} + x_{\mathrm{m}}^2\right)$, it is evident that it includes terms contributing to a change in the oscillation frequencies as

$$\omega_{\mathrm{m}}^2 = \omega_{\mathrm{m},0}^2 + \frac{U_{\mathrm{c}}''\left[d\right]}{M} \tag{2.52}$$

$$\omega_{\mathrm{at}}^2 = \omega_{\mathrm{at},0}^2 + \frac{U_{\mathrm{c}}''\left[d\right]}{m} \tag{2.53}$$

but more importantly it has a term linear in the oscillation amplitudes $x_{\mathrm{at}}x_{\mathrm{m}}$. This term can be interpreted as the interaction part of the Hamiltonian

$$H_{\mathrm{int}} = U_{\mathrm{c}}''\left[d\right] x_{\mathrm{at}} x_{\mathrm{m}}. \tag{2.54}$$

It is useful to write

$$H_{\mathrm{int}} = \epsilon \cdot m\omega_{\mathrm{at}}^2 x_{\mathrm{at}} x_{\mathrm{m}}, \tag{2.55}$$

where the coupling strength parameter is defined as

$$\epsilon = \frac{U_{\mathrm{c}}''[d]}{m\omega_{\mathrm{at}}^2}. \tag{2.56}$$

Note that the condition $|\epsilon| \leq 1$ must hold, otherwise the atom trap vanishes [34]. The interaction Hamiltonian can be quantized in terms of the annihilation and creation operators defined as in Eq. 2.24[1],

$$H_{\mathrm{int}} = \epsilon \frac{\hbar\omega_{\mathrm{at}}}{2} \sqrt{\frac{\omega_{\mathrm{at}}}{\omega_{\mathrm{m}}}} \sqrt{\frac{m}{M}} \left(a^\dagger + a\right) \left(b^\dagger + b\right). \tag{2.57}$$

The coupling is strongest on resonance, $\omega_{\mathrm{m}} \approx \omega_{\mathrm{at}}$. We neglect the fast, counter-rotating terms of the form $a^\dagger b^\dagger$ and ab (rotating-wave approximation, RWA) and the resulting total Hamiltonian has the simple form

$$H = \hbar\omega_{\mathrm{at}} a^\dagger a + \hbar\omega_{\mathrm{m}} b^\dagger b + \hbar g \left(a^\dagger b + a b^\dagger\right), \tag{2.58}$$

where the near-resonant coupling constant is defined as

$$g = \epsilon \frac{\omega_{\mathrm{at}}}{2} \sqrt{\frac{m}{M}}. \tag{2.59}$$

Three important features are evident in the coupling constant g:

- The coupling constant scales with the mass ratio of the oscillators $\sqrt{m/M}$. This "impedance" mismatch imposes quite strict limit on the coupling strength in atom-mechanical oscillator systems. A single atom or ion with a mass $m = 10^{-22}$ g coupled to a micro- or nano-structured oscillator with $M \sim 10^{-13} - 10^{-7}$ g [57, 58] has $\sqrt{m/M} = 10^{-8} - 10^{-5}$.
- The coupling constant scales with the resonance frequency. This is limited by the experimentally realizable potential curvature. Magnetic and optical traps for neutral atoms can reach $\omega_{\mathrm{at}}/2\pi \approx 1$ MHz [59, 60]. Ions in electric traps can have frequencies up to 50 MHz [61].
- The coupling scales with ϵ, which in most cases is quite small, $\epsilon \ll 1$.

In order to overcome the small mass ratio, one can experiment with molecular-scale oscillators such as carbon nanotubes [34]. Another trick to overcome the small coupling rate is to use high-finesse optical cavity, as is standard in the cavity QED experiments [62]. In the experiment described in this thesis, we overcome the small mass-ratio by using an ensemble of N atoms. This results in a collectively enhanced coupling by $\sqrt{N}$ as described in Chapter 3. Furthermore, in our system, the coupling potential provides both the coupling and the trap for the atoms, in which case $\epsilon = 1$.

---

[1] The zero-point energy contributions are omitted from the Hamiltonian from now on, as is the typical convention in the literature.

2.2 Optomechanics with Micromechanical Oscillators

Light forces can be exploited for cooling and control of the vibrations of mechanical oscillators ranging from macroscopic mirrors to micro-membranes and nanoscale cantilevers. The optomechanical setups vary from free-space Michelson interferometers [19, 63] to various types of cavity based setups [11], to waveguides [64] and evanescently coupled systems [65], where the latter experiments are operating on a chip. For an excellent review on the current state of optomechanics the reader is referred to Ref. [11] by M. Aspelmeyer, T. Kippenberg, and F. Marquart. Here we briefly discuss the most well-known optomechanical system of a Fabry-Pérot cavity in which a mechanical oscillator is used as one of the end mirrors of the cavity. In such a setup, the radiation pressure provides the dominant optomechanical coupling. Such a system has analogies to the coupling rate and cooling efficiency in our atom-membrane coupling experiment.

2.2.1 Dispersive Optomechanical Coupling

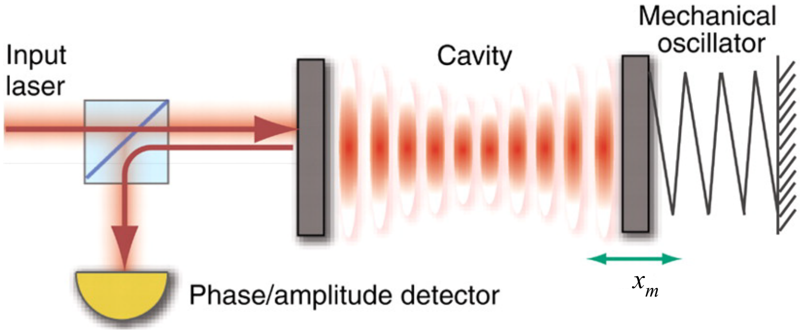

Figure 2.4: An optomechanical Fabry-Pérot cavity. Figure taken from [8].

A standard Fabry-Pérot based optomechanical system is illustrated in Fig. 2.4. A reflective mechanical oscillator is used as the other end mirror of a cavity. The reflection or transmission signal from the cavity gives information about the position fluctuations of the oscillator. The Hamiltonian for the system is

$$H = \hbar\omega_{\mathrm{cav}} a^\dagger a + \hbar\omega_{\mathrm{m}} b^\dagger b, \tag{2.60}$$

where ω_{cav} is the cavity resonance frequency, $a^\dagger a$ refers to the optical mode and $b^\dagger b$ describes the mechanical mode oscillating at ω_{m}. The cavity is resonant to the incoming light, when $q\lambda = 2L_{\mathrm{cav}}$, where q is an integer, λ is the wavelength of laser light, and L_{cav} is the cavity length[2]. The resonance frequency of the cavity is then $\omega_{\mathrm{cav}} = q\pi c/L_{\mathrm{cav}}$. When the end mirror moves by x_{m}, the cavity resonance

---

[2] For more details on the basics of Fabry-Pérot cavities, see Sec. 6.2.1

frequency changes by

$$\omega_{\mathrm{cav}} \approx \omega_{\mathrm{cav}} + \frac{\partial \omega_{\mathrm{cav}}}{\partial x_{\mathrm{m}}} x_{\mathrm{m}} = \omega_{\mathrm{cav}} - G_{\mathrm{opt}} x_{\mathrm{m}}, \tag{2.61}$$

where $G_{\mathrm{opt}} = -\partial \omega_{\mathrm{cav}} / \partial x_{\mathrm{m}}$ is the optical frequency shift per displacement. For the simple Fabry-Pérot cavity, $G_{\mathrm{opt}} = \omega_{\mathrm{cav}} / L_{\mathrm{cav}}$. Using this in Eq. 2.60, the coupled Hamiltonian can be expressed as

$$H = \hbar \omega_{\mathrm{cav}} a^\dagger a + \hbar \omega_{\mathrm{m}} b^\dagger b - \hbar G_{\mathrm{opt}} x_{\mathrm{m}} a^\dagger a. \tag{2.62}$$

We can express x_{m} in terms of its quantum operators, Eq. 2.24, and the interaction part of the Hamiltonian becomes [11]

$$H_{\mathrm{int}} = -\hbar g_0 a^\dagger a \left(b^\dagger + b \right), \tag{2.63}$$

where the single photon–single phonon optomechanical coupling is defined by

$$g_0 = G_{\mathrm{opt}} x_{\mathrm{zp}}. \tag{2.64}$$

The interaction of the oscillator with a single photon is fundamentally a *nonlinear* process on a single photon level.

2.2.2 Driven Cavity, Linearized Coupling

Often the single-photon interaction is small. To increase the interaction the cavity can be driven with a strong, coherent laser field [11]. A standard way to write the driven cavity field is in terms of its coherent amplitude $\langle a \rangle = \alpha$ and the quantum fluctuations δa around the amplitude as

$$a = \alpha + \delta a. \tag{2.65}$$

Using this in Eq. 2.63 and keeping only terms of first order in δa we get the linearized interaction term

$$H_{\mathrm{int}} \approx -\hbar g_0 \left(\alpha^* \delta a + a \delta a^\dagger \right) \left(b + b^\dagger \right). \tag{2.66}$$

The term proportional to $|\alpha|^2$ is omitted in Eq. 2.66 as it is a constant and results in an offset of the equilibrium position of the mirror. Finally, by writing this in the rotating-frame at $\Delta_{\mathrm{c}} = \omega_{\mathrm{L}} - \omega_{\mathrm{cav}}$, where ω_{L} is the laser frequency incident on the cavity, we encounter the linearized Hamiltonian of two coupled harmonic oscillators

$$H_{\mathrm{int}} = \hbar \omega_{\mathrm{m}} b^\dagger b - \hbar \Delta_{\mathrm{c}} \delta a^\dagger \delta a - \hbar g_{\mathrm{opt}} \left(\delta a + \delta a^\dagger \right) \left(b + b^\dagger \right). \tag{2.67}$$

Here the coupling constant g_{opt} is defined as

$$g_{\mathrm{opt}} = g_0 \alpha \equiv g_0 \sqrt{\bar{n}_{\mathrm{cav}}}. \tag{2.68}$$

The resulting Hamiltonian is linear in the displacement of the mechanics and quantum fluctuations of the laser field. Furthermore, the overall coupling becomes collectively enhanced via the square root of the number of cavity photons, $\sqrt{\bar{n}_{\rm cav}}$, and can consequently have large values.

In the strong-coupling regime, defined by $g_{\rm opt} > 2\kappa, \gamma_{\rm m}$, the coupling leads to optomechanical normal mode splitting [66]. To enter the quantum coherent coupling regime, the system must further satisfy

$$g_{\rm opt} > 2\kappa, \gamma_{\rm th}, \tag{2.69}$$

where $\gamma_{\rm th} = \gamma_{\rm m}\bar{n}_{\rm th}$ is the thermal decoherence rate. For example, in the Fabry-Pérot type of experiment in Ref. [66], the experimental parameters for the oscillator were $\omega_{\rm m} = 2\pi \cdot 947\,{\rm kHz}$, $m = 145\,{\rm ng}$ corresponding to $x_{\rm zp} = 2.4 \cdot 10^{-16}\,{\rm m}$; and for the cavity $L_{\rm cav} = 2.5\,{\rm mm}$, $\omega_{\rm cav} = 2\pi \cdot 2.82 \cdot 10^{14}\,{\rm Hz}$. The effective single photon coupling strength is $g_0 = 2\pi \cdot 2.7\,{\rm Hz}$. By enhancing the intensity inside the cavity, the total coupling was increased to $g_{\rm opt} = 2\pi \cdot 325\,{\rm kHz}$, which satisfied the strong coupling condition. Stronger single photon couplings have been achieved in another type of systems, e.g., Ref. [12] reports $g_0 = 2\pi \cdot 910\,{\rm kHz}$. The quantum coherent coupling regime has been demonstrated in Ref. [14], where a toroidal micro-cavity ($L_{\rm cav} = 31\,\mu{\rm m}$) is coupled to an intrinsic breathing mode ($\omega_{\rm m} = 2\pi \cdot 78\,{\rm MHz}$) of the toroid. In this experiment, $g_{\rm opt} = 2\pi \cdot 2\,{\rm MHz}$, which exceeds both the 2κ and the thermal decoherence rate at a base temperature of $T_{\rm bath} = 0.65\,{\rm K}$.

2.2.3 Optical Cooling of a Mechanical Oscillator

Optomechanical quantum control requires the oscillator to be close to its ground state, which necessitates the cooling of the selected mode of the oscillator. The first radiation pressure cooling experiment was demonstrated using an *active optical feedback* [67] for the vibrations of a cavity end-mirror. The position fluctuations of the oscillator were read from the cavity reflection signal (as illustrated in Fig. 2.4), and the information was used to modulate the intensity inside the cavity via an active feedback. Similar feed-back-cooling was later demonstrated in *free-space*, and in lower base-temperatures [68, 69]. The active optical cooling schemes operate usually in the adiabatic regime, where $\omega_{\rm m} < 2\kappa$, or in free-space. It has been theoretically shown that ground state cooling via active feedback is possible [70].

In the sideband-resolved regime $\omega_{\rm m} > 2\kappa$, the effects of dynamical backaction are larger than in the adiabatic regime, and can result in significant *passive optomechanical cooling.* Let us consider the Fabry-Pérot cavity in Fig. 2.4. The mechanical oscillator motion modulates the cavity resonance (Eq. 2.61), which in turn will lead to a modulated intensity inside the cavity. The intensity leads to radiation pressure modulation on the oscillator that has a phase lag with respect to the oscillator phase, due to the finite cavity decay time $(2\kappa)^{-1}$. The effect of backaction damping is largest when the $\Delta_\mathrm{c} = -\omega_\mathrm{m}$ which will result in damping of the mechanical mode at a rate [11]

$$\Gamma_\mathrm{opt} = 4\bar{n}_\mathrm{cav}\frac{g_0^2}{2\kappa} = \frac{2g_\mathrm{opt}^2}{\kappa}. \tag{2.70}$$

In order to reach a high cooling rate, 2κ should be small, which requires the use of high-finesse cavities. By using passive optical cavity cooling and starting from a cryogenic base temperature, Refs. [12, 14] have reached the ground state regime of a mechanical oscillator. A versatile spread of other types of optomechanical systems are also operating close to, or approaching the ground state regime [11].

2.3 Oscillator of Ultracold Atoms

In the main experiment we couple atoms to mechanical oscillator via a long-distance optical interface. The interface is an optical lattice which provides a nearly harmonic, periodic confinement for the atoms and mediates the long-distance coupling. In general, optical lattices have a broad range of applications varying from studying the dynamics of many-body Hamiltonians in periodic potentials (for review see Ref. [4]), usage as platforms for quantum information processing (for review see Ref. [71]), or serving as setups for precision measurements in atomic and molecular physics [72]. These systems allow to manipulate and detect the motional and internal states of atoms, and control atom-atom interactions on a single quantum level [4].

2.3.1 Optical Potential

Polarizable Particle in an Electric Field

When a polarizable particle is placed into an electric field $\mathbf{E}(\mathbf{r},t) = \hat{e}\frac{1}{2}E_0(\mathbf{r})\,e^{-i\omega t} +$ c.c, the field will induce a dipole moment $\mathbf{p}$ in the particle along its polarization direction $\hat{e}$. The dipole moment oscillates at the frequency of the driving field, and is related to the field by

$$\mathbf{p} = \alpha(\omega)\mathbf{E}, \tag{2.71}$$

where α is the complex polarizability of the particle. At the same time the electric field interacts with the induced dipole giving rise to a dipole potential [73]

$$\begin{aligned} V_\mathrm{dip} &= -\frac{1}{2}\langle \mathbf{p}\cdot\mathbf{E}\rangle && (2.72)\\ &= -\frac{1}{2\epsilon_0 c}\mathrm{Re}\,(\alpha)\,I\,(\mathbf{r})\,. && (2.73)\end{aligned}$$

The angular brackets in Eq. 2.72 denote the time average and the field intensity in Eq. 2.73 is

$$I\,(\mathbf{r}) = \frac{1}{2}\epsilon_0 c\,|E_0\,(\mathbf{r})|^2\,. \tag{2.74}$$

The real part of the polarizability gives rise to a conservative dipole force

$$F_{\text{dip}}\left(\mathbf{r}\right) = -\nabla V_{\text{dip}}\left(\mathbf{r}\right) = \frac{1}{2\epsilon_0 c}\text{Re}\left(\alpha\right)\nabla I\left(\mathbf{r}\right). \tag{2.75}$$

which is proportional to the intensity gradient of the trapping light. The imaginary part of the polarizability describes the out-of-phase component of the dipole oscillation and results in dissipative scattering of photons from the field at a rate [73]

$$\Gamma_{\text{sc}}\left(\mathbf{r}\right) = \frac{1}{\hbar\epsilon_0 c}\text{Im}\left(\alpha\right) I\left(\mathbf{r}\right). \tag{2.76}$$

This description holds in general for any polarizable particle in an oscillating electric field.

Rubidium Atom in an Electric Field

Let us consider a ^{87}Rb atom interacting with an optical field. The optical field is detuned by $\Delta_{\text{L}} = \omega_{\text{L}} - \omega_0$, from the resonance frequency ω_0 of the atomic transition. When $|\Delta_{\text{L}}|$ is a lot larger than the hyperfine splitting of the excited state, the atom experiences a dipole potential of the form [73]

$$V\left(\mathbf{r}\right) = \frac{\pi c^2 \gamma_{\text{se}}}{2\omega_0^3}\left(\frac{2+\mathcal{P}g_{\text{F}}m_{\text{F}}}{\Delta_{2,F}} + \frac{1-\mathcal{P}g_{\text{F}}m_{\text{F}}}{\Delta_{1,F}}\right) I\left(\mathbf{r}\right). \tag{2.77}$$

Here g_{F} is the Lande-factor and $\mathcal{P}$ characterizes the laser polarization; $\mathcal{P} = 0, \pm 1$ for linearly and circularly $\sigma^{\pm}$ polarized light. The natural line width of the Rubidium D-line is $\gamma_{\text{se}} = 2\pi \cdot 6$ MHz. The detunings $\Delta_{2,F}$ and $\Delta_{1,F}$ are defined with respect to the center of the D2 and D1 lines, respectively, where F=1,2 is the ground hyperfine state of the atom.

The ground state hyperfine splitting is small ($2\pi \cdot 6.8\,\text{GHz}$) for ^{87}Rb in comparison to the ground and excited state separation, ($|\Delta_{2,F} - \Delta_{1,F}| = 2\pi \cdot 7.1\,\text{Thz}$). By tuning the laser close to the D2-line, we can neglect the D1-line. In this case, and for linearly polarized light, the potential has a simple form

$$V_{\text{dip}} = \frac{\pi c^2 \gamma_{\text{se}}}{2\omega_0^3}\frac{2}{\Delta_{2,F}} I\left(\mathbf{r}\right) \tag{2.78}$$

This can be further written in terms of the saturation intensity $I_{\text{s}} = \hbar\gamma_{\text{se}}\omega_0^3/12\pi c^2$ of a two-level atom as

$$V_{\text{dip}} = \frac{\hbar\gamma_{\text{se}}^2}{12\Delta_{2,F}}\frac{I\left(\mathbf{r}\right)}{I_{\text{s}}}. \tag{2.79}$$

2.3.2 Optical Lattice with a Partially Reflecting Mirror

A periodic interference pattern of two or more beams is called an optical lattice, consisting of a large number of micro-traps for atoms. A simple, one dimensional lattice is formed by retro-reflecting a laser beam onto itself. Let us assume a Gaussian laser beam with a wave vector $k = \frac{2\pi}{\lambda}$ propagating along the z-axis. The Gaussian beam is focused to a waist of w_0 at the position $z = 0$. The Gaussian beam is described by its complex amplitude [74]

$$A(r,z) = A_0 \frac{w_0}{w(z)} \exp\left[-\frac{r^2}{w^2(z)}\right] \exp\left[-ikz - ik\frac{r^2}{2R(z)} + i\xi(z)\right]. \tag{2.80}$$

The term $w(z) = w_0 \left(1 + \left(\frac{z}{z_0}\right)^2\right)^{1/2}$ is the $(1/e)^2$radius of the beam intensity, and it increases within the Rayleigh range, $z_0 = \frac{\pi {w_0}^2}{\lambda}$, by a factor of $\sqrt{2}$. The term $R(z) = z\left(1 + \left(\frac{z_0}{z}\right)^2\right)$ is the curvature of the wave fronts, and $\xi(z) = \arctan\left(\frac{z}{z_0}\right)$ is the phase retardation due to the curvature, generally known as the Gouy-phase. When the Rayleigh length of the beam is a lot larger than the extension of the atomic ensemble trapped in the focus of the beam, the variation in the beam envelope along z can be neglected, and the complex amplitude can be written as

$$A(r,z) = A_0 \exp\left(-\frac{r^2}{w_0^2}\right) \exp(-ikz). \tag{2.81}$$

Let us now consider a case, where a linearly polarized Gaussian beam is retro-reflected from a mirror to create a lattice for atoms. We extend the general theory on optical lattices [73] to include experimental losses of the lattice light in the system. Experimental losses originate for example from the optical components in the beam path between the atoms and the mirror. We denote the finite amplitude transmissivity between the atoms and the mirror with t. Furthermore, the mirror is allowed to have a finite amplitude reflectivity $r_\mathrm{m} \leq 1$. This case is of specific interest to our experiment, where the lattice-mirror is a partially reflecting SiN-membrane. Under these considerations, the beam reflected from the mirror has a reduced amplitude by $r_\mathrm{m}t^2$ at the position of the atoms. Consequently, the resulting interference pattern at the position of the atoms,

$$I(r) = |A_\mathrm{inc} + A_\mathrm{ref}|^2 = |A_\mathrm{inc} + r_\mathrm{m}t^2 A_\mathrm{inc}|^2, \tag{2.82}$$

will consist of a sinusoidally modulated part and an offset as

$$I = I_0 \exp\left(-\frac{2r^2}{w_0^2}\right)\left(\left(1 + r_\mathrm{m}t^2\right)^2 - 4r_\mathrm{m}t^2 \sin^2(2kz)\right). \tag{2.83}$$

Here I_0 is the intensity at the focus of the incoming Gaussian beam, and it is defined as $I_0 = |A_0|^2 = 2P/(\pi w_0^2)$. Consequently, the peak intensity of the lattice has a value $\left(1 + r_\mathrm{m}^2 t^4 + 2r_\mathrm{m}t^2\right) I_0 \leq 4I_0$.

The intensity distribution results in a dipole potential of similar form, and according to Eqs. 2.79 and 2.83 we get

$$V(r,z) = \exp\left(\frac{-2r^2}{{w_0}^2}\right)\left(V_0 - V_\mathrm{m}\sin^2(kz)\right), \tag{2.84}$$

where the total potential and the modulation depth are given by

$$V_0 = \frac{\hbar\gamma_{\text{se}}^2}{12\Delta_{2,F}}\frac{I_0}{I_\text{s}}\left(1 + r_\text{m}t^2\right)^2, \tag{2.85}$$

and

$$V_\text{m} = \frac{\hbar\gamma_{\text{se}}^2}{12\Delta_{2,F}}\frac{I_0}{I_\text{s}}4r_\text{m}t^2. \tag{2.86}$$

If the thermal energy k_BT of an atomic ensemble is much smaller than the modulation depth V_m, the extension of the atomic wave function is radially small compared to the beam waist and axially small compared to the wavelength. In this case, the lattice potential wells can be approximated by a harmonic potential. By using the Taylor expansion, the trap frequencies ω_rad and ω_ax can be calculated by taking the harmonic term from an expansion of Eq. 2.84:

$$\omega_\text{rad} = \left(\frac{4|V_0|}{m{w_0}^2}\right)^{1/2} \tag{2.87}$$

$$\omega_\text{ax} \equiv \omega_\text{at} = \left(\frac{2|V_\text{m}|k^2}{m}\right)^{1/2}. \tag{2.88}$$

The ratio of the axial and radial trap frequencies is

$$\frac{\omega_\text{ax}}{\omega_\text{rad}} = \left(\frac{2w_0^2k^2r_\text{m}t^2}{\left(1 + r_\text{m}t^2\right)^2}\right)^{1/2}, \tag{2.89}$$

which implies that the axial trap frequency is higher by a factor of $\sim w_0/\lambda$ than the radial one. The trap frequencies of the atoms can be tuned experimentally, simply by changing the ratio of I_0/Δ. Optical traps for neutral atoms can reach $\omega_\text{at}/2\pi \approx 1\,\text{MHz}$ [34, 60].

An example of a partially modulated, one dimensional lattice potential is shown in Fig. 2.5. The potential is calculated using Eq. 2.84 and beam parameters similar to those used in our main experiment (see Ch. 5): $P = 64\,\text{mW}$, $w_0 = 355\,\mu\text{m}$, $\Delta_\text{2,F} = -2\pi\cdot 20.8\,\text{GHz}$, $\mathfrak{r} = |r_\text{m}|^2 = 0.28$, $\mathfrak{t} = |t|^2 = 0.81$. For ^{87}Rb the parameters are $m = 1.44\cdot 10^{-25}\,\text{kg}$, $\gamma_\text{se} = 2\pi\cdot 6.0\,\text{MHz}$, and $I_\text{s} = 1.7\,\text{mW/cm}^2$ [75]. The modulation depth is $|V_\text{m}| = 197\,\mu\text{K}$ and the total potential depth is $|V_0| = 253\,\mu\text{K}$. The resulting radial and axial trap frequencies are $\omega_\text{rad}/2\pi = 141\,\text{Hz}$ and $\omega_\text{ax}/2\pi = 246\,\text{kHz}$. Figure 2.6 shows the validity of the harmonic approximation. The closer the atoms are to the bottom of the trap, the better the approximation.

2.3.3 Cooling of Atoms

Typical dipole traps have depth on the order of hundreds of µK to mK [73]. In order to trap an atom in a dipole trap it needs to have a temperature below

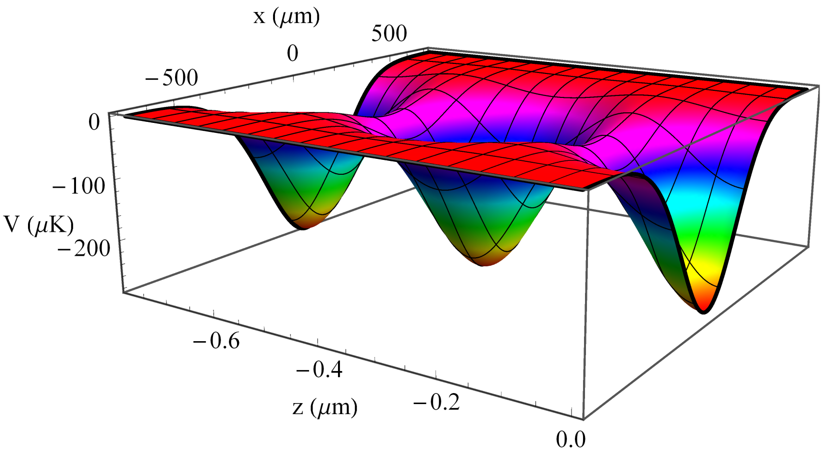

Figure 2.5: Optical lattice potential for ^{87}Rb. The potential is calculated using Eq. 2.84 and assuming $P = 64\,\mathrm{mW}$, $w_0 = 355\,\mu\mathrm{m}$, $\lambda = 780\,\mathrm{nm}$, $\Delta_{2,\mathrm{F}} = -2\pi \cdot 20.8\,\mathrm{GHz}$, $\mathfrak{r} = 0.28$, $\mathfrak{t} = 0.81$. The potential consist of a linear chain of tightly confining microtraps along the z-axis which are spaced by $\lambda/4$. The potential wells are harmonic around their minimum.

the trap depth. Once trapped, further cooling can be continued in the lattice to reach the motional ground state of the harmonic potential. The motional ground state requires that the temperature of the atoms is less than $\hbar\omega_{\mathrm{at}}/k_B$, where k_B is the Boltzmann constant. A standard way to capture atoms from background pressure is to use a magneto-optical trap which provides Doppler- and polarization gradient cooling on the atoms. The cold atoms can then be loaded to the lattice and cooled further in the lattice [76]. By using the powerful technique of Raman sideband cooling, $3 \cdot 10^8$ atoms have been prepared in the ground state of a large volume 3D lattice [77]. An excellent review of various laser cooling schemes is provided by one of the standard introductory books in

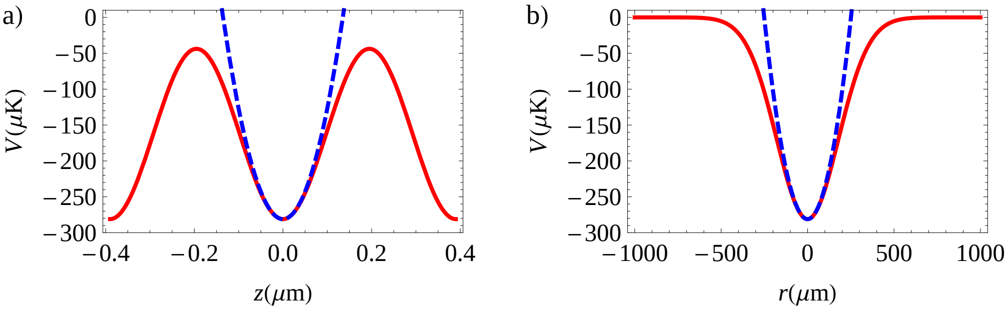

Figure 2.6: a) Trapping potential along the axial z direction (red) and the corresponding harmonic approximation (dashed blue). b) Trapping potential along the radial direction r (red) and the corresponding harmonic approximation (dashed blue).

the field, Reference [78].

2.3.4 Dissipation in Atomic Systems

As the atoms are trapped in free-space, they have no direct contact to their environment. In a standard setting of ultra-high vacuum only minute external dissipation is present due to collisions with the background gas.

In an optical trap, a spontaneous scattering event of a photon by the atom may result in a change of the internal state of the atom. This sets a limit on the internal state coherence. The scattering rate, Eq. 2.76, can be expressed in terms of trap depth V_0 as

$$\Gamma_{\mathrm{sc}} = \frac{\gamma_{\mathrm{se}}}{\hbar}\frac{V_0}{\Delta_{\mathrm{L}}}. \tag{2.90}$$

Because of the inverse dependence of Γ_{sc} on the detuning, optical dipole traps are often operated in the far-detuned regime, where scattering effects are suppressed. It has been shown experimentally that the spontaneous emission rate in far detuned optical lattices can be of the order of one emission in several minutes [79]. Furthermore, the spontaneous scattering rate is less strong for a blue-detuned lattice, where $\Delta_{\mathrm{L}} > 0$, than for red-detuned lattices. This is because for a blue-detuned optical lattice, the lattice sites are at positions of zero laser intensity while for a red-detuned optical lattice ($\Delta_{\mathrm{L}} < 0$) they are at locations of maximum laser intensity.

When considering the motion of the atoms in an optical trap, the photon scattering rate will lead to eventual momentum diffusion of the atomic motion at a rate [80]

$$\gamma_{\mathrm{at}}^{\mathrm{diff}} = (kl_{\mathrm{at}})^2 \gamma_{se}\frac{V_0}{\hbar\Delta_{\mathrm{L}}}, \tag{2.91}$$

where $l_{\mathrm{at}} = \sqrt{\hbar/m\omega_{\mathrm{at}}}$. In the Lamb-Dicke regime, where $kl_{\mathrm{at}} \ll 1$, a spontaneously scattered photon is unlikely to change the vibrational state of the atoms along the lattice. The momentum diffusion rate is smaller than the scattering rate by the Lamb-Dicke factor $(kl_{\mathrm{at}})^2$ and interestingly, it is the same for red and blue-detuned lattice [80]. The Lamb-Dicke suppression has been experimentally demonstrated in a tight confining optical lattice in Ref. [77].

An important contribution to the dephasing can arise from the trap anharmonicity. The potential created by a retroreflected Gaussian laser beam is harmonic only around the minimum of the trap, as shown in Fig. 2.6. When the higher order derivatives of the potential do not vanish in the Taylor expansion, the oscillation frequency of the atoms will depend on their oscillation amplitude. This leads to dephasing and excitation of higher order modes of the atomic ensemble as experimentally shown in Ref. [81]. Furthermore, in a lattice potential created by a Gaussian beam, the axial trapping frequency has a dependency on the radial position of the atom [82]. This spread in the axial trapping frequencies over the ensemble of atoms leads to additional dephasing of the atomic cloud.

This effect is analyzed in detail for a Gaussian lattice beam in Sec. 5.2. The contributions to dephasing from both the anharmonicity and the spread in the axial trapping frequencies can be minimized by ground state cooling of the atoms. The spread in axial trapping frequencies can also be reduced by proper beam shaping of the lattice beam. Other effects on the atomic diffusion typically originate from residual heating due to technical noise. In particular, slow drifts of the lattice parameters lead to a drift in the trap frequency and cause dephasing.

Levitated Nano-Objects

It has been proposed to use optical dipole traps to create conservative harmonic potential for dielectric objects in the context of optomechanics. The advantage of an optically levitated particle is its decoupling from the environment as discussed previously for the case of atoms. In two similar proposals [83, 84], a dielectric nano-object is trapped in a standing wave formed inside a cavity. The estimated Q-factor of a nano-sphere in a background pressure of 10^{-10} Torr is around 10^{12} [84]. In a wilder vision, the trapped nano-particle could be a living organism, like a virus. By creating a quantum superposition in the living object, one could test the quantum nature of living organisms [83].

Levitation of micro-meter size silica spheres in vacuum has been first demonstrated by Ashkin [85], and their cooling to ~mK regime has been achieved in Ref. [86]. Since then, also sub-micrometer sized particles have been trapped inside a vacuum and cooled via active feed-back [87] and cavity-cooling [88] techniques.

2.3.5 Backaction of Atoms on Trapping Beams

The light field creates a potential for the atoms, but the atoms also affect the light field. If an atom is displaced by x_{at} from the bottom of its potential well, it experiences a restoring optical dipole force according to Eq. 2.75

$$F_{\mathrm{d}} = -\frac{\partial V}{\partial x_{\mathrm{at}}} = -m\omega_{\mathrm{at}}^2 x_{\mathrm{at}} \tag{2.92}$$

from the lattice. On a microscopic level, F_{d} arises from absorption followed by stimulated emission, leading to a redistribution of photons between the two running wave components forming the lattice [89, 90]: the displaced atom preferentially absorbs photons from one of the lattice beams and re-emits them into the other. Each redistribution event results in a momentum transfer of $\pm 2\hbar k$ to the atom. On the other hand, the absorption and stimulated emission of photons from the same beam have no net effect on the atom. Let the rate of photon redistribution events be given by $\dot{n}$, then the change of momentum per unit time is $2\hbar k\dot{n} = NF_{\mathrm{d}}$, where N is the number of atoms in the lattice. Consequently, the photon redistribution modulates the power of the laser beam as

$$\Delta P = \hbar\omega\dot{n} = \frac{c}{2}NF_{\mathrm{d}}. \tag{2.93}$$

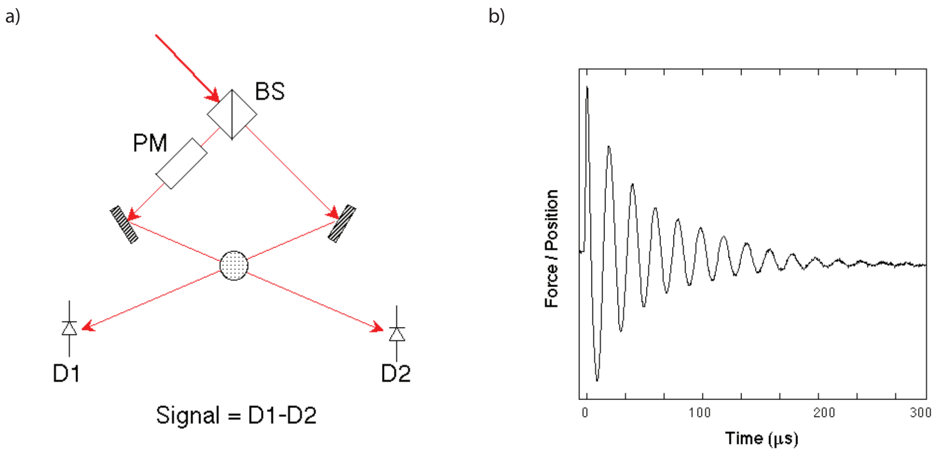

Figure 2.7: a) Configuration to measure the backaction of atoms on lattice laser beams: A laser beam is split at the beam splitter (BS). The phase modulator (PM) at the other arm is used to abruptly displace the minima of the lattice potential along the lattice axis. b) The moving atoms atoms redistribute light between the counter-propagating lattice beams until they reach the equilibrium. This effect has been studied in References [89, 91, 90]. Figure by courtesy of G. Raithel [92].

This type of backaction of atoms onto the light field has been previously studied in Ref. [89, 91, 90]. A simple schematic of the setup used in Ref. [89] to directly measure the ΔP predicted by Eq. 2.93 is shown in Fig. 2.7a. In the experiment, two counter-propagating laser beams form an optical lattice. The lattice minima are abruptly displaced by a phase modulator acting onto one of the lattice beams (as illustrated in Fig. 2.7). The power in each of the beams is measured after they have interacted with the atoms. A typical plot of this power modulation as a function of time is shown in Fig. 2.7b. Importantly, the amplitude of the oscillation decays in time. This is due to both anharmonic dephasing and decoherence due to spontaneous emission, as discussed previously.

Such an experimental setting has been used to determine the position of the oscillating wave-packet in time, and study the collapse and revival dynamics of the atoms in the lattice [89]. Furthermore, this technique has been used for real-time feedback control of the atomic motion [91], in analogy to passive cavity cooling of mechanical oscillators [93], and since then it has been extended to study and control polarizable particles in an optical trap [94].

Finally, and most importantly regarding this thesis, this type of backaction is the essence of our atom-membrane coupling scheme: the atoms imprint a signature of their motion as a power modulation onto the light field. This power modulation results then in a modulated radiation pressure force on the mechanical oscillator. This is discussed in detail in Chapter 3.

3

Theory of Atom–Membrane Coupling

This Chapter describes the theory of a hybrid optomechanical system, where the center of mass mode of an ensemble of ultracold atoms in an optical lattice is coupled via the lattice laser light to a microscopic membrane oscillator. Two related scenarios are discussed. In the first scenario, the atoms are trapped in a light field that is directly reflected from the membrane. In the second scenario, the membrane is enclosed inside an optical cavity, and the atoms are trapped in the light field directly reflected from the cavity. This theory was developed in collaboration with the group of P. Zoller. It is described in detail in References [33, 41].

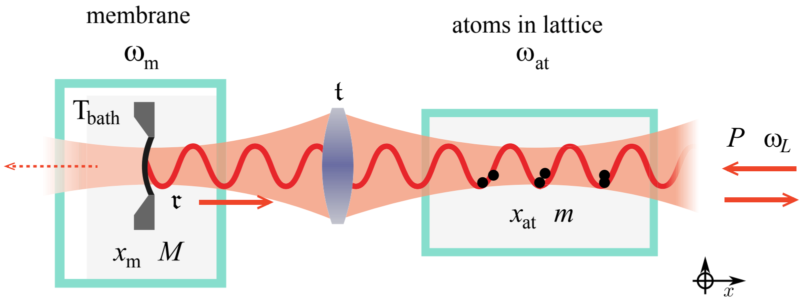

Figure 3.1: Schematic setup for long-distance, optomechanical coupling of ultracold atoms and membrane oscillator. The membrane is coupled to a thermal bath at temperature T_{bath}. The membrane oscillates at its eigenfrequency ω_{m} and with an amplitude x_{m}. A laser beam of power P and frequency ω_{L} is partially reflected at the membrane of reflectivity $\mathfrak{r} = |r_{\mathrm{m}}|^2$, and forms a one-dimensional optical lattice for an ultracold atomic ensemble. The atoms oscillate in the lattice at ω_{at}. The transmission losses in the optics between the membrane and the atoms are denoted by $\mathfrak{t} = |t|^2$.

3.1 Coupling in Free-Space

The coupling scheme we investigate is illustrated in Fig. 3.1. The membrane and atoms reside in separate vacuum chambers. The membrane has an eigenfrequency of ω_{m}, and it is connected to a support at temperature T_{bath}. A laser beam of power P, whose frequency ω_{L} is red detuned with respect to an atomic transition, impinges from the right onto the membrane and is partially retroreflected. The symbol $\mathfrak{r} = |r_{\mathrm{m}}|^2$ denotes the power reflectivity of the membrane. The reflected beam is overlapped with the incoming beam such that a 1D optical lattice potential of the form $V(x) = V_0 - V_{\mathrm{m}} \sin^2 [k(x - x_{\mathrm{m}})]$ is generated (Eq. 2.84). The potential is harmonic at the bottom of the potential wells and the axial trap frequency of the atoms is denoted by ω_{at} (Eq. 2.88). The modulation depth V_{m} is large enough to trap the pre-cooled ensemble of ultracold atoms. In addition, continuous laser cooling of the atoms in the lattice can be provided by additional laser beams.

3.1.1 Semiclassical Model

In the system presented in Fig. 3.1, the membrane-light coupling is due to radiation pressure and the atom-light coupling is due to the optical dipole force. To understand this coupling, let us start by investigating the effect of the membrane onto the atoms, which is illustrated in Figure 3.2a. A displacement of the membrane, x_{m}, displaces the lattice potential, resulting in a dipole force $F = m\omega_{\mathrm{at}}^2 x_{\mathrm{m}}$ onto each atom, where m is the atomic mass. The membrane motion thus couples through $F_{\mathrm{com}} = NF$ to the center of mass (c.o.m.) motion of an ensemble of N

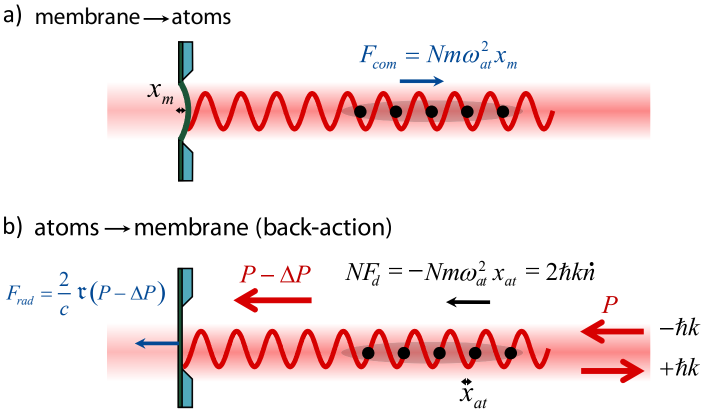

Figure 3.2: a) Illustration of the action of the membrane onto the atoms. b) The atoms act back onto the membrane via redistribution of photons between the two counter-propagating laser beams, which causes a power modulation ΔP of the light that hits the membrane.

atoms trapped in the lattice. An oscillating membrane will parametrically excite the atoms that have a trap frequency equal to that of the membrane.

Vice versa, the atoms will imprint a signature of their c.o.m. motion onto the light field. An atom displaced by x_{at} from the bottom of its potential well experiences a restoring optical dipole force

$$F_{\text{d}} = -\frac{\partial V}{\partial x_{\text{at}}} = -m\omega_{\text{at}}^2 x_{\text{at}} \tag{3.1}$$

from the lattice. This is illustrated in Figure 3.2b. The dipole force is due to a redistribution of photons between the two running wave components forming the lattice, as discussed in Sec. 2.3.5. The photon redistribution modulates the power of the laser beam traveling towards the membrane by

$$\Delta P = \hbar\omega\dot{n} = -\frac{c}{2}NF_{\text{d}}, \tag{3.2}$$

where $\dot{n}$ is the total photon redistribution rate due to the N atoms. This leads to a modulation of the radiation pressure force acting on the membrane

$$\Delta F_{\text{rad}} = \frac{2}{c}\mathfrak{r}\mathfrak{t}\Delta P = -\mathfrak{r}\mathfrak{t}NF_{\text{d}} = \mathfrak{r}\mathfrak{t}Nm\omega_{\text{at}}^2 x_{\text{at}}. \tag{3.3}$$

Some of the photons that have interacted with the atoms are lost from the system because of the finite reflectivity of the membrane and losses in the optics $\mathfrak{r}\mathfrak{t} < 1$. The lost photons do not contribute to the force on the membrane, which leads to *asymmetric* coupling, i.e., $|\Delta F_{\text{rad}}| = \mathfrak{r}\mathfrak{t}|F_{\text{com}}|$. If the losses in the beam path and finite membrane reflectivity are neglected ($\mathfrak{r}\mathfrak{t} = 1$), the forces experienced by the displaced atoms and the membrane are exactly equal in magnitude, but opposite in sign, following the action-reaction principle.

3.1.2 Coupled Oscillator Dynamics under Dissipation

In a simple model of damped harmonic oscillators coupled through F_{com} and ΔF_{rad}, the equations of motion for the fundamental vibrational mode of the membrane and the c.o.m. motion of the atoms can be written as

$$\begin{aligned}
\dot{p}_{\mathrm{at}} &= -\gamma_{\mathrm{at}} p_{\mathrm{at}} - N m \omega_{\mathrm{at}}^2 x_{\mathrm{at}} + N m \omega_{\mathrm{at}}^2 x_{\mathrm{m}} \\
\dot{x}_{\mathrm{at}} &= p_{\mathrm{at}}/Nm \\
\dot{p}_{\mathrm{m}} &= -\gamma_{\mathrm{m}} p_{\mathrm{m}} - M \omega_{\mathrm{m}}^2 x_{\mathrm{m}} + \mathfrak{rt} N m \omega_{\mathrm{at}}^2 x_{\mathrm{at}} \\
\dot{x}_{\mathrm{m}} &= p_{\mathrm{m}}/M, \qquad (3.4)
\end{aligned}$$

where γ_{m} (γ_{at}) is the motional damping rate of the membrane (atoms). The atomic and membrane momentum and displacement can be conveniently written in terms of the quadratures. For example, for the atoms we define

$$a = \sqrt{\frac{N m \omega_{\mathrm{at}}}{2\hbar}} \left(x_{\mathrm{at}} + \frac{i}{m\omega_{\mathrm{at}}} p_{\mathrm{at}}\right) \qquad (3.5)$$

resulting in

$$\begin{aligned}
x_{\mathrm{at}} &= \sqrt{\frac{\hbar}{2 N m \omega_{\mathrm{at}}}} \left(a^\dagger + a\right) \qquad (3.6) \\
p_{\mathrm{at}} &= i\sqrt{\frac{\hbar N m \omega_{\mathrm{at}}}{2}} \left(a^\dagger - a\right). \qquad (3.7)
\end{aligned}$$

Using similar quadratures for the membrane and denoting the membrane annihilation operator by b, Eqs. 3.4 can be written as

$$\begin{aligned}
\dot{a} &= -i\omega_{\mathrm{at}} a + \frac{\gamma_{\mathrm{at}}}{2}(a^\dagger - a) + ig(b^\dagger + b) \qquad (3.8) \\
\dot{b} &= -i\omega_{\mathrm{m}} b + \frac{\gamma_{\mathrm{m}}}{2}(b^\dagger - b) + i\mathfrak{rt} g(a^\dagger + a) \qquad (3.9)
\end{aligned}$$

where the coupling constant is defined as

$$g := \frac{\omega_{\mathrm{at}}}{2}\sqrt{\frac{N m \omega_{\mathrm{at}}}{M \omega_{\mathrm{m}}}}. \qquad (3.10)$$

Eqs. 3.8 and 3.9 can be transferred to a frame rotating at ω_{m} using the variables

$$\begin{aligned}
c &:= a e^{i\omega_{\mathrm{m}} t} \qquad (3.11) \\
d &:= b e^{i\omega_{\mathrm{m}} t} \qquad (3.12)
\end{aligned}$$

resulting in the coupled equations of motion for the atoms and the membrane

$$\begin{aligned}
\dot{c} &= -i(\omega_{\mathrm{at}} - \omega_{\mathrm{m}})c + \frac{\gamma_a}{2}(c^\dagger e^{i2\omega_{\mathrm{m}} t} - c) + ig\left(d^\dagger e^{i2\omega_{\mathrm{m}} t} + d\right), \qquad (3.13) \\
\dot{d} &= \frac{\gamma_{\mathrm{m}}}{2}\left(d^\dagger e^{i2\omega_{\mathrm{m}} t} - d\right) + i\mathfrak{rt} g\left(c^\dagger e^{i2\omega_{\mathrm{m}} t} + c\right). \qquad (3.14)
\end{aligned}$$

The two systems can exchange energy, when they are near-resonantly coupled, $\omega_\mathrm{m} \approx \omega_\mathrm{at}$. Furthermore, if $\omega_\mathrm{m} \approx \omega_\mathrm{at} \gg g, \gamma_\mathrm{at}, \gamma_\mathrm{m}$, as is the case in our experiment, the fast rotating terms $\propto e^{\pm i 2\omega_\mathrm{m} t}$ can be neglected in the equations of motion for c and d. This rotating-wave approximation (RWA) results in a set of coupled equations:

$$\begin{aligned} \dot{c} &= -i\delta c - \frac{\gamma_\mathrm{at}}{2} c + igd \\ \dot{d} &= -\frac{\gamma_\mathrm{m}}{2} d + i\mathfrak{rt} g c, \end{aligned} \tag{3.15}$$

where $\delta = \omega_\mathrm{at} - \omega_\mathrm{m}$ is the atom-membrane detuning.

Even though the mass ratio of an atom to the membrane will be exceedingly small under reasonable conditions ($m/M \approx 10^{-14}$), the coupling constant g can still be significant due to collective enhancement by the large number of atoms N. The coupling leads to both a modified damping rate (dispersive part of the coupling) as well as a frequency shift (reactive part). Both effects are obtained by solving for the eigenvalues $v_\pm$ of Eqs. (3.15):

$$v_\pm = -\frac{\gamma_\mathrm{at} + \gamma_\mathrm{m} + 2i\delta}{4} \pm \sqrt{\left(\frac{\gamma_\mathrm{at} - \gamma_\mathrm{m} + 2i\delta}{4}\right)^2 - \mathfrak{rt} g^2}. \tag{3.16}$$

The normal mode oscillation frequencies are given by $\mathfrak{Im}\{v_\pm\}$, while the amplitude damping rates are given by $-\mathfrak{Re}\{v_\pm\}$. In our experiment (described in Ch. 5), we operate in the weak-coupling regime, where $\gamma_\mathrm{at} \gg g, \gamma_\mathrm{m}$. In this regime, the frequency shift due to the coupling is zero on resonance within the RWA. A calculation beyond the RWA shows that the frequency shift is $\ll 1$ Hz for our parameters, and thus not observable in the experiment. On the other hand, in the strong-coupling regime where $g \gg (\gamma_\mathrm{at}, \gamma_\mathrm{m})$, the coupling leads to a normal-mode splitting of $2g\sqrt{\mathfrak{rt}}$ on resonance.

Weak-Coupling Regime

In the weak-coupling regime ($\gamma_\mathrm{at} \gg g, \gamma_\mathrm{m}$), the energy damping rate of the membrane, $-2\mathfrak{Re}\{v_+\}$, is given to lowest order in g by

$$\Gamma_\mathrm{c} = \gamma_\mathrm{m} + \gamma_\mathrm{at} \frac{g^2 \mathfrak{rt}}{\delta^2 + (\gamma_\mathrm{at}/2)^2}. \tag{3.17}$$

The second term in Eq. (3.17) is the additional dissipation rate of the membrane motion due to coupling to atoms,

$$\begin{aligned} \Delta\gamma = \Gamma_\mathrm{c} - \gamma_\mathrm{m} &= \gamma_\mathrm{at} \frac{g^2 \mathfrak{rt}}{\delta^2 + (\gamma_\mathrm{at}/2)^2} && (3.18) \\ &= \frac{\gamma_\mathrm{at}}{4} \frac{Nm}{M} \frac{\omega_\mathrm{at}}{\omega_\mathrm{m}} \frac{\omega_\mathrm{at}^2 \mathfrak{rt}}{\delta^2 + (\gamma_\mathrm{at}/2)^2} \propto N, && (3.19) \end{aligned}$$

which scales linearly with N.

In the experimental realization, we have two different contributions to the overall atomic damping rate

$$\gamma_{\mathrm{at}} = \gamma_\phi + \gamma_{\mathrm{c}}. \tag{3.20}$$

The first term, γ_ϕ, describes additional dephasing of the c.o.m. motion due to finite temperature of the atoms and the spatial dependence of the trap frequency on the lattice laser intensity profile. The value of γ_ϕ is intrinsic to the experimental realization and constant when the atomic motion is in steady-state. The second term, γ_{c}, is the laser cooling rate of the atoms, which can be adjusted, and thus provides an experimental handle to tune the dissipation in the system. In the experiment, we apply strong laser cooling to the atoms, $\gamma_c \gg g, \gamma_{\mathrm{m}}$, so that the atomic c.o.m. amplitude is approximately in steady state ($\dot{c} \simeq 0$) on the much slower timescale of membrane dynamics. This results in sympathetic damping of the membrane vibrations as (Eq. 3.17)

$$b(t) = b_0 e^{-\frac{\Gamma_{\mathrm{c}}}{2} t} e^{-i\omega_{\mathrm{m}} t}. \tag{3.21}$$

Thus, the atoms can be used for sympathetic cooling of the membrane mode.

An estimate for the change in the damping of the membrane due to the atoms is shown in Fig. 3.3. In the weak-coupling regime, the width of the resonance in Eq. 3.18, is dominated by γ_{at}. As long as $\gamma_{\mathrm{c}} \gg \gamma_\phi$, we can neglect the effect of γ_ϕ on the coupling strength. The full quantum calculation in Ref. [33] solves the dynamics of the system beyond the weak-coupling regime and shows that an optimum for the laser-cooling rate exists. The optimum is reached at $\delta = 0$, when $\gamma_{\mathrm{c}} \sim g$. Increasing the atomic cooling rate γ_c further will only broaden the atomic resonance, but does not increase the cooling rate of the membrane.

3.1.3 Quantum Dynamics

The foregoing considerations did not provide any information about the noise processes that fundamentally limit the performance of our system, and essentially define the final phonon occupation number in the membrane mode. The semiclassical description allows the membrane amplitude (Eq. 3.21) decay to zero which is in controversy with the quantum mechanical description of zero-point fluctuations, as discussed Sec. 2.1 (Eq. 2.29). To account for these effects, a fully quantized treatment of our system has been developed together with K. Hammerer, K. Stanningel, C. Genes and P. Zoller, and is described in Ref. [33]. The theory shows that the results of the simple model described above hold for the corresponding quantum-mechanical expectation values in the absence of noise processes.[1] Here, the relevant noise terms are reviewed in terms of the master

---

[1] Note a difference in notation: here and in Ref. [39] we define the coupling constant as $g = \frac{\omega_{\mathrm{at}}}{2}\sqrt{\frac{Nm\omega_{\mathrm{at}}}{M\omega_{\mathrm{m}}}}$, whereas in Ref. [33] it is defined as $g = \omega_{\mathrm{at}}\sqrt{\frac{Nm\omega_{\mathrm{at}}}{M\omega_{\mathrm{m}}}}$. Note also that there is a typo in the effective cooling rate on resonance given in Ref. [33], it should read $\Gamma_{\mathrm{c}} = \gamma_{\mathrm{m}} + \mathfrak{r} g^2/\gamma_{\mathrm{at}}^{cool}$ using the notation of that paper.

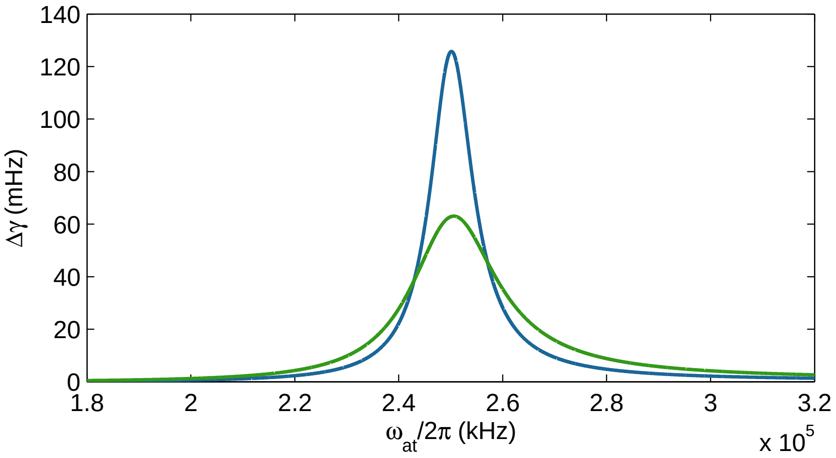

Figure 3.3: The increase in the damping of the membrane due to coupling to atoms using Eq. 3.18 and for two different atomic damping rates: $\gamma_{\rm at} = 2\pi \cdot 10\,{\rm kHz}$ (blue) and $\gamma_{\rm at} = 2\pi \cdot 20\,{\rm kHz}$ (green). The other parameters assumed in the calculation are: $\omega_{\rm m} = 2\pi \cdot 250\,{\rm kHz}$, $N = 1 \cdot 10^6$, $m = 1.4410^{-25}\,{\rm kg}$, $M = 1 \cdot 10^{-11}\,{\rm kg}$, $\mathfrak{r} = 0.28$, $\mathfrak{t} = 0.82$.

equation formalism.

Master Equation of a Quantum Cascaded System

The total Hamiltonian for our optomechanical system is

$$H = H_{\rm m} + H_{\rm at} + H_{\rm field} + H_{\rm m-f} + H_{\rm a-f}, \tag{3.22}$$

where $H_{\rm m}$, $H_{\rm at}$ and $H_{\rm field}$ describe the free evolution of the mechanics, the external atomic degrees of freedom, and the field modes. Further, $H_{\rm m-f}$ represents the coupling between mechanical and field modes, and $H_{\rm at-f}$ is the interaction between atoms and field modes. We are only interested in the dynamics between the membrane and the atoms that is mediated by the light field. In the regime, where retardation effects of the light-field do not play a role, the light field is assumed to be in steady-state on the time-scale of the atomic and membrane dynamics. Such a Born-Markov approximation justifies an adiabatic elimination of the light field, and the resulting quantized Hamiltonian [41]

$$H_{\rm eff} = \hbar\omega_{\rm m} b^\dagger b + \hbar\omega_{\rm at} a^\dagger a - \hbar g \tilde{x}_{\rm m} \tilde{x}_{\rm at}, \tag{3.23}$$

corresponds to that of two coupled harmonic oscillators, similar to the description in Sec. 2.1.4. In equation 3.23 we use dimensionless variables $\tilde{x}_{\rm at} = \frac{1}{\sqrt{2}}\left(a^\dagger + a\right)$ and $\tilde{x}_{\rm m} = \frac{1}{\sqrt{2}}\left(b^\dagger + b\right)$. Using this notation g is defined by Eq. 3.10.

In the limit where the reflectivity of the membrane is $\mathfrak{r} = 1$, Eq. 3.23 can be used to describe our system. However, when $\mathfrak{r} < 1$ we encounter asymmetric coupling between the membrane and the atoms. This implies that the dynamics are not anymore purely Hamiltonian. The semiclassical model in Sec. 3.1.1 explains well the asymmetric coupling between the atoms and the membrane originating from the finite reflectivity of the membrane $\mathfrak{r}$. To include the asymmetry in the quantized description, the dynamics of the system can be derived from the following master equation [33]

$$\dot{\rho} = -\frac{i}{\hbar}[H_{\text{eff}}, \rho] + C\rho + \mathcal{L}_{\text{m}}\rho + \mathcal{L}_{\text{at}}\rho, \tag{3.24}$$

where H_{eff} is as in Eq. 3.23, and the second term

$$C\rho = -\frac{i}{2}(1-\mathfrak{r})g([\tilde{x}_{\text{m}}, \tilde{x}_{\text{at}}\rho] - [\rho\tilde{x}_{\text{at}}, \tilde{x}_{\text{m}}]) \tag{3.25}$$

accounts for the asymmetry in the coupling. $C\rho$ is proportional to the membrane transmittivity, $(1-\mathfrak{r})$. The peculiar form of this term is a generic feature of so-called *cascaded quantum systems* [95, 96]. This type of cascaded master equation reproduces the semiclassical considerations on the asymmetry as $\langle\dot{p}_{\text{at}}\rangle = -g\langle x_{\text{m}}\rangle + ...$, while $\langle\dot{p}_{\text{m}}\rangle = -g\mathfrak{r}\langle x_{\text{at}}\rangle + ...$, where the dots denote terms that do not depend on g. The other Lindblad terms in Eq. 3.24 are addressed below.

Decoherence and Imperfections at the Membrane: $\mathcal{L}_{\text{m}}\rho$

The Lindblad term $\mathcal{L}_{\text{m}}$ describes thermal heating of the membrane due to clamping losses and absorption, and in addition takes into account the radiation pressure noise on the membrane. Let us assume the membrane support is at temperature T_0. The heating of the membrane due to absorbance can be modeled by introducing an effective bath temperature $T_{\text{bath}} = T_0 + \Delta T$, where $\Delta T = \frac{P_{\text{abs}}}{K_{\text{th}}}$ is the temperature increase of the membrane due to absorbed power P_{abs} in the center of the membrane. K_{th} is the thermal link that connects the center of the membrane to the support. It is defined by the thermal conductivity and the size of the membrane, as well as the beam waist of the laser on the membrane (see Ch. 4.2 and Eq. 4.14). Consequently, an effective bath occupation can be defined as

$$\bar{n}_{\text{th}} \approx \frac{k_B T_{\text{bath}}}{\hbar\omega_{\text{m}}} = \frac{k_B}{\hbar\omega_{\text{m}}}\left(T_0 + \Delta T\right), \tag{3.26}$$

which gives rise to a thermal decoherence rate

$$\gamma_{\text{th}} = \gamma_{\text{m}}\bar{n}_{\text{th}} \approx \frac{k_B\left(T_0 + \Delta T\right)}{\hbar Q}. \tag{3.27}$$

The $\mathcal{L}_{\text{m}}$ also includes the radiation pressure noise on the membrane, which scales linearly with the power on the membrane as [33, 97]

$$\gamma_{\text{m}}^{\text{diff}} = \left(\frac{4\mathfrak{r}P_{\text{mem}}}{Mc^2}\right)\left(\frac{\omega_{\text{L}}}{\omega_{\text{m}}}\right), \tag{3.28}$$

where ω_{L} is the photon frequency.

Decoherence and Laser Cooling of the Atoms: $\mathcal{L}_{\rm at}\rho$

The atoms undergo diffusion processes in the lattice. $\mathcal{L}_{\rm at}$ accounts for the momentum diffusion rate of the atoms [80, 41] according to Eq. 2.91

$$\gamma_{\rm at}^{\rm diff} = (kl_{\rm at})^2 \gamma_{se} \frac{V_0}{\hbar|\Delta_{\rm L}|}, \tag{3.29}$$

where γ_{se} is the natural line-width of the transition, $l_{\rm at} = \sqrt{\hbar/m\omega_{\rm at}}$ and V_0, is the depth of the potential. Uniquely, we can also introduce *controlled dissipation* into the system via continuous laser cooling of the atoms at a rate $\gamma_{\rm c}$.

Sympathetic Cooling

In the weak-coupling limit, $\gamma_{\rm at} \sim \gamma_{\rm c} \gg g, \gamma_{\rm m}, \gamma_{\rm m}^{\rm diff}, \gamma_{\rm at}^{\rm diff}$, a strong laser-cooling of the atoms results in sympathetic cooling of the membrane mode at a rate given by Eq. 3.17. The membrane dynamics follow the equation

$$\frac{d}{dt}\langle b^\dagger b\rangle = -\Gamma_{\rm c}\left(\langle b^\dagger b\rangle - \bar{n}_{\rm ss}\right), \tag{3.30}$$

where the steady-state phonon occupation of the membrane mode is [33, 41]

$$\begin{aligned} \bar{n}_{\rm ss} &\approx \frac{\gamma_{\rm m}\bar{n}_{\rm th} + \gamma_{\rm m}^{\rm diff}/2}{\Gamma_{\rm c}} + \left(\frac{\gamma_{\rm c}}{4\omega_{\rm at}}\right)^2 + \frac{\gamma_{\rm at}^{\rm diff}}{2\gamma_{\rm c}} \\ &\equiv n_{ss,1} + n_{ss,2} + n_{ss,3}. \end{aligned} \tag{3.31}$$

The $n_{ss,i}$ are contributions due to mechanical heating, 'counter-rotating' terms in the coupling $(ba, b^\dagger a^\dagger)$ and atomic heating, respectively.

3.1.4 Experimental Requirements for Coherent Coupling

Theoretical estimates show that sympathetic ground-state cooling of the membrane via the atoms as well as the strong coherent coupling regime could be achieved with present technology [33]. This is, however, very challenging. The coherent coupling regime becomes accessible, when the condition

$$g > \gamma_{\rm at}^{\rm diff}, \gamma_{\rm m}^{\rm diff}, \gamma_{\rm th}, \tag{3.32}$$

is fullfilled. One possible set of membrane and lattice parameters that fulfill the requirements for coherent coupling regime is tabulated in Tab. 3.1.

The parameters for the atom module result in an optical lattice that satisfies the resonant coupling requirement $\omega_{\rm m} \sim \omega_{\rm at} \sim 2\pi \cdot 0.86\,\mathrm{MHz}$. As the coupling scales with $\sqrt{N}$, large atom number in the trap is crucial. Atom numbers as large as $N = 3 \cdot 10^8$ have been prepared in the ground-state of a 3D-lattice using Raman sideband cooling. At the same time, Raman sideband cooling rate of $\gamma_{\rm c} = 20\,\mathrm{kHz}$ was demonstrated [77]. This would result in sympathetic cooling

Membrane		**Lattice**		**Rates**	
size	$(150\,\mu\mathrm{m})^2 \times 50\,\mathrm{nm}$	λ	$780\,\mathrm{nm}$	g	40 kHz
ω_m	$2\pi \cdot 0.86\,\mathrm{MHz}$	ω_at	$2\pi \cdot 0.86\,\mathrm{MHz}$	$\gamma_\mathrm{m}^\mathrm{diff}$	52 Hz
M	$8 \cdot 10^{-13}\,\mathrm{kg}$	P	$7\,\mathrm{mW}$	$\gamma_\mathrm{at}^\mathrm{diff}$	16 kHz
Q	10^7	w_0	$230\,\mu\mathrm{m}$	γ_th	6 kHz
$\mathfrak{r}$	0.31	Δ_L	$-2\pi \cdot 1\,\mathrm{GHz}$		

Table 3.1: An example of experimental parameters required to enter the strong, coherent coupling regime starting from a cryogenic bath temperature of 500 mK. The parameters are those of Ref. [33]. The membrane reflectivity $\mathfrak{r}$ and the atom number N are demonstrated in Refs. [58] and [77]. The table on the right displays the resulting coupling and decoherence rates.

of the membrane by a factor of $\bar{n}_\mathrm{th}/\bar{n}_\mathrm{ss} \simeq 2 \cdot 10^4$ [33], resulting in a $\bar{n}_\mathrm{ss}$=0.8 at $T_\mathrm{bath} = 500\,\mu\mathrm{K}$.

The inhomogeneous intensity profile of the lattice beam will lead to some spread $\Delta\omega_\mathrm{at}$ of atomic vibrational frequencies as discussed in Sec. 2.3, which leads to dephasing of the center of mass motion of the atoms. This effect can be neglected, when considering the sympathetic cooling of the membrane in the weak-coupling regime as long as

$$\Delta\omega_\mathrm{at} \ll \gamma_\mathrm{c}. \tag{3.33}$$

For the coherent coupling regime we must in addition require

$$\Delta\omega_\mathrm{at} \ll g. \tag{3.34}$$

The estimates given in Tab. 3.1 assume operation in a regime, where Eqs. 3.33 and 3.34 are satisfied.

The challenge on the membrane side is set by the thermal decoherence rate. This can be reduced by decreasing the bath temperature. For example, γ_th is 4 MHz at room temperature, but only 6 kHz at 500 mK cryogenic environment. Another factor affecting γ_th is the heating of the membrane due to absorption. The heating can be modeled as an increase in the bath temperature of the membrane, Eq. 3.27, which is determined by the thermal conductivity and absorbance $\mathrm{Im}\,(n_\mathrm{m})$ of the membrane. We have measured $\mathrm{Im}\,(n_\mathrm{m})$ to be $1.5 \cdot 10^{-3}$ and $\lesssim 2 \cdot 10^{-5}$ for low-stress and high-stress membranes, respectively (see Ch. 4.2). On the other hand, the thermal conductivity of thin SiN membranes in cryogenic temperatures is not well known. As an example, assuming $\mathrm{Im}\,(n_\mathrm{m}) \sim 10^{-5}$ and a thermal link $K_\mathrm{th} = 2.5 \cdot 10^{-7}\,\mathrm{W/K}$, the resulting temperature increase is $\Delta T \sim 0.22\,\mathrm{K}$, which would increase the γ_th by a factor of 1.4. The value of K_th is calculated here assuming the measured 2 K heat conductivity for low-stress, SiN membranes from [98]. However, for a high-stress membrane the value can be different, and furthermore it seems to depend on the thickness of the membrane [99].

3.2 Cavity-Enhanced Coupling

A relatively simple trick to enhance the atom-membrane coupling is to enclose the membrane inside an optical cavity as illustrated in Fig. 3.4. In this scheme, the atoms remain outside the cavity, as they are trapped in the light field reflected from the cavity. Adding the cavity to the setup preserves the modularity, while the coherent coupling between the two system is enhanced by the cavity finesse in addition to the collective enhancement via the $\sqrt{N}$. Furthermore, the asymmetric coupling is not encountered anymore, as all the light is reflected back to the atoms by the cavity.

3.2.1 Theoretical Model

The enhancement in the coupling due to the cavity can be understood qualitatively. A laser beam comes from the right, passes through the atoms and enters the resonant cavity as illustrated in Fig. 3.4. The membrane is placed inside the cavity on the middle of the cavity field slope, where its coupling to the cavity field is largest. The cavity is single-sided, such that most of the light inside the cavity is reflected back forming an optical lattice for the atoms. A displacement of the membrane inside the cavity by x_{m} detunes the cavity (Eq. 6.25). This leads to a phase-shift $\delta\theta \sim \mathfrak{F} x_{\mathrm{m}}/\lambda$ of the reflected light in proportion to the cavity finesse $\mathfrak{F}$ (Eq. 6.12). The phase shift results in spatial translation of the lattice potential. As the dipole force acting onto the atoms scales linearly with the translation (Eq. 3.1), the action of the membrane onto the atoms becomes enhanced $\propto \mathfrak{F}$.

On the other hand, the oscillating atoms will imprint a power modulation onto the lattice (Eq. 3.2) which will be enhanced on the membrane by the cavity $\mathfrak{F}$, resulting in a radiation pressure force on the membrane that is increased by $\mathfrak{F}$. Overall, these effects will lead to an increase of the atom-membrane coupling constant defined in Eq. 3.10 as

$$g \propto m\omega_{\mathrm{at}}^2 \sqrt{\frac{m}{M}} \mathfrak{F} \sqrt{N}. \tag{3.35}$$

A rigorous, quantum mechanical treatment of this type of cavity-enhanced coupling scheme has been derived in Ref. [41]. The optical cavity is operated in the non-resolved sideband regime, where the cavity half line-width is much larger than the mechanical frequency, i.e., $\kappa \gg \omega_{\mathrm{m}}, \omega_{\mathrm{at}}$. This is illustrated schematically in Fig. 3.5. In this regime, the time retardation between mechanics and the atomic ensemble is short compared to the systems evolution, and consequently the light field follows the dynamics of the membrane and atoms instantaneously. This assumption corresponds to the Born-Markov approximation and allows similar elimination of the light field from the Hamiltonian dynamics as in the free-space case discussed earlier. The remaining Hamiltonian is that for two coupled oscillators (cf. Eq. 3.23)

$$H_{\mathrm{eff}} = \hbar\omega_{\mathrm{m}} a_{\mathrm{m}}^{\dagger} a_{\mathrm{m}} + \hbar\omega_{\mathrm{at}} \omega_{\mathrm{at}}^{\dagger} - \hbar g \tilde{x}_{\mathrm{m}} \tilde{x}_{\mathrm{at}}, \tag{3.36}$$

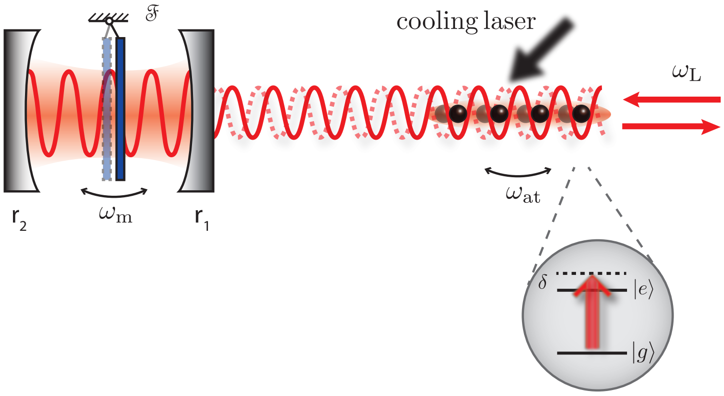

Figure 3.4: In a modified coupling scheme the membrane is enclosed inside an optical cavity. The optical cavity is single-sided such that the back mirror has reflectivity $r_2 \sim 1$ and most of the light in the cavity is transmitted via the input mirror $r_1 \ll r_2$ creating an optical lattice trap for the atoms. Such a simple modification results in an enhanced coupling strength proportional to the cavity finesse, $\mathfrak{F}$, while it still preserves the modularity of the coupling scheme.

where a unified coupling constant can be defined as [41]

$$g = \frac{\omega_\mathrm{at}}{2}\sqrt{N}\sqrt{\frac{m}{M}\frac{2\mathfrak{F}}{\pi}}. \tag{3.37}$$

The coupling constant g differs by a factor of $2\mathfrak{F}/\pi$ from the free-space g introduced in Eq. 3.10. This result can be intuitively understood in terms of the power enhancement on the membrane, which is exactly $2\mathfrak{F}/\pi$ at the slope of the intracavity field. The optomechanical coupling of a membrane and a cavity is discussed further in the experimental Chapter. 6.

3.2.2 Quantum Dynamics

The presence of the cavity will increase the power level on the membrane. Both the thermal decoherence rate and the radiation pressure noise on the membrane increase as $\mathfrak{F}$ is increased. These decoherence processes will fundamentally limit the $\mathfrak{F}$ and consequently the achievable coupling rate $g \propto \mathfrak{F}$. On the other hand, the atomic diffusion does not depend on $\mathfrak{F}$ (Eq. 3.29).

Decoherence and Imperfections at the Membrane

The circulating intra-cavity power scales with cavity finesse $\mathfrak{F}$ as

$$P_\mathrm{circ} = \frac{2P}{\pi}\mathfrak{F}, \tag{3.38}$$

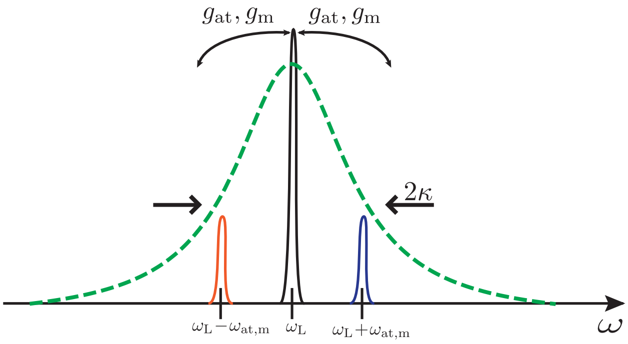

Figure 3.5: The light fields involved in mediating the effective coupling. The laser light $\omega_{\rm L}$ is resonant to the cavity. The laser light photons are converted to sidebands photons $\omega_{\rm L} \pm \omega_{at,m}$ (blue and red). The cavity response is presented with the green dashed line. As the cavity linewidth κ is $\gg \omega_{\rm at}, \omega_{\rm m} \gg g_{\rm at}^2, g_{\rm m}^2$ one can eliminate the light field from the dynamical equations. $g_{\rm at}$ and $g_{\rm m}$ are the coupling of the light field to the atoms and membrane, respectively. Figure adopted from Ref. [41].

where P is the incoming lattice beam power and mode-matching of the beam into the cavity is assumed to be 1. The peak power for a standing wave inside the cavity is $P_{\rm st} = 4P_{\rm circ}$. Here we assume that the membrane is placed on the slope of the intracavity field where the power on the membrane is

$$P_{\rm mem} = \frac{4P}{\pi}\mathfrak{F}. \tag{3.39}$$

Let us first consider the thermal decoherence rate of the membrane. The absorbed power in the membrane can be written in terms of the absorbed fraction[2] $\mathfrak{a}_{\rm m}^2 = 1 - \mathfrak{r} - \mathfrak{t}$ as

$$P_{\rm abs} = \mathfrak{a}_{\rm m}^2 P_{\rm mem} = \mathfrak{a}_{\rm m}^2 \frac{4P}{\pi}\mathfrak{F} \propto \mathfrak{F}. \tag{3.40}$$

The absorbed power results in an increase of the bath temperature by ΔT. This leads to increased thermal decoherence rate (Eq. 3.27) as

$$\gamma_{\rm th} = \gamma_{\rm m}\bar{n}_{\rm th} \approx \frac{k_B}{\hbar\omega_{\rm m}}\left(T_0 + \frac{\mathfrak{a}_{\rm m}^2}{K_{\rm th}}\frac{4P}{\pi}\mathfrak{F}\right). \tag{3.41}$$

As the membrane absorbance is in general in the range of $\mathfrak{a}_{\rm m}^2 < 2\cdot 10^{-5}$, for low $\mathfrak{F}$ the absorbance plays a small role. However, for higher finesse, $\gamma_{\rm th} \propto \mathfrak{F}$, and the absorption becomes significant.

The radiation pressure shot noise on the membrane, Eq. 3.28, can be written in terms of the $\mathfrak{F}$ as

$$\gamma_{\rm m}^{\rm diff} = \frac{4P}{Mc^2}\frac{\omega_{\rm L}}{\omega_{\rm m}}\mathfrak{r}\left(\frac{2\mathfrak{F}}{\pi}\right)^2. \tag{3.42}$$

---

[2] The membrane absorption is defined in terms of the $\mathrm{Im}\,(n_{\rm m})$ in Sec. 4.2. This is related to $\mathfrak{a}_{\rm m}^2$ as $\mathfrak{a}_{\rm m}^2 \approx 2k\mathrm{Im}\,(n_{\rm m})\,d_{\rm m}$.

This scales as $\propto \mathfrak{F}^2$ and will eventually dominate the decoherence for high $\mathfrak{F}$.

Optimizing the Cavity Finesse

Using the expressions for the various decoherence rates, one can optimize the ratio of total decoherence to coherent coupling or the ground-state membrane occupation. In doing so, a clear trend towards minimizing the atomic detuning emerges: while increasing the $\mathfrak{F}$, the power on the membrane can only be reduced by reducing P, while at the same time keeping the ratio P/Δ_{L} fixed such that $\omega_{\mathrm{at}} \sim \omega_{\mathrm{m}}$. For sufficiently large detuning and linear polarization, all ground-state hyperfine levels m_{F} experience the same trapping potential. At smaller detunings, the potential becomes state dependent and optical pumping between different m_{F} levels induced by scattering of photons from the light will reduce the coupling to the membrane. In order to leave such effects outside this discussion, we consider $\Delta_{\mathrm{L}} = 2\pi \cdot 1\,\mathrm{GHz}$ as a compromise in our optimization.

Membrane		**Lattice**		**Rates**	
size	$(1\,\mathrm{mm})^2 \times 50\,\mathrm{nm}$				
ω_{m}	$2\pi \cdot 400$ kHz	ω_{at}	$2\pi \cdot 400$ kHz		
M	$3.6 \cdot 10^{-11}$ kg	ω_{L}	$2\pi \cdot 384$ THz		
Q	10^7	Δ_{L}	$2\pi \cdot 1.0$ GHz	g	214 kHz
T_0	1.6 K	m	$1.44 \cdot 10^{-25}$ kg	$\gamma_{\mathrm{m}}^{\mathrm{diff}}$	60 kHz
ΔT	4 K	P	2.8 mW	$\gamma_{\mathrm{at}}^{\mathrm{diff}}$	8 kHz
K_{th}	$4 \cdot 10^{-7}$ W/K	N	10^8	γ_{th}	73 kHz
$\mathfrak{a}_{\mathrm{m}}^2$	10^{-6}	w_0	350 µm		
$\mathfrak{r}$	0.47				
$\mathfrak{F}$	450				

Table 3.2: Optimized parameter set for cavity-enhanced experiment [41]. The two left-most columns show mechanical and atomic parameters, respectively, while the column on the right displays the resulting couplings and decoherence rates. Values for N, Q, and $\mathfrak{a}_{\mathrm{m}}^2$ have been measured previously [77, 100, 101, 102]. The value of K_{th} is consistent with available literature.

Table 3.2 introduces one set of optimized experimental parameters for a membrane with eigenfrequency of $\omega_{\mathrm{m}} = 2\pi \cdot 400\,\mathrm{kHz}$ and lattice detuning of $\Delta_{\mathrm{L}} = 2\pi \cdot 1\,\mathrm{GHz}$. The lattice beam waist is chosen to be $w_0 = 350\,\mu\mathrm{m}$. Fixing the value of Δ_{L} and w_0 fixes the value of the input laser power P such that $\omega_{\mathrm{m}} \sim \omega_{\mathrm{at}}$. This leaves $\mathfrak{F}$ as the remaining experimental parameter. Figure 3.6 compares the ratio of the decay rates to the coupling constant g as a function of $\mathfrak{F}$ using the parameters in Tab. 3.2. It is useful to make general statements of the ratio between the different coupling rates in relation to g. First of all, the atomic diffusion rate $\gamma_{\mathrm{at}}^{\mathrm{diff}}$ is constant, and hence $\gamma_{\mathrm{at}}^{\mathrm{diff}}/g$ decreases as $1/\mathfrak{F}$ (light blue dashed line). On the other hand, there is a trade-off between mechanical heating

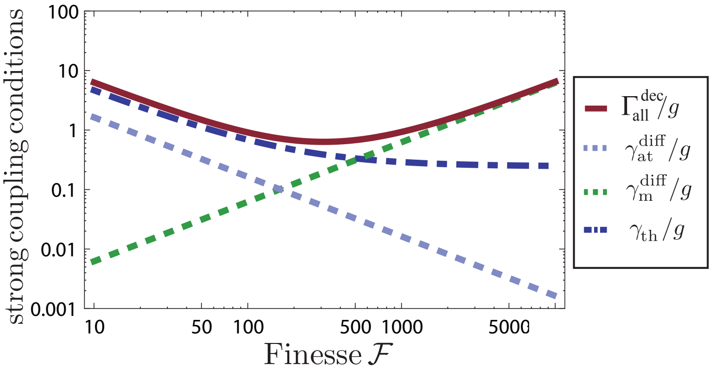

Figure 3.6: A calculation of the ratios $\gamma_{\rm at}^{\rm diff}/g$, $\gamma_{\rm m}^{\rm diff}/g$, and $\gamma_{\rm th}/g$ as a function of finesse to illustrate the coherent coupling conditions in 3.32. A trade-off between thermal heating ($\gamma_{\rm m}^{\rm th}$) and radiation pressure noise ($\gamma_{\rm m}^{\rm diff}$) is visible. Parameters other than $\mathfrak{F}$ are taken from Tab. 3.2. Figure adopted from Ref. [41].

(blue dash-dotted line) and the radiation pressure noise (green dashed line). For higher $\mathfrak{F}$ the radiation pressure noise on the membrane will be the limiting decoherence mechanism, and there is an *optimum* for the $\mathfrak{F}$ around 300. The red line shows the ratio of the sum of the decoherence rates, $\Gamma_{\rm all}^{\rm dec} = \gamma_{\rm at}^{\rm diff} + \gamma_{\rm m}^{\rm diff} + \gamma_{\rm th}$ to g. Around the optimal $\mathfrak{F}$, $\Gamma_{\rm all}^{\rm dec}/g \approx 1$, and the coherent coupling regime defined in Eq. 3.32 becomes accessible.

In the weak-coupling regime, the quantum dynamics of the cavity-enhanced system follow the description presented in Sec. 3.1.3 with the cavity-enhanced coupling constant given by Eq. 3.37. The final steady-state occupation number can be calculated using Eq. 3.31. A full calculation beyond the weak-coupling limit for the $\bar{n}_{\rm ss}$ results in an optimum finesse of $\mathfrak{F} \approx 450$ [41]. The exact solution of the for $\bar{n}_{\rm ss}$ is presented as a function of $\mathfrak{F}$ and the atomic cooling rate $\gamma_{\rm c}$ in Figure 3.7. Like in the free-space setup presented earlier an optimum for the laser cooling rate of the atoms exists when $g \approx \gamma_{\rm c}$. Further details on the exact calculation can be found in Ref. [41].

3.3 Comparison with Cavity Cooling

Both of the optomechanical systems discussed in this Chapter share some features with optomechanical cavity cooling, as described in Sec. 2.2. In a standard cavity-optomechanical scheme, the coupling constant $g_{\rm opt}$ is collectively enhanced by the intra-cavity photon number $\sqrt{\bar{n}_{\rm cav}}$ using a strong laser drive. In the atom-membrane systems, similar collective enhancement is provided by the number of atoms $\sqrt{N}$. Furthermore, by comparing Eq. 3.17 to the corresponding equation for cavity-optomechanical cooling, Eq. 2.70, we find that our atomic damping rate $\gamma_{\rm at}$ is analogous to the cavity decay rate 2κ in the resolved-sideband regime.

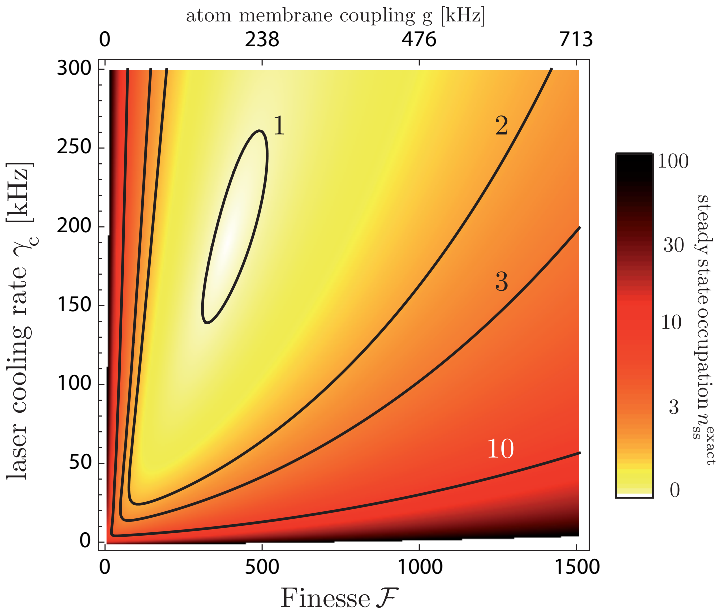

Figure 3.7: Exact steady state occupation number $n_{\mathrm{ss}}^{\mathrm{exact}}$ as a function of $\mathfrak{F}$ and γ_{c}. The top axis displays the corresponding coherent coupling g and the contours indicate the associated occupation numbers. The assumed parameters are from Table 3.2. Details of this exact calculation are presented in Ref. [41]. Figure adopted from [41].

Laser cooling of the atoms results in sympathetic cooling of the membrane, similar to side-band resolved cavity cooling. However, in contrast to the usual cavity-optomechanical setup where κ is a fixed parameter, in our system γ_{at} is *tunable* via γ_{c}. Thus, the atomic cooling can be conveniently switched off when the ground-state regime has been reached, allowing one to study the system evolution in the regime of strong coherent coupling.

Another experimental benefit of our cavity scheme is that it does not require 'resolved sideband' conditions for the cavity. The sideband-resolved regime is experimentally challenging to reach for low-frequency oscillators such as the membranes. On the contrary, we want to operate in a regime where $\kappa \gg \omega_{\mathrm{m}}, \omega_{\mathrm{at}}$, which greatly relaxes the experimental requirements on the cavity. Hence, this type of resonant cooling setup could prove useful in the context of cooling other dielectric objects in a cavity such as levitated dielectric particles, or even molecules, which also have frequencies in the hundreds of kHz regime [83, 84].

4

Silicon-Nitride Membranes

Silicon nitride (SiN) membranes have garnered a great deal of interest in optomechanics experiments owing to their extraordinary mechanical and optical properties [100, 101, 46, 103, 36, 30, 63]. Laterally millimeter scale but 50 nm thin SiN membranes support mechanical modes which can reach Q-values $> 10^7$ even in room temperature [104], which means that the mechanical mode is extremely well decoupled from its environment. At the same time the membrane mass amounts to some nanograms. Furthermore, such a thin membrane can serve as a partially reflecting mirror at optical frequencies.

One of the first important steps into the field of membrane optomechanics was taken by J. Harris' group, where they simply placed a commercially available SiN membrane inside a high-finesse cavity [100, 58, 105]. By passive optomechanical cavity cooling they reduced the mode temperature of the membrane by a factor of $4.4 \cdot 10^4$ below the room temperature. Their experimental approach solved some of the technical issues related to integrating micromechanical elements into a high-finesse cavity. Furthermore, in such a setup the optomechanical coupling can be tuned from linear to quadratic, which may allow quantum non-demolition measurement on the membrane state [102]. Recently, C. Regal's group measured radiation pressure shot noise on a membrane [106], which truly highlights the *quantum*-scale sensitivity available in integrated membrane-systems.

The membranes we use in the experiments are commercially available from Norcada Inc. [107]. A photograph of such a membrane is shown in Fig. 4.1a. The membranes are square in shape, have thickness of 50 nm and their areal size can be customized. The SiN membranes are fabricated by depositing SiN on Si substrate using low pressure chemical vapor deposition techniques (LPCVD). Such membranes are more generally used as sample holders for transmission electron microscopy and as vacuum windows for x-ray spectroscopy. Owing to their excellent optomechanical properties, many groups working with optomechanics use these commercial membranes "off-the-shelf". Recently, some groups have also

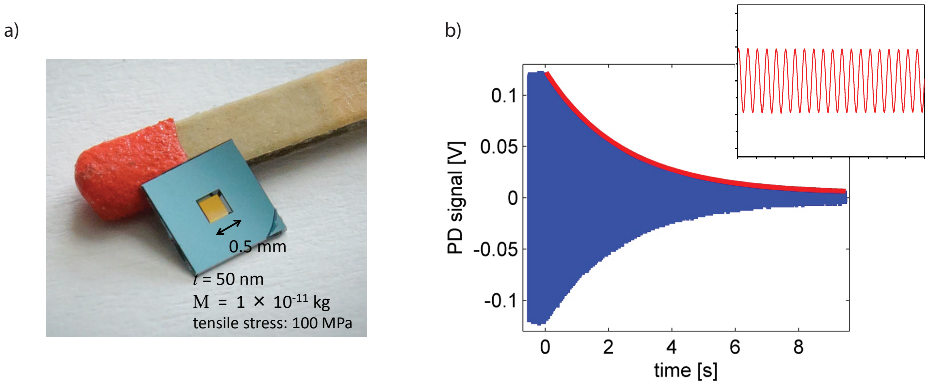

Figure 4.1: a) A photograph of a commercially available SiN membrane. We use a similar membrane in the main experiment described in Ch. 5. b) A ringdown measurement of the membrane reveals an extraordinarily high Q-factor of $2 \cdot 10^6$.

started to fabricate and develop membranes that are tailored for optomechanics experiments [108, 101, 109, 36, 110, 111, 112]. For example, by structuring the membranes, one can significantly reduce their damping [108]. This could enable membrane optomechanics experiments on quantum scale above cryogenic base temperatures, possibly even in room temperature [101, 109].

This Chapter discusses the optomechanical characterization measurements we perform on the commercially available SiN membranes that are used in our main experiments. In the first, free-space experiment, we use SiN membranes which have a relatively low tensile stress $S_0 = 70\,\mathrm{MPa}$ [100]. In the second, cavity-enhanced experiment, we use high-stress SiN membranes of tensile stress $S_0 = 1\,\mathrm{GPa}$ [101]. We characterize the Q-factor and eigenfrequency of these membranes as a function of laser power on the membrane, and determine their absorbance and reflectivity at 780 nm.

4.1 Membrane Characterization Setup

Before integrating a membrane into the main experiment, its eigenfrequency ω_m and Q-factor for the fundamental mode are characterized in a separate test chamber. The test chamber is also used to study the absorbance properties of the membranes. The membrane characterization setup was initially built by M. Mader as part of a bachelor thesis project [113]. Figure 4.2 shows a photograph of the vacuum chamber that can accommodate 18 membranes at the same time. The membrane holder is designed such that it can be directly transferred to the main experiment (see Fig. 6.11b for the technical details of the holder design).

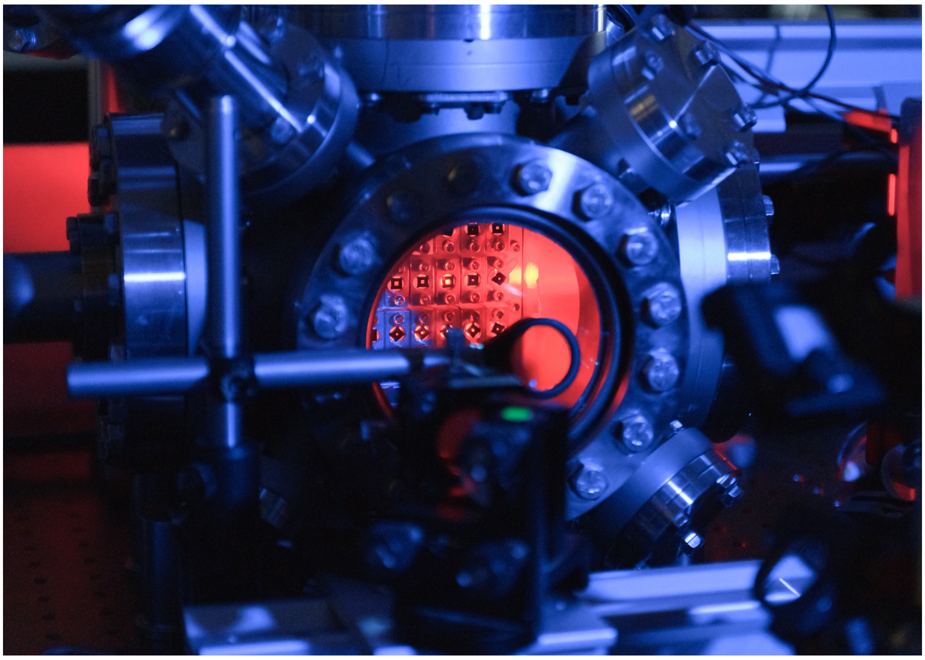

Figure 4.2: The membrane characterization chamber for measuring the eigenfrequency, Q-factor and absorption. One sees an array of membranes in the chamber. The lens visible in the front is used to focus the read-out laser beam onto the membrane.

Requirement for the Vacuum

When the lateral membrane size l_m is smaller than the mean free path l_mfp of the surrounding gas particles, the membrane is in a free molecular flow damping regime. The mean free path of an ideal gas is given by $l_\mathrm{mfp} = k_\mathrm{B}T/\sqrt{2}\pi d_0^2 P_\mathrm{gas}$, where P_gas is the gas pressure. Assuming the diameter of a typical residual gas particle to be $d_0 \approx 4 \cdot 10^{-10}\,\mathrm{m}$ [114], and the lateral size of the membrane $l_\mathrm{m} = 1.5\,\mathrm{mm}$, the free molecular flow regime is reached for $P_\mathrm{gas} < 4 \cdot 10^{-2}\,\mathrm{mbar}$. In this regime, the air damping limits the quality factor of the membrane to [115, 116]

$$Q_{\text{gas}} = \frac{\rho d_{\text{m}} \omega_{\text{m}}}{4} \sqrt{\frac{\pi}{2}} \sqrt{\frac{RT}{M_{\text{NA}}}} \frac{1}{P_{\text{gas}}} \propto \frac{1}{P_{\text{gas}}}, \tag{4.1}$$

where $\rho = 2.9\,\text{g/cm}^3$ is the density of SiN [98], $M_{\text{NA}} = 28.96\,\text{g/mol}$ is the molar mass of air, T is the air temperature, and R is the ideal gas constant. In room temperature ($T = 293\,\text{K}$) and for $\omega_{\text{m}} = 2\pi \cdot 250\,\text{kHz}$ and $d_{\text{m}} = 50\,\text{nm}$ we get $Q_{\text{gas}} = 2 \cdot 10^7$, when $P_{\text{gas}} = 10^{-5}\,\text{mbar}$. Consequently, the pressure in the chamber should be less than $10^{-5}\,\text{mbar}$ such that our quality factor measurement is not limited by gas damping. We have also experimentally measured the dependence of the Q of the membrane on the pressure in the chamber, and observed that below $5 \cdot 10^{-5}\,\text{mbar}$ the Q of a 277 kHz membrane is indeed independent of background pressure. The measurement result is shown in Fig. 4.3. For the membrane characterization measurements, the test chamber is in vacuum of $2 \cdot 10^{-7}\,\text{mbar}$ and in room temperature. In such a low pressure $Q_{\text{gas}} \geq 8 \cdot 10^8$ for any of the membranes we use in the experiment and we can neglect air damping.

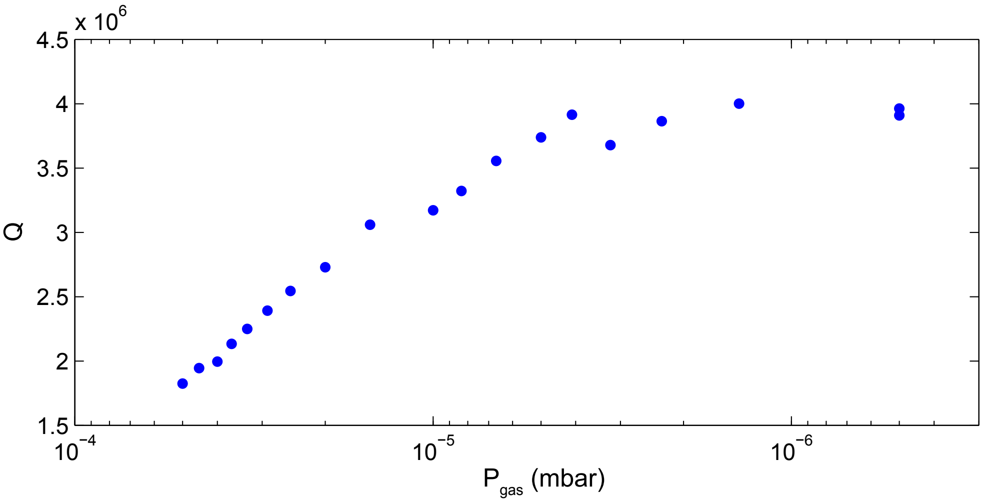

Figure 4.3: The Q-factor of a high-stress SiN membrane with $\omega_{\text{m}} = 2\pi \cdot 277\,\text{kHz}$ as a function of pressure in the vacuum chamber. This measurement was carried out by our Master student T. Lauber.

4.1.1 Interferometric Read-Out and Heating Laser

The laser setup for the membrane study is shown in Fig. 4.4. A Michelson interferometer (MI) at 852 nm is used to read out the membrane motion. For further details of the MI see the main experimental section Sec. 5.3, where a similar read-out scheme is explained in more detail. The interferometer is stabilized by

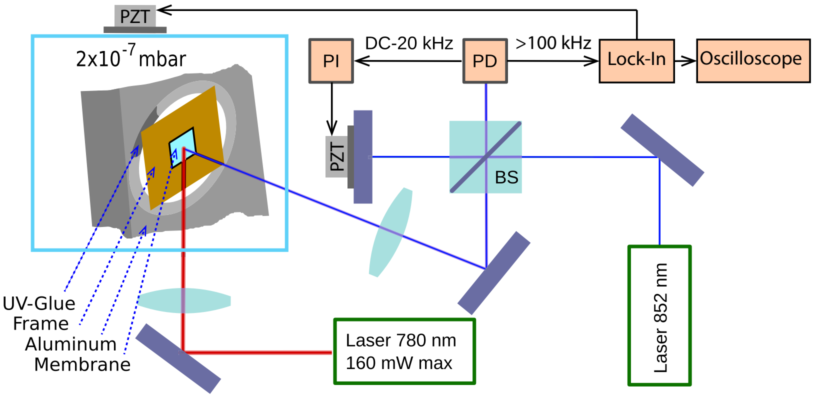

Figure 4.4: Experimental setup. The SiN membrane in a Si frame is glued at one edge to an aluminum holder inside a room-temperature vacuum chamber. The heating laser (red) at 780 nm is power stabilized to $2 \cdot 10^{-4}$ RMS in a bandwidth of 12 kHz, and focused onto the membrane under an angle. The membrane vibrations are read out with a stabilized Michelson interferometer (blue). The interferometer signal is also used for feedback driving of the membrane with a piezo (PZT). The figure is modified from that presented in Ref. [46].

the DC to 20 kHz part of the photodiode (PD) signal. The incident power on the membrane is 580 µW in a diameter of 150 µm and the position sensitivity is $1 \cdot 10^{-14}\,\mathrm{m}/\sqrt{\mathrm{Hz}}$. The > 100 kHz part of the signal is fed into a lock-in amplifier with integrated phase locked loop, which measures the membrane amplitude and drives its motion via a piezo mounted outside of the vacuum chamber. To measure the Q-factor of the membrane, we switch the membrane drive off and record the amplitude decay. An example of such a ring-down measurement signal on the PD is shown in Fig. 4.1b. The Q-factor is then straightforwardly determined using Eq. 2.15. In order to characterize absorbance-related effects, we have integrated another laser into the system operating at 780 nm. The laser is power stabilized to $2 \cdot 10^{-4}$ (r.m.s) and focused onto the membrane to a diameter of 350 µm. This laser is the same as the one used for the lattice and described in Sec. 5.1.2.

4.1.2 Membrane Mounting

The exact way in which the membrane frame is mounted on its holder can influence the Q-factor of the membrane by several orders of magnitude. Initially, we glued the membrane frame rigidly to its holder by applying a drop of glue to its all 4 corners and measured Q values of maximally 10^3 (low stress membrane, 0.5 mm × 0.5 mm × 50 nm). Thereafter we experimented with different type of glues and applied just a minute drop of glue to one or more of the corners of the membrane. The best results were obtained by gluing the frame only from one of its corners. Furthermore, viscous, liquid-like glues resulted in higher Q-factors. We obtained good results when the membrane frame was glued either with `OP-4-20632` from DYMAX, or with `OG116-31` from EPOTEK. The DYMAX glue has low outgassing, is single component and UV/Visible curable. Importantly, the glue has ultra low shrinking during curing. In a characterization measurement series done with high-stress membranes of $1.5\,\mathrm{mm}\times1.5\,\mathrm{mm}\times50\,\mathrm{nm}$ in size, the Q-factor of the DYMAX-glued membrane was measured to be $Q = 3{\cdot}10^6$. The glue from EPOTEK is UV-curable, UHV compatible, and single component glue. The EPOTEK-glued membrane had a Q of $2 \cdot 10^6$.

In the experimental setup for free-space coupling discussed in Ch. 5, the membrane is placed vertically into the vacuum chamber (see Fig. 5.14) and gluing of the frame to its holder is required. The second generation cavity-enhanced coupling setup, introduced in Ch. 6, is designed such that the membrane can be placed horizontally to its holder. Thus, the membrane frame can rest free-lying on top of the holder, supported by gravity and friction alone, as shown in Fig. 6.12. So far, the first Q-factor measurement we have performed with a free-lying membrane ($(1.5\,\mathrm{mm})^2 \times 50\,\mathrm{nm}$) resulted in Q of $6 \cdot 10^7$. This is the highest Q-value we have measured, suggesting that the free-lying configuration may be optimal for maintaining the high Q of the membrane.

4.2 Membrane Absorbance

The absorbance of the membrane results in heating when laser hits the membrane. The heating results in thermal expansion of the membrane and a subsequent reduction in its stress. As a consequence, the eigenfrequency of the membrane ω_m shifts. By comparing the temperature increase required to cause the measured shift in ω_m with a theoretical model for heat transport in the membrane, we make estimates on the absorption coefficient of the membrane. At certain power levels, we also observe a non-monotonic dependence of the mechanical Q on power. We have reported these kind of measurements for low-stress membranes in Ref. [46]. Here we extend these measurements on stoichiometric, high-stress membranes and discuss a model for the thermal decoherence rate in the membrane.

4.2.1 Shift of Membrane Eigenfrequency

The eigenfrequencies of a square membrane under tension are given by

$$f_{m,n} = \frac{1}{2l_\mathrm{m}}\sqrt{\frac{S}{\rho}\,(m^2+n^2)}, \tag{4.2}$$

where l_m is the side length, $\rho = 2.9$ g/cm^3 is the density [98], and S the tensile stress in the membrane. The modes are labeled by the number of anti-nodes m and n along the two dimensions. The stress $S = E\,(l_\mathrm{m} - l_0)\,/l_0$, where E is Young's modulus, arises in the fabrication process when the SiN membrane is stretched from its equilibrium length l_0 to the length l_m of the Si frame. Figure 4.5 shows the recorded mode spectrum as a function of heating laser power P at 780 nm. The spectra are recorded by Fourier transforming the PD signal. One can see a reversible decrease of all mode frequencies $f_{m,n}$ with P.

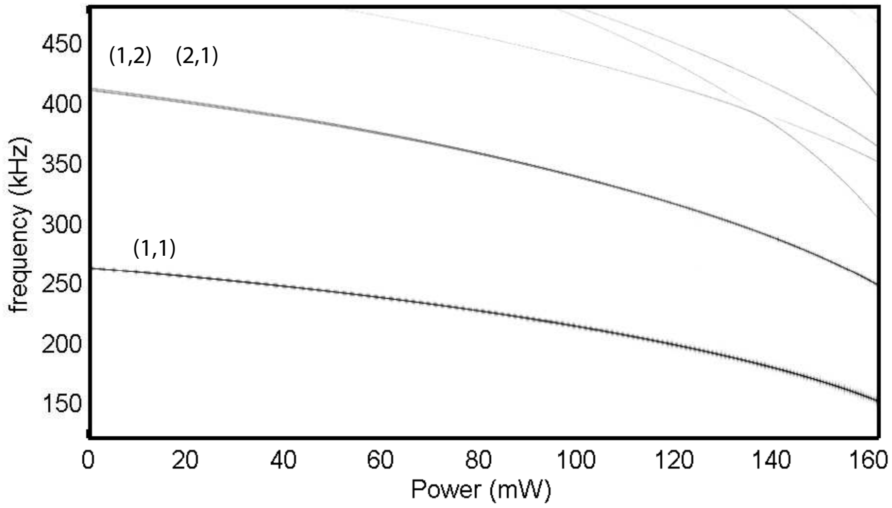

Figure 4.5: Shift of the lowest eigenfrequencies of a low-stress membrane versus power at 780 nm. The membrane modes are labeled by (m, n). The membrane has dimensions of $(0.5\,\mathrm{mm})^2 \times 50\,\mathrm{nm}$ and is similar to that used in the main experiment described in Ch. 5.

The change in frequency as a function of power P, can be attributed to a thermal expansion of the membrane $\Delta l_0/l_0 = \alpha_0 \Delta T + \alpha_1 \Delta T^2$, where Δl_0 is the equilibrium length change and α_0 (α_1) the first (second) order expansion coefficient for a temperature change ΔT. A temperature change affects the tensile stress by $\Delta S = -E\,(\Delta l_0/l_0)$. In a simple model, we assume a spatially homogeneous and linear temperature change with power as [46]

$$\Delta T = \chi P, \tag{4.3}$$

and describe the power-dependence of the stress as

$$S = S_0 - E\,(\Delta l_0/l_0) = S_0 - E\left(\alpha_0 \chi P + \alpha_1 \chi^2 P^2\right). \tag{4.4}$$

By using an auxiliary measurement, as described in Ref. [46], we have determined the thermal expansion coefficients in Eq. 4.4 to be $\alpha_0 = 1.6 \cdot 10^{-6}\,\mathrm{m/K}$ and $\alpha_1 = 1.3 \cdot 10^{-8}/\mathrm{K}^2$ for the SiN membranes. Using these values we fit Eq. 4.2 with Eq. 4.4 to the data and determine a value of $\chi = 0.6\,\mathrm{K/mW}$ for the low stress-membrane. The fit of $f_{1,1}(P)$ to the data describes the observed dependence within ±1 kHz.

4.2.2 Determining the Absorbance

The absorbed power is related to the imaginary part of the refractive index of the membrane $\mathrm{Im}\,(n_\mathrm{m})$ as

$$P_\mathrm{abs} = P_\mathrm{mem}\left(1 - e^{(-2k\mathrm{Im}(n_\mathrm{m})d_\mathrm{m})}\right) \approx 2k\mathrm{Im}\,(n_\mathrm{m})\,d_\mathrm{m}P_\mathrm{mem}, \tag{4.5}$$

where P_mem is the power on the membrane and d_m is the thickness of the membrane. In order to extract the absorption of the membrane, $\mathrm{Im}\,(n_\mathrm{m})$, we model the heat transport in the membrane explicitly, as described also in Ref. [41]. This resulting temperature increase in the membrane is then compared with the experimental value determined using Eq. 4.3. For a circular membrane of diameter l, a simple analytical solution can be obtained and the case of the square membrane can then be approximately described by including a “geometric prefactor” of order unity. The results of the analytical model are checked against a finite element method (FEM) simulation.

Heat transport inside the membrane is governed by the heat equation

$$\rho c_\mathrm{p}\frac{\partial T}{\partial t} = \kappa_\mathrm{th}\nabla^2 T + Q_\mathrm{th}, \tag{4.6}$$

where κ_th is the thermal conductivity, ρ the mass density, c_p the specific heat capacity of the membrane material, ∇^2 the Laplace operator, and Q_th is a source term describing the power dissipated per unit volume. The heating laser is modeled as a circular disk of radius w_h at the position of the membrane. This gives rise to absorbance within a circle of area $\mathcal{A}_\mathrm{m} = \pi w_\mathrm{h}^2$. Thus, the source term can be expressed as

$$Q_\mathrm{th} = P_\mathrm{abs}/(\mathcal{A}_\mathrm{m} d_\mathrm{m}). \tag{4.7}$$

For a 2D temperature distribution inside a thin membrane ($d_\mathrm{m} \ll l$) in steady-state ($\partial T/\partial t = 0$), the heat equation reads

$$\nabla^2 T = \frac{1}{r}\frac{\partial}{\partial r}\left(r\frac{\partial T}{\partial r}\right) + \frac{1}{r^2}\frac{\partial}{\partial \phi}\left(\frac{\partial T}{\partial \phi}\right) = -Q_\mathrm{th}/\kappa_\mathrm{th}. \tag{4.8}$$

A simple solution can be found for the circular membrane. Making use of the azimuthal symmetry ($\partial T/\partial \phi = 0$), the equation simplifies to

$$\frac{1}{r}\frac{\partial}{\partial r}\left(r\frac{\partial T}{\partial r}\right) = \begin{cases} -Q_\mathrm{th}/\kappa_\mathrm{th} & \text{for } 0 \le r \le w_\mathrm{h}, \\ 0 & \text{for } w_\mathrm{h} < r \le l/2. \end{cases} \tag{4.9}$$

We solve this equation subject to the boundary condition that the frame is at constant temperature, $T(r = l/2) = T_0$, yielding the temperature distribution

$$T(r) = \begin{cases} T_0 + \Delta T_\mathrm{cal} - \frac{Q_\mathrm{th}}{4\kappa_\mathrm{th}} r^2 & \text{for } 0 \le r \le w_\mathrm{h}, \\ T_0 + \frac{Q_\mathrm{th} w_\mathrm{h}^2}{2\kappa_\mathrm{th}} \ln\left(\frac{l}{2r}\right) & \text{for } w_\mathrm{h} < r \le l/2, \end{cases} \tag{4.10}$$

where

$$\Delta T_{\mathrm{cal}} = T(r=0) - T_0 = \frac{Q_{\mathrm{th}} w_{\mathrm{h}}^2}{2\kappa_{\mathrm{th}}} \left[\ln\left(\frac{l}{2w_{\mathrm{h}}}\right) + \frac{1}{2} \right] \tag{4.11}$$

is the temperature increase of the membrane center compared to the frame. The average membrane temperature, obtained by integrating $T(r)$ over the membrane, is

$$T_{\mathrm{avg}} = T_0 + \frac{Q_{\mathrm{th}} w_{\mathrm{h}}^2}{4\kappa_{\mathrm{th}}} \left[1 - 2\left(\frac{w_{\mathrm{h}}}{l}\right)^2 \right]. \tag{4.12}$$

We have confirmed the analytical results to agree with a FEM simulation. Running the FEM simulation instead for a square membrane of side length l_{m}, we obtain similar results but with a geometric prefactor f_g so that $\Delta T_{\mathrm{square}} = f_g\, \Delta T_{\mathrm{cal}}$, where f_g decreases from $f_g = 1.075$ for $w_{\mathrm{h}}/l_{\mathrm{m}} = 0.3$ to $f_g = 1.017$ for $w_{\mathrm{h}}/l_{\mathrm{m}} = 0.01$ [41]. The absorbance of the membrane can be now determined by comparing the measured ΔT in Eq. 4.3 with the analytical formula for the average temperature increase in the membrane $\Delta T_{\mathrm{avg}} = T_{\mathrm{avg}} - T_0$.

Low-Stress Membrane

For low power of the heating laser we observe a linear shift of $\Delta f_{1,1} = -363\,\mathrm{Hz/mW}$ as shown in Fig. 4.5. A fit to the experimental data gives $\chi = 0.6\,\mathrm{K/mW}$. Using Eqs. 4.3 and the average temperature increase in the membrane from Eq. 4.12, and assuming $\kappa_{\mathrm{th}} = 3\,\mathrm{WK^{-1}m^{-1}}$ and $S_0 = 70\,\mathrm{MPa}$ (see Tab. 4.1) we find an absorption of $\mathrm{Im}\,(n_{\mathrm{m}}) = 1.5 \cdot 10^{-3}$ at 780 nm. This is an order of magnitude larger than the absorption in low-stress membranes at 1064 nm [58, 105].

High-Stress Membrane

The absorbance of a stoichiometric membrane is measured by placing a $(1.5\,\mathrm{mm})^2 \times 50\,\mathrm{nm}$ membrane into the middle of the field slope of a symmetric optical cavity and monitoring the shift of the membrane frequency as a function of intra-cavity power. The cavity has finesse of $\mathfrak{F} = 78$ and it is locked on-resonance. More details on the cavity and the membrane read-out can be found in Secs. 6.3 and 6.5. The absorbed power for a membrane sitting on a slope of the intracavity intensity standing wave is given by $P_{\mathrm{mem}} = 2P_{\mathrm{circ}} = \frac{2\mathfrak{F}}{\pi} P_{\mathrm{in}}$, such that we obtain half peak power at the position of the membrane. Here $P_{\mathrm{circ}} = \frac{\mathfrak{F}}{\pi} P_{\mathrm{in}}$, where P_{in} is the power coupled into the cavity.

The power spectral density of the membrane is shown in Fig. 4.6 for two different power levels, $P_{\mathrm{mem}} = 64\,\mathrm{mW}$ and $P_{\mathrm{mem}} = 21\,\mathrm{mW}$. We observe $\Delta f_{1,1} = 0.40\,\mathrm{Hz/mW}$, and determine $\chi = 6.5 \cdot 10^{-3}\,\mathrm{K/mW}$ and $S_0 = 0.92\,\mathrm{GPa}$ from Eqs. 4.2-4.4. The measured χ is two orders of magnitude lower than that of the low-stress membrane. There is broad range of values reported for the thermal conductivity of $\mathrm{Si_3N_4}$. A general reference [117] reports $\kappa_{\mathrm{th}} \geq 25 - 36\,\mathrm{WK^{-1}m^{-1}}$. Since the appearance of Ref. [117], a lot of research has been done on nanoscale thin films in room temperature. A recent paper, Ref. [99] reports thermal conductivity of $2.7\,\mathrm{WK^{-1}m^{-1}}$ for 50 nm thin $\mathrm{Si_3N_4}$ films. Other references report room temperature values of 0.4 – 4 $\mathrm{WK^{-1}m^{-1}}$ for films thinner than 500 nm (see [99] and references therein). Using here the value of 2.7 $\mathrm{WK^{-1}m^{-1}}$ we get $\mathrm{Im}\,(n_\mathrm{m}) = 1.4 \cdot 10^{-5}$ at 780 nm. Our measurement is consistent with the absorption of high-stress membranes at 1064 nm, which has been measured to be $\mathrm{Im}\,(n_\mathrm{m}) = 0.6 \cdot 10^{-5}$ [101]. Importantly, our measurement indicates that absorption of 780 nm light in high-stress membranes is lower by two orders of magnitude compared to the low-stress membranes.

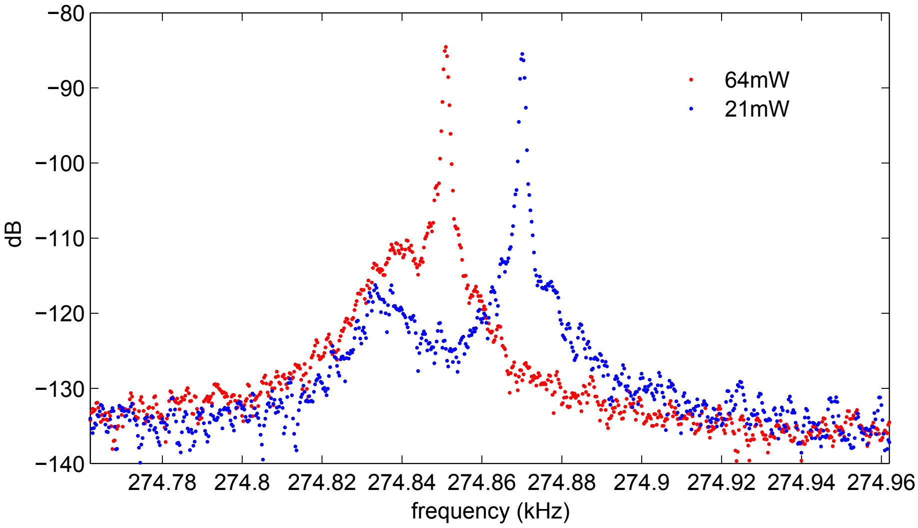

Figure 4.6: The power spectrum of the membrane placed into the middle of the cavity field slope. The power at the membrane is 64 mW (red) and 21 mW (blue). The smaller peak to the left of the membrane signal is electronic noise. It originates from our custom-built lock-box, and has since the measurement been suppressed.

Thermal Decoherence Rate

The heating of the membrane due to absorption leads to a faster thermal decoherence rate of the membrane. This is modeled by introducing an effective bath temperature $T_\mathrm{eff} = T_0 + \Delta T_\mathrm{cal}$, where

$$\Delta T_\mathrm{cal} = \frac{P_\mathrm{abs}}{K_\mathrm{th}} \tag{4.13}$$

is the temperature increase due to absorbed power P_abs in the center of the membrane. Using equation 4.11, we can define the temperature increase via the thermal link as

$$K_\mathrm{th} = \frac{P_\mathrm{abs}}{\Delta T_\mathrm{cal}} = \frac{2\pi\kappa_\mathrm{th} d_\mathrm{m}}{\ln\left(\frac{l}{2w_\mathrm{h}}\right) + \frac{1}{2}}. \tag{4.14}$$

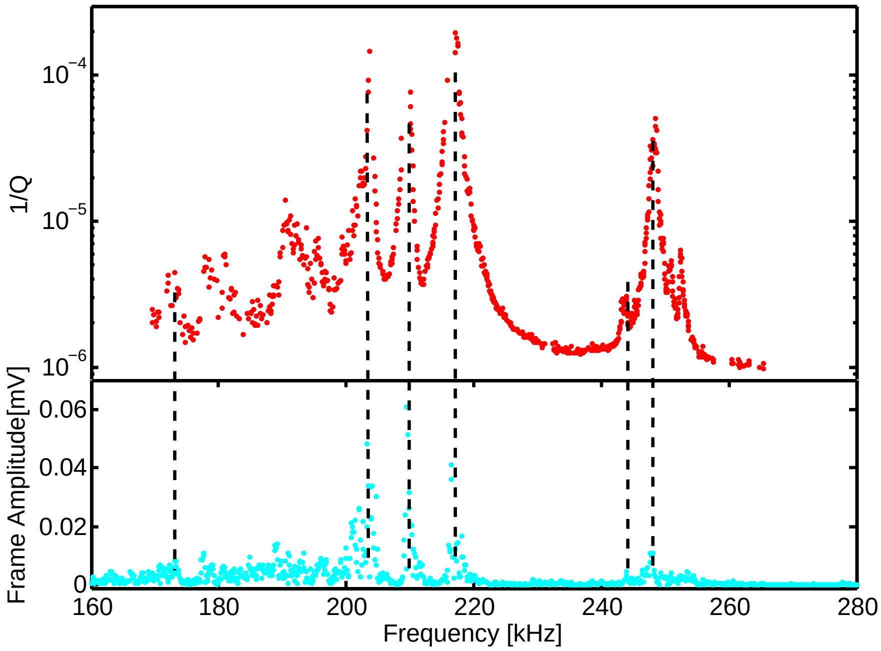

Figure 4.7: Top panel: The resonances in the inverse quality factor of a membrane Q^{-1} as a function of the eigenfrequency of the fundamental mode of the membrane. Bottom panel: Eigenfrequencies of the frame. The eigenfrequencies of the frame overlap with the resonances in Q^{-1} of the membrane. The measurement is performed on a low stress membrane that has dimensions of $(0.5\,\mathrm{mm})^2 \times 50\,\mathrm{nm}$ and is similar to that used in the main experiment described in Ch. 5.

The thermal link K_{th} depends on the membrane geometry, the beam waist, and the thermal conductivity κ_{th}. This equation is used for the estimates of thermal decoherence in Sec. 3.1.3.

4.2.3 Quality Factor

We measure distinct resonances of the Q of the low-stress membrane as a function of membrane frequency $f_{n,m}(P)$. At certain laser powers P, the $Q(f_{1,1})$ is observed to be more than two orders of magnitude smaller than the highest recorded value, as shown by the measurement result in the top panel of Fig. 4.7. The sudden decrease in $Q(f_{1,1})$ takes place when the membrane mode becomes resonant with a mode of the frame. We have identified the frame modes interferometrically by focusing the laser beam onto the frame (Fig. 4.4). The measured frame modes clearly overlap with the resonances in Q^{-1} as shown in the lower panel of Fig. 4.7. Further details on the analysis can be found in Ref. [46].

4.3 Membranes in the Main Experiments

Free-Space Coupling Experiment

In the first, free-space, experiment we use a low-stress SiN membrane, which has specified dimensions of 0.5 mm × 0.5 mm × 50 nm [107], power reflectivity of $\mathfrak{r} = |r_\mathrm{m}|^2 = 0.28$ at $\lambda = 780\,\mathrm{nm}$, quality factor of $Q = 2 \cdot 10^6$, and a fundamental vibrational mode with $\omega_\mathrm{m}/2\pi = 272$ kHz. The reflectivity of the membrane is estimated by measuring the transmission and reflection signal from the membrane. The amplitude reflectivity depends on the membrane thickness as

$$|r_\mathrm{m}| = \left| \frac{\left(n_\mathrm{m}^2 - 1\right) \sin k n_\mathrm{m} d_\mathrm{m}}{2 i n_\mathrm{m} \cos k n_\mathrm{m} d_\mathrm{m} + \left(n_\mathrm{m}^2 + 1\right) \sin k n_\mathrm{m} d_\mathrm{m}} \right| . \tag{4.15}$$

The amplitude reflectivity as a function of membrane thickness is plotted in Fig. 4.8. The measured reflectivity together with Eq. 4.15 would imply a thickness of $d_\mathrm{m} = 45\,\mathrm{nm}$ instead of the stock-specified value of 50 nm. Indeed, previous extensive studies have shown the commercial film thicknesses to vary as much as 30% [118]. On the other hand, the lateral dimensions of the membranes match the specified values, as confirmed by SEM imaging, also the membrane eigenfrequencies match the calculated values of Eq. 4.2. The mass of a 45 nm membrane is $M = 8 \cdot 10^{-12}\,\mathrm{kg}$.

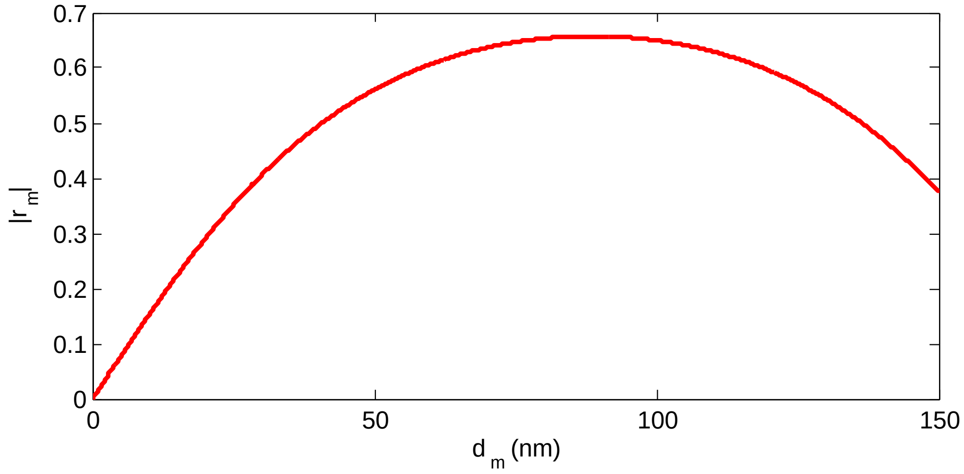

Figure 4.8: Amplitude reflectivity as a function of membrane thickness calculated for low-stress membrane assuming $n_\mathrm{m} = 2.2 + 1.5i \cdot 10^{-3}$, where $\mathrm{Re}\,(n_\mathrm{m})$ is taken from [105]. The calculation is done for 780 nm. From the measured reflectivity one can estimate the thickness and thus the mass of the membrane.

In the main experiment (Ch. 5) we detect the optomehcanical coupling of the atoms to the membrane as a small change ($\sim 1\,\%$) in the Q of the membrane over a range of lattice power levels. We choose to measure the coupling at predefined power levels of the lattice beam, where ω_{m} is tuned away from the frame resonances and the Q of the membrane is high.

Cavity-Enhanced Coupling Experiment

In the second, cavity-enhanced experiment we use a stoichiometric $\mathrm{Si_3N_4}$-membrane supplied by Norcada [107]. The membrane has specified dimensions of $1.5\,\mathrm{mm} \times 1.5\,\mathrm{mm} \times 50\,\mathrm{nm}$, fundamental vibrational mode of $f_{1,1}(P=0) = 274\,\mathrm{kHz}$ and quality factor of $Q = 3 \cdot 10^7$. We determine the reflectivity of the membrane via its optomechanical coupling to the cavity, as discussed in Sec. 6.7, and find a value of $\mathfrak{r} = |r_{\mathrm{m}}|^2 = 0.1733$. Assuming $n_{\mathrm{m}} = 1.98$ [118][1], we estimate the thickness of the membrane from its reflectivity (Eq. 4.15) to be 42 nm, and the corresponding mass $M = 6.4 \cdot 10^{-11}\,\mathrm{kg}$ (assuming $\rho = 2.7\,\mathrm{g/cm^3}$ [101]). The high-stress membrane has a considerably lower absorption at 780 nm than the low-stress membrane, on the order of $\mathrm{Im}\,(n_{\mathrm{m}}) \lesssim 2.0 \cdot 10^{-5}$. This reduces the technical and fundamental limitations in the main experiment due to membrane absorbance. In the power regime we operate at the moment ($P_{\mathrm{mem}} \lesssim 2\,\mathrm{W}$), we observe constant $Q\,(P)$, which eases the technical requirements for the measurements.

Table of the Science Membrane Properties

The parameters of the low- and high-stress science membranes in the respective free-space (Ch. 5) and cavity-enhanced (Ch. 6) experiments are listed in Tab. 4.1.

---

[1] A value of $n_{\mathrm{m}} = 2.0$ has also been reported in Ref. [102] for similar stoichiometric membranes, whereas the reported value for the low stress membranes is $n_{\mathrm{m}} = 2.2$ [105].

SiN membrane	**low-stress**	**stoichiometric**
Density ρ	$2.9\,\mathrm{g/cm^3}$ [46]	$2.7\,\mathrm{g/cm^3}$ [101]
Thermal conductivity κ_{th}	$3\,\mathrm{WK^{-1}m^{-1}}$ [46]	$2.7\,\mathrm{WK^{-1}m^{-1}}$ [99]
(293 K)		$0.4 - 4\,\mathrm{WK^{-1}m^{-1}}$ [99],
		$25 - 36\,\mathrm{WK^{-1}m^{-1}}$ [117]
Specified dimensions	$(0.5\,\mathrm{mm})^2 \times 50\,\mathrm{nm}$	$(1.5\mathrm{mm})^2 \times 50\,\mathrm{nm}$
$\mathrm{Re}\,(n_{\mathrm{m}})$ (1064 nm)	2.2 [105]	1.98 [118], 2.0 [102]
Tensile stress S_0	$70\,\mathrm{MPa}$ [46]	$0.92\,\mathrm{GPa}$
Measured dimensions	$(0.5\,\mathrm{mm})^2 \times 45\,\mathrm{nm}$	$(1.5\,\mathrm{mm})^2 \times 42\,\mathrm{nm}$
Effective mass M	8 ng	64 ng
$f_{1,1}$	272 kHz	274 kHz
Q	$2 \cdot 10^6$	$3 \cdot 10^6$
$\mathfrak{t}$ at 780 nm	0.28	0.17
$\mathrm{Im}\,(n_{\mathrm{m}})$ at 780 nm	$1.5 \cdot 10^{-3}$	$\lesssim 2 \cdot 10^{-5}$

Table 4.1: Material properties of the low-stress and stoichiometric SiN membranes used in our main experiment. The values are for room temperature. The upper part of the table contains literature values, and the lower part separated by the two horizontals, summarizes the measurement results reported in this Chapter.

5

Observation of Backaction of Ultracold Atoms on a Mechanical Oscillator

This Chapter describes in detail the experimental realization of the free-space, optomechanical interface between an ensemble of ultra cold atoms and membrane oscillator, which has been addressed theoretically in Sec. 3.1. By using $\sim 10^6$ atoms in an optical lattice that is formed by retroreflecting a laser beam from the membrane, we measure energy transfer between the two systems when they are tuned on resonance. Moreover, we demonstrate sympathetic damping of the membrane motion via continuous laser cooling of the atoms. The experiments described in this Chapter represent the first observations of the backaction of ultra cold atoms on a macroscopic object. This is striking, as the mass ratio between the membrane and the atoms is on the order of 10^8.

Figure 5.1 gives an illustrative guideline on the experimental realization and the main topics that are covered in this Chapter. The membrane and the atoms are placed into separate vacuum chambers and a long-distance coupling is provided by an optical lattice. The atom module is built by partially exploiting an already existing magneto-optical trapping system (MOT) for ^{87}Rubidium atoms, whereas the membrane module is built up completely from scratch. As we had no previous experience in experimenting with the membranes, we benefit considerably from the modularity of the setup which allowed us to change the mechanical oscillators relatively quickly without affecting the cold atom preparation in the ultra-high vacuum (UHV) chamber and optimize the two modules independently.

For resonant coupling, the trap frequency of the atoms is matched to the oscillation frequency of the membrane, $\omega_{\mathrm{at}} \sim \omega_{\mathrm{m}} \sim 2\pi \cdot 250\,\mathrm{kHz}$, which constrains us to work with a near-resonant lattice. Section 5.1 will focus on the optical lattice setup. The membrane module is discussed in Sec. 5.3. We probe the

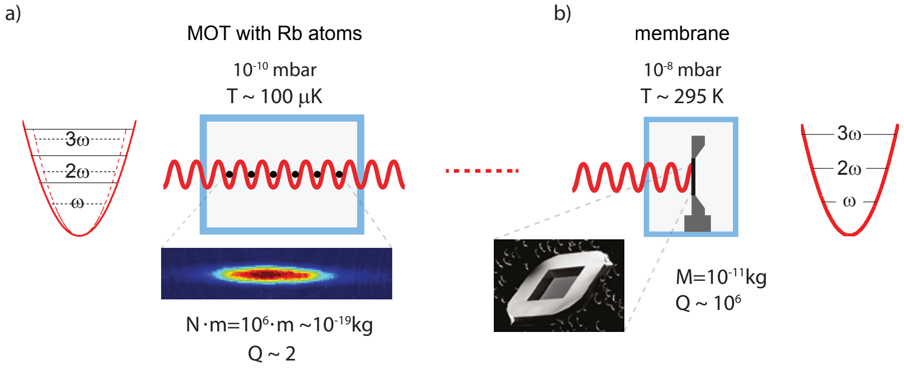

Figure 5.1: Main features of our two experimental modules: a) The ^{87}Rb atoms are collected and cooled in a magneto-optical trap (MOT) inside an ultra-high vacuum chamber. The cold atoms are loaded from the MOT into an optical lattice. Inset: The atoms are detected via absorption imaging. b) The SiN membrane (inset) resides in a separate vacuum chamber at room-temperature and serves as partially reflective end mirror for the 1D optical lattice. The membrane motion is detected interferometrically (not shown). The distance between the atoms and the membrane is about 1 m in the laboratory setup.

optomechanical coupling via the atoms and the membrane independently to verify that the coupling is bi-directional. On the atom module, we use absorption imaging to monitor the resonant temperature increase of the atoms in the trap, as discussed in Sec. 5.4. On the membrane-side, we measure a resonant enhancement in the damping of the membrane motion as represented in Sec. 5.5. The finite temperature of the atoms and a spatially inhomogeneous trapping potential lead to inhomogeneous broadening of the atomic resonance which is addressed in Sec. 5.2. By taking this into account in our theoretical model, we can accurately model the effect of the atoms onto the membrane 5.5.

Historical Remarks

The measurements presented in this Chapter were performed in Munich in the laboratory of Prof. T. W. Hänsch. During Summer 2010 we measured a significant coupling between the membrane and the atoms [39]. In Fall 2010, we moved from the labs in Munich to Basel, where P. Treutlein had been appointed as assistant professor. This meant a complete disassembling of the setup, a part of which was left in Munich and a part of which moved in pieces with us to Basel. Motivated by the results described in this Chapter, we designed a dedicated, second generation setup in Basel starting from scratch (see impressions from the lab move in App. C).

5.1 Atom Preparation in the Lattice

This section describes the atom preparation procedure in the lattice. The atom module is built by partially exploiting an already existing magneto-optical trapping system (MOT) for ^{87}Rubidium atoms. The existing MOT was built on an atom chip [119, 120, 121] and originally intended for different purposes [120, 122], but with slight modifications it is successfully used to load and cool atoms into the new lattice. The lattice is relatively near-resonant as the trap frequency of the atoms, ω_{at}, is required to match the oscillation frequency of the membrane, $\omega_{\mathrm{m}} \sim 2\pi \cdot 250\,\mathrm{kHz}$. The atoms are loaded to the lattice from the chip-MOT and imaged via absorption imaging. A sophisticated imaging sequence is developed to image only the atoms trapped in the lattice while the MOT resides in the background. The MOT alone is not sufficient to cool the atoms to the ground-state of the lattice potential, but by using subsequent molasses cooling this is possible. Characterization measurements on the MOT- and molasses-loaded lattice are presented.

5.1.1 Magneto-Optical Trap

Before the atoms are loaded into the lattice, they are spatially confined in a magneto-optical trap (MOT) and simultaneously cooled to a sufficiently low temperature to allow optical trapping in the lattice. The MOT consists of a set of red-detuned laser-beams that laser-cool the atoms in a quadrupole magnetic field. The magnetic field gradient provides position dependence on the laser cooling-forces, thereby creating a trap minimum where the atoms are collected. The reader is referred to Ref. [123] for basic introduction to the operation principle of a MOT.

Atom Chip MOT Configuration

In our experiment the MOT is on an atom chip [119, 120, 121]. The atom chip forms one facet of a glass cell that is attached to a compact ultrahigh vacuum system as shown in Fig. 5.2. Rubidium atoms are released into the UHV chamber by a resistively heated alkali dispenser. The magnetic potential is generated by a "U"-shaped current-carrying copper wire behind the chip (illustrated in Fig. 5.4). The wire field is then superimposed with a homogeneous bias field created by three pairs of Helmholtz coils that surround the vacuum cell. At the point in space, where the bias field exactly compensates the U-wire field, a quadrupole field minimum is created.

A standard laser field configuration for MOT-cooling consists of three circularly polarized, counter-propagating and perpendicular beam pairs to provide cooling of the atoms in 3D [78]. As the chip blocks the light along one axis, we use a so-called mirror-MOT configuration instead [124, 120]. It replaces two cooling beams by the reflection of two beams inclined by 45° on a dielectric mirror that

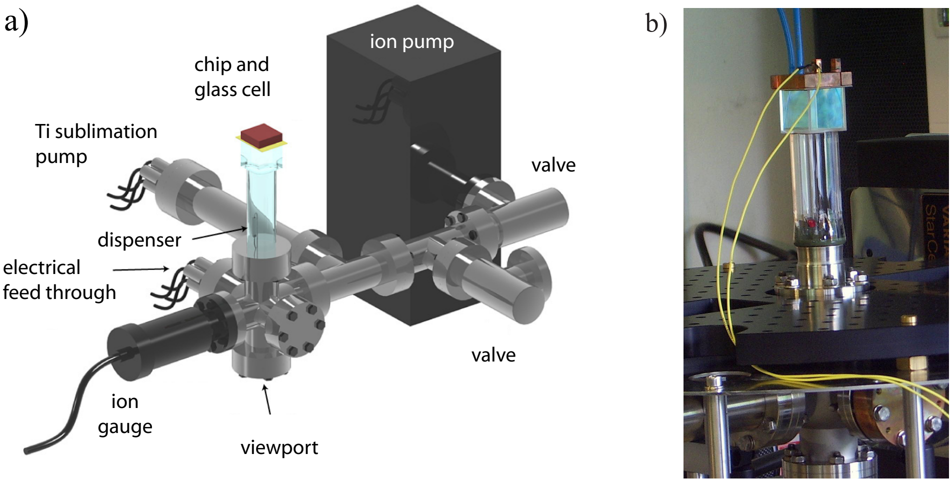

Figure 5.2: a) The atom chip is attached to a glass cell which is connected to a vacuum system. b) Photograph of the glass cell. A copper block for cooling the the chip structures is mounted on top of the chip. The figure is taken from [122].

is applied on the chip. Figure 5.4 shows an illustration of the 45° MOT beams and the other beam pair which we denote as the horizontal beams (hor). The atom chip used in this experiment was fabricated by D. Hunger and the details of the chip can be found in his doctoral thesis, Ref. [122].

The laser system for the optical cooling, optical pumping and absorption imaging of atoms is based on home made diode lasers. This is documented in detail in Ref. [122]. An overview of the laser frequencies used is shown in Fig. 5.3.

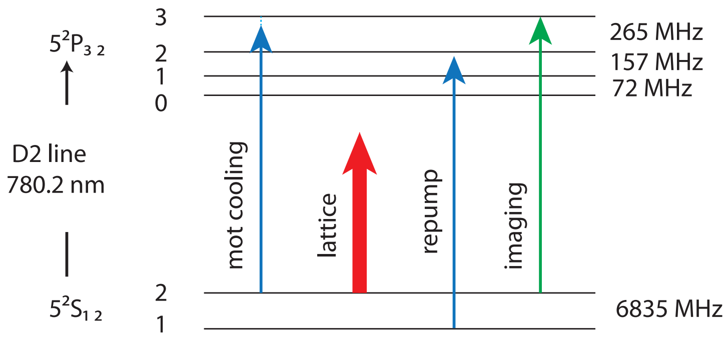

Figure 5.3: Level scheme of the ^{87}Rb D2 line and laser frequencies used in our experiment.

- The **cooling lasers** are provided by home-built grating stabilized diode-lasers. The frequency of the cooling lasers is stabilized by Doppler-free saturation spectroscopy in a Rb vapor cell [125] and frequency-locked via a feedback signal to the grating piezo [122]. The laser cooling beam is locked to the $F = 2 \rightarrow F' = (2, 3)$ crossover resonance and frequency-shifted with a double-pass AOM near to $F = 2 \rightarrow F' = 3$ resonance.
- The cooling light drives some atoms via the non-resonant transition $F = 2 \rightarrow F' = 2$. The excited state $F' = 2$ can also decay to the 'dark' $F = 1$ ground state. To bring the population in this state back to the cooling cycle we use a so-called **repump beam**, which is tuned to the $F = 1 \rightarrow F' = 2$ transition. The repump beam is coupled into the 45° fibers (Fig. 5.3).
- Lastly, the beam for **absorption imaging** (see Sec. 5.1.3) is derived from a cooling laser and frequency-shifted with an AOM to the resonant transition $F = 2 \rightarrow F' = 3$. The imaging beam propagates along the horizontal MOT beams, as illustrated in Fig. 5.3.

In the main experiment, we typically load $2 \cdot 10^7$ atoms in the MOT in 3 s and the measured temperature is around 150 µK. The MOT has a magnetic field gradient of 15 Gauss/cm along the lattice and the circular-polarized MOT beams are detuned by $\Delta_{\text{MOT}} = -2.2\,\gamma_{\text{se}}$ from the $F = 2 \rightarrow F' = 3$ transition of the Rubidium D2 line. To reduce the temperature below the values achievable in a MOT, we perform optical molasses cooling and reach temperatures below 10 µK.

Optimization of the MOT Loading Rate

The experimental sequence to measure the atom-membrane coupling requires the experiment to run stable over several days. Hence, it is important to minimize the time required for each experimental step within the complete measurement run. The MOT loading rate, which is one of the most time consuming phases in the run, is optimized with respect to the rubidium dispenser current that sets the rubidium pressure in the chamber.

The time dependence of the MOT population $N(t)$ can be modeled by [126]

$$\frac{dN}{dt} = \alpha n_{\text{ss}} - (\beta n_{\text{ss}} + \gamma)N(t) = R_0 - \Gamma_0 N(t). \tag{5.1}$$

The first term corresponds to the capturing of the atoms, with α proportional to the trapping cross section. The capturing rate, $R_0 = \alpha n_{\text{ss}}$, depends on the fraction of slower Rb atoms in the chamber and is thus proportional to the density of the untrapped Rb atoms, n_{ss} in the chamber. The second term describes the collisional loss processes, where β describes the collisions between untrapped and trapped Rb atoms, and γ describes the collisions between other background atoms and trapped atoms. The solution for Eq. 5.1 is

$$N(t) = \frac{R_0}{\Gamma_0}\left(1 - \exp^{-\Gamma_0 t}\right), \tag{5.2}$$

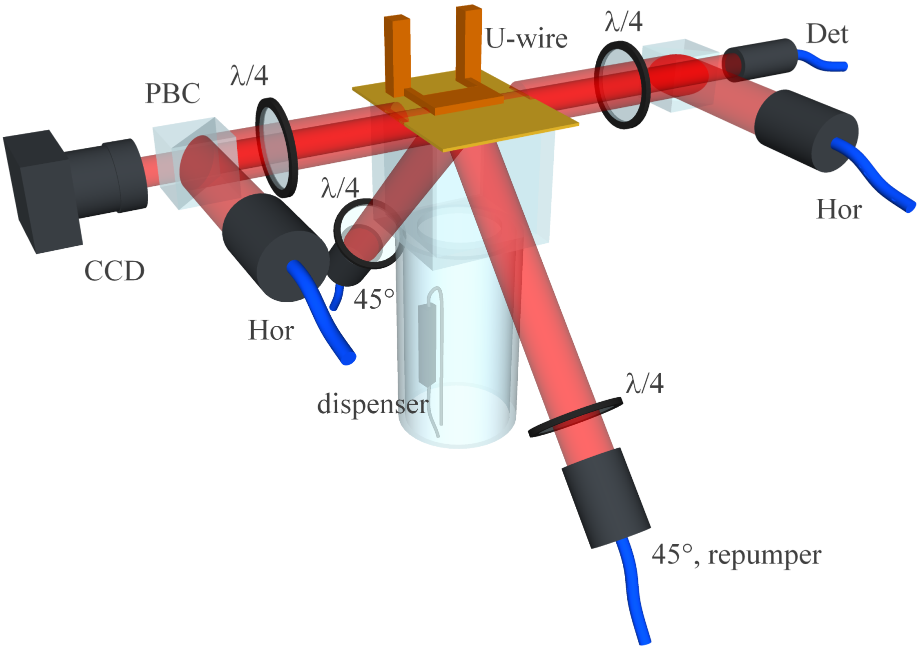

Figure 5.4: Laser configuration for the mirror-MOT on a chip. The chip forms one end facet of the glass-vacuum cell. The U-shaped copper wire is shown in orange on top of the chip. Two horizontal beams and two beams inclined by 45° with respect to the chip provide cooling and repumping light. Imaging is done along the x-axis. The picture is modified from Ref. [120].

where $\frac{R_0}{\Gamma_0}$ is the stationary number of trapped atoms in the MOT, which is reached on time scale of Γ_0^{-1} is the MOT.

We measure the MOT loading curve for various dispenser current values I_{disp}. After changing the dispenser current to the subsequent value, the pressure in the chamber is allowed to equilibrate for an hour. The equilibrium pressure in the chamber is observed to increase linearly with I_{disp} within the explored range. Figure 5.5 shows the MOT loading rate as a function of I_{disp} in the chamber. The Γ_0 follows linearly the I_{disp} as observed in Fig. 5.5a. On the other hand, the steady state number of atoms increases with the I_{disp} and levels off when $\beta n_{\mathrm{ss}} \geq \gamma$ as shown in Fig. 5.5. A dispenser current of $I_{\mathrm{disp}} = 4.55\,\mathrm{A}$ corresponding to a pressure reading of $p = 1.26 \cdot 10^{-9}$ mbar was chosen for the experiments. This is still sufficiently far from the point where the collisional losses with the background Rb atoms limit the loading, but yet enables relatively fast loading of the MOT.

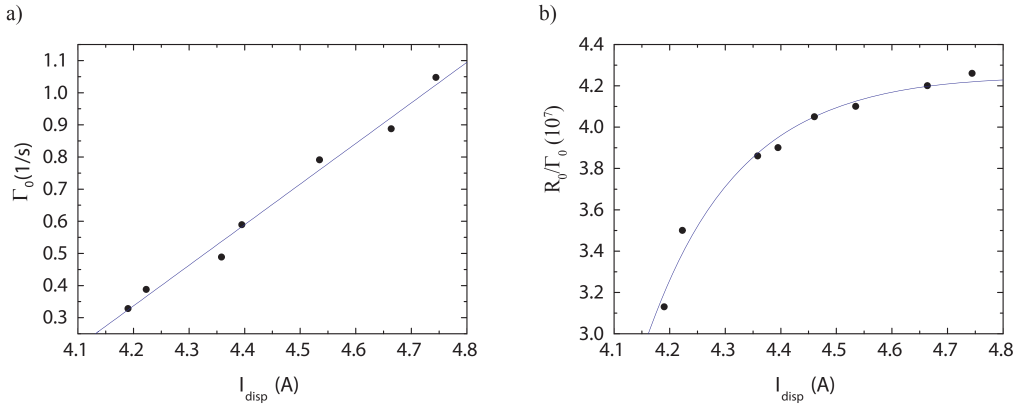

Figure 5.5: Optimizing the MOT loading. a) The Γ_0, as defined in Eq. 5.1; and b) the steady-state number of atoms as a function of dispenser current I_{disp}. Note that our ion gauge does not accurately measure the absolute pressure in the whole chamber, since the Rubidium atoms may locally contaminate the cell walls and create local variations in the pressure.

5.1.2 Laser System for the Optical Lattice

Figure 5.6 presents a schematic of the lasers in our experimental setup. The lattice laser light is provided by a master-amplifier configuration in order to have sufficient laser power. The master laser is a grating stabilized diodelaser (`DLPro`, Toptica Photonics), operating around 780 nm (`LD-0780-0100-AR-1`). The maximum output power of the DLPro is 80 mW and its linewidth is specified to be 100 kHz (within 5 µs). The DLPro can be tuned mode-hop free over $\sim$ 4 GHz. We characterize the lattice for various detunings, and for the main coupling experiment, the detuning is set to $\Delta_{\text{L}} = -2\pi \cdot 21\,\text{GHz}$ from the D2-line of ^{87}Rb ($F = 2 \leftrightarrow F' = 3$). The frequency drift of the DLPro is observed to be very slow at room-temperature and negligible compared to Δ_{L} on a time scale of days. This allows us to operate the laser free-running.

The master laser is seeding a tapered amplifier (`BoosTA`, Toptica Photonics, chip `TA_780_808`). The master+BoosTA configuration can deliver up to 1 W of laser power when properly aligned. The output of the TA is coupled into an acousto-optic modulator (AOM), and the first order diffracted beam out of the AOM is coupled to a polarization maintaining fiber[1]. The AOM is driven by a custom-designed AOM controller by Anton Scheich (Ludwig-Maximilians Universität, München). The power output of the AOM is regulated via an intensity stabilization circuitry that stabilizes the power level of the lattice beam to a given setpoint. In addition, the AOM controller has an option for fast switch-off of the output voltage in the nanosecond range, which can be used to quickly turn off

---

[1] Fiber `PM780-HP`, and aspheric mode-matching lens $f_1 = 4.51\,\text{mm}$, `C230TME-B`. Both from Thorlabs.

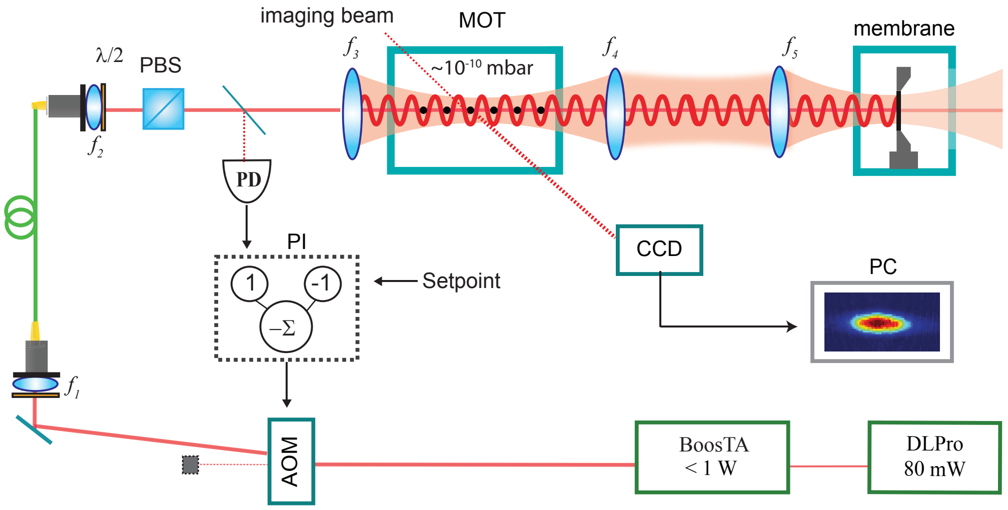

Figure 5.6: The optical lattice laser is provided by a frequency tunable DLPro laser operating at 780 nm. The DLPro beam is injected to a tapered amplifier (TA). The TA output is coupled to an optical fiber. The polarization of the fiber output is cleaned (polarizing beam splitter, PBS) and the intensity of the fiber output is actively stabilized via the acousto-optic modulator (AOM).

the lattice (∼ 50 ns).

The fiber output is collimated[2] and its polarization is cleaned and aligned with a $\lambda/2$-plate and a polarizing beam splitter (PBS). A fraction of the horizontally polarized lattice beam is picked up by a thin glass wedge (4%) for the intensity stabilization of the lattice beam. The rest of the beam is focused ($f_3 = 400\,\mathrm{mm}$) to a waist size of $w_0 = 350 \pm 30\,\mu\mathrm{m}$ in the center of the vacuum cell, where the ultracold atoms are prepared in a MOT. After exiting the MOT vacuum chamber, the laser is focused on the membrane to a spotsize of 50 µm ($f_4 = 260\,\mathrm{mm}$, $f_5 = 150\,\mathrm{mm}$). The reflected and incoming laser beams are overlapped, forming an optical lattice at the position of the atoms.

Aligning the Lattice

The lattice output coupler is coarse aligned with the center of the optimized MOT by modulating the lattice laser around the $F = 2 \rightarrow F' = 2$ resonance. When the lattice traverses through the center of the MOT, a strong *in-situ* modulation in the fluorescence of the MOT on top of the fluorescence due to cooling is observed on a CCD camera that is connected to a TV-screen. The fine adjustment of the lattice output coupler is done by monitoring the atom number loss from the MOT by means of absorption imaging (Sec. 5.1.3). After this the backreflected beam is overlapped with the incoming lattice beam in the cell, and fine-aligned with

---

[2] Aspheric mode-matching lens $f_2 = 6.24\,\mathrm{mm}$, `C110TME-B`, from Thorlabs.

respect to the maximum atom number trapped in the lattice (Sec. 5.1.3).

Lattice Parameters

The optical fiber can provide up to 300 mW of power at the position of the MOT. However, the operating power of the lattice beam is constrained by the requirement that the trap frequency of the atoms needs to match the oscillation frequency of the membrane, i.e., $\omega_{\mathrm{at}} \sim \omega_{\mathrm{m}} \leq 2\pi \cdot 270\,\mathrm{kHz}$. The power of the lattice beam on the membrane is further restricted for two reasons: the absorbance of the membrane and the resulting heating, and by the power-dependent coupling of the membrane eigenfrequency to the supporting frame modes, as described in Chapt. 4. These constraints limit us to work with relatively near resonant lattice, where the lattice power is less than 150 mW, and the detuning is $|\Delta_{\mathrm{L}}| \leq 2\pi \cdot 30\,\mathrm{GHz}$. Another practical constraint on the lattice parameter regime is the lattice-lifetime, which sets a lower limit on the detuning, as discussed in Sec. 5.1.5.

The reflected beam is weaker than the incoming beam due to the finite reflectivity of the membrane, $|r_{\mathrm{m}}|^2 = \mathfrak{r} = 0.28$, but also due to the transmission losses in the optical components between the membrane and the atoms, which for a single pass amount to $\mathfrak{t} = 0.82$. This results in a lattice potential that consists of a modulation part on top of an offset, as described in Sec. 2.3. For the main experiment, we choose $w_0 = 350 \pm 30\,\mu\mathrm{m}$, and $\Delta_{\mathrm{L}} = -2\pi \cdot 21\,\mathrm{GHz}$. For these parameters with an incoming beam of $P = 76\,\mathrm{mW}$, the calculated modulation depth of the sinusoidal potential is $V_{\mathrm{mod}} = k_B \times 290 \pm 50\,\mu\mathrm{K}$ resulting in a calculated trap frequency of $\omega_{\mathrm{at}}/2\pi = 305 \pm 25\,\mathrm{kHz}$ (Eq. 2.88), which is close to the membrane eigenfrequency. At $P = 76\,\mathrm{mW}$, we typically load $N = 2 \cdot 10^6$ atoms into the lattice from the MOT with a temperature of $T = 100\,\mu\mathrm{K}$.

Intensity Stabilization of the Lattice

The intensity of the TA output was observed to fluctuate by $2 \cdot 10^{-2}$ (rms) for frequencies below 10 kHz. Such power fluctuations cause fluctuations in the trap frequency of the atoms and also in the membrane eigenfrequency $\omega_{\mathrm{m}}(P)$ due to absorbance effects. In addition, a change in the power impinging on the membrane may result in a dramatic drop in the Q-factor of the membrane mode, as explained in Sec. 4.2. As we want to measure a small change in the Q-factor of the membrane due coupling to the atoms, stable laser power is necessity.

The power stabilization circuitry is based on a PI-servo amplifier design [127], which is schematically illustrated by the gray box labeled "PI"-box in Fig. 5.6. A small glass wedge picks up a part of the lattice beam. The picked-up power is measured on a photodiode (PD), and the PD-current is converted into a voltage at the input of the PI-circuitry. This voltage is then compared with the setpoint value, and their difference is fed as a correction signal with a proper gain to the external control input of the AOM controller. The setpoint to the PI-circuitry is given via a linearly responding analog input, which is computer controlled and programmed as a part of the experimental sequence.

The stabilization circuit diagram is presented in App. B. The filtering of the power supplies of the operational amplifiers (OPAs in App. B) with high capacitors of 100 nF is essential to reduced the supply noise. The bandwidth of the circuit is limited to 12 kHz and the intensity stability is measured with an independent photodiode (1 MHz) to be $1.8 \cdot 10^{-4}$ (r.m.s).

Furthermore, we observed that the AOM controller's power supply imprints 50 Hz noise onto the laser. In addition, the TA output has intrinsic power modulations around $1 - 300$ kHz depending on the exact operation setting of the TA. Both of these intensity noise sources are suppressed by capacitive filtering.

5.1.3 Detection of the Atoms

The number of trapped atoms and their temperature are determined by standard absorption imaging [128]. The atoms are irradiated perpendicular to the lattice-direction with a 50 µs long pulse of σ^+-polarized light resonant with the cycling transition $F = 2 \rightarrow F' = 3$ and the light that has passed through the atoms is detected on a CCD camera. To account for spatial modulations of the imaging beam, two images are taken: one with atoms (A) and a second without (B). In addition, a third image without the imaging beam is taken once a day that accounts for the dark counts and stray light (C). These three images allow us to determine the pixelwise optical density (OD). When the imaging intensity I is considerably smaller than the saturation intensity of the atomic transition, $I_\mathrm{s} = 1.67\,\mathrm{mW/cm^2}$, the atoms cast a shadow onto the camera with optical density

$$\mathrm{OD} = -\ln \frac{A - C}{B - C}. \tag{5.3}$$

The two dimensional atomic column density can then be calculated as

$$n\left(y, z\right) = \mathrm{OD}\left(y, z\right)/\sigma_0, \tag{5.4}$$

where σ_0 is the on-resonance absorption cross section. For σ^+-polarized light this is given by

$$\sigma_0 = \frac{3\lambda^2}{2\pi} = 2.905 \cdot 10^{-13}\,\mathrm{m}^2. \tag{5.5}$$

The atom number located in an area A_pixel is then calculated by summing over all relevant pixels

$$N = \frac{A_\mathrm{pixel}}{\sigma_\mathrm{abs}} \sum_{i,j} \mathrm{OD}\left(i, j\right). \tag{5.6}$$

The temperature of the atoms is determined by monitoring the expansion of the thermal cloud. For a harmonic trap and a thermal cloud well above the BEC transition temperature, the in-trap density distribution follows the Boltzmann distribution

$$n\left(r\right)=n_0\exp^{-\frac{1}{2}\left(\frac{z^2}{\sigma_\mathrm{z}^2}+\frac{r^2}{\sigma_\mathrm{r}^2}\right)},\tag{5.7}$$

where $r^2=x^2+y^2$, n_0 is the peak atomic density,

$$n_0=\frac{N}{(2\pi)^{3/2}\sigma_\mathrm{z}\sigma_\mathrm{r}^2},\tag{5.8}$$

and we have defined the cloud widths $\sigma_\mathrm{z,r}$ as

$$\sigma_\mathrm{z,r}^2=\frac{1}{\omega_\mathrm{z,r}^2}\frac{k_BT}{m}.\tag{5.9}$$

When the confining potential is switched off at time $t=0$, the cloud starts to expand ballistically and begins to fall under gravity. The evolution of the cloud width is defined by the Boltzmann distribution as [128]

$$\sigma\left(t\right)_\mathrm{z,r}^2=\sigma\left(t=0\right)_\mathrm{z,r}^2+\frac{k_BT}{m}t^2.\tag{5.10}$$

By releasing the atoms from the trap and letting them expand by a varying time-of-flight (TOF) before imaging them allows us to determine the temperature of the atoms.

We image the atoms along x-axis, perpendicular to the lattice propagation axis (z), as illustrated in Fig. 5.7. We use a CCD camera from JAI with a quantum efficiency of 35% at 780 nm. The pixel size is $\left(8.4\cdot10^{-6}\right)^2\,\mathrm{m}^2$. The imaging beam is provided by a fiber output coupler that collimates the beam to a diameter of 8 mm with an acromatic lens of $f=40\,\mathrm{mm}$. We use a peak intensity of $\leq 0.2I_\mathrm{s}$ to avoid saturation of the atoms. In front of the CCD camera we use two acromatic lenses with $f_1=100\,\mathrm{mm}$ and $f_2=150\,\mathrm{mm}$, resulting in a magnification of 1.28 and a resolution of 9 µm.

5.1.4 Imaging of the Lattice in the Presence of the MOT

The lattice is loaded from the MOT, after which the MOT is switched off and the MOT atoms that are not trapped in the lattice, start to diffuse and accelerate due to gravity. In order to determine the number of atoms trapped in the lattice independently of these background MOT atoms, the background MOT atoms are optically pumped to the 'dark' state $F=1$ before imaging, and the number of atoms in the lattice occupying the state $F=2$, N_2 is measured. In an auxiliary measurement, we determine the fraction of atoms in the lattice occupying the ground-state $F=1$, N_1. The total number of atoms in the lattice is then given by $N=N_1+N_2$.

The MOT scatters atoms into $F=1$ via non-resonant transition $F=2\rightarrow F'=2$ (see the ^{87}Rb level diagram in Fig. 5.3), which are then pumped back to

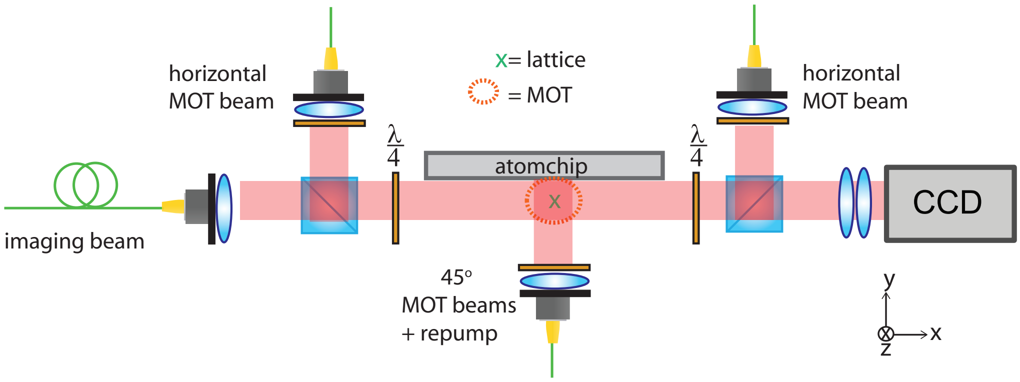

Figure 5.7: Laser configuration for the MOT, lattice and the imaging system. The lattice is aligned with respect to the center of the MOT and the lattice beam propagates along the z-direction. The imaging is along the x-direction, and the 45° beams propagate in the zy-plane in 45° angle with respet to both of the axis, as illustrated in Fig. 5.4.

the cooling cycle by the repump beam. The optical pumping rate of the MOT, $\Gamma_{21,\mathrm{MOT}}$ ($F = 2 \rightarrow F = 1$), is measured without the presence of the lattice by switching the repump beam off after loading the MOT for 2 s. After a varying MOT hold time, we measure the number of atoms remaining in the state $F = 2$ and determine $\Gamma_{21,\mathrm{MOT}} = 2.7 \cdot 10^3\,\mathrm{s}^{-1}$. In the presence of the lattice, the total pumping rate increases to $\Gamma_{21,\mathrm{MOT+L}} = 4.5 \cdot 10^3\,\mathrm{s}^{-1}$. Thus, by switching the repumper off for 1.5 ms, we expect to pump most of the MOT atoms ($> 99\%$) to the 'dark' state $F = 1$ in the presence of the lattice. We do this at the end of the MOT-loading stage.

In the absence of the repumper, the lattice beam creates a steady-state population-distribution between the states $F = 1$ and $F = 2$. Figure 5.8 shows a measurement of the atom number decay in the lattice imaged both with (red datapoints) and without (black datapoints) the presence of the repumper after a long lattice hold time of > 20 ms. A fit to either one of the data sets results in the same exponential decay, and we determine the lattice lifetime to be 25 ms in this measurement. The single exponential decay in Fig. 5.8 indicates that mostly lattice-bound atoms are imaged and the MOT has fallen out of the imaging region. We observe that the atom number with repumper on is 1.76 times larger, i.e., $N = N_1 + N_2 = 1.76N_2$. Thus, to determine the total atom number in the lattice in the presence of the dark MOT atoms, we measure the atoms in $F = 2$ and scale the result with the measured population distribution fraction. The number of atoms initially trapped in the lattice can be then extrapolated from the measured lattice lifetime.

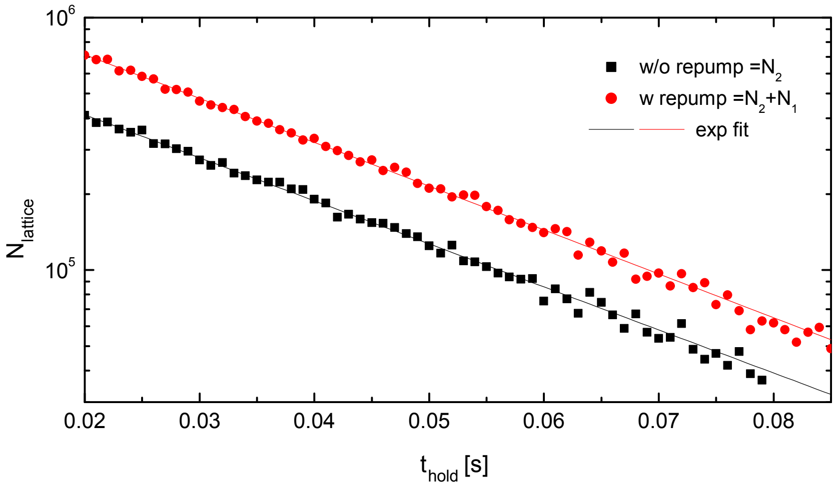

Figure 5.8: The number of atoms remaining in the lattice in state F=2 after a hold-time of t_{hold} imaged with (red dots) and without (black dots) the repumper. Exponential fits to the data give a same value for the $1/e$- lattice decay time, namely $\tau = 25\,\mathrm{ms}$, and indicate the initial total atom number in the lattice to be $1.6 \cdot 10^6$ (red fit). The lattice detuning is $\Delta_{\mathrm{L}} = -2\pi \cdot 20.8\,\mathrm{GHz}$.

5.1.5 Simultaneous MOT and Lattice Operation

In the atom-membrane coupling measurements presented in this Chapter, the lattice is loaded directly from the MOT. The MOT is also kept continuously on during the back-action measurement, such that the atoms are constantly replenished into the lattice and the atomic motion is roughly in steady-state during the measurement.

When the optical lattice beam is switched abruptly on, the membrane eigenfrequency starts to shift. Only after the membrane is thermalized with respect to the absorbed heat, we can measure the membrane eigenfrequency and excite the membrane motion at this frequency, which is required for our back-action sequence. The membrane excitation to the desired value takes about 2 s (see Sec. 5.3). Hence, in our main coupling experiment (Secs. 5.4 and 5.5), the MOT and the lattice are switched on simultaneously. In this way, we can excite the membrane motion during the loading of the MOT, and simultaneously load the atoms into the lattice.

In the absence of the lattice, we typically trap $2 \cdot 10^7$ (after 3 s of loading) atoms in the MOT and the typical temperature of the MOT is around 150 µK. When the lattice is overlapped with the MOT, we observe a decrease in both the atom number in the MOT, and the temperature of the MOT. The former is measured to be $1 \cdot 10^7$ and the latter 100 µK (for $P = 70\,\mathrm{mW}$, $\Delta_{\mathrm{L}} = -2\pi \cdot 21\,\mathrm{GHz}$, $w_0 = 350 \pm 30\,\mu\mathrm{m}$, i.e., for the resonant lattice parameters). The number of atoms trapped in the lattice is $\sim 2 \cdot 10^6$.

The presence of the lattice changes the MOT operation, as the lattice effectively detunes the MOT beams further off from the atomic resonance. The lattice beam creates a light shift of the $F = 2$ ground-state of

$$\delta E_0 = V_0/\hbar \propto P, \tag{5.11}$$

where V_0 is the overall depth of the dipole trap. The δE_0 is on the order of γ_{se} when the lattice power is around 70 mW. This is comparable to the absolute detuning of the MOT beams, $\Delta_{\mathrm{MOT}} = -2.2\,\gamma_{\mathrm{se}}$ from the $F = 2 \rightarrow F' = 3$ transition (see Fig. 5.3). The MOT cooling rate, and consequently the final temperature of the atoms in the MOT depends on the effective detuning of the MOT fields, $\Delta'_{\mathrm{MOT}} = \delta E_0 + \Delta_{\mathrm{MOT}}$, as [78]

$$T_{\mathrm{MOT}} \propto \frac{1}{\Delta'_{\mathrm{MOT}}}. \tag{5.12}$$

Therefore, we measure lower T_{MOT} in the presence of the lattice. On the other hand, in the near-resonant MOT regime, the capture velocity of the MOT depends inversely on the detuning [78]:

$$v_c \propto 1/(\Delta'_{\mathrm{MOT}}). \tag{5.13}$$

This explains the observed drop in the atom number of the MOT in the presence of the lattice beam.

Figure 5.9 shows an example of an absorption image of the MOT after 4 ms of time of flight (TOF) without (a) and with (b) the lattice beam. The lattice beam appears as a density bump in the spherically shaped MOT cloud. The lattice is aligned to the center of the MOT.

5.1.6 Lattice Lifetime Measurements and Choosing the Detuning

Losses from the trap can be caused by heating mechanisms and scattering processes. Contributions to heating can arise from spontaneously scattered lattice-light photons, background gas collisions, intensity fluctuations, and the pointing instability of the lattice beam. The two latter contributions are minimized by intensity stabilization of the lattice beam and robust mounting of the fiber output-coupler of the lattice. Furthermore, a large beam waist is preferred to make the trap less sensitive to beam pointing fluctuations due to vibrations of the components in the beam path.

Typically, optical lattices are operated in the far-detuned regime to minimize scattering effects, which scale with detuning Δ_{L} and intensity I as $\Gamma_{\mathrm{sc}} \propto I/\Delta_{\mathrm{L}}^2$. This requires high intensity, to obtain a large trap depth $V_0 \propto I/\Delta_{\mathrm{L}}$ (Eq. 2.90 and Ref. [73]). However, in our experiment the lattice detuning is constrained by the requirement of the lattice frequency, $\omega_{\mathrm{at}} \sim \omega_{\mathrm{m}}$, which essentially fixes the ratio I/Δ_{L}. In addition, we want to keep the overall power level below

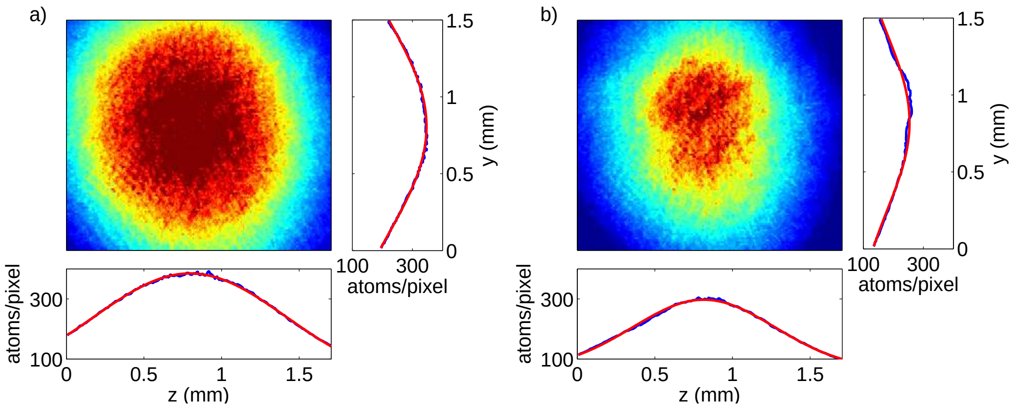

Figure 5.9: An absorption image of the MOT cloud after 3 s of loading a) without, and b) in the presence of the lattice. For this image the repumper was not switched off (see Sec. 5.1.4). The TOF is 4 ms. Insets: blue curve is the 1D integrated atomic density, Eq. 5.4, and red curves result from 2D Gaussian fits to the respective 2D profiles.

150 mW to avoid significant heating of the membrane due to absorbance. For small detunings, $|\Delta_\mathrm{L}| \leq 2\pi \cdot 16\,\mathrm{GHz}$, we measure the lattice losses to be dominated by detuning-dependent effects, i.e, the spontaneous scattering events and light-assisted collisions, resulting in a lattice lifetime $< 10\,\mathrm{ms}$. Thus, for the main experiment, a higher lattice detuning of $\Delta_\mathrm{L} = -2\pi \cdot 20.8\,\mathrm{GHz}$ is chosen, where the lattice lifetime is around 25 ms.

We characterize the atom number decay in the lattice for the chosen $\Delta_\mathrm{L} = -2\pi \cdot 20.8\,\mathrm{GHz}$ over the power regime (0...140 mW). The lattice is loaded for 3 s from the MOT, and the atom number is measured after a varying hold time of the lattice. Typical decay curves are shown in Fig. 5.10a and b for the distinct cases of a shallow and a deep lattice.

For shallow lattices, two different time constants are visible in the atom number decay in Fig. 5.10a, whereas the atom number decay in a deep lattice is described by a single exponential. An exponential fit $N(t) = N_0 e^{-t/t_\mathrm{i}}$ is used to characterize both the first $8 - 17\,\mathrm{ms}$ ($t_\mathrm{i} = t_1$, blue curve) and the last $21 - 36\,\mathrm{ms}$ ($t_\mathrm{i} = t_2$, red curve) atomic decay. A summary of the fitted decay constants t_1 and t_2 as a function of lattice power is presented in Fig. 5.11a.

For shallow lattices, initial evaporation is observed during the first 20 ms of lattice hold time. This is mostly due to the MOT atoms that reside in the lattice volume, but are not bound in the lattice. During the 20 ms these atoms diffuse and drop due to gravity away from the lattice region. This initial evaporation reduces as the depth of the potential is increased, as is visible in Fig. 5.11a. For deep lattices, the losses are well described by a single exponential decay, and we measure $t_1 \sim t_2$, as shown by the red data points in Fig. 5.11a.

Interestingly, the lattice lifetime t_2 stays nearly constant when the power is increased. Since the trap depth V_0 scales linear with P, this suggests that the

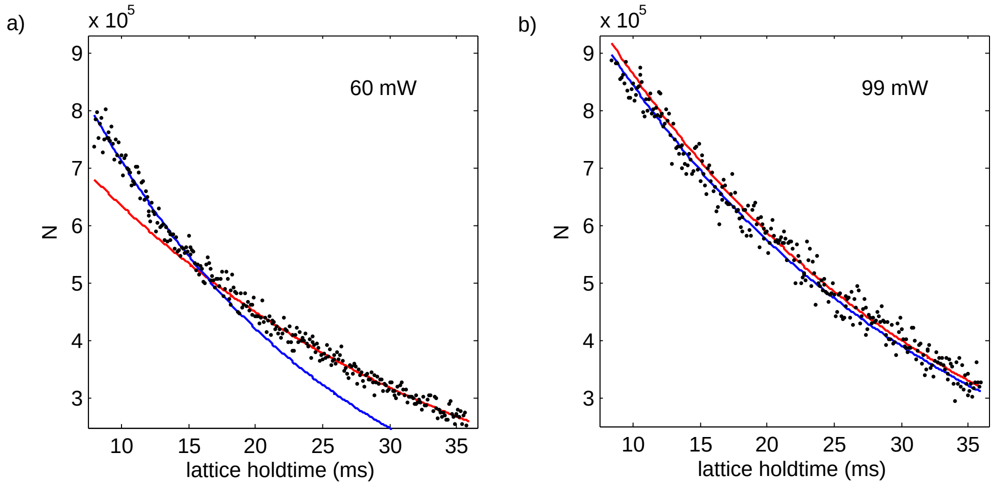

Figure 5.10: Atomic decay in the lattice for lattice power of a) 60 mW and b) 99 mW as a function of lattice hold time. The blue and red curves are single exponential fits to the beginning and end of the atom number curve.

effects contributing to heating and eventual evaporation of the atoms out of the trap would also scale linearly. Such scaling is expected for heating due to spontaneous scattering. Indeed, in the main experiment, Fig. 5.24, we observe linear temperature increase as a function of lattice power. Note that losses due to light-assisted collisions would also increase with power, but would not be compensated by the increasing trap depth.

The red data points in Figure 5.11b show an estimate for the initial atom number bound in the lattice, N_0. The N_0 is extrapolated from the t_2 fits. The N_0 increases as the lattice depth is increased and saturates to a constant value of $\sim 1.2 \cdot 10^6$. This value is influenced by the MOT density. The blue data points in Figure 5.11b show an estimate of the initial atom number within the lattice volume as extrapolated from the t_1 fits. This is the sum of the lattice-trapped atoms and the higher-energy MOT atoms that are not trapped in the lattice. From this we can infer the MOT density to stay roughly constant within the lattice region over the P regime of interest.

Ground State Cooling of Atoms in the Lattice

We made initial trials on molasses cooling of the atoms in the lattice in order to reduce the temperature of the atoms in the trap. Using an optical molasses configuration we can cool the atoms to the axial ground state of the lattice potential, defined by atomic temperature of $T \sim \hbar\omega_{\mathrm{at}}/k_B$. The experimental sequence starts with a 3 s optimized MOT phase. For a subsequent molasses phase, the MOT magnetic fields are switched off, such that only the compensation fields for the external magnetic field remain, and the MOT beams are detuned

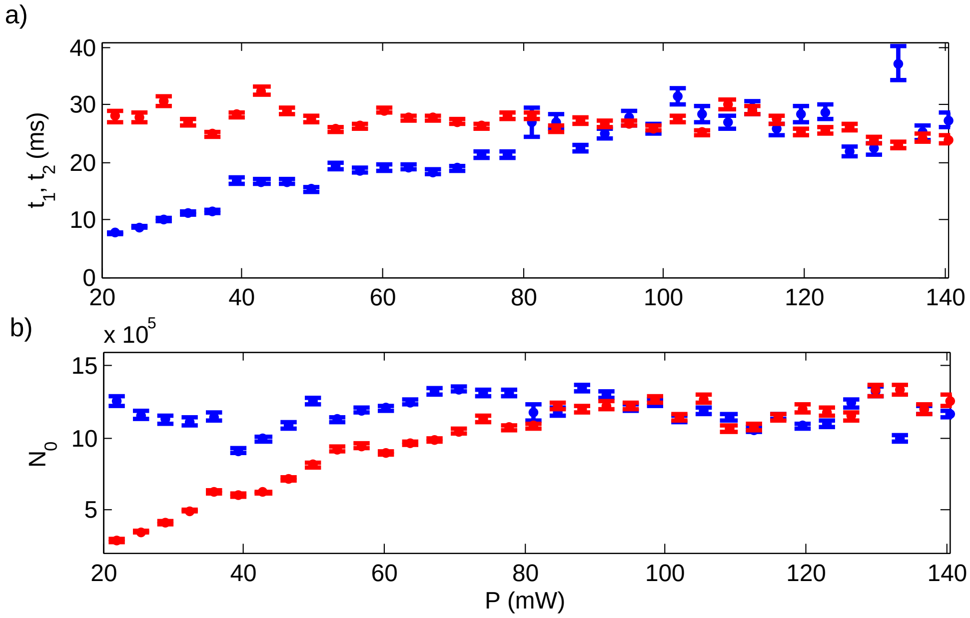

Figure 5.11: a) The initial t_1 (blue) and final t_2 (red) time constants for atom decay in the lattice. b) The initial atom number in the lattice is extrapolated from the fits for t_1 and t_2.

from $-2.2\,\gamma_{\mathrm{se}}$ to $-12\,\gamma_{\mathrm{se}}$. During 4 ms of molasses phase the atoms are cooled to 5 µK. Thereafter the lattice is switched on and the molasses-cooled atoms are loaded into the lattice.

We measured the molasses-loaded lattice lifetime τ for various lattice detunings as reported in Tab. 5.4. Figure 5.12 shows a typical measurement of the atom number decay in the lattice. The lifetime of the lattice is estimated from a single exponential decay. In comparison, Figure 5.12b shows the atom number decay in the lattice with continuous molasses cooling. This curve is characterized by two time constants, and we estimate the lattice lifetime to be given by the longer time constant, τ_{cool}. The initial decay constant has a value ~ 20 ms in all the measurements reported in Tab. 5.4. The initial faster decay in the presence of the molasses light may be due to light-assisted collisions as the molasses is colder and denser than the MOT.

We did not investigate the molasses-loaded lattice performance at this stage any further. Within our parameter regime of interest, the molasses-loaded lattice-lifetime remains short in comparison to the ring-down time of the membrane (on the order of seconds), which is the time scale over which we measure the optomechanical coupling (as described in Sec. 5.5). Thus, for the first coupling experiment, we decided to load the optical lattice directly from the MOT and provide continuous MOT cooling for the atoms during the backaction measurement. In this way we assure the atom number to stay in steady-state in the

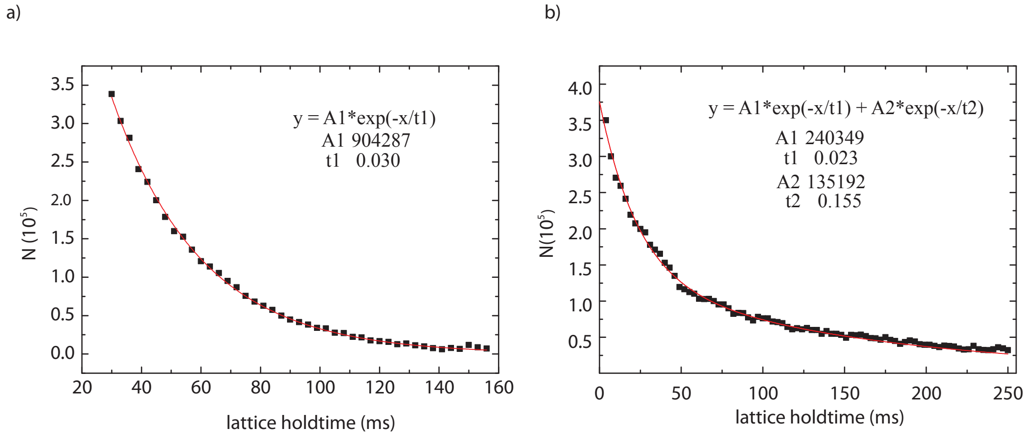

Figure 5.12: a) Lifetime measurement of the molasses loaded optical lattice. An exponential fit results in a lattice lifetime of $\tau = 30\,\mathrm{ms}$. b) The lattice lifetime with simultaneous molasses cooling. The lifetime of the molasses-cooled lattice is estimated from the longer decay to be $\tau_{\mathrm{cool}} = 155\,\mathrm{ms}$. The lattice parameters in this measurement are: $P = 31\,\mathrm{mW}$, $w_0 = 145\,\mu\mathrm{m}$, $\Delta_{\mathrm{L}} = -2\pi \cdot 6.3\,\mathrm{GHz}$.

Power (mW)	$\Delta_{\mathrm{L}}/2\pi$ (GHz)	τ (ms)	τ_{cool} (ms)
31	-6.3	30	155
47	-9.7	46	119
71.6	-14.3	39	140
93	-18.7	66	143

Table 5.4: Molasses-loaded lattice lifetime without (τ) and with (τ_{cool}) continuous molasses cooling for different lattice P and Δ_{L}. The ratio of P/Δ_{L} is roughly fixed such that V_0 is comparable for the various measurements.

lattice during the optomechanical coupling measurement. The continuous MOT-cooling is simple to implement into the experimental sequence, but it comes with a trade-off. The MOT-cooled atoms have a relatively high temperature in the trap which results in broadening of the atomic resonance, as will become clear in the following Sections 5.2, 5.4 and 5.5.

5.2 Spatial Spread in the Trap Frequencies

Due to the Gaussian nature of the lattice beam, the axial trap frequency of the atom depends on its radial position around the potential minimum. The MOT-cooling is not sufficient to cool the atoms to the ground-state of the lattice potential. As a consequence, part of the atoms will oscillate further away from the beam axis at lower trap frequencies. Before discussing the optomechanical coupling results, it is useful to get some insight into the magnitude of the spread in the atomic vibrational frequencies in our trap. The spread in the vibrational frequencies of the atoms, $\Delta\omega_{\text{at}}$, has already been introduced in Eqs. 3.33 and 3.34. It contributes to the overall dephasing of the center of mass motion of the atoms, which we denote γ_ϕ (Eq. 3.20).

Figure 5.13a shows a calculation of the potential distribution for a single lattice site. The calculation is done using Eq. 2.84 and assuming the following experimental parameters for the Gaussian lattice beam: $P = 76\,\text{mW}$, $w_0 = 370\,\mu\text{m}$, $\Delta_{\text{L}} = -2\pi \cdot 20.8\,\text{GHz}$. The simulation also takes into account the single pass transmission loss $\mathfrak{t} = 0.82$ in the optical path between the atoms and the membrane that is present in the experiment. The modulation depth of the sinusoidal potential is $V_{\text{m}} = 260\,\mu\text{K}$ (Eq. 2.86) and the total potential depth is $V_0 = 310\,\mu\text{K}$ (Eq. 2.85), where the offset derives from the finite reflectivity of the membrane $\mathfrak{r} = 0.28$. As the potential is radially symmetric, we define $r^2 = x^2 + y^2$.

The Gaussian intensity profile gives rise to a *radial* dependence of the axial trap frequency, $\omega_{\text{at}}(r)$. This distribution is shown in Fig. 5.13b. We assume the atoms are radially distributed in the potential according to the Maxwell-Boltzmann distribution

$$n(r,T) = n_0 e^{-V(r)/k_B T}, \tag{5.14}$$

where T is the temperature of the atoms. The inset in Fig. 5.13c shows radial density of atoms $2\pi r n(r)$ for three different atomic temperatures: $T = (100, 50, 20)\,\mu\text{K}$. We normalize the total atom number to $N = 2 \cdot 10^6$ within the region where $|V| > 1\,\mu\text{K}$.

While the atoms at the bottom of the trap are expected to oscillate at the harmonic vibrational frequency, the more energetic ones have a lower frequency, because of the decreased curvature of the potential. The density of atoms oscillating within a frequency interval $d\omega_{\text{at}}$ is given by

$$n(\omega_{\text{at}}) = \frac{2\pi r n(r)\,dr}{d\omega_{\text{at}}}. \tag{5.15}$$

Figure 5.13c shows $n(\omega_{\text{at}})$ for the above-mentioned temperatures. As an estimate for the effective spread in the vibrational frequencies we calculate the range $\Delta\omega_{\text{at}}$ which contains half of the atoms. We find $\Delta\omega_{\text{at}} = 2\pi \cdot (148, 37, 11)\,\text{kHz}$ for $T = (100, 50, 20)\,\mu\text{K}$.

This analysis shows that combination of the relatively large temperature of the atoms together with the spatially inhomogeneous trapping potential leads to inhomogeneous broadening of the atomic resonance. By reducing the temperature of the trapped atoms, the effect of spatial inhomogeneities can be made smaller. In the long term we want to operate the lattice in the ground-state regime, where the atoms have a spatial spread given by $\sqrt{\hbar/2m\omega_{\text{at}}}$ (Eq. 2.33). In this regime, the intensity variation of the lattice beam over the cloud of atoms is small, and the effect of $\Delta\omega_{\text{at}}$ on the dephasing of the atoms is suppressed.

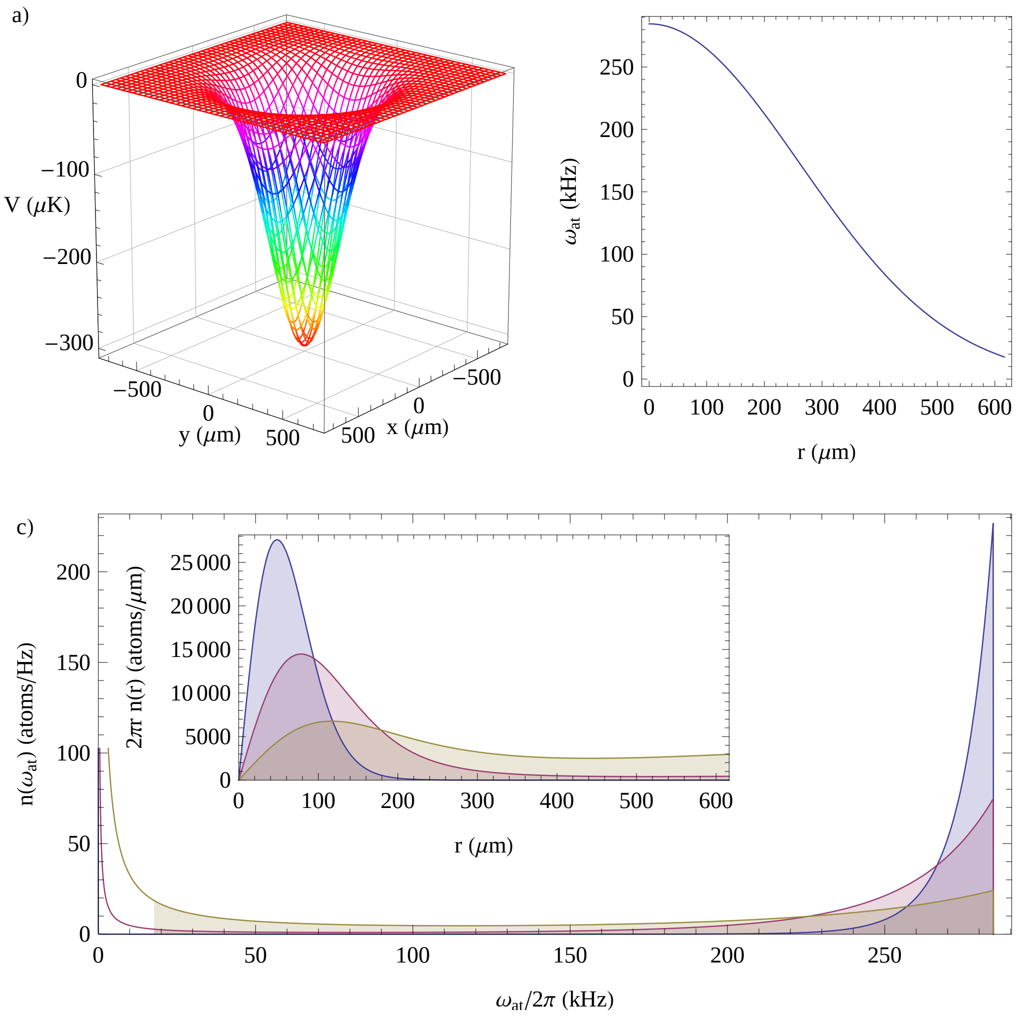

Figure 5.13: Simulation of the radial variation in the vibrational trap frequencies for a Gaussian lattice beam with $P = 76\,\mathrm{mW}$, $\Delta = -2\pi \cdot 20.8\,\mathrm{GHz}$, and $w_0 = 370\,\mu\mathrm{m}$. a) Spatial potential distribution. b) The radial distribution of trap frequencies. c) The effective density of atoms oscillating at ω_{at}, when the temperature of the atoms is $100\,\mu\mathrm{K}$ (brown), $50\,\mu\mathrm{K}$ (red), and $20\,\mu\mathrm{K}$ (blue). The distribution is normalized to $N = 2 \cdot 10^6$ within the region where $|V| > 1\,\mu\mathrm{K}$. The colored area shows the corresponding cut-off in ω_{at}. Inset: the radial distribution on atoms around the potential minimum.

5.3 Detection of the Membrane Motion and the Ringdown Technique

5.3.1 Membrane Mounting and Vacuum System

The membrane is glued on a metallic flat spacer with a UV-curable glue by applying a minimal amount of glue between one edge of the membrane frame and the spacer. This type of gluing procedure is critical in order to maintain the high Q-value of the membrane (see Sec. 4.1). The metallic spacer is further screwed onto a bigger aluminum block which is mounted with screws to a vacuum flange. The vacuum flange encloses the top part of a 6-way cross (CF40) vacuum chamber, such that the membrane plane is fixed vertically in the chamber. Figure 5.14 shows a picture of the membrane mount. The chamber has two broadband antireflection coated windows which are mounted on opposite sides of the membrane. The good optical access allows us to focus a laser beam onto both sides of the membrane and in addition image the membrane. The plane of the membrane is tilted by 10 ° with respect to the vacuum windows in order to avoid interference effects due to reflections from the windows. A vacuum of 10^{-7} mbar is achieved and sustained with a standard turbo+ion pump configuration. The membrane is at room temperature.

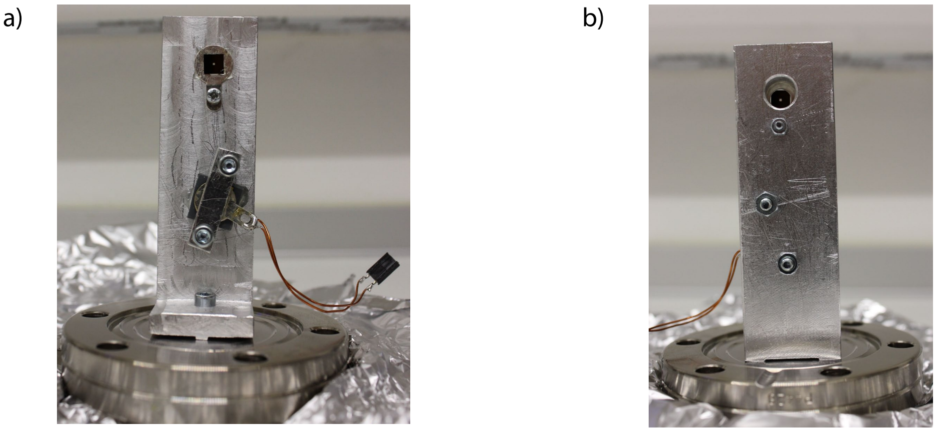

Figure 5.14: a) A SiN membrane is glued from one corner to a metallic, ring-shaped spacer. The spacer is then screwed to a bigger lever type of holder that is fixed to one of the vacuum flanges. In the picture one also sees a piezo attached to the membrane holder. b) View from the backside of the membrane holder. The SiN membrane has an areal size of $0.5 \times 0.5\,\mathrm{mm}^2$ and a thickness of 50 nm. The frame has dimensions of $5\,\mathrm{mm}^2$.

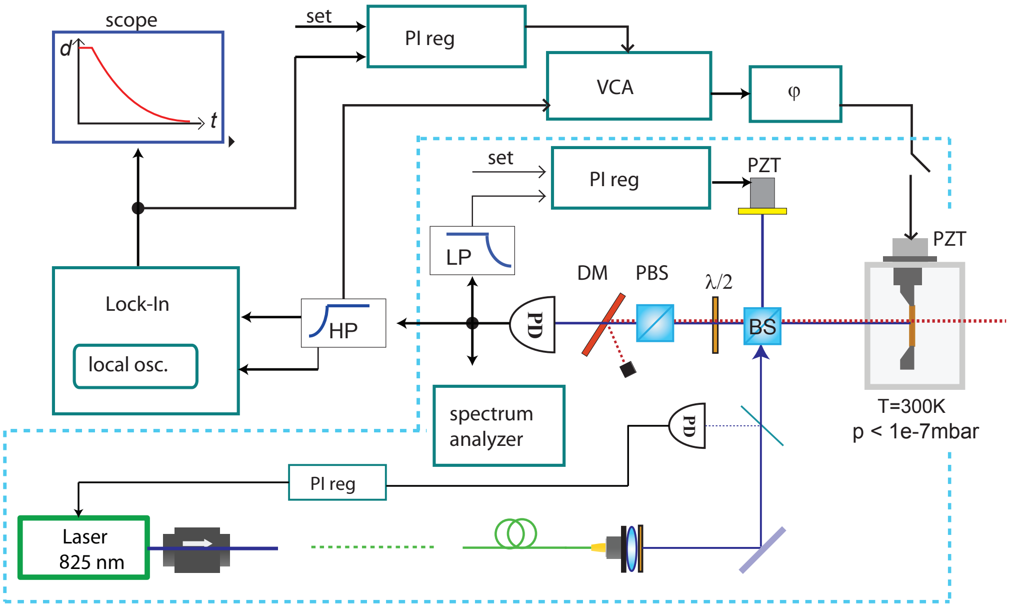

Figure 5.15: The membrane motion is read out with a Michelson interferometer which is enclosed within blue dashed line. For the read-out we use a diode laser at 825 nm (blue line), which is fiber coupled for mode-cleaning and intensity stabilized via the pick-up PD. It is separated from the lattice laser (red dashed) with a $\lambda/2$-plate (WP), a polarizing beam splitter (PBS) and a dichroic mirror (DM). The interferometer signal from the photodetector (PD) is frequency-split: the low-frequency part (LP) is used for interferometer stabilization; the high-frequency part (HP) including the membrane signal is used for readout and a piezo (PZT) feedback drive of the membrane. The membrane amplitude is measured with a lock-in amplifier and an oscilloscope. We can also measure the membrane motion in the frequency domain with a spectrum analyzer. The driven membrane amplitude is stabilized with a PI regulator and a voltage controlled amplifier (VCA) in the feedback loop.

5.3.2 Displacement Readout: Michelson Interferometer

We use a Michelson interferometer (MI) for read-out of the membrane motion, where the membrane acts as an end mirror for one arm of the interferometer. Our Michelson interferometer is illustrated in Fig. 5.15. A home-built, grating-stabilized diode laser at 825 nm is used as a coherent light source. The beam is coupled into a single-mode, polarization-maintaining fiber for mode-cleaning (Thorlabs `PM-780HP`). Both fiber end facets are angle cleaved to avoid unwanted reflections in the Michelson interferometer. A part of the fiber output is picked up by a glass plate for intensity stabilization of the laser. A PI-servo amplifier stabilizes the intensity to $2 \cdot 10^{-3}$ (r.m.s) via the current controller of the laser beam. The lattice beam enters the vacuum chamber from one side (red dashed line in Fig. 5.15). The part of the lattice beam that transmits the membrane is filtered out of the Michelson interferometer by a wave plate, polarizing beam splitter and a dichroic mirror. In this way the transmitted lattice beam does not interfere or cause a background on the detected signal at the MI-photodiode (PD). A photograph of the MI is shown in Fig. 5.16.

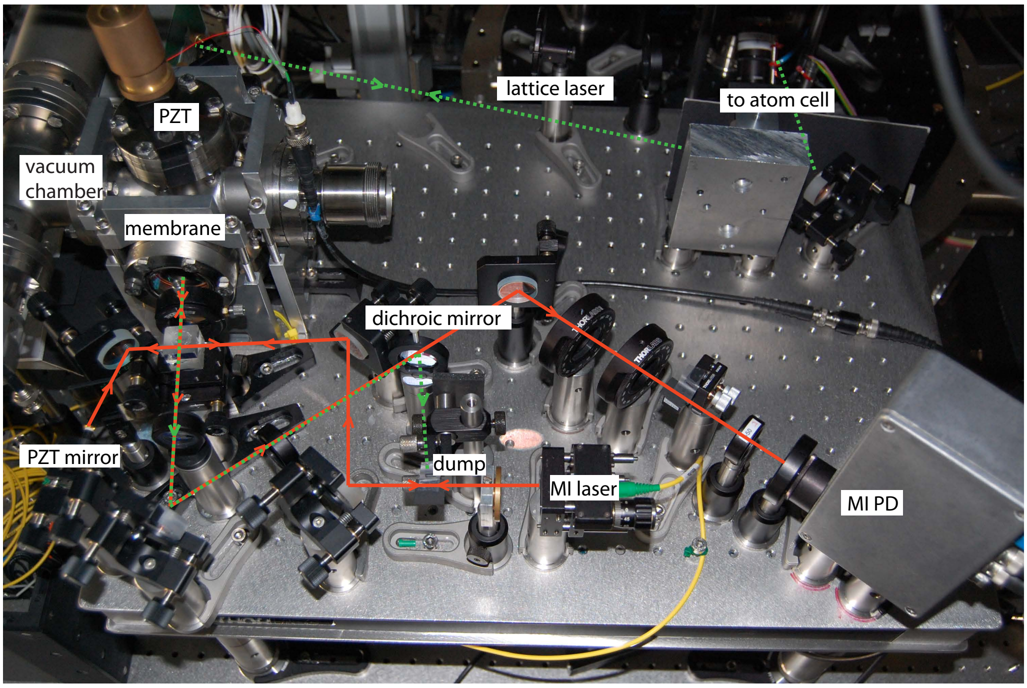

Figure 5.16: Membrane module. The Michelson Interferometer (MI) is shown in the front and the laser path of the MI is illustrated with a red line. On the left upper corner one sees the membrane vacuum chamber. The MI laser beam is reflected from one side of the membrane and the lattice laser (green dashed line) from the other. Part of the lattice light transmits the membrane, which is filtered in the MI by a dicroic mirror.

The membrane motion causes a change in the relative phase between the two arms and thus an intensity variation which is detected on the PD. The sensitivity to this variation depends on the path length difference X and the difference in the intensities in the two arms, and the overall intensity in the interferometer. The X will vary as a result of the temperature changes in the lab and acoustic perturbations. In order to resolve amplitudes equal and smaller than the thermal motion of the membrane, that is on the order of 10^{-12} m, we stabilize the path length difference X electronically. The interferometer is locked to the optimum X by a piezo (PZT) that is attached to the other end mirror of the MI (Fig. 5.15) via a PI regulator. Next we will discuss the optimal locking point for our interferometer and the sensitivity to membrane motion. The discussion here will follow that in Ref. [129].

The power at the PD depends on the phase difference ϕ between the two arms of the interferometer [130, 129]

$$P_{\mathrm{PD}} = \frac{1}{2}\alpha P_0 \left(1 + C\sin\phi\right), \tag{5.16}$$

where P_0 is the input power to the interferometer, α is an attenuation of this power due to reflections at the glass-air interfaces and due to the finite reflectivity of the membrane. C is a contrast factor accounting for the inequality of the power in the two arms. The factor $\frac{1}{2}$ takes into account the fact that half of the power is reflected back to the fiber at the beam-splitter (BS). The sinusoidal membrane motion, $x_{\mathrm{m}} = x_0 \sin\omega_{\mathrm{m}} t$, will be imprinted on the phase as

$$\phi = [2\left(X + x_{\mathrm{m}}\right)/\lambda]2\pi. \tag{5.17}$$

The current at the PD is given by $I_{\mathrm{PD}} = \frac{\eta q}{h\nu} P_{\mathrm{PD}}$, where η is the quantum efficiency of the PD, q is the electron charge, and $\nu = c/\lambda$ is the laser frequency. For small membrane amplitudes, $x_0 \ll \lambda$, the current is given by [129]

$$I_{\mathrm{PD}} = \frac{\eta q}{h\nu}\frac{1}{2}\alpha P_0 \left[1 + C\sin\left(\frac{4\pi X}{\lambda}\right) + \left(\frac{4\pi x_{\mathrm{m}}}{\lambda}\right) C\cos\left(\frac{4\pi X}{\lambda}\right)\right] = \langle I_{\mathrm{PD}}\rangle + I_{\mathrm{sig}}. \tag{5.18}$$

The third term contains the information about the membrane motion, I_{sig}, whereas the first and the second terms determine the mean current $\langle I_{\mathrm{PD}}\rangle$, from which the shot noise can be calculated [129]

$$\left\langle i^2\right\rangle = 2q\left\langle I_{\mathrm{PD}}\right\rangle \Delta f, \tag{5.19}$$

for a measurement bandwidth Δf. The signal to noise ratio can then be defined as

$$\mathfrak{S} = \left(\langle I_{\mathrm{sig}}^2\rangle/\langle i^2\rangle\right)^{1/2} = \frac{2\pi x_0}{\lambda} N_e^{1/2}\left(\frac{C^2\cos^2\left(4\pi X/\lambda\right)}{1 + C\sin\left(4\pi X/\lambda\right)}\right)^{1/2}. \tag{5.20}$$

where $N_e = \eta\alpha P_0/2h\nu\Delta f$ is the number of electrons generated in the PD within a measuring time.

First of all, by inspecting Eq. 5.20, we see that the $\mathfrak{S}$ scales as $\sqrt{P_0}$. Furthermore, the $\mathfrak{S}$ depends both on the inequality of the power between the two arms and the path length difference X. Quite interestingly, if $C < 1$, the optimal lock-point X is not necessarily at the middle of the interference fringe, i.e., at $X/\lambda = 0.25$. Fig 5.17 shows the mean PD current and $\mathfrak{S}$ as a function of the locking point X for contrast values $C = 0.99, 0.8, 0.16$. In order to optimize the $\mathfrak{S}$ in our experiment we place an optical attenuator to the reference arm of the MI to compensate for the unequal intensities in the two arms, mostly originating from the membrane transmittance. In practice it is impossible to get the contrast exactly to 1. Final optimization of the path length X can be done by monitoring the $\mathfrak{S}$ at the spectrum analyzer, while adjusting the DC-offset of the PZT mirror. Furthermore, to reduce possible frequency noise, the MI arms should ideally have equal lengths.

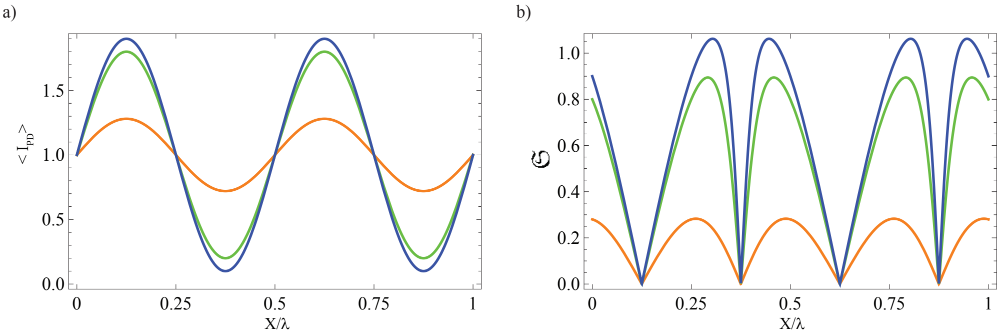

Figure 5.17: a) The mean photodiode current $\langle I_{\text{PD}} \rangle / [(\eta q/h\nu)\, \frac{1}{2}\alpha P_0]$ is a sinusoidal function of the path length difference X. b) The signal to noise ratio, $\mathfrak{S}/\left(2\pi x_0/\lambda\right) N_e^{1/2}$, depends strongly on the contrast C and the locking point X. The blue, green and orange lines are calculated assuming contrast $C = 0.99, 0.8, 0.16$.

Figure 5.18 shows the Brownian motion of a membrane measured with a spectrum analyzer. The power, P_0 into the MI was 0.4 mW. The sensitivity of our interferometer is $< 10^{-14}\,\text{m}/\sqrt{\text{Hz}}$. We can calculate the theoretical optimum for our system, assuming that photon shot-noise on the PD is the limiting factor. To compensate for the membrane reflectivity, we add an optical density to the reference arm, such that $\alpha = 0.5$ and $C = 0.9$. Using Eq. 5.20 and assuming $P_0 = 0.4\,\text{mW}$, $\lambda = 825\,\text{nm}$, $\eta = 0.65$ (BPW 34), $\Delta f = 1\,\text{Hz}$, and $C = 0.9$ we get $N_e = 3.8 \cdot 10^{14}$, $X = 0.3\lambda$ and $x_{\text{min}} = 8.5 \cdot 10^{-15}\,\text{m}$. Our detection sensitivity is consistent with shot-noise limited detection [3].

---

[3] The example shown in Fig. 5.18 was measured after rebuilding the interferometer in Basel. We measured shot-noise sensitivity with the same interferometer also in Munich [43].

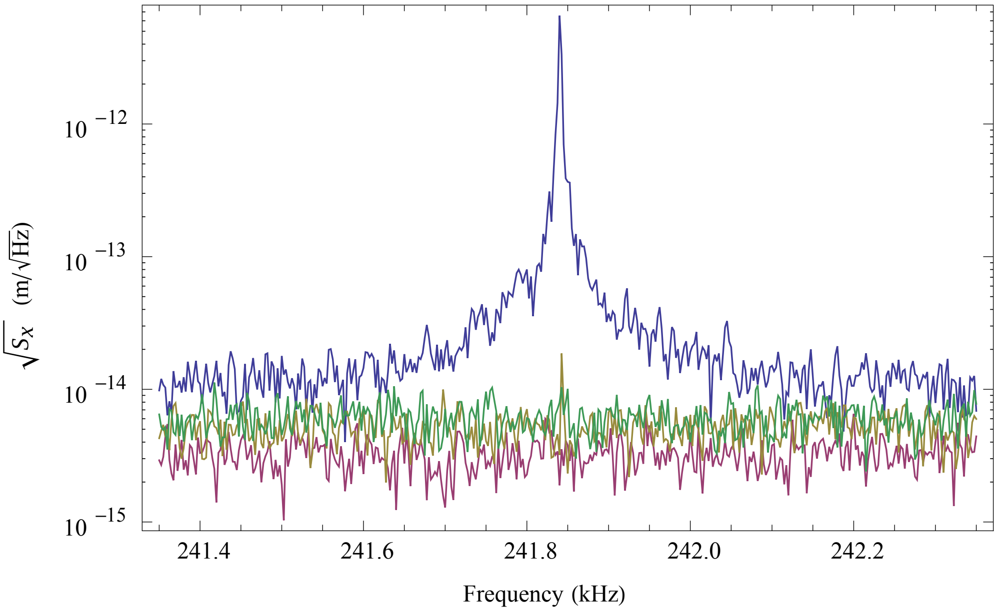

Figure 5.18: An example of the Brownian motion of a membrane (blue) on the spectrum analyzer. The input power to the MI was 0.4 mW. The red line is the photodiode signal when there is no light in the interferometer, the yellow and green lines are the signals produced by a single interferometer arm when the other arm is replaced by an absorbing and non-reflecting element.

5.3.3 Stabilized Amplitude-Drive and Ring-Down Technique

The backaction of atoms onto the membrane is measured by recording a change in the ring-down time of an initially excited membrane. We also monitor the direct action of the membrane onto the atoms by driving the membrane with a stable amplitude and measuring the resonant temperature increase of the atomic ensemble. For these measurements we actively excite the membrane motion by feeding the measured membrane oscillations back to a piezotransducer in the vicinity of the membrane.

The membrane excitation scheme is shown in Fig. 5.15. The MI signal contains information about the membrane oscillations at ω_m (Eq. 5.18). The MI-signal is high-passed filtered (HP) ($> 200\,\mathrm{kHz}$), phase shifted and sent to the piezo transducer (PZT) via a voltage controlled amplifier (VCA). Another part of the high-passed MI-signal is sent to a Lock-In amplifier, where the signal also serves as the reference oscillator. The Lock-In measures both quadratures of the membrane motion. The information of the amplitude is sent to a PI regulator, which actively stabilizes the drive amplitude via the VCA gain. Further details on the circuitry can be found in Ref. [43].

The PZT is mounted on top of the membrane vacuum chamber. We also have a piezo clamped directly to the membrane holder, as shown in Fig. 5.14, but the electrical feedthroughs got disconnected during the vacuum assembly. However, the high Q of the membrane makes excitation outside the vacuum chamber possible. The typical time scale for excitation from thermal noise, x_{th}, to $x_{\mathrm{d}} = 30 \cdot x_{\mathrm{th}}$ requires $< 2\,\mathrm{s}$. This type of self-excitation of the membrane motion is useful as it ensures that the membrane is always driven on-resonance despite possible long-term drifts or the power dependence of the eigenfrequency.

To perform a ring-down measurement, the excitation feed-back is switched off by an electrically controlled relay, and the decay of the membrane amplitude is monitored on an oscilloscope that is connected to the Lock-In. An example of a membrane ringdown is shown in Fig. 5.19a. The backaction of the atoms onto the membrane is observed as a faster ringdown as illustrated in Fig. 5.19b. In principle, one could also monitor the increased damping of the membrane in the frequency-domain on the spectrum analyzer as shown in Fig. 5.18 and described by Eq. 2.18. However, for our experimental parameters we expect the linewidth $\gamma_{\mathrm{m}} = 0.8\,\mathrm{Hz}$ to change by a few mHz. Such a small change would be lost within the minimum resolution bandwidth of 1 Hz of the spectrum analyzer. On the other hand, the high Q of the membrane makes it possible to measure such minute changes in the Q in the time domain using the ring-down technique.

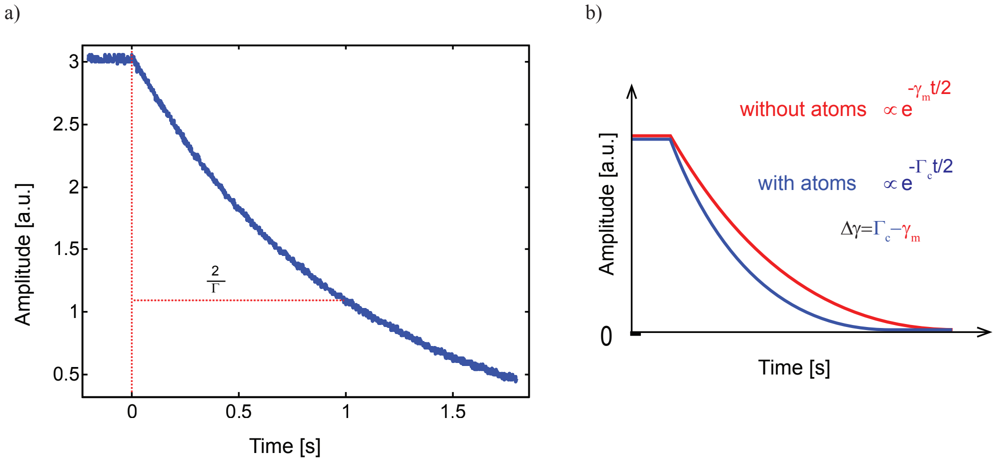

Figure 5.19: a) An example of a measured membrane ring-down on the oscilloscope. The exponential decay is described by Eq. 2.14. b) A simple and exaggerated illustration of the backaction measurement, where the optomechanical coupling is observed as a faster ring-down of the membrane amplitude (see also Eq. 3.21).

5.4 Direct Action of Membrane onto the Atoms

In the first experiment, we study the action of the membrane onto the atoms and use the atoms as a probe for the optomechanical coupling. The resonant coupling is observed by monitoring the temperature increase of the atoms in the lattice as a function of their trap frequency, ω_{at}. On resonance, when $\omega_{\mathrm{at}} \sim \omega_{\mathrm{m}}$ we observe significant heating of the atoms, which for longer interaction times leads to evaporation of the atoms out of the trap. We call this type of resonant energy transfer *the direct action of the membrane onto the atoms.* A careful analysis of the fine details of the direct action gives valuable information about the thermalization dynamics and the spread in the vibrational frequencies of the atoms in the trap. Essentially, the high-Q membrane provides a narrow, parametric drive for the atoms and can serve as a sensitive probe for the trap vibrational modes.

5.4.1 Parametrically Driven Lattice

The membrane motion modulates the spatial position of the lattice minima and parametrically couples to the motion of the atoms that oscillate at the same frequency $\omega_{\mathrm{at}} \sim \omega_{\mathrm{m}}$ in the trap. The atoms are not ground-state cooled and occupy higher laying vibrational levels in the trap as discussed in Sec. 5.2. This implies that a modulation at a single frequency will be resonant with a few trap levels only.

The membrane eigenfrequency depends on the lattice laser power P on the membrane, $\omega_{\mathrm{m}}(P)$ (see Sec. 4.2). Hence, it is useful to define the detuning of the atomic frequency from the membrane frequency as a function of P

$$\delta(P) = \omega_{\mathrm{m}}(P) - \omega_{\mathrm{at}}(P), \tag{5.21}$$

where $\omega_{\mathrm{at}}(P)$ is the nominal trap frequency in the center of the lattice, given by Eq. 2.88, and $\omega_{\mathrm{m}}(P)$ is a measured value, according to Fig. 4.5. The power dependence of ω_{at} and ω_{m} is illustrated in Fig. 5.20. The top axis in the figure denotes the detuning $\delta(P)$. For low lattice laser powers P, the membrane modulation is blue-detuned with respect to ω_{at}, whereas for high P-regime the membrane modulation becomes strongly red-detuned.

5.4.2 Experimental Sequence and Data Analysis

To study the effect of the membrane oscillation onto the atoms, the membrane is driven with a stabilized amplitude of $x_{\mathrm{d}} = 330\,\mathrm{pm}$. The lattice is loaded from a MOT for 3 s. The MOT is switched off and the lattice holds the atoms for an additional 5 ms. The temperature of the atoms both along the axial T_{ax} and radial T_{rad} directions of the lattice is determined from a fit to 4 different time-of-flight (TOF) measurements (see Sec. 5.1.3), namely to TOF values of 1, 2, 3 and 4 ms. For each TOF value the measurement is repeated 5 times. This measurement

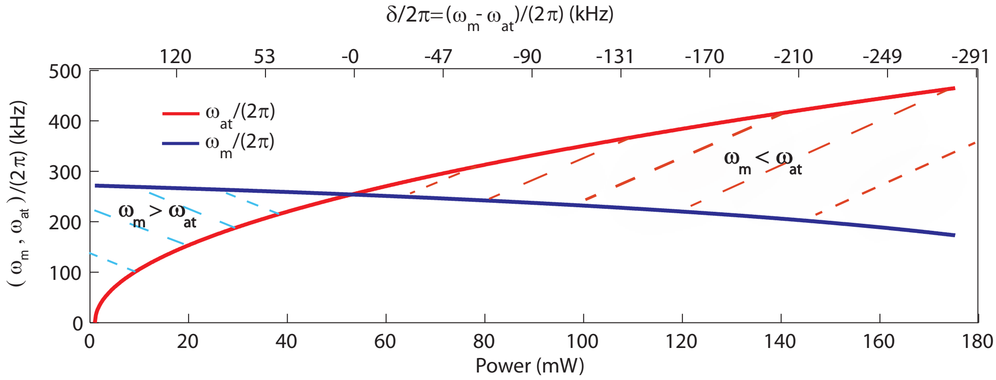

Figure 5.20: Membrane eigenfrequency ω_{m} and the calculated nominal atomic trap frequency as a function of power in the lattice beam. The assumed lattice parameters are: beam waist $w_0 = 350\mu\mathrm{m}$, detuning $\Delta_{\mathrm{L}} = -2\pi \cdot 20\,\mathrm{GHz}$. The top axis shows the detuning $\delta/2\pi = (\omega_{\mathrm{m}} - \omega_{\mathrm{at}})/2\pi$, which is nonlinear in P. The red dashed lines denote a regime where the membrane is red-detuned with respect to the atoms and blue dashed lines denote the blue-detuned regime.

series is then compared with a similar reference measurement series, where the membrane is not driven, but oscillates at its thermal amplitude of $x_{\mathrm{th}} = 12\,\mathrm{pm}$. The driven and reference measurements are done for lattice power levels between $P = 0 - 130\,\mathrm{mW}$.

Figure 5.21 shows an example of an absorption image and a corresponding 2D Gaussian fit for a power value of $P = 56\,\mathrm{mW}$ and a TOF of $3\,\mathrm{ms}$ when the membrane is driven. The 2D Gaussian fit has an offset that takes into account the background atoms from the MOT. The fitting region is fixed with respect to the TOF and is the same for the measurements where the membrane is driven and undriven, allowing quantitative comparison of the atom number and temperature of the two measurement series.

The relative uncertainties in the Gaussian widths, $\Delta\sigma_i/\sigma_i$, where $i = (\mathrm{ax}, \mathrm{rad})$ for different lattice powers are shown in Fig 5.22a and b for the reference and driven measurements. In general, the fitting is less reliable for lower than for higher lattice powers. This is because the background signal from the remaining MOT atoms in the lattice region becomes relatively large compared to the small number of atoms initially trapped in the lattice. The same reasoning holds for longer TOFs that require larger fitting region and consequently the background signal from the MOT is larger. All in all, the relative error stays less than $5 \cdot 10^{-3}$ over the whole lattice power regime allowing reliable determination of the temperature of the atoms using the Gaussian fits.

Figure 5.23 shows an example for $P = 56\,\mathrm{mW}$ of the axial and radial widths of the Gaussian (σ_{ax}, σ_{rad}) for the 4 different TOF measurements. Each black dot in the figure consists of 5 overlapping, subsequently measured data points with a relative standard deviation of less than $< 0.5\,\%$, referring to excellent short-term

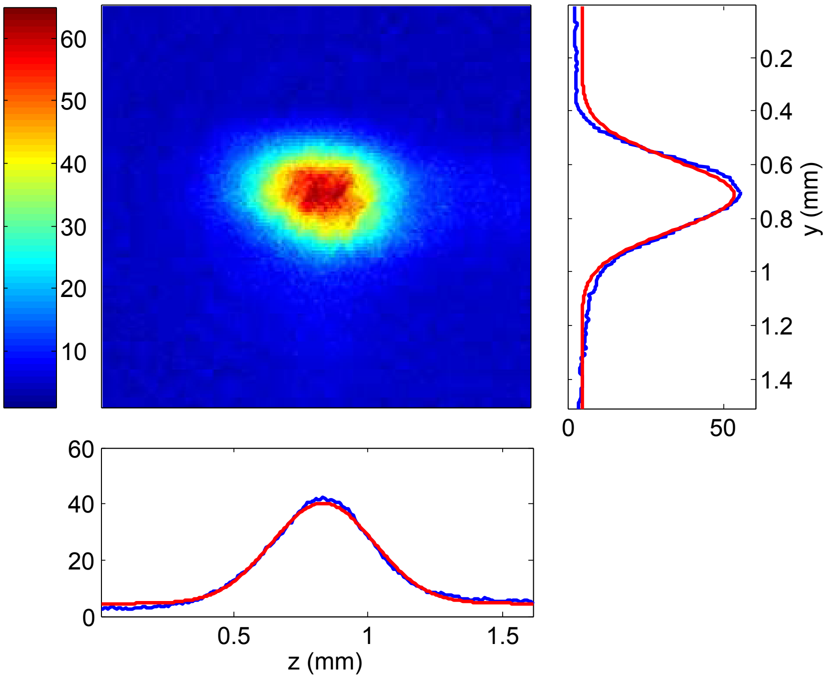

Figure 5.21: An absorption image of the initially driven lattice for $P = 56\,\mathrm{mW}$ and TOF$=3\,\mathrm{ms}$. The color bar on the left indicates the mean number of atoms per pixel. The bottom and right panels around the image show the result of a 2D Gaussian fit along the axial and radial lattice directions, respectively. The MOT drops along the y-direction due to gravity and causes a non-uniform offset along y.

stability of the atom preparation. For the short TOF of 1 ms the distribution of atoms closely reflects the in-trap density distribution σ_0, while for larger TOFs the atomic distribution mimics the momentum distribution. A fit of the measured σ values to Eq. 5.10 gives the temperature along the axial and radial directions. For this power level we measure $T_{\text{ax}} = 142 \pm 0.2\,\mu\text{K}$ and $T_{\text{rad}} = 88 \pm 0.1\,\mu\text{K}$.

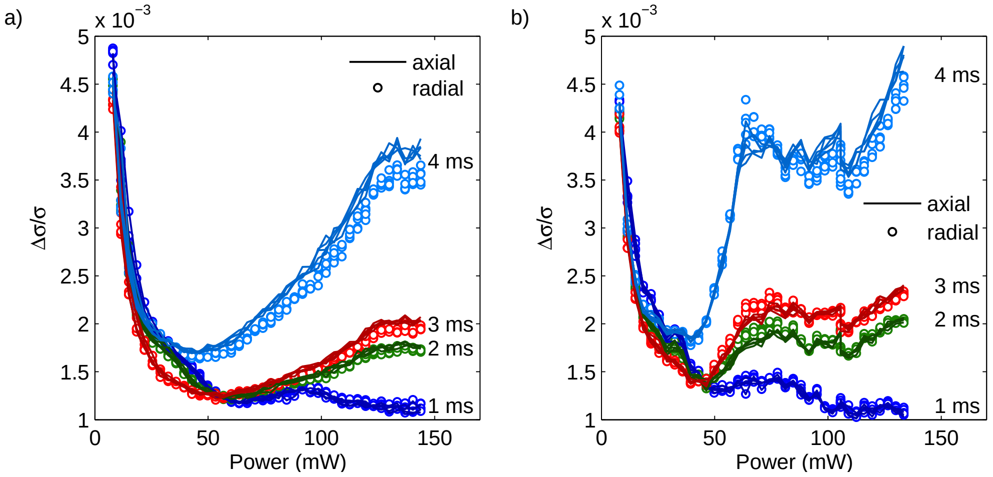

Figure 5.22: The relative error in the Gaussian fit for different TOFs as a function of the lattice laser power. The lines and the dots correspond to axial and radial errors. a) Relative uncertainty of the fit when the membrane is oscillating at its thermal amplitude. b) Relative uncertainty of the fit when the membrane is driven with a constant amplitude of 330 pm.

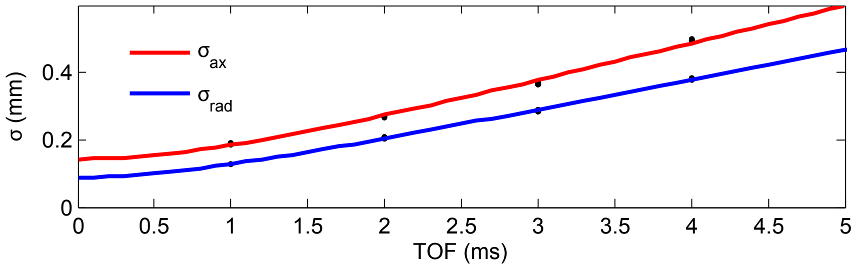

Figure 5.23: An example of the temperature determination of the atoms. 4 different TOF measurements are used to determine the temperature of the atoms along the axial and radial lattice directions. For each TOF value the experiment is repeated 5 times. The red and blue lines are fits according to Eq. (5.10), and the black dots are the data points. In this measurement the lattice power was 56 mW and the membrane was driven at an amplitude of 330 pm.

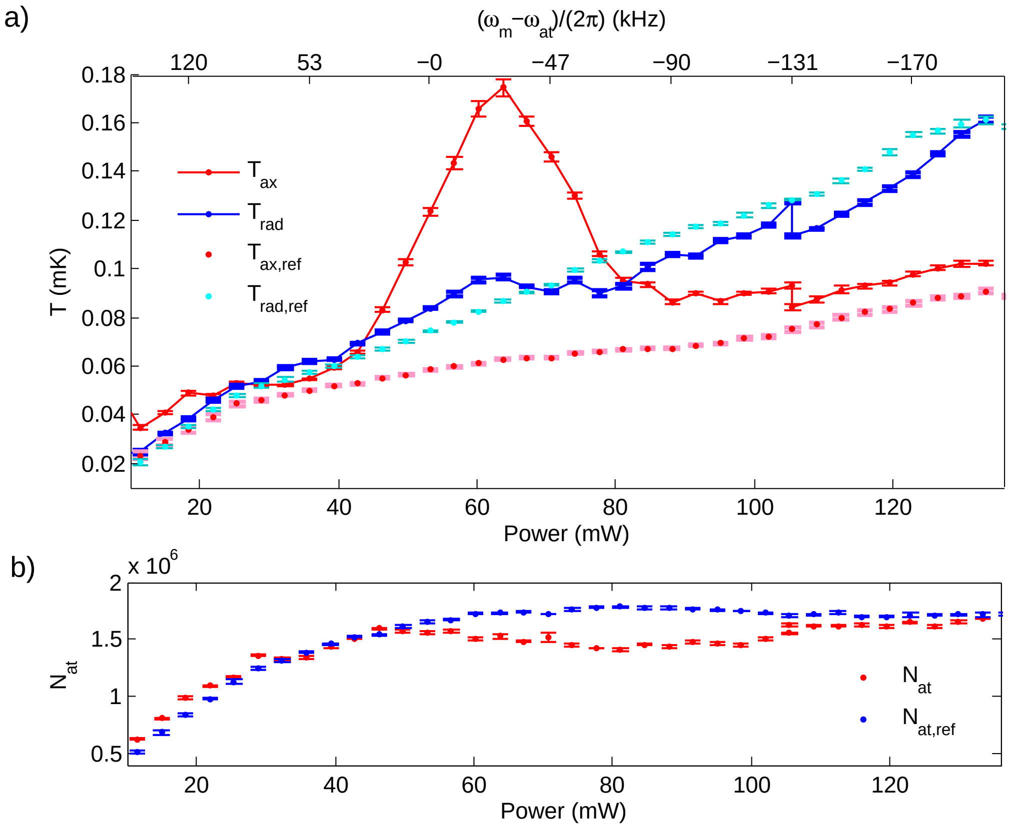

Figure 5.24: Direct action measurement. a) Temperature of the atoms in the lattice along the axial T_{ax} (red dots connected with a line) and radial T_{rad} (blue dots connected with a line) lattice directions when the membrane is driven. The axial and radial temperatures without the membrane drive, $T_{\mathrm{ax,ref}}$ and $T_{\mathrm{rad,ref}}$, are shown by the red and light blue dots without a connecting line, respectively. b) Dependence of lattice atom number N_{at} on the lattice power P, for driven and undriven membrane. The lattice hold-time in these measurements is 5 ms.

5.4.3 Result: Direct Action

The absolute temperature of the atoms for various lattice power levels in the trap is shown in Fig. 5.24a. The detuning of the membrane eigenfrequency from the harmonic trapping frequency of the atoms is shown on the top axis of the figure. The membrane amplitude for the data points with drive is $x_{\mathrm{d}} = 330\,\mathrm{pm}$ and the lattice-hold time is 5 ms. When the membrane is driven, we observe a clear resonant increase in the axial temperature T_{ax} of the atom cloud for lattice power levels around $40 \sim 80\,\mathrm{mW}$. The increased T_{ax} is accompanied by a resonant loss in the atom number as shown in Fig. 5.24b. The radial temperature, T_{rad}, is less affected by the membrane, but follows the same trend as T_{ax}; a relative temperature increase is also visible in T_{rad} around $40 \sim 70\,\mathrm{mW}$ in comparison to the radial reference measurement. It is worth noting that the data for $P \geq 106\,\text{mW}$ for the driven membrane was measured on a different day. This explains the small drop in the temperature profiles at $P = 106\,\text{mW}$.

In conclusion, we observe resonant energy transfer from the membrane to the atoms when the two systems are tuned on-resonance. As the atoms are not continuously cooled in this measurement, the direct action of the membrane is strong enough to heat and eventually evaporate some of the atoms out of the trap.

Evaporation and Parametric Heating

The observed shape of the resonance reflects the distribution of the vibrational frequencies in the trap as discussed in Section 5.2. The most energetic atoms have a much lower frequency than the ones oscillating at the bottom of the trap because of the decreased curvature of the potential. When the membrane is red-detuned with respect to the atoms, that is, for $\delta < 0$, the most energetic atoms are parametrically excited and ejected from the trap, and we observe atom number loss due to forced evaporation. These observations match theoretical predictions that anticipate the peak in the resonance of atomic losses to occur at lower excitation frequency than the actual harmonic, nominal frequencies [131]. This type of parametric selective excitation of the atoms has been previously exploited for evaporative cooling of atoms in an optical lattice [132]. In contrast, we observe that modulation frequencies resonant with the nominal harmonic trap frequencies, i.e. $\delta \sim 0$, excite primarily atoms at the bottom of the trap (which have the lowest energy), resulting in parametric heating of the ensemble, but reduced atom number loss.

Temperature Profiles

A generic temperature increase with increasing power of the lattice beam is visible in all the temperature profiles in Fig. 5.24a. The larger temperature for deeper traps can be explained by the gain in the potential energy of the atoms during loading of the optical trap [133]. Other effects affecting the temperature of the atoms in the lattice are increased heating due to photon scattering at higher lattice beam powers and possibly light-assisted collisions.

Furthermore, in Fig. 5.24a we observe that the radial and axial reference temperatures are not equilibrated after a lattice hold time of 5 ms. The $T_{\text{rad,ref}}$ is consistently larger than the $T_{\text{ax,ref}}$. The temperature difference, $T_{\text{rad,ref}} - T_{\text{ax,ref}}$, seems to scale with power. During longer hold-time of the atoms in the lattice, collisions between the atoms thermalize the sample. This is observed in another reference measurement where the membrane motion is thermally driven and the lattice hold time is 18 ms. The measurement result is shown in Fig. 5.25. In this measurement the TOF was 3 ms which is long enough for the cloud expansion to be independent of its initial size as shown in Fig. 5.23. The σ_{ax} and σ_{rad}

are approaching each other outside the resonance regime. The thermalization of the atoms for longer hold-times in the lattice suggests that the temperature difference observed in Fig. 5.24a is due to initial imbalance between the axial and radial temperatures in the lattice. This may originate from an imbalance in the radiation pressure force of the MOT along the axial and radial directions. For example, as the MOT is operated in the presence of the lattice, spontaneous photon scattering leading to a change in the motional state is suppressed in the axial direction due to the tight lattice confinement. This could lead to lower axial MOT temperatures.

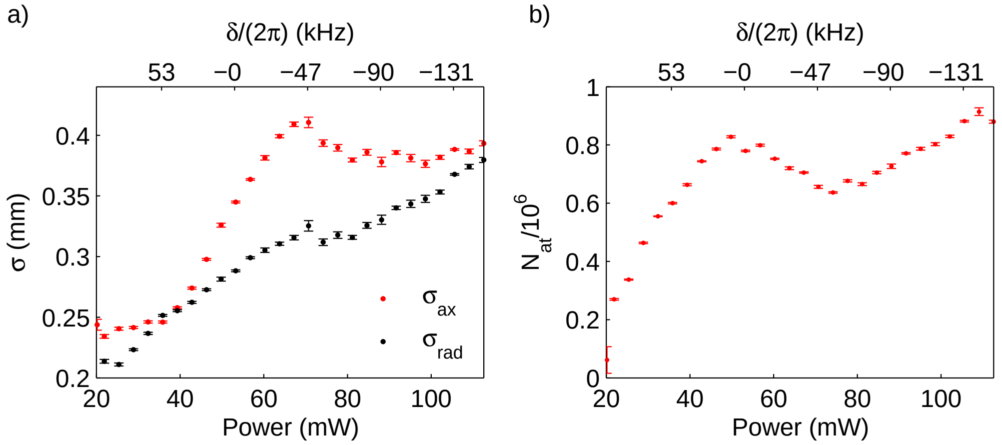

Figure 5.25: a) Axial and radial width of the cloud after an interaction time of 18 ms with a thermally driven membrane. b) The remaining number of atoms in the lattice after 18 ms.

Brownian Motion of the Membrane

Interestingly, the resonant coupling between the atoms and the membrane is also visible in Fig. 5.25, where the membrane is thermally driven, but the lattice hold-time is long, 18 ms. We observe similar features than in the measurement shown in Fig. 5.24. A clear resonant increase in the axial width of the cloud is visible in Fig. 5.25a. The resonance is also accompanied by forced evaporation of atoms from the trap, as is visible in Fig. 5.25b. The maximum in the axial temperature is shifted to $\delta < 0$, and the peak in the resonance of atom loss occurs at even larger red-detuning of the membrane drive.

Figure 5.26 shows a direct comparison of the behavior of σ_{ax} and σ_{rad} for both 5 ms and 18 ms lattice hold time for the thermally driven membrane, and a TOF of 3 ms[4]. The influence of the longer hold time on the resonant axial heating is

---

[4] We made this measurement only with TOF = 3 ms, as this measurement was intended for other purpose. At that point we did not expect to see any effect of the Brownian motion onto the atoms.

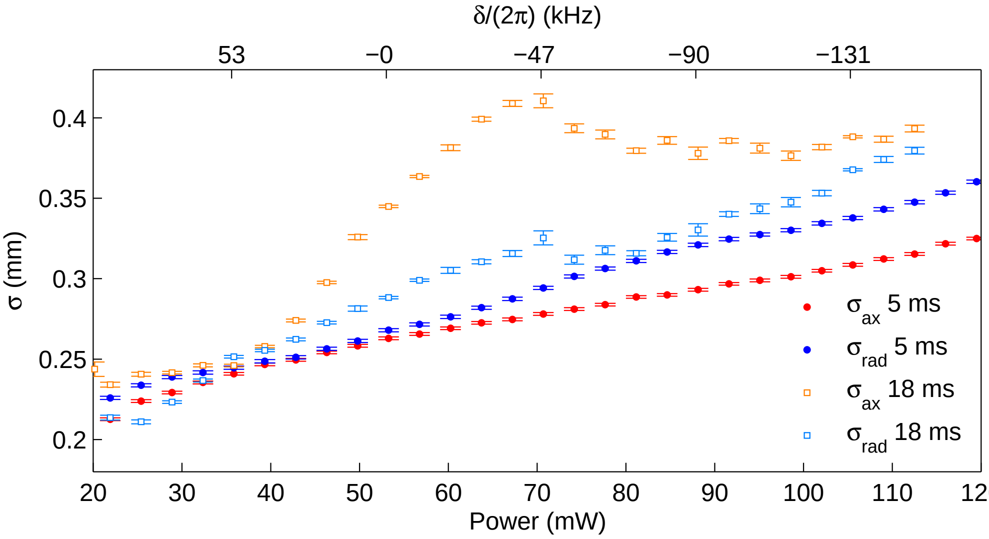

Figure 5.26: Axial and radial widths of the atom cloud in the reference TOF measurement of 3 ms for lattice hold times of 5 ms and 15 ms.

evident, as well as the thermalization of the axial and radial directions outside the resonance.

Atomic Dephasing

Quantitative modeling of the data in Fig. 5.24 would have to account for trap anharmonicity, atomic collisions, and evaporation. An estimate for the atomic dephasing γ_ϕ can be obtained from a Lorentzian fit to the relative axial temperature increase of the atoms due to membrane drive. Figure 5.27 shows the relative temperature increase along the axial direction for both the 5 ms driven and 18 ms thermal measurements. We calculate the relative temperature increase along the axial direction as $T_{\mathrm{rel,5ms}} = T_{\mathrm{ax}}/T_{\mathrm{ax,ref}}$ (red datapoints). For the longer hold-time measurement we assume the axial and radial directions to be in thermal equilibrium outside the resonance and define $T_{\mathrm{rel,18ms}} = \sigma^2_{\mathrm{ax,18ms}}/\sigma^2_{\mathrm{rad,18ms}}$ (blue data points). We fit a Lorentzian to the data

$$T_{\mathrm{rel}} \propto \frac{w_0}{\frac{1}{4\pi^2}\left(\delta-\delta_0\right)^2+\left(\frac{w_0}{2}\right)^2}, \tag{5.22}$$

where w_0 is the width and δ_0 is the peak position. The fits result in widths of $w_{0,\mathrm{5ms}} = 57 \pm 3\,\mathrm{kHz}$ and $w_{0,\mathrm{18ms}} = 93 \pm 18\,\mathrm{kHz}$ for the two measurements. The latter value is a better estimate for γ_ϕ, as the effect of evaporation in this measurement is smaller. The evaporation of the hottest atoms out of the trap results most likely in a relative temperature decrease of the ensemble and effectively

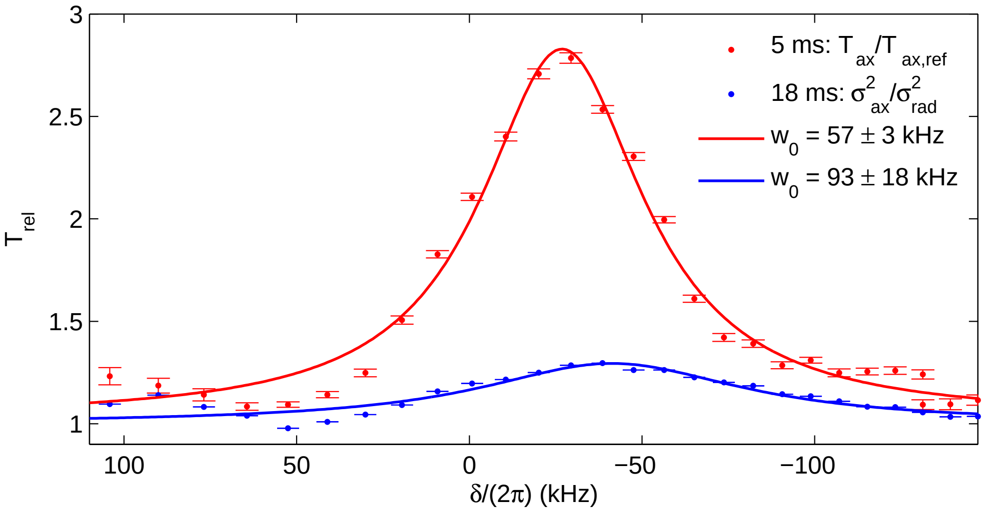

Figure 5.27: Red data points: relative temperature along the axial direction when the membrane is driven at 330 pm. The lattice-hold time is 5 ms. Blue data points: relative temperature when the membrane oscillates at its thermal amplitude of 12 pm. The lattice hold time is 18 ms. The lines are the corresponding Lorentzian fits to the resonance profiles.

narrower resonance profile. In this case, $\gamma_\phi \geq 2\pi \cdot (93 \pm 18)\,\text{kHz}$, can be taken as the lower bound estimate.

Population in F=1 and F=2 states

The last remark will be on the occupation of the states $F = 2$ and $F = 1$ in the lattice. During the lattice hold time, the repumper beam is off and part of the atoms are pumped into the state $F = 1$ by the lattice (see p. 77). These atoms see a shallower trap than the atoms at $F = 2$, by a factor of Δ_2/Δ_1 and the resulting trap frequencies are also lower by a factor of $\sqrt{\Delta_2/\Delta_1} = 0.88$. The large spread in the vibrational frequencies of the atoms and the evaporation washes out these features from our measurement signal. For a colder atomic sample, we would expect to see a separate resonant feature originating from the atoms at $F = 1$.

5.5 Backaction of Atoms onto the Membrane

In the second experiment, we study the effect of the atoms onto the membrane and use the membrane as a probe for the optomechanical coupling. On resonance, when $\omega_{\mathrm{at}} \sim \omega_{\mathrm{m}}$, we observe enhanced damping of the membrane, which scales linearly with the number of atoms in the lattice. We call this type of resonantly enhanced damping *the backaction of the atoms onto the membrane.* To interpret the measurements, we develop a numerical model which can accurately predict the broad shape of the measured resonance. The model takes into account finite temperature effects of the atoms, and imperfections of the lattice potential due to non-Gaussian beam profile of the lattice beam.

5.5.1 Experimental Sequence and Data-Analysis

The backaction of the laser-cooled atomic ensemble onto the membrane vibrations is observed in membrane ringdown measurements. The lattice is continuously loaded from the MOT (Sec. 5.1.5) while the membrane is resonantly excited to an amplitude of $x_{\mathrm{d}} = 540\,\mathrm{pm}$ (see Sec. 5.3). After 3 s of MOT loading, the membrane excitation is switched off and the decay of the membrane amplitude is recorded. During the ringdown of the membrane, the MOT is kept on and the atoms are continuously loaded into the lattice. We perform alternating experiments with and without atoms in the lattice, where the presence of atoms is controlled by detuning the MOT laser frequency, while the lattice laser power on the membrane is kept fixed. This reference measurement allows straightforward determination of the change in the decay rate $\Delta\gamma = \Gamma_{\mathrm{c}} - \gamma_{\mathrm{m}}$ as predicted by Eq. (3.18), without being perturbed by the change in the Q-factor of the membrane with laser power (see Sec. 4.2). The membrane used in the experiment has $Q = 8.5 \times 10^5$ ($Q = 1.5 \times 10^6$) for $P = 0$ ($P = 76\,\mathrm{mW}$). Furthermore, as the Q has abrupt drops at certain P-levels due to coupling to its frame modes (see Fig. 4.7 and discussion therein), we choose to measure at values of P, where the coupling to frame-modes is absent.

For each lattice power we measure 2×550 ringdowns subsequently alternating the presence of the atoms in the lattice. In this way we can average out any experimental drifts that occur over the course of the measurement run. One dominant reason for the drifts in the decay constant γ_{m} and in the atom preparation during this particular measurement was a drift in the room temperature of the laboratory. During the humid and hot summer season of the measurements, the temperature stabilization feedback gave up, and the lab temperature was drifting by several degrees within a day. Figure 5.28a shows an example of the statistics of one such measurement series recorded at a near-resonant power level of 82 mW. Despite the experimental drifts visible in the data, the subsequent ringdowns measured with atoms are consistently faster than without atoms. Also, the histograms of these ringdown-sets are clearly separated with respect to their decay rates and follow a Gaussian distribution as shown in Fig. 5.28b.

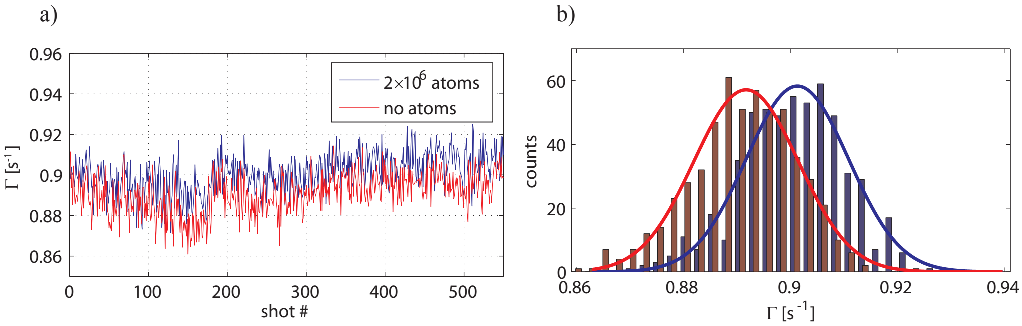

Figure 5.28: a) The decay rate Γ extracted from exponential fits to individual ringdown measurements with (blue) and without (red) atoms in the lattice. The uncertainty of fits is on average ±0.7 mHz. b) Histogram of the decay rates with and without atoms. The standard deviation of the distributions is 9.6 mHz (with atoms) and 9.9 mHz (without atoms). The uncertainty of the center of the fitted Gaussian is 0.90 mHz (with atoms) and 0.58 mHz (without atoms), and the difference in energy decay rate is $\Delta\gamma = 19.2 \pm 2.1$ mHz. This data is measured for lattice power level of $P = 82$ mW.

5.5.2 Result: Backaction

Figure 5.29 shows the change in the membrane dissipation rate due to the atoms in the lattice as a function of lattice power P and the detuning δ (Eq. 5.21). The plotted value $\Delta\gamma = \langle \Gamma_c - \gamma_m \rangle_{550}$ is the mean taken over 550 measurement runs and the errorbar is the standard error. When the atoms are close to resonance with the membrane, we observe an enhanced damping of the membrane motion. The resonance in $\Delta\gamma$ is broad and peaked around $P \approx 76$ mW. The full-width at half maximum (FWHM) of the resonance is $\gamma_{at} = 2\pi \cdot 130 \pm 26$ kHz. This is in reasonable agreement with the observed direct action resonance in Sec. 5.4. The lower panel in Fig. 5.29 shows the number of atoms in the lattice, which does not change significantly around the resonance.

We observe that the resonance peak is shifted to $\delta < 0$. The shape, magnitude, and the position of the resonance can be explained accurately with a more elaborate theory that includes the finite temperature of the atoms and the spatial dependence of the trap frequency on the lattice laser intensity profile (Sec. 5.2). The theory results in the solid curve shown in red in Fig. 5.29. The details of the theory curve are discussed below.

In a second experiment, we measure the scaling of $\Delta\gamma$ with atom number N. The system is prepared on resonance ($P = 76$ mW) and the number of atoms that are loaded into the lattice is varied by changing the power of the MOT repump laser. We observe a linear dependence of $\Delta\gamma$ on N as shown in Fig. 5.30. This is in agreement with the theory (Eq. 3.18) that predicts linear scaling with N.

In order to compare quantitatively our measurements with theory, we calculate $\Delta\gamma$ from Eq. (3.18). The overall atomic damping rate γ_{at} is taken as the FWHM of the resonance and the atom number is measured to be $N =$

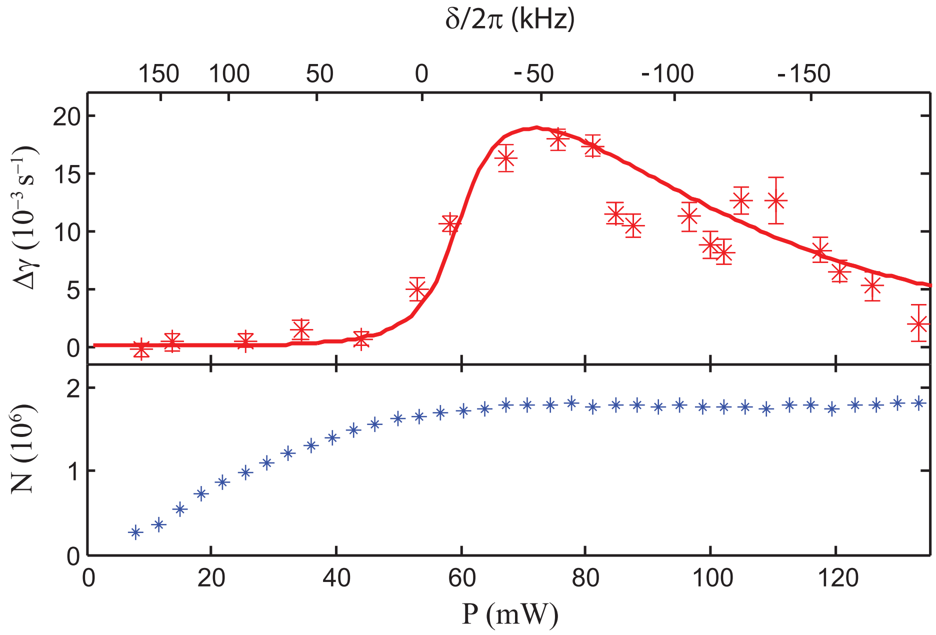

Figure 5.29: Backaction of laser-cooled atoms onto the membrane. Top: measured additional membrane dissipation rate $\Delta\gamma = \Gamma_{\mathrm{c}} - \gamma_{\mathrm{m}}$ due to coupling to atoms as a function of P. The rates Γ_{c} and γ_m are extracted from exponential fits to averaged decay curves (2×550 experimental runs per datapoint). The solid line results from a theory for a thermal ensemble in the lattice. Bottom: atom number N in the lattice measured.

$10^6 \cdot (2.3 \pm 0.5)$. For these values, the theory predicts enhanced damping by $\Delta\gamma = 0.023 \pm 0.005\,\mathrm{s}^{-1}$ for $\delta = 0$, whereas the measured maximum value is $\Delta\gamma = 0.018 \pm 0.001\,\mathrm{s}^{-1}$. The quantitative agreement of measurement and theory is rather remarkable, as this theoretical estimate does not explicitly account for the finite temperature of the atoms, lattice trap anharmonicity, and the spatial variation of the lattice laser intensity giving rise to a spread in ω_{at}. These effects are only implicitly included in the measured γ_{at}.

5.5.3 Shape of the Backaction Resonance

The observed resonance is broad, shifted to $\delta < 0$, and asymmetric. It is peaked around $P \approx 76\,\mathrm{mW}$ and has another less pronounced peak at $P \approx 110\,\mathrm{mW}$. In general, the resonance shape may be affected by several factors: the lattice beam profile and lattice alignment, laser cooling rate of the atoms, the temperature of the atoms in the trap, and the number of trapped atoms as a function of lattice power. We include these factors in a more elaborate theoretical model to analyze their influence on the signal. In particular, we consider the finite temperature of the atoms and the transverse spread in the trap frequencies originating from the

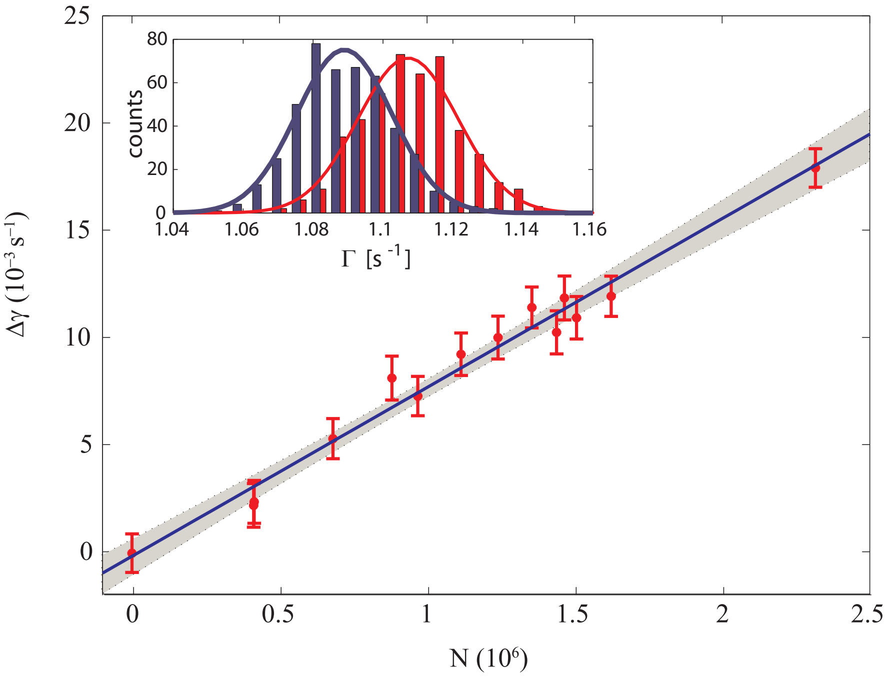

Figure 5.30: Measured additional membrane dissipation $\Delta\gamma$ as a function of atom number N for resonant coupling ($P = 76\,\mathrm{mW}$). The blue line is a linear fit. The observed dependence agrees well with theory. Inset: histogram of measurements of Γ for $N = 2.3 \cdot 10^6$ (red) and $N = 0$ (blue).

intensity profile of the lattice laser beam.

The atoms are described by a thermal density distribution $n\,(r, P)$ (Eq. 5.14) with a temperature $T\,(P)$ in the trap. For each atom in the distribution, we calculate $\omega_{\mathrm{at}}(r)$ from $V_{\mathrm{m}}\,(r)$ and determine the corresponding membrane damping rate within the RWA approximation as in Eq. (3.17). We set $\gamma_{\mathrm{at}} = \gamma_{\mathrm{c}}$, as the effects contributing to γ_ϕ are now explicitly modeled. We then sum the damping rates of all the atoms in the ensemble, and finally do this for all the lattice powers in the experiment.

For the red theory curve in Fig. 5.29, we assume the temperature of the atoms to be $T(P) = 100\,\mu\mathrm{K}$ in the lattice potential. For simplicity, N is assumed to be constant for all power levels of the lattice laser beam across the resonance. The laser cooling rate is assumed to be $\gamma_{\mathrm{c}} = 2\pi \cdot 30\,\mathrm{kHz}$. This is motivated by an estimate of the sub-Doppler laser cooling rate $\gamma_{\mathrm{c}} \simeq \omega_{\mathrm{rec}}(2|\Delta'_{\mathrm{MOT}}|/\gamma_{\mathrm{se}})$, where $\gamma_{\mathrm{se}} = 2\pi \cdot 6.1\,\mathrm{MHz}$ is the natural linewidth and $\omega_{\mathrm{rec}} = 2\pi \cdot 3.8\,\mathrm{kHz}$ the recoil frequency of the ^{87}Rb cooling transition [78]. The MOT detuning, $\Delta'_{\mathrm{MOT}} = -2\pi \cdot 28\,\mathrm{MHz}$, includes the light shift of the cooling transition due to the lattice laser as discussed in Sec. 5.1.5. Notably, a change of $\pm 2\pi \cdot 10\,\mathrm{kHz}$ in γ_{c} does not significantly change the shape or magnitude of the theory curve. Consequently, within our parameter regime we may neglect the power dependence of γ_c.

The resulting line in Fig. 5.29 shows good agreement with the data for $w_0 = 370\,\mu\mathrm{m}$ and $N = 2.0 \cdot 10^6$, within the uncertainty of these parameters. By taking the experimentally measured $N(P)$ and $T(P)$ profiles into account results only in minute change of the simulation result. In conclusion, this analysis shows that dephasing due to the spread in ω_{at} dominates the atomic damping γ_{at} in the experimental realization.

Note: Validity of the RWA Approximation

The red curve in Fig. 5.29 is calculated within the rotating wave approximation of Eq. 3.17. A simulation using the exact solution of Eqs. 3.12 that takes into account the rotating terms is presented in Fig. 5.31 for comparison. The green dashed line is the exact solution, where $\gamma_c = 8\,\omega_{\mathrm{rec}}$, and the black dots are result of the exact solution taking into account the power dependence of $\gamma_c(P)$. The RWA approximation describes accurately the resonance over the whole lattice power regime.

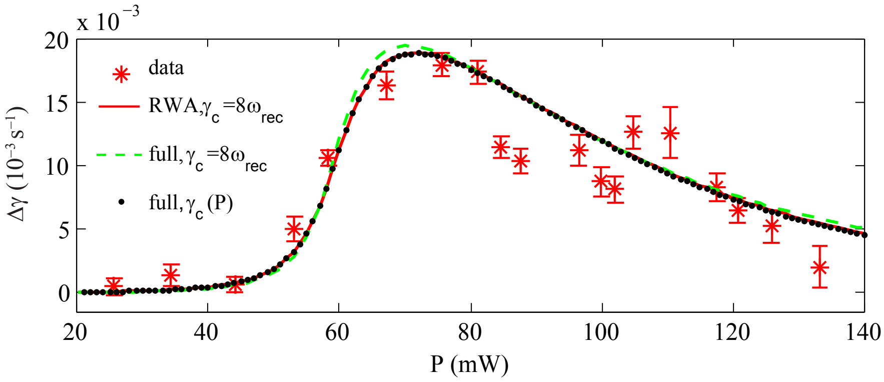

Figure 5.31: Comparison of the RWA approximation to the full calculation. Experimental data (red stars) and simulation. Lattice parameters: $w_0 = 370\,\mu\mathrm{m}$, $N = 2 \cdot 10^6$, $T = 100\,\mu\mathrm{K}$. Red curve: RWA, assuming $\gamma_c = 8\,\omega_{\mathrm{rec}}$. Green curve: full calculation assuming $\gamma_c = 8\,\omega_{\mathrm{rec}}$. Black curve: full calculation taking into account $\gamma_c(P)$.

Beam Profile of the Reflected Beam

In the experimental realization the beam profile of the back-reflected laser beam deviated considerably from a Gaussian at the position of the atoms. This was noticed during the disassembly of the experimental setup, when the setup was prepared for the move from Munich to Basel. In the following, we investigate, whether the feature at $P \approx 110\,\mathrm{mW}$ could originate from the non-Gaussian beam profile of the lattice beam.

The back-reflected beam profile was measured between the lens f_4 and the atom cell (f_4 is shown in Fig. 5.6) by picking it up with a thin glass plate and directing it to a beam profiler. The measured beam profile is shown in Fig. 5.32. We observed that the exact profile of the backreflection depends strongly on the fine-alignment of the lattice. Consequently, there is a large uncertainty on how strong the beam distortion has been during the backaction measurement. Fig. 5.32 shows the most Gaussian-like alignment.

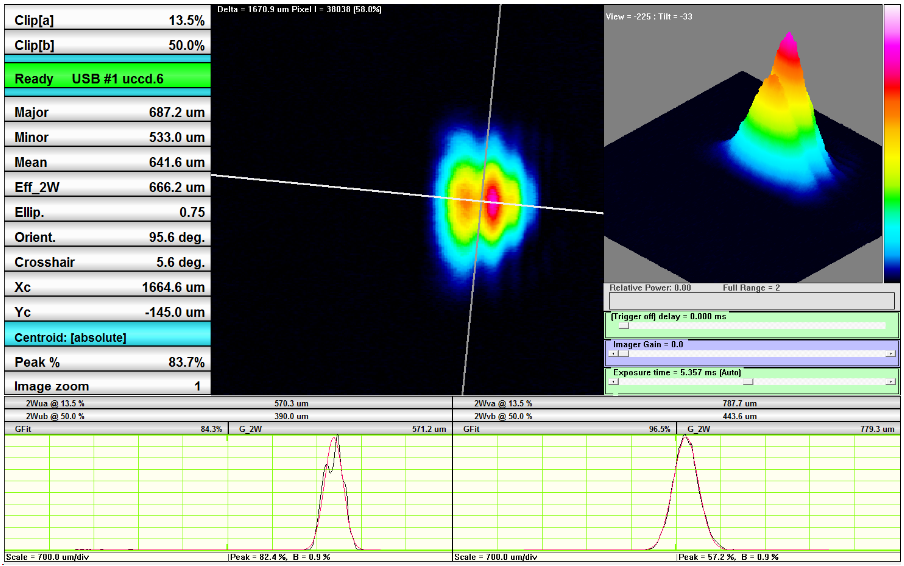
Clip[a] 13.5%
Clip[b] 50.0%
Ready USB #1 uccd.6
Major 687.2 um
Minor 533.0 um
Mean 641.6 um
Eff_2W 666.2 um
Ellip. 0.75
Orient. 95.6 deg.
Crosshair 5.6 deg.
Xc 1664.6 um
Yc -145.0 um
Centroid: [absolute]
Peak % 83.7%
Image zoom 1
Delta = 1670.9 um Pixel I = 38038 (58.0%)
View = -225 : Tilt = -33
Relative Power: 0.00 Full Range = 2
(Trigger off) delay = 0.000 ms
Imager Gain = 0.0
Exposure time = 5.357 ms (Auto)
2Wua @ 13.5 % 570.3 um
2Wub @ 50.0 % 390.0 um
GFit 84.3% G_2W 571.2 um
Scale = 700.0 um/div Peak = 82.4 %, B = 0.9 %
2Wva @ 13.5 % 787.7 um
2Wvb @ 50.0 % 443.6 um
GFit 96.5% G_2W 779.3 um
Scale = 700.0 um/div Peak = 57.2 %, B = 0.9 %

Figure 5.32: Backreflected beam profile at the position of the atoms.

A Gaussian fit along the two main axes (denoted by the cross-hairs in Fig. 5.32) gives respective diameters of $2w_{\mathrm{y}}$ =780 µm and $2w_{\mathrm{x}} = 570$ µm. Along the horizontal cross-hair, which we denote as x-direction, the intensity profile consist of two spatially separated intensity maxima. The two local intensity maxima in the back-reflected beam will result in a lattice with two localized potential minima and give rise to a complex profile of the vibrational frequencies $\omega_{\mathrm{at}}(x, y)$ in the trap.

To estimate the effect of the beam distortion on the backaction resonance, we calculate the $\omega_{\mathrm{at}}(x, y)$ for a non-Gaussian backreflection, and determine the corresponding membrane damping rate as described in Sec. 5.5.3. As an example, the reflected beam is chosen to be formed by two Gaussians. These are displaced laterally with respect to the incoming Gaussian beam by x_i, their beam waist is w_i, and each of them carries a power of p_i, where the sub-indices denote the beam 1 or 2, respectively. The intensity of the reflected beam is (Eq. 2.82)

$$I_{\mathrm{refl}} \equiv |A_{\mathrm{refl}}\,(x, y, z)\,|^2 = \mathfrak{r}\mathfrak{t}^2 \sum_{i=1,2} |A_i\,(x, y, z, x_i, w_i, p_i)\,|^2. \tag{5.23}$$

The parameters are constrained by the total power in the reflected beam, which is normalized to $\mathfrak{r}\mathfrak{t}^2 P$ at the position of the atoms.

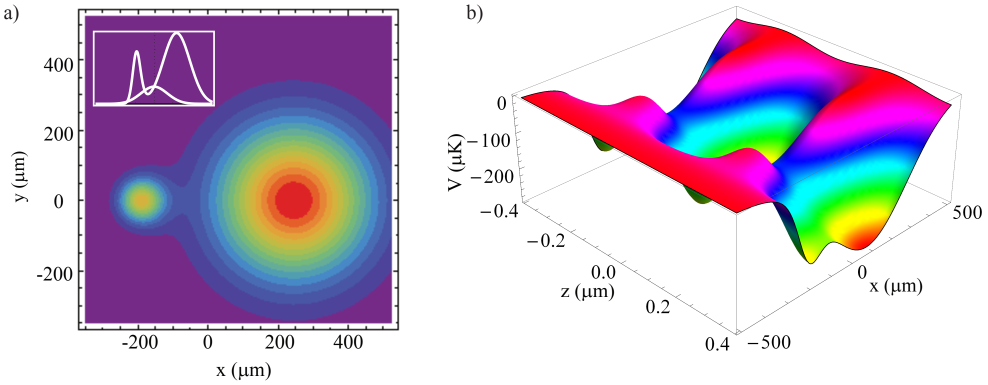

Figure 5.33: a) Intensity distribution of the reflected beam at the position of the atoms, $z = 0$. The The parameters used are $w_0 = 350\,\mu\mathrm{m}$, $w_1 = 0.2239\,w_0$, $w_2 = 0.9836\,w_0$, $p_1 = 0.04\,P$, $p_2 = 96\,P$, $x_1 = -0.553\,w_0$, and $x_2 = 0.9\,w_0$. The inset shows the intensity along a line at $x = 0$ and $y = 0$. b) The resulting lattice potential has a double well structure. The potential depth is for $P = 76\,\mathrm{mW}$.

Even a mild distortion can cause an observable effect on the backaction resonance. Let us consider the reflected intensity distribution shown in Fig. 5.33a. The resulting optical potential is shown in Fig. 5.33b. We calculate the resonant damping of the membrane for the simplified case of constant atom number and temperature; $T(P) = 100\,\mu\mathrm{K}$, $N(P) = 2 \cdot 10^6$. Figure 5.34a shows the calculation for fixed $\gamma_c = 8\,\omega_{\mathrm{rec}}$ (red) and $\gamma_c = 4\omega_{\mathrm{rec}}$ (blue). A clear dent in the signal is visible due to the intensity profile of the lattice beam. Fig. 5.34b shows another example, where we assume $\gamma_c = 4\,\omega_{\mathrm{rec}}$ (green), and in addition take the temperature dependence of the atoms on the lattice power, $T(P)$, into account. The assumed $T\,(P)$ is that from the reference measurement in Fig. 5.24.

Essentially, this analysis shows that the finer details of the resonance shape depend strongly on the exact beam shape of the lattice beam in combination with the temperature of the atoms and the atomic cooling rate. In conclusion, the non-Gaussian shape of the lattice beam is a likely reason for the observed second peak at $P \approx 110\,\mathrm{mW}$ in the back-action resonance.

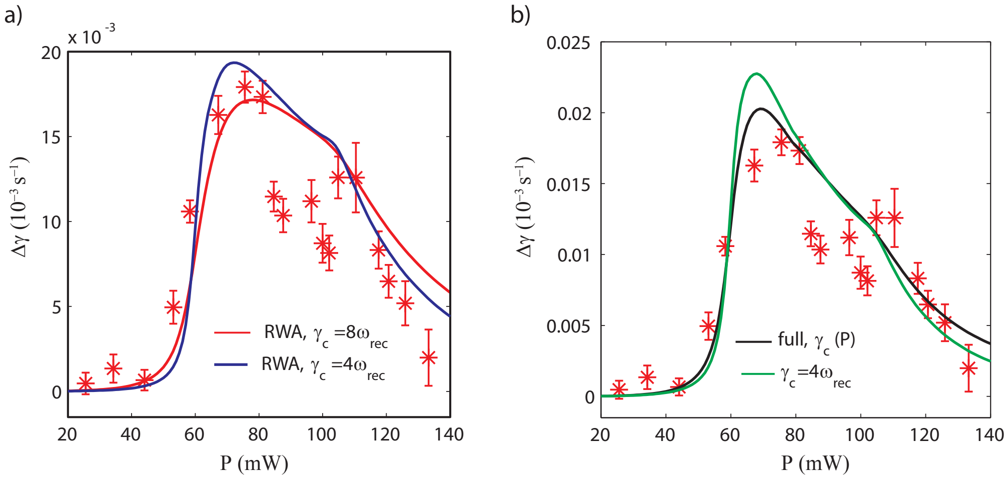

Figure 5.34: Simulation of the backaction signal assuming a non-Gaussian backreflected lattice beam for a) fixed temperature $T(P) = 100\,\mu\mathrm{K}$ and $\gamma_c = 8\,\omega_{\mathrm{rec}}$ (red), and $\gamma_c = 4\,\omega_{\mathrm{rec}}$ (blue); b) $T(P)$ that is derived from measurement and for $\gamma_c = 4\,\omega_{\mathrm{rec}}$ (RWA - green, full calculation - black). The atom number in these calculations is $N = 2 \cdot 10^6$.

5.6 Concluding Remarks

We have realized a hybrid optomechanical system composed of ultracold atoms and a membrane where an optical lattice mediates a long-distance coupling. Despite the enormous mass difference between the atoms and the membrane, $Nm/M \simeq 10^{-8}$, we clearly observe the backaction of the atoms onto the membrane. The measured change in the damping of the membrane and the predictions of the theoretical description in Sec. 3.1 agree remarkably well, suggesting that the theory can be used for extrapolation to optimized parameters. These proof-of-principle experiments have inspired us to design a new, second generation atom-membrane setup, ultimately having the quantum-coherent coupling regime as a goal.

The experiments presented in this Chapter were performed with a setup where the optical access to the MOT chamber was rather limited. Our atomchip MOT traps $\sim 10^7$ atoms and we loaded $\sim 2 \cdot 10^6$ atoms into the red-detuned 1D optical lattice. We demonstrated ground-state cooling of the atoms in the lattice with optical molasses, but the trap lifetime with continuous molasses cooling remained short compared to the ringdown time of the membrane. In order to overcome this, we chose to apply continuous MOT cooling to the atoms. In this way the number of atoms in the trap could be kept in steady-state during the ringdown of the membrane. The observed coupling resonance was broad, $2\pi \cdot 130$ kHz. Its shape was dominated by the spread in the vibrational frequencies of the relatively hot atoms in the spatially inhomogeneous trapping potential.

In the following, some improvements for both the membrane and atomic module are proposed which can lead to considerable enhancement of the coupling strength. The modularity of our setup allows us to easily modify the atom and the membrane parts independently, and we are currently working towards implementing these improvements in a new setup.

Improvements on the Atomic Module:

- **Increase Atom Number in the Lattice:** To increase the number of lattice-trapped atoms, one should improve the MOT density and increase the lattice volume [76]. One way to improve the loading of the lattice over the full range of lattice powers, would be to optimize the MOT detuning with respect to each of the lattice beam powers in order to compensate for the light shift induced by the lattice beams. Furthermore, more elaborate loading sequences consisting of ramping up the lattice power and detuning to the desired value have been demonstrated to considerably increase the number and lifetime of the atoms in the lattice [133].

  In addition, not to be limited by the initial temperature of the loaded atoms, more efficient cooling technique is required. Atom numbers as large as 3×10^8 have been prepared in the ground state of a large volume 3D lattice using Raman sideband cooling [77].

- **Reduce Spread of Vibrational Frequencies** Ground-state cooling of the atoms [77] would reduce the contributions to γ_{at} from spatial inhomogeneities of the trapping beam and the finite temperature of the atoms. By shaping the beam profile of the lattice beam to be 'flat-top'-like, the effect of the spatial inhomogeneities could be reduced further.

- **Sophisticated Lattice Configuration:** The atoms could be confined in the transverse direction by an additional, far detuned 2D lattice. The resulting three dimensional lattice isolates the atoms from each other, mitigating trap loss due to light-assisted collisions [77]. A blue-detuned lattice could then be used to couple the atoms to the membrane. This would suppress effects due to spontaneous emission of the atoms and thus allow for smaller laser detuning and power.

Improvements on the Membrane Module:

- **High-Stress Membranes:** While performing the experiments presented in this Chapter, we found out about the stoichiometric SiN membranes [101]. The measured absorbance of a high-stress membrane seems to be at least two orders of magnitude lower ($\lesssim 2 \cdot 10^{-5}$) at 780 nm than that of the low-stress membrane ($1.5 \cdot 10^{-3}$) used in the experiment (see Sec. 4.2). Consequently, limitations on the actual cooling performance due to heating of the membrane will be less stringent and the power incident on the membrane can be increased. Operating at lattice power levels, where the power dependence of $\omega_{\mathrm{m}}(P)$ and $Q_{\mathrm{m}}(P)$ is minute, sophisticated lattice loading sequences involving ramps of P are possible.

- **Cavity-Enhanced Coupling:** A relatively simple trick to enhance the coupling is to enclose the membrane inside a cavity, as discussed in theory in Sec. 3.2, and in practice in Chapter 6.
- **Reduce Bath Temperature:** In the long term, one can enclose the membrane module inside a cryostat to reduce the bath temperature. This is a prerequisite to explore the ground-state cooling of the membrane with current parameter estimates.
- **Patterning of the Membrane:** One can also work towards optimizing the oscillator itself. By patterning a SiN membrane with sub-wavelength diffraction gratings reflectivity of 99.8% has been achieved [110, 111]. Simultaneously the mass of the membrane is decreased. Despite being patterned, the membrane has a high Q of 10^6 at room temperature [110, 111].

6

Experimental Setup for Cavity-Enhanced Coupling of Membrane and Ultracold Atoms

This Chapter discusses the experimental realization of our new, second generation atom-membrane coupling setup. The atom and membrane module designs are based on the results and conclusions reported in Sec. 5.6. The conceptual difference compared to the coupling scheme presented in Ch. 5 is that we use an optical cavity around the membrane. This leads to an enhancement in the atom-membrane coupling constant g in proportion to the cavity finesse $\mathfrak{F}$ as discussed theoretically in Sec. 3.2. Furthermore, our single-sided cavity design allows us to overcome the leakage of the light out of the system due to finite reflectivity of the membrane and is expected to improve the read-out sensitivity of the membrane motion compared to a standard Michelson interferometer.

This Chapter starts with a brief description of the new MOT in Sec. 6.1, but the focus of the Chapter is on the implementation and operation of the cavity-enhanced membrane module. Sec. 6.2 covers the basic principles of optical cavities and proceeds further to explain the optomechanical properties of a cavity that encloses a membrane in the middle (MIM-setup). Section 6.3 discusses the MIM-cavity design and the vacuum system. Sections 6.4 and 6.5 describe the laser system for the cavity mode matching, locking and interrogation, and Section 6.6 explains the vibration isolation required to operate the MIM-cavity. The optomechanical characterization measurements of the MIM-cavity are reported in Sec. 6.7.

The complete MIM-module is designed and built from scratch as a part of this thesis and it is now "ready to go" for first atom-membrane coupling experiments. As an outlook, I discuss our preliminary measurements on sympathetic cooling of the membrane mode via the laser-cooled atoms in Sec. 6.8. The effect of the atoms onto the damping of the membrane is observed to be 10^4 times larger in the new setup than in the first, free-space coupling setup, presented in Sec. 5.5.

6.1 Atomic Module Design

The atomchip-MOT used in the free-space experiments in Ch. 5 was originally designed and used for micrometer-scale quantum optics experiments with a BEC on a chip [120, 122]. The chip-MOT design has a limited optical access and the MOT can maximally capture a few times 10^7 atoms. For the new experiment we decided to set up a standard three-dimensional (3D) MOT. The new MOT design implements the suggested improvements on the atomic module that are discussed in the conclusions of Sec. 5.6. It was built up by Andreas Jöckel, and the details of the MOT construction and operation will be found in his thesis.

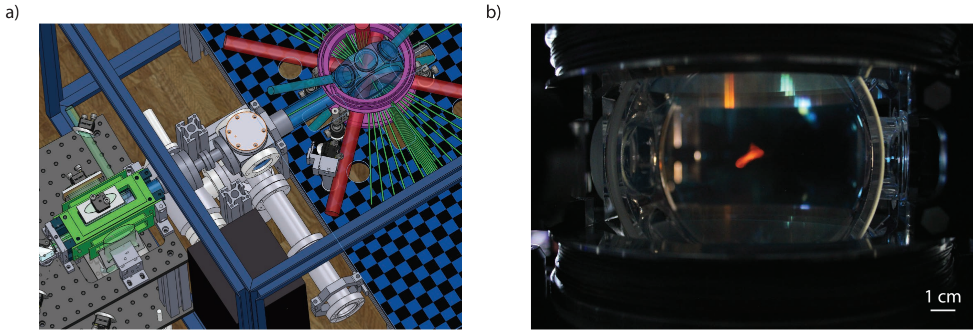

Figure 6.1: a) The second generation MOT layout. The atoms are first loaded in a 2D MOT (cage colored green, on the left of the figure) and then transported with a push beam into the main 3D MOT chamber (on the right). The MOT coil-cage is colored magenta around MOT chamber. The main MOT chamber is casted out of glass for maximum optical access. The red laser beams impinging the cell are for MOT cooling, and the blue beams illustrate a possible configuration for the transverse lattice for tighter confinement of the atoms. The green lines illustrate the optical lattice beam, and also any other possible laser beams that may be implemented in the future for probing and controlling the atoms. b) A photograph of the actual MOT cloud inside the glass vacuum chamber.

The MOT-setup is based on a so-called 2D+3D MOT configuration [134]. An illustration of the setup is shown in Fig. 6.1a. The Rb atoms are first captured in a 2D MOT from background pressure. The atoms are then transferred with a push beam via a differential pumping hole to a 3D MOT chamber. Such a sequence enables higher loading rate of the 3D MOT ($1.6 \cdot 10^9$ atoms/s) compared to direct capture from background pressure (Sec. 5.1.1). In addition, the lifetime of the atoms in the trap will be longer owing to a lower background pressure in the main MOT chamber that is around $1 \cdot 10^{-10}$ mbar. The new MOT operation is currently being optimized. So far we have measured MOT lifetimes up to 10 s for an ensemble of $2 \cdot 10^9$ atoms. The number of atoms in the MOT is two orders of magnitude more than previously. After molasses cooling the atoms have a temperature of 15 μK. A photograph of a MOT inside the glass chamber is shown in Fig. 6.1b.

The optical lattice (which is illustrated with the beam colored green and traversing the glass cell in Fig. 6.1a) is implemented using a similar beam path and beam parameters as in the free-space experiment, see Sec. 5.1.2. The beam waist of the lattice is set to $w_0 = 350\,\mu\text{m}$ as before, but we plan to experiment with a smaller detuning of the lattice beam, Δ_L, which requires less intensity. The optimization of the optical lattice is work in progress. At the moment we load $\sim 4 \cdot 10^7$ atoms to the lattice ($\lambda = 780\,\text{nm}$, $\Delta_\text{L} = -2\pi \cdot 20\,\text{GHz}$, $P = 70\,\text{mW}$). We expect to increase this number into the 10^8 regime. Furthermore, we are planning to implement step by step the improvements on the lattice configuration as proposed in Sec. 5.6. These include a 2D lattice for additional transverse confinement of the atoms, a blue detuned lattice, and an integrated Raman-sideband cooling scheme.

6.2 Theory: Membrane Inside a Cavity

This section starts by describing the general properties of optical cavities that are required to understand the more complex cavity operation when a thin, partially reflecting membrane is placed in the middle of the cavity (MIM-system). The simplest type of an idealized optical cavity consists of two parallel, planar mirrors. This model provides an easy understanding of the axial modes of a cavity. A practical cavity consisting of non-planar mirrors has in addition a set of transverse modes. I derive these for the experimentally relevant case of a cavity with spherical mirrors. Finally, in Sec. 6.2.2, I describe the optomechanical properties of such a cavity when it encloses a membrane in its middle. The discussion of the MIM-system is restricted to the non-resolved sideband regime ($\omega_\text{m} \ll \Delta\omega$), and considerations on the optimal cavity-operation regime for the atom-membrane experiment are discussed.

6.2.1 Optical Cavity Basics

Longitudinal Modes of a Simple Fabry-Pérot Cavity

Let us start by considering a cavity consisting of planar mirrors spaced by a distance L_cav; the Fabry-Pérot cavity. The optical cavity modes can be calculated using Maxwell's equations. A monochromatic light wave of frequency ω inside the cavity can be written in terms of its complex wavefunction [74]

$$E(\mathbf{r}, t) = A(\mathbf{r}) e^{i\omega t} \tag{6.1}$$

The complex amplitude $A(\mathbf{r})$ satisfies the Helmholtz equation, i.e., $\nabla^2 A(\mathbf{r}) + k^2 A(\mathbf{r}) = 0$, where $k = \omega/c$ and $c = c_0/n$ is the speed of light in the resonator medium with refractive index n, and c_0 is the speed of light in vacuum. The cavity modes are solutions to the Helmholtz equation constrained by the boundary

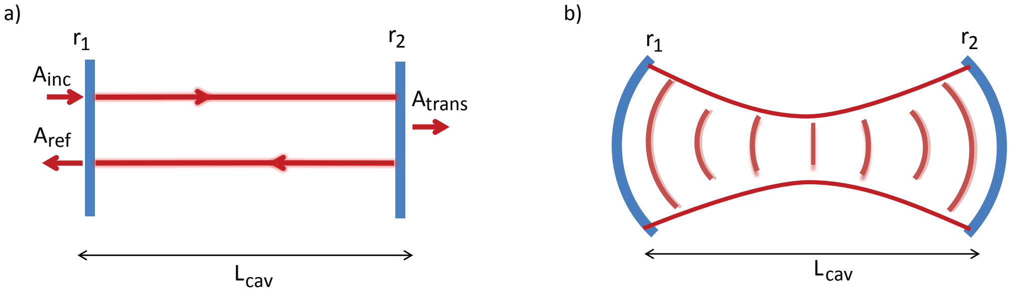

Figure 6.2: a) Fabry-Pérot cavity consisting of two parallel mirrors with amplitude reflectivities r_1 and r_2. The spacing between the mirrors is L_cav. The incoming wave is a plane wave. b) A cavity with spherical mirrors supports Laguerre-Gaussian and Hermite-Gaussian modes. In order to mode-match the incoming laser beam into the desired cavity mode, the incoming beam should also occupy the respective spatial mode.

conditions set by the two mirrors. For perfectly reflecting metallic mirrors, the field at the mirrors must vanish. The standing wave

$$A(\mathbf{r}) = A_q \sin(k_q z), \tag{6.2}$$

where A_q is a constant, satisfies these conditions when $k = k_q = q\pi/L_\mathrm{cav}$, where $q \in 1, 2, 3, \ldots$. This is equivalent to the condition that the round-trip phase ϕ_tr acquired by a resonant wave has to satisfy $\phi_\mathrm{tr} = 2kL_\mathrm{cav} = q \cdot 2\pi$, so that it will reproduce itself after each round-trip. Consequently, the solutions for the eigenfrequencies of the resonator are $\nu_q = qc/2L_\mathrm{cav}$. These axial modes are spaced by the free spectral range (FSR)

$$\mathrm{FSR} = \frac{c}{2L_\mathrm{cav}}. \tag{6.3}$$

The cavity losses will change the amplitude of the circulating field inside the cavity, and also relax the strict condition on the frequencies ν_q permitted to exist inside the cavity. Let us consider mirrors with finite amplitude reflectivities of r_1 and r_2 as illustrated in Fig. 6.2a. The corresponding mirror transmittances are $t_{1,2} = \sqrt{1 - r_{1,2}^2 - \alpha_{\mathrm{m},1,2}^2}$, where $\alpha_{\mathrm{m},1,2}^2$ is the power transmittance loss in the mirrors. Furthermore, a real resonator has always additional loss due to absorption or scattering losses in the cavity medium/elements inside the cavity, for example. Any sort of extra loss is modeled by an attenuation coefficient α_0, and we define a round-trip gain in the resonator as $h\,(\omega) = r_1 r_2 e^{-2\alpha_0 L_\mathrm{cav} - i\frac{2\omega L_\mathrm{cav}}{c}}$. Let us assume an incident electric field A_inc on the first mirror, as in Fig. 6.2a. Consequently, after m round-trips the circulating amplitude has a value [135]

$$A_\mathrm{circ} = \sum_\mathrm{m} h^m i t_1 A_\mathrm{inc} \approx \frac{i t_1 A_\mathrm{inc}}{1-h}, \tag{6.4}$$

where the last approximation holds when $m \to \infty$. Thus, the amplitude of the circulating field is related to the amplitude of the incoming field as

$$\frac{A_{\mathrm{circ}}}{A_{\mathrm{inc}}} = \frac{it_1}{1-h}. \tag{6.5}$$

Similarly, the transmitted and reflected fields can be written as

$$\frac{A_{\mathrm{trans}}}{A_{\mathrm{inc}}} = \frac{-t_1 t_2}{\sqrt{r_1 r_2}} \frac{\sqrt{h}}{1-h} \equiv t_{\mathrm{cav}}\left(\omega\right), \tag{6.6}$$

and

$$\frac{A_{\mathrm{ref}}}{A_{\mathrm{inc}}} = r_1 - \frac{{t_1}^2}{r_1} \frac{h}{1-h} \equiv r_{\mathrm{cav}}\left(\omega\right), \tag{6.7}$$

which define the amplitude reflection $r_{\mathrm{cav}}\left(\omega\right)$ and transmission $t_{\mathrm{cav}}\left(\omega\right)$ of the cavity. The corresponding intensities are simply given by $I_{\mathrm{circ}}/I_{\mathrm{inc}} = \left|\frac{A_{\mathrm{circ}}}{A_{\mathrm{inc}}}\right|^2$, $I_{\mathrm{trans}}/I_{\mathrm{inc}} = \left|\frac{A_{\mathrm{trans}}}{A_{\mathrm{inc}}}\right|^2$, and $I_{\mathrm{ref}}/I_{\mathrm{inc}} = \left|\frac{A_{\mathrm{ref}}}{A_{\mathrm{inc}}}\right|^2$.

Figure 6.3a shows the calculated intensity transmission and reflection of a symmetric Fabry-Pérot cavity consisting of two mirrors of $r_1 = r_2 = 0.96$. The transmission and reflection of the cavity consist of sharp resonance peaks separated by one free spectral range (Eq. 6.3). On-resonance, the transmitted intensity is maximum, and in this specific case equal to the incoming intensity. The reflected intensity is zero. This is an example of impedance matching: when r_1 exactly equals the additional loss terms given by $\left(1-\alpha_{\mathrm{m},1}^2\right) r_2 e^{-2\alpha_0 L_{\mathrm{cav}}}$, the

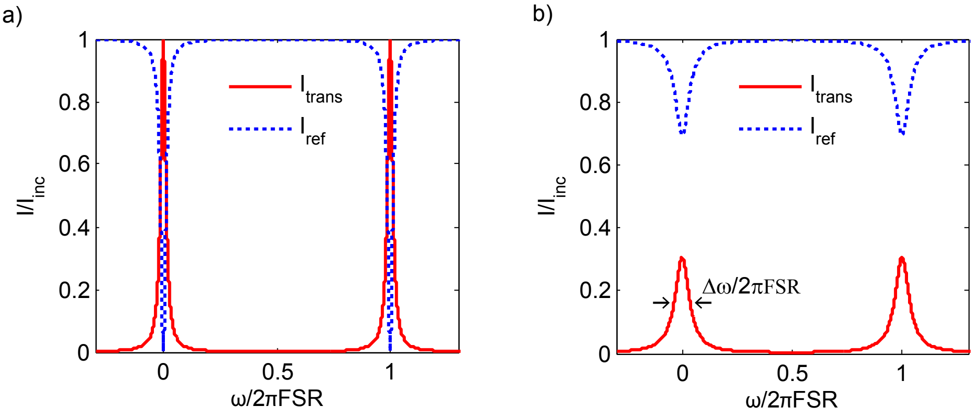

Figure 6.3: Typical frequency response of an optical cavity. The power of the transmitted (red solid line) and the reflected (blue dashed line) fields are plotted against the frequency of the incoming light in units of FSR for a) a symmetric cavity with $r_1 = r_2 = 0.96$. b) an asymmetric cavity $r_1 = 0.80$, $r_2 = 0.98$. The additional cavity loss and mirror transmittance loss are assumed to be negligible, i.e., $\alpha_0 = 0$, $\alpha_{\mathrm{m},1,2}^2 = 0$.

reflected field (Eq. 6.7) becomes zero exactly on resonance. In a real experiment perfect impedance matching is hard to achieve. On the other hand, in our experiment we intentionally use a single-sided cavity design, that is optimized to reflect most of the light back to the atoms, and at the same time minimize the resonant transmission. By choosing the reflectivity of the first mirror lower, the fraction of reflected and transmitted light can be tuned arbitrarily. Fig. 6.3b shows an example of a single-sided cavity, where $r_1 = 0.80$, $r_2 = 0.98$.

The bandwidth of a cavity is defined as the full width at half maximum (FWHM) of the intensity transmission spectrum

$$\frac{I_{\mathrm{trans}}(\omega)}{I_{\mathrm{trans}}(\omega)} = \left|\frac{A_{\mathrm{trans}}}{A_{\mathrm{inc}}}\right|^2 = \frac{t_1^2 t_2^2}{r_1 r_2} \frac{|h(\omega)|}{|1 - h(\omega)|^2}, \tag{6.8}$$

and it is given by

$$\Delta\omega = \frac{2c}{d} \arcsin\left[\frac{1 - h(\omega_{\mathrm{q}})}{2\sqrt{h(\omega_{\mathrm{q}})}}\right] \approx \frac{c}{d} \frac{1 - h(\omega_{\mathrm{q}})}{\sqrt{h(\omega_{\mathrm{q}})}}, \tag{6.9}$$

where $h(\omega_{\mathrm{q}}) = r_1 r_2 e^{-2\alpha_0 L_{\mathrm{cav}}}$ and the last approximation holds when $h(\omega_{\mathrm{q}}) \to 1$. The quality, or resolving power, of the cavity is expressed in terms of finesse $\mathfrak{F}$ as

$$\mathfrak{F} = \frac{\pi\sqrt{h(\omega_{\mathrm{q}})}}{1 - h(\omega_{\mathrm{q}})} \approx 2\pi \frac{\mathrm{FSR}}{\Delta\omega}. \tag{6.10}$$

It is worth noting that in parallel to $\Delta\omega$ the literature often uses the amplitude decay rate, $\kappa = \frac{\Delta\omega}{2} \approx \frac{\pi \mathrm{FSR}}{\mathfrak{F}}$. It is the half width at half maximum (HWHM) of the resonance.

Finally, the phase of a field $A(\mathbf{r})$ is in general given by

$$\theta(\omega) = \tan^{-1} \frac{\mathrm{Im}(A(\mathbf{r}))}{\mathrm{Re}(A(\mathbf{r}))}. \tag{6.11}$$

The phase of the transmitted and reflected cavity fields has a maximum gradient on resonance with respect to the incoming field. In particular, in our atom-membrane experiment, we are interested in the phase gradient of the reflected field $\frac{A_{\mathrm{ref}}}{A_{\mathrm{inc}}}$ with respect to the incominf field on-resonance (Eq. 6.7), which for $\mathfrak{F} \gg 1$ can be approximated simply as

$$\frac{\partial\theta_{\mathrm{ref}}(\omega)}{\partial\omega}|_{\omega=\omega_q} \approx -\frac{2\mathfrak{F}}{\pi \mathrm{FSR}}. \tag{6.12}$$

Importantly, the phase gradient scales linearly with $\mathfrak{F}$. Figure 6.4 shows the reflected intensity $I_{\mathrm{ref}}(\omega)$ and $\theta_{\mathrm{ref}}(\omega)$ a for a single sided cavity.

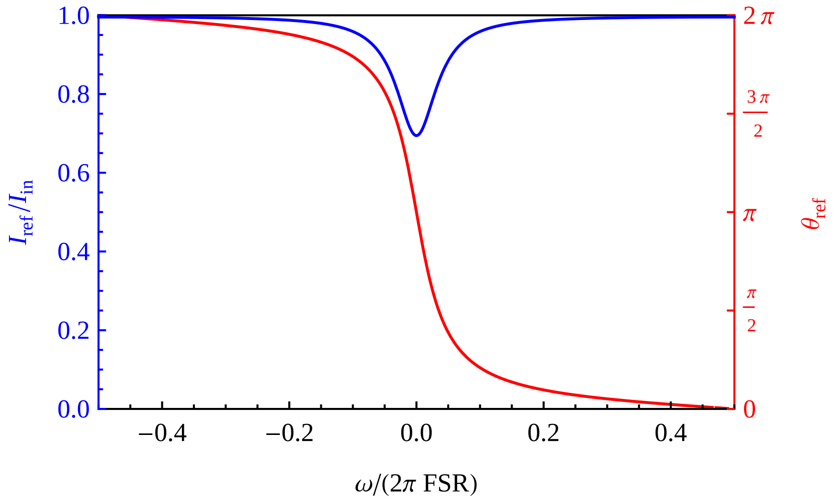

Figure 6.4: The phase of the reflected field θ changes by 2π over cavity resonance and it has its maximum gradient on-resonance (red line). The width of the reflection resonance (blue line) and the steepness of the phase-gradient slope are defined by the finesse of the cavity. Here we assume lossless mirrors of $r_1 = 0.80$, $r_2 = 0.98$ as in Fig. 6.3b, and $\alpha_0 = 0$.

Transverse Modes

The description above was limited to plane waves and cavities consisting of planar mirrors. In practice, it is unfavorable to make a cavity of planar mirrors, as they have to be perfectly aligned with respect to each other. Furthermore, the incoming laser beam should be a perfect plane wave, which would require infinitely large mirrors for high-performance. Any deviations from this ideal case causes the light to escape the optical resonator. In most cases, spherical mirrors are used to make the cavity stable. A cavity consisting of spherical mirrors is illustrated in Fig. 6.2b. The condition for a cavity of length d to be stable is [74]

$$0 \leq \left(1 + \frac{L_{\rm cav}}{C_1}\right)\left(1 + \frac{L_{\rm cav}}{C_2}\right) \leq 1, \tag{6.13}$$

where $C_{1,2}$ are the radii of curvature of the cavity mirrors. Planar mirrors have $C = \infty$, convex mirrors $C > 0$ and concave mirrors $C < 0$. Our science cavity is a symmetric resonator, consisting of two concave mirrors with equal C. Furthermore, the science (lattice) beam coupled into the cavity has a nearly Gaussian intensity profile defined by Eq. 2.80. In addition to a discrete set of longitudinal modes, the cavity will now support also a set of transverse modes.

A mode of a resonator is a self-consistent field configuration. Thus, in order for the Gaussian beam to be resonant with the cavity, its wavefront radius of curvature $R(z)$ must match the radius of curvature of the mirrors C at the position of the mirrors. This means that the incident beam must match the Rayleigh length of the cavity [136],

$$z_{\mathrm{r,cav}} = \frac{\sqrt{g_1 g_2 \left(1 - g_1 g_2\right)}}{g_1 + g_2 - 2 g_1 g_2} L_{\mathrm{cav}} \tag{6.14}$$

where $g_{1,2} = (1 + d/C_{1,2})$. This is illustrated in Fig. 6.2b. In addition to such a spatial mode matching requirement, the phase change of the Gaussian beam per round-trip in the cavity must be a multiple of 2π on resonance. This means that $\phi_{\mathrm{tr}} = 2\left(kd + \Delta\xi\right) = q \cdot 2\pi$, where $\Delta\xi$ is the round-trip Gouy-phase of a Gaussian beam. Thus, going from a simple plane waves picture to a Gaussian picture, the free spectral range stays the same, but only the absolute resonance frequency shifts by $\Delta\xi \cdot \mathrm{FSR}/\pi$.

The Gaussian cavity mode is the lowest order spatial solution to the wave equation. The higher-order modes can either take the form of Laguerre-Gaussian or Hermite-Gaussian modes. The former ones require spherical symmetry, whereas the latter are more common as they exist in cases where the symmetrical geometry is broken. Although these modes have the same wavefront as the Gaussian beam, their amplitude distribution differs. The resonance frequencies of these modes depend on the mode indices (l, m) as [74]

$$\nu_{l,m,q} = q \cdot \mathrm{FSR} + (l + m + 1)\,\frac{\Delta\xi}{\pi} \cdot \mathrm{FSR}. \tag{6.15}$$

Some of the lower order cavity modes are shown in Fig. 6.18a that can be also observed with our experimental cavity. If the mode matching is done carefully, as discussed in Sec. 6.4.2, almost all of the incident power can be coupled into the desired mode.

6.2.2 Membrane in the Middle of a Cavity

A thin membrane inside the cavity will modify the cavity resonances in a nontrivial way. Next we solve for the steady-state intracavity fields and optomechanical coupling for a system where the membrane is placed in the middle of the cavity (MIM). We find out that interference effects inside the cavity will lead to a dependence of the circulating, transmitted and reflected fields on the membrane position. In the case of a single-sided cavity, the cavity finesse $\mathfrak{F}$ will also depend on the membrane position.

6.2.2.1 Optomechanical Coupling

The derivation here follows that in [105] and is generalized for our case of a single-sided cavity. A dielectric membrane is placed in the middle of the cavity as shown in Fig. 6.5. The membrane has a thickness of d_{m} and complex index of refraction n_{m}. The complex-valued amplitude reflection and transmission coefficients for the dielectric membrane can be written as

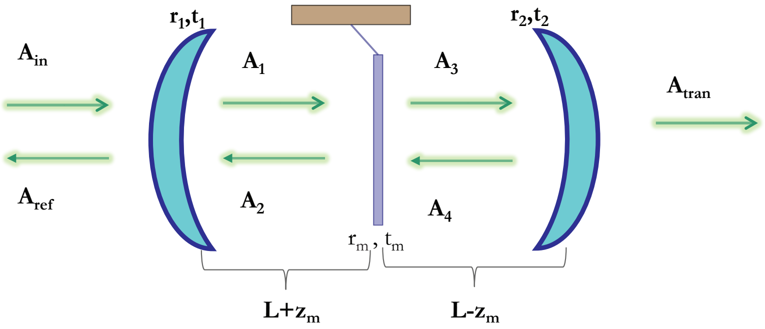

Figure 6.5: Membrane-in-the-middle cavity geometry. A membrane of thickness d_{m} has amplitude reflection and transmission coefficients of r_{m} and t_{m}, respectively. We describe the system in terms of left- and right-going plane-waves. The z_{m} is the position of the membrane with respect to the center of the cavity.

$$r_{\mathrm{m}} = \frac{\left(n_{\mathrm{m}}^2 - 1\right)\sin kn_{\mathrm{m}}d_{\mathrm{m}}}{2in_{\mathrm{m}}\cos kn_{\mathrm{m}}d_{\mathrm{m}} + (n_{\mathrm{m}}^2+1)\sin kn_{\mathrm{m}}d_{\mathrm{m}}} \tag{6.16}$$

$$t_{\mathrm{m}} = \frac{2n_{\mathrm{m}}}{2in_{\mathrm{m}}\cos kn_{\mathrm{m}}d_{\mathrm{m}} + (n_{\mathrm{m}}^2+1)\sin kn_{\mathrm{m}}d_{\mathrm{m}}}. \tag{6.17}$$

Note that when n_{m} is real, then $|r_{\mathrm{m}}|^2 + |t_{\mathrm{m}}|^2 = 1$. We want to solve the electric field amplitudes inside and outside the cavity. In the center of the cavity the Gaussian cavity mode can be well approximated to have planar wavefronts parallel to the membrane surface, and a plane-wave description is sufficient to describe the system. The set of equations for the field amplitudes as illustrated in Fig. 6.5 is

$$A_1 = it_1A_{\mathrm{in}} + r_1A_2e^{ik(L+z_{\mathrm{m}})} \tag{6.18}$$

$$A_2 = r_\mathrm{m} A_1 e^{ik(L+z_\mathrm{m})} + it_\mathrm{m} A_4 e^{ik(L-z_\mathrm{m})} \tag{6.19}$$

$$A_3 = it_\mathrm{m} A_1 e^{ik(L+z_\mathrm{m})} + r_\mathrm{m} A_4 e^{ik(L-z_\mathrm{m})} \tag{6.20}$$

$$A_4 = r_2 A_3 e^{ik(L-z_\mathrm{m})} \tag{6.21}$$

$$A_\mathrm{ref} = it_1 A_2 e^{ik(L+z_\mathrm{m})} + r_1 A_\mathrm{in} \tag{6.22}$$

$$A_\mathrm{trans} = it_2 A_3 e^{ik(L-z_\mathrm{m})} \tag{6.23}$$

where $L \pm z_\mathrm{m}$ is the length of the cavity formed on the left or right side of the membrane and z_m is the position of the membrane with respect to the center of the cavity. The total length of the cavity is $L_\mathrm{cav} = 2L + d_\mathrm{m} \approx 2L$. A translation of the membrane by z_m will detune the MIM-cavity. By solving the Eqs. 6.18-6.23 we obtain the variation in the cavity resonance frequency as a function of membrane position. In practice, we are interested in the case, where the membrane absorbance is small and the cavity finesse is high, $\mathfrak{F} \gg 1$. For the case where membrane absorption is neglected, $\mathrm{Im}\,(n_\mathrm{m}) = 0$, the solution has an analytical form [105]

$$\omega_\mathrm{cav}\,(z_\mathrm{m}) = \mathrm{FSR}\left[2\phi_\mathrm{r} + 2\cos^{-1}\left(|r_\mathrm{m}|\cos\left(2kz_\mathrm{m}\right)\right)\right], \tag{6.24}$$

where $\phi_\mathrm{r} = \arg\,(r_\mathrm{m})$. A theoretical calculation for the cavity eigenfrequencies is shown in Fig. 6.6 for membrane reflectivities of $r_\mathrm{m} = 0.46$ (blue), 0.8 (green), and 1 (red). For $|r_\mathrm{m}| \to 1$ we encounter the case of two separate cavities, each of

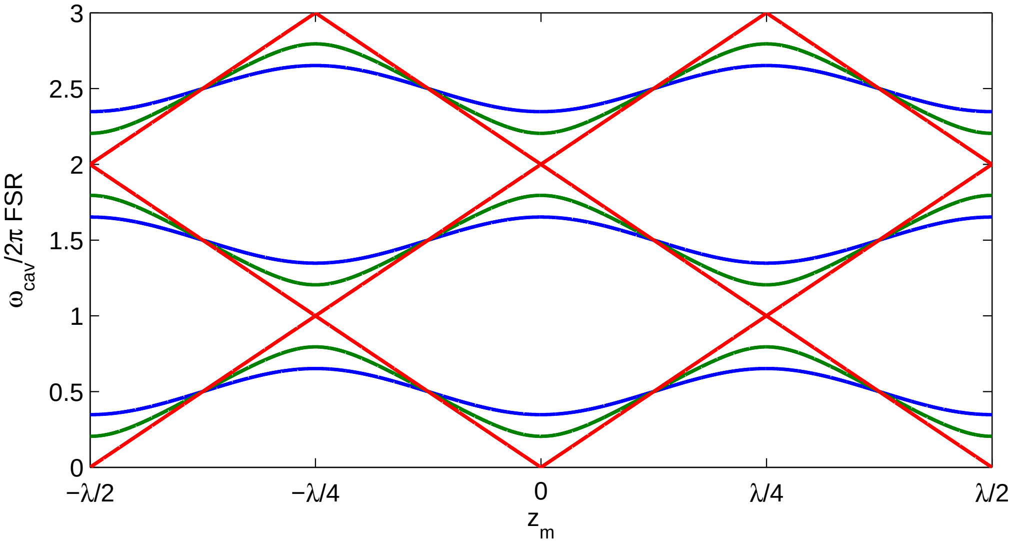

Figure 6.6: A plot of the theoretical variation in cavity resonance frequency $\omega_\mathrm{cav}\,(z_\mathrm{m})$ as a function of membrane position z_m. The cavity resonance $\omega_\mathrm{cav}/2\pi$ is plotted in units of the empty cavity FSR. The different curves represent different membrane reflectivities: $r_\mathrm{m} = 0.46, 0.8, 1$ for blue, green red.

which has a FSR of twice the original cavity. On the other hand, for $|r_\mathrm{m}| \to 0$ we naturally encounter the case of a single, empty cavity.

The optomechanical coupling constant of the membrane to the cavity field is defined as $G_\mathrm{opt} = d\omega_\mathrm{cav}/dz_\mathrm{m}$ (Eq. 2.61). The coupling vanishes when the membrane is placed at the node, $z_\mathrm{m} = 2q \cdot \frac{\lambda}{4}$, or anti-node, $z_\mathrm{m} = (2q+1)\frac{\lambda}{4}$ $(q \,\epsilon\, \mathcal{Z})$, of the cavity field, and G_opt has a maximum when the membrane is placed onto the slope of the cavity field, half between the node and antinode. In addition, G_opt scales with the reflectivity $|r_\mathrm{m}|$. For $|r_\mathrm{m}| \ll 1$, the optomechanical coupling reduces to

$$G_\mathrm{opt} \equiv \frac{\partial \omega_\mathrm{cav}}{\partial z_\mathrm{m}} \approx \mathrm{FSR} \cdot 4k\,|r_\mathrm{m}| \sin(2kz_\mathrm{m}), \tag{6.25}$$

and the cavity resonance has a sinusoidal dependence on the membrane position.

6.2.2.2 Membrane Absorbance

Membrane absorbance adds to the overall loss of the cavity. This results in a modified finesse (Eq. 6.10) as a function of the membrane position z_m. The absorbance loss is essentially proportional to the intensity of the cavity field at the position of the membrane. Consequently, it has its minima and maxima, when the membrane is placed on an antinode or node of the cavity field. Figure 6.7 shows a calculation of the variation in $\mathfrak{F}(z_\mathrm{m})$ for different membrane absorbances $\mathrm{Im}(n_\mathrm{m})$. The finesse is solved numerically from the width of the transmission resonances. In this example we use similar parameters as those in Ref. [105] and find that our numerical calculations are consistent with the results in Ref. [105]. The cavity parameters used for the calculation are: $r_1 = r_2 = 0.99991$ and a power transmission loss of $\alpha_{m,1,2} = 1.52 \cdot 10^{-4}$ in the mirrors is assumed, giving $t_1 = t_2 = 5.28 \cdot 10^{-3}$. These parameters give an empty cavity finesse of $1.7 \cdot 10^4$.

Membrane absorbance of $\mathrm{Im}(n_\mathrm{m}) = 1.5 \cdot 10^{-4}$ ($\lambda = 1064\,\mathrm{nm}$) for a low-stress SiN membrane has been detected with a high finesse cavity of $\mathfrak{F} = 1.65 \cdot 10^4$ [105]. In our experiment, we use high-stress SiN membranes for which we measure the absorbance to be $\mathrm{Im}(n_\mathrm{m}) \lesssim 2 \cdot 10^{-5}$ at 780 nm (Sec. 4.2). Absorbance values of $\mathrm{Im}(n_\mathrm{m}) = 0.6 \cdot 10^{-5}$ at 935 nm [101] and $\mathrm{Im}(n_\mathrm{m}) \leq 1.5 \cdot 10^{-6}$ at 1064 nm [102] have been reported previously. In our experiment, we work with a relatively low finesse cavity ($\mathfrak{F} < 300$). The maximum deviation of the finesse for an empty cavity of of $\mathfrak{F} \sim 150$ due to membrane absorbance of $\mathrm{Im}(n_\mathrm{m}) = 1.0 \cdot 10^{-5}$ is $\Delta\mathfrak{F}(z_\mathrm{m})/\mathfrak{F}(z_\mathrm{m}) \sim 9 \cdot 10^{-4}$.

6.2.2.3 Interference inside MIM-Cavity

The cavity reflection and transmission are modified as a function of z_m due to interference of the light circulating in the left and right halves of the cavity as illustrated in Fig. 6.5. It is important to distinguish interference effects from the absorbance of the membrane, or any other loss mechanisms present in the cavity.

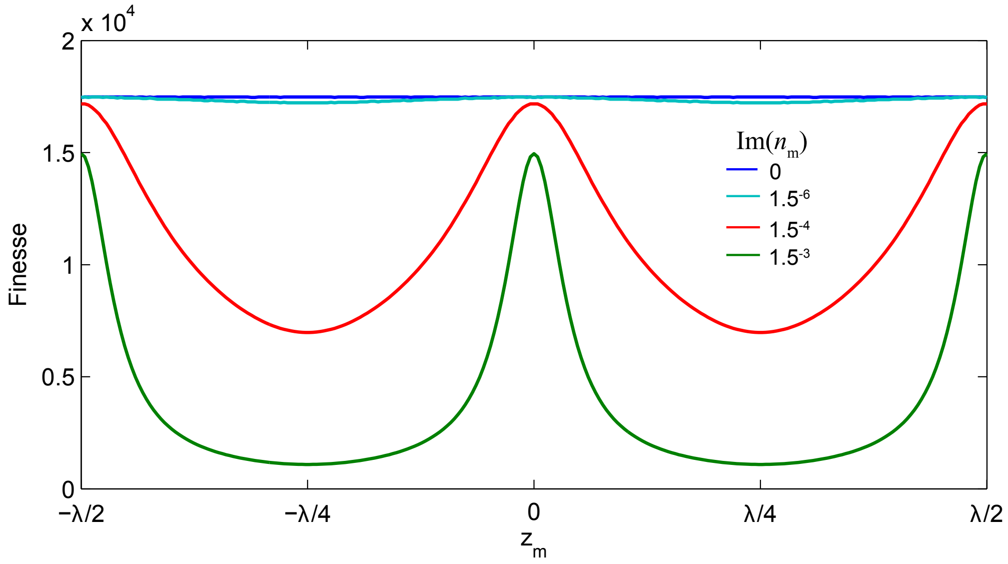

Figure 6.7: The calculated cavity finesse as a function of membrane position for various values of membrane absorbance. The membrane thickness is $d_\mathrm{m} = 50\,\mathrm{nm}$ and the absorbance is $\mathrm{Im}\,(n_\mathrm{m}) = 1.5 \cdot 10^{-3}$ (green), $\mathrm{Im}\,(n_\mathrm{m}) = 1.5 \cdot 10^{-4}$ (red), $\mathrm{Im}\,(n_\mathrm{m}) = 1.5 \cdot 10^{-6}$ (light blue), and $\mathrm{Im}\,(n_\mathrm{m}) = 0$ (blue). When n_m is complex, the intracavity photons can be lost to the membrane absorption. This additional loss process lowers the cavity finesse by an amount proportional to the overlap of the cavity mode with the membrane, giving rise to the dips in the finesse. For a non-absorbing membrane the finesse is independent of z_m has the same value as an empty cavity (blue line).

One way to qualitatively describe the MIM-system is to think of it in terms of two subcavities. Let us assume one of the subcavities is resonant with the light field, and call it CAV1, and the other one, CAV2, is detuned somewhere to the slope of the subcavity resonance. Consequently, the detuned CAV2 will have a smaller circulating intensity. As the light leaking out of the resonant CAV1 transmits the CAV2, it will interfere with the light field in the CAV2. This leads to a modified overall transmittance. If the intensity in the CAV2 is small compared to the intensity in CAV1, transmission through the CAV2 will mostly cause a phase shift on the light field. The phase shift depends on the membrane position with respect to the cavity mode, i.e, on the detuning of CAV2. This simple picture gives also intuition why the cavity eigenmodes are modified by the membrane.

When the cavity finesse is high, both interference and membrane absorption will contribute to the modulation in cavity transmission and reflection as a function of membrane position. The calculated transmission through the symmetric, high finesse ($\mathfrak{F} = 1.8 \cdot 10^4$) cavity introduced earlier is shown in Fig. 6.8a for different membrane absorbances. The transmission is maximum, when the membrane is on a node of the field, because absorbance loss is minimized. On the

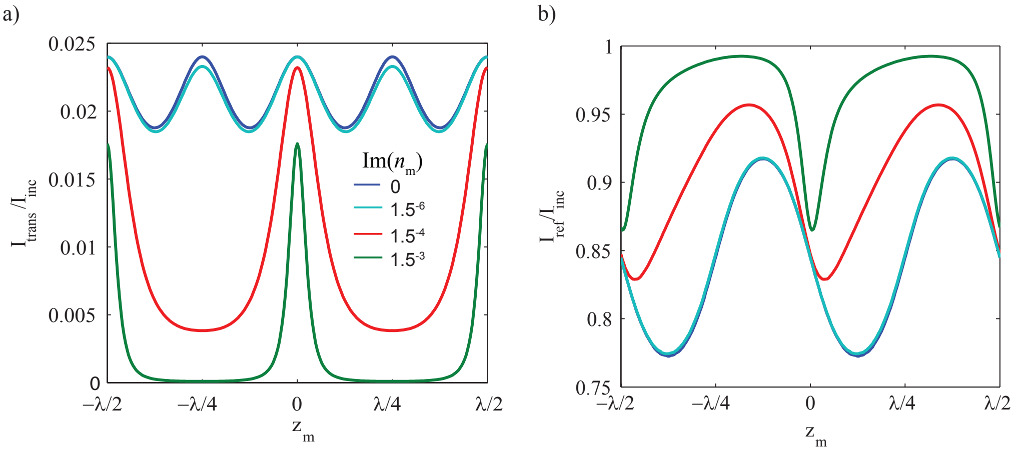

Figure 6.8: Resonant a) transmission and b) reflection of a symmetric MIM-cavity for various values of $\mathrm{Im}\,(n_\mathrm{m})$. The numerical simulation assumes cavity parameters of $r_1 = r_2 = 0.99991$, $\lambda = 780\,\mathrm{nm}$, $t_1 = t_2 = 5.28 \cdot 10^{-3}$; and membrane parameters of $d_\mathrm{m} = 50\,\mathrm{nm}$, $\mathrm{Re}\,(n_\mathrm{m}) = 1.98$, $\mathrm{Im}\,(n_\mathrm{m}) = 1.5 \cdot 10^{-3}$ (green), $\mathrm{Im}\,(n_\mathrm{m}) = 1.5 \cdot 10^{-4}$ (red), and $\mathrm{Im}\,(n_\mathrm{m}) = 1.5 \cdot 10^{-6}$ (light blue), and $\mathrm{Im}\,(n_\mathrm{m}) = 0$ (dark blue).

other hand, the resonant transmission has pronounced dips when the membrane is away from a node. As the transmission dips derive from absorption, they get more pronounced as the $\mathrm{Im}\,(n_\mathrm{m})$ increases. Note that even if the membrane is non-absorbing, the transmission is modulated due to interference effects in the two sub-cavities.

The phase of the light that has been circulating inside the cavity is affected by the membrane, whereas the phase of the directly reflected part is not. The reflected light will interfere with the light directly reflected from the left-hand end mirror resulting in the signal in Fig. 6.8b. The membrane absorption will lead to an asymmetric dependence of the reflected intensity on membrane position. Such interference effects have been confirmed by measurements [100].

In the case of an asymmetric cavity, where $r_1 \ll r_2$, the interference effects lead to a more pronounced dependence of I_trans and I_ref on z_m than in the symmetric case. Let us next consider our experimental parameter range. We assume $n_\mathrm{m} = 2.2 + i1.5 \cdot 10^{-5}$ for the high-stress membrane and $r_2 = 0.99991$ for the high-reflectivity end-mirror, and vary the input mirror reflectivity r_1. In addition to membrane absorbance loss we assume $t_{1,2} = \sqrt{1 - r_{1,2}^2}$, i.e., lossless mirrors. The transmitted and reflected intensities for various r_1 are shown in Figure 6.9a and Figure 6.9b. When the membrane is placed in the middle of a cavity field slope at $z_\mathrm{m} = -\lambda/8$, the transmitted intensity has a maximum and the reflected intensity has a minimum. The situation is reversed, when the membrane is placed onto the opposite slope at $z_\mathrm{m} = \lambda/8$.

The absorbance effects of the membrane are negligible in the cavity signal

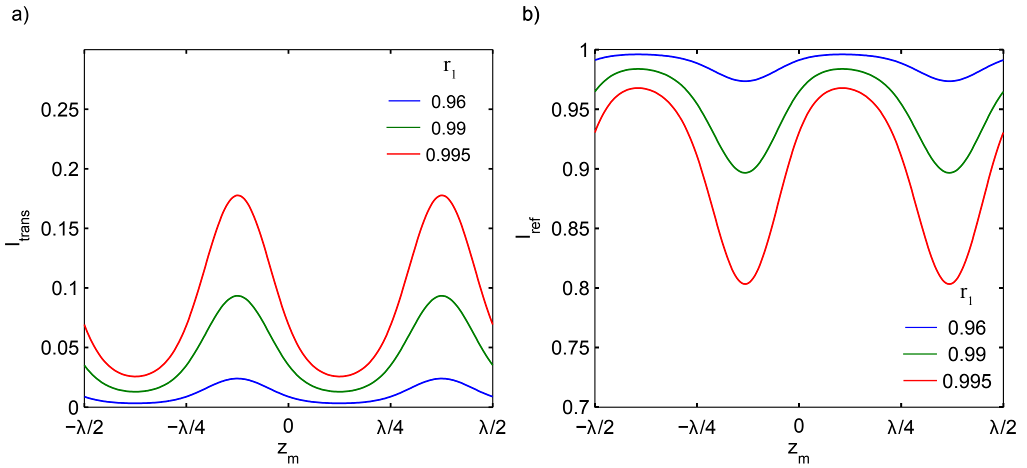

Figure 6.9: The transmitted (a) and reflected (b) resonant intensities for an asymmetric cavity as a function of the membrane position z_{m}. For low r_1, I_{trans} can be close to zero and most of the light is reflected. The I_{ref} is modulated by interference of the light reflected from the left-cavity and the light reflected promptly from the in-coupling mirror. The different colors (blue, green, red) correspond to input coupling mirror reflectivities of $r_1 = (0.96, 0.993, 0.995)$. The back mirror of the cavity has $r_2 = 0.99991$.

in Fig. 6.9 and do not contribute significantly to the cavity finesse. A detailed analysis reveals feeble asymmetry in the reflected signal, but its effect is difficult to observe in an experiment. However, the calculations predict that the finesse is a function of z_{m} for an asymmetric cavity, as shown in Fig. 6.10a. The finesse is defined here numerically from the width of cavity transmission peaks according to Eq. 6.10 as $\mathfrak{F}(z_{\mathrm{m}}) = 2\pi\mathrm{FSR}/\Delta\omega(z_{\mathrm{m}})$, where FSR is the empty cavity free spectral range. The modulation in the finesse derives from interference effects inside the MIM-cavity and is in contrast to the case of a symmetric cavity, where a non-absorbing membrane in the middle of the cavity does not influence the finesse (see Fig. 6.7). The $\mathfrak{F}(z_{\mathrm{m}})$ obtains its minimum and maximum when the membrane is placed at the opposing slopes of the cavity field, at $z_{\mathrm{m}} = \pm\lambda/8$. Furthermore, the maximum finesse at $z_{\mathrm{m}} = -\lambda/8$, $\mathfrak{F}_{\mathrm{max}}$ is larger than the empty cavity finesse which is depicted by the dashed horizontal lines in Fig. 6.10a. In general, the relative modulation in the finesse $\Delta\mathfrak{F}/\mathfrak{F}_{\mathrm{max}}$ increases as r_1 decreases, i.e., the more asymmetric the cavity is. In Ref. [109] it is found out that modulation in the finesse can also be observed in a symmetric cavity, when the membrane is not in the middle of a cavity.

6.2.2.4 Cavity for Atom-Membrane Experiment

In the atom-membrane experiment, we operate the MIM-cavity on resonance such that the light that has interacted with the atoms will be enhanced inside the cavity. The membrane is placed onto the slope of the resonant cavity field, where

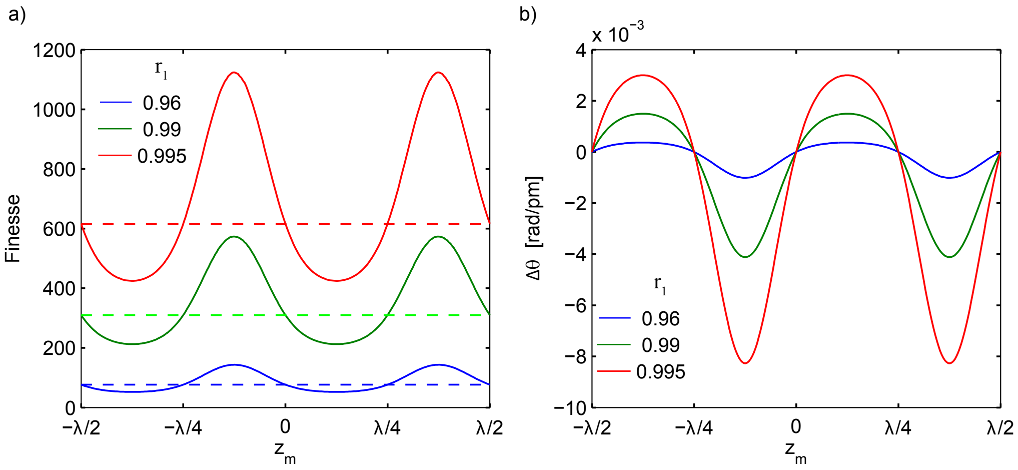

Figure 6.10: The calculated $\mathfrak{F}$ as a function of z_{m} for various $r_1 = 0.96, 0.99, 0.995$. The cavity end mirror has $r_2 = 0.99991$. Interference effects inside the cavity lead to a variation in the finesse as a function of z_{m}. $\mathfrak{F}$ is maximum at the slope $z_{\mathrm{m}} = -\lambda/8$, and minimum at the opposing slope $z_{\mathrm{m}} = \lambda/8$. The finesse of a MIM-cavity can increase beyond its the empty-cavity value, which is depicted by the horizontal lines for the corresponding reflectivity. b) The phase shift of the reflected beam $\Delta\theta$ due to a displacement of the membrane by one picometer. The $|\Delta\theta|$ has maximum at the same point as $\mathfrak{F}$, as expected.

its coupling to the cavity field $G_{\mathrm{opt}}(z_{\mathrm{m}})$ is maximized. We use a single-sided cavity, where the back-mirror is chosen to have as high reflectivity as available $r_2 \rightarrow 1$ in order to maximize the reflection. The front mirror reflectivity r_1 is adjusted to match the desired $\mathfrak{F}$. The $\mathfrak{F}(z_{\mathrm{m}})$ depends on the membrane position and has a minimum and a maximum at the opposing slopes of the cavity field which must be taken into account when choosing the desirable r_1. In general, we use simulations to determine the desired cavity finesse as discussed in Sec. 3.2, and from this determine the required r_1.

Figure. 6.10b shows the absolute phase change for the reflected field $\Delta\theta$ if the membrane is displaced by $x_{\mathrm{m}} = 1\,\mathrm{pm}$ at z_{m}, when the cavity is operated on resonance. The $\Delta\theta$ results in translation of the standing wave outside the cavity, and consequently couples to the atoms trapped in this standing wave. For small displacements of the membrane ($x_{\mathrm{m}} \ll \lambda$) placed on the slope of the cavity field, the membrane-atom coupling scales with linearly with $\mathfrak{F} \cdot x_{\mathrm{m}}$ according to Eqs. 6.12 and 6.25.

6.3 Cavity Construction and Vacuum System

6.3.1 Design Considerations

The MIM-cavity construction is required to be passively stable and vacuum compatible. Furthermore, one should be able to align the membrane plane with respect to the cavity axis and position the membrane inside the cavity with an axial precision $\ll \lambda$. To gain some experience with a MIM-cavity, we experimented with an existing symmetric InVar cavity of $\mathfrak{F} \sim 800$. The cavity length was 5 cm and the mirror radius $R = 30\,\mathrm{mm}$ resulting in a waist size of 50 µm on the membrane. The membrane was glued on top of a long lever arm which reached inside the cavity. The lever was on top of a vertical piezo stack relatively far from the cavity. We found the criteria for the mechanical stability of the membrane holder and the mirror holders to be stringent. The long cavity body suffered also from mechanical instabilities and its alignment was elaborate. Based on this experience, the most important design considerations of the MIM-cavity discussed in this Chapter are the following:

- A relatively short cavity: easy to align, rigid, not so sensitive to thermal drifts as a longer cavity. However, the cavity length should be long enough to allow us to scan the laser over a few FSR of the cavity. The mode-hop-free tuning range of the laser is $\sim 30\,\mathrm{GHz}$.
- Membrane positioning system should be rigidly attached to the cavity mount. The membrane should be easy to place at the center of the cavity and to align perpendicular to the cavity mode with high precision. Furthermore, the positioning system should allow to translate the membrane along the cavity axis.
- Cavity mount, or the membrane positioning system, should not support any low frequency modes or have resonances close to the membrane frequency.
- The complete MIM system (i.e., cavity holder, mirrorholders, membrane holder and positioning system) should be passively stable against thermal drifts.
- The cavity mirrors should be rigidly mounted on axis.
- The cavity mirrors and the membrane should be easily exchangeable if desired.
- The mirror radius and cavity length should be chosen such that the waist size of the cavity mode on the membrane is smaller than the lateral dimensions of the membrane, $w_0 \ll l_\mathrm{m}$ to avoid clipping of the cavity beam on the membrane frame.
- The cavity length should be tunable for more flexibility; for example to allow for the option of locking the cavity length to the laser frequency
- The complete MIM system should be placed inside a vacuum chamber at a pressure of $< 10^{-6}$ mbar such that the mechanical quality of the membrane

is not limited by air damping, and that possible air currents do not influence the stability of the cavity.

- The cavity-system should be supplied with vibration isolation.

In ref. [109] another type of a MIM-cavity design is described. This is helpful reference for understanding the MIM-system.

6.3.2 Cavity and Nanopositioning System

High passive stability of the MIM-system against thermal drifts is achieved by making all the required components out of material with low thermal expansion. Thermal expansion coefficients for possible options are shown in Tab. 6.1. A compound material InVar (Fe-Ni) is generally the choice for high-finesse $\left(\mathfrak{F} > 10^4\right)$ cavities where ultimate stability is required. InVar is however challenging to machine. We chose to machine the cavity holder from Titanium. The main reason for this is that the desired piezo-positioning system for the membrane alignment was available in Titanium (see later in text). The cavity body and the membrane alignment system should be machined out of the same material such that thermal drifts of the cavity length and the membrane position take place in common mode. This enhances the passive stability of the MIM-system.

Metal	**Coefficient** $\left[10^{-6}K^{-1}\right]$
Al	23.6
Fe	11.7
Pb	28.8
Steel	10-20
Titanium	8.6
InVar (Fe-Ni Alloy)	1.7 - 2.0

Table 6.1: Thermal expansion coefficients of selected metals [48].

Cavity Body

Figure 6.11a shows a sketch of our cavity design. The cavity mount accommodates two cylindrical holes for mirror-mounting that are vertically opposing each other. The mirrors (colored blue) are slided into the holes as shown in Fig. 6.11a, and sandwiched between thin plastic spacers for surface protection. A geometrically stable, vertical orientation is achieved by rigidly pressing the top mirror against the plastic spacer by a screw from the top (colored brown in the figure). The lower mirror is glued with a vacuum compatible ultra-violet curable glue (EPO-TEK `OG116-31`, single component, ultralow outgassing) on top of a high-load and vacuum compatible tubular piezo (`P-010.00H` from PI GmbH) and this system is sandwiched rigidly on its place by two screws and spacers, as shown in Fig. 6.11a. Note, that neither of the mirrors is screwed into the mount in order to avoid any

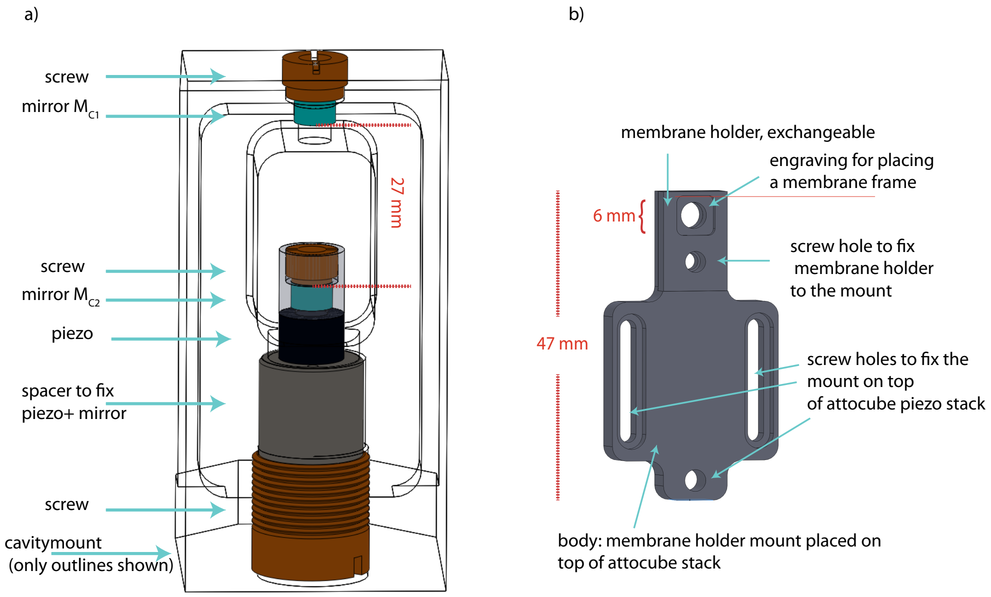

Figure 6.11: a) The optical cavity mount is machined of Titanium. Only the outlines of the mount are shown for clarity. The cavity mirrors are placed vertically and on-axis into cylindrical holes within the mount. The top mirror, M_{C1}, is fixed by pressing it against the mount by a screw. The lower mirror, M_{C2}, is glued on top of a high-voltage piezo and pressed against the mount from the top with a screw. The mirror-piezo system is fixed with an additional screw from below. The spacing between the mirrors is 27 mm. A plastic spacer is always used between mirror and metal interfaces to protect the mirror coating at the very edges of the mirrors, where the contact is formed. b) The membrane frame (5mm x 5mm) is glued or free standing on a Titanium holder groove of 6mm x 6mm in size. The membrane holder is fixed with a screw on top of a larger membrane mount. The membrane mounting system is fixed with screws on top of an attocube piezostack (see Fig. 6.12).

possible tilt of the mirrors with respect to each other[1]. The effective spacing between the mirrors is calibrated to be $L_{\mathrm{cav}} = 26.8\,\mathrm{mm}$ (see Section. 6.7). The piezo has a displacement range of $5\,\mu\mathrm{m}$, allowing us to easily scan the cavity length over several FSR, and a specified resonant frequency of 144 kHz. This resonant frequency is furthermore suppressed by the mass of the mirror on top, and is thus far enough from the membrane eigenfrequency. The tubular geometry of the piezo allows the transmittance of the laser beam out of the cavity. We use a high-voltage piezo controller from PI (`E-508.00`).

---

[1] Off-axis tilt of threaded mirrors in the first test cavity was problematic.

Membrane Mount

The membrane mounting system consists of two parts made of Titanium, as sketched in Fig. 6.11b. The membrane frame is placed or glued on a smaller holder (the top part of the complete membrane mount in the figure), which can be attached to a larger "membrane mount". Such a mounting design is advantageous, as the optomechanical properties of the membranes can be pre-characterized in another test chamber that also accommodates the small membrane holder (see Sec. 4.1). When a high quality membrane is found, it can be readily exchanged from the test setup to the science setup without the need to remove it from its holder, which would be detrimental for the mechanical quality factor. In the membrane characterization setup, the membrane holder is mounted vertically (see Fig. 4.2) and the membrane frame needs to be glued to the holder. On the other hand, in the science setup, the membrane mount is fixed horizontally by screws on top of a vertical piezo positioning stage as shown in Fig. 6.12. Thus, the membrane can also be placed onto the holder simply free-laying, supported by friction and gravity. Such a horizontal mounting seems to be advantageous for pertaining the high Q of the membrane as discussed in Sec. 4.1.

Membrane Positioning

The membrane is aligned perpendicular to the cavity axis with an Attocube systems' `FLEX` positioner system which allows fine and coarse positioning of the membrane around the center of the cavity. The attocube positioners are made of Titanium. We chose the Attocube positioning system having also the long term goals in mind: it can operate under high vacuum, but also in cryogenic temperatures; an important criteria for future experiments. Important for the stability of the MIM-system is that the piezo positioners are an integral part of the cavity mounting body. Figure 6.12 shows the MIM-system with the cavity mounting body and the integrated attocube stack.

Our positioning system is assembled of three separate stages for Θ (`ANGp101`), Φ (`ANGt101`), and Z (`ANPz101 attoFLEX`) alignment. The Θ (Φ) goniometer has a coarse positioning range of $6.6°(5.4°)$ with a minimum step size of $0.1\,\mathrm{m}°$. The vertical Z-stepper has a coarse positioning mode with a range of 5 mm, and a typical minimum step size of 50 nm. The vertical stepper has also a fine-positioning mode with a range of 5 μm and sub-nm resolution, allowing us to scan the membrane position along the slope of the cavity field.

Vacuum

The whole setup is enclosed in a high vacuum of 10^{-7} mbar as shown in Fig. 6.13. The vacuum system is assembled of standard CF components. The cavity chamber has two parallel AR-coated windows (Vacom, 780 nm) above and below the cavity for good optical access. The chamber is attached via a 4-way cross to the

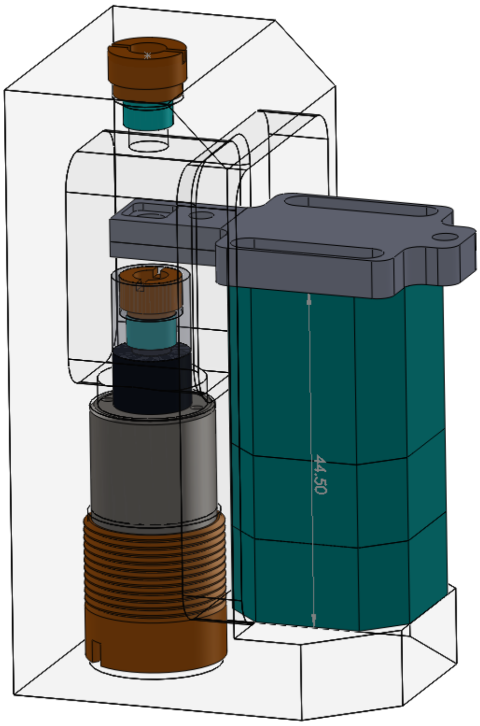

Figure 6.12: Cavity design. The membrane positioning system is integrated into the cavity mount. The membrane holder is placed on top of a 3-stage piezo stack (green), which allows to center and align the membrane with respect to the cavity axis. When exchanging the membrane, only the membrane mount is unscrewed from the piezo stack and slided out of the cavity, without the need to disassemble the setup further. The proportions of the sketch match the realization.

pumping system. A turbo-pumping stage consisting of a turbo and a roughing pump (Agilent `TPS compact`) is used for the initial pumping and an ion pump (StartCell `VacIon 40`) sustains the final pressure. The current in the ion pump is used to monitor the pressure in the chamber. The ion pump current values were calibrated with a separate gauge and found to be linear in pressure. The membrane can be exchanged relatively quickly by unmounting the top window-flange of the chamber. The turbo-pumping system reaches the final pressure over a night.

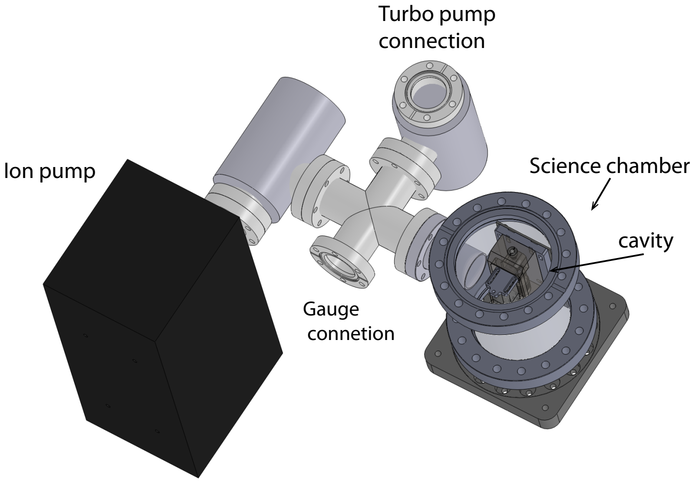

Figure 6.13: Vacuum assembly. The cavity is enclosed in a vacuum chamber that has two AR coated window flanges on the top (shown) and bottom for optical access. A vacuum of 10^{-7} mbar is sustained in the chamber by an ion pump.

Cavity Parameters

The condition for a stable cavity as a function of the mirror radius R and cavity length L_{cav} is given by Eq. 6.13. Furthermore, we match the cavity length to the mirror radius R in such a way that the resulting spotsize of the TEM$_{00}$-mode on the membrane

$$w_0 = \left(\frac{2R}{L_{\text{cav}}} - 1\right)^{1/4} \left(\frac{\lambda L_{\text{cav}}}{2\pi}\right)^{1/2} \tag{6.26}$$

is smaller than the lateral dimensions of the membrane for $\lambda = 780\,\text{nm}$. In general, a shorter cavity is easier to align and more stable, but on the other hand the FSR (Eq. 6.3) of the cavity scales as L_{cav}^{-1}. With these considerations in mind together with the restriction on the availability of high-quality-mirror substrates, we chose $L_{\text{cav}} = 27\,\text{mm}$ and $R = 30\,\text{mm}$. The resulting cavity waist on the membrane is 60 µm. Since our membrane is a $1.5\,\text{mm}^2$ square, clipping of the beam should not limit the finesse in any way, unless the beam is positioned significantly off-center of the membrane. The FSR of the cavity is 5.6 GHz. Our laser can be tuned mode-hop-free over more than 4 FSR.

The cavity mirrors are fabricated by Layertec Gmbh. The reflectivity of the output-coupling mirror M_{C2} is required to be as high as possible and at the same time have ultra low losses such that we can still monitor the signal transmitted through the cavity. According to specifications the back mirror M_{C2} has intensity reflectivity of R(0°, 780nm)$>$ 99.99% and transmission of T(0°, 780nm)$\sim$ 0.001%. The input-coupling (top) mirror M_{C1} is chosen to have reflectivity of R=96.0±0.25%. Extreme care is taken when handling the mirrors, especially the high-reflectivity mirror M_{C2}, as minute scattering or absorption

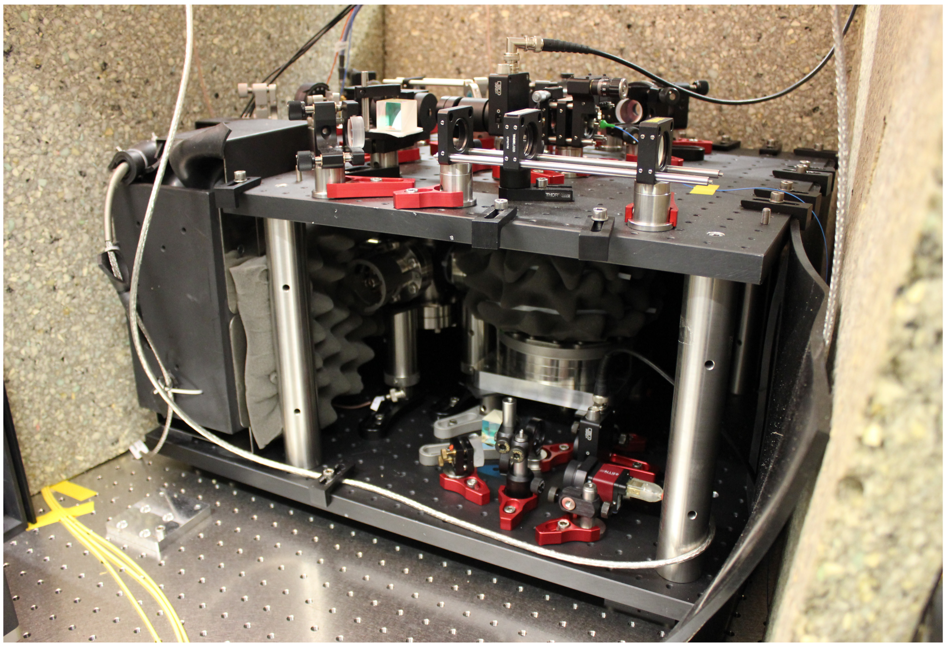

Figure 6.14: The MIM-chamber is placed between two optical breadboards. The optics on the higher breadboard are used to couple the laser beams into the cavity, and on the lower one to detect cavity transmission. One sees some pyramid foam in the picture that is used to prevent vibrations within the membrane chamber body. The whole setup is enclosed inside large sound isolation walls visible in the background (see Sec. 6.6).

loss can dominate over the mirror transmission. The mirror specifications result in an empty cavity finesse of $\gtrsim 150$. The finite penetration depth into the coatings adds roughly a micrometer into the effective cavity length, which is insignificant in our case.

6.4 MIM-Module

The MIM-vacuum chamber is placed between two optical breadboards, as shown in Fig. 6.14. The laser beams for the lattice and for locking and interrogating the cavity are guided in optical fibers from another optical table. The optics required to couple the laser beams into the vertical cavity reside on the optical breadboard above the chamber. The lower breadboard contains optics for imaging the cavity field modes and monitoring the transmission signal. The two-layer breadboard system is placed on vibration-isolating feet as discussed in Sec. 6.6. One can see some of the cone-shaped, foamy, sound isolation material next to the ion pump in Fig. 6.14 that in the end is used to surround the whole vacuum chamber. Furthermore, on the background one sees two of the sound isolation walls that enclose the whole MIM-setup during its operation.

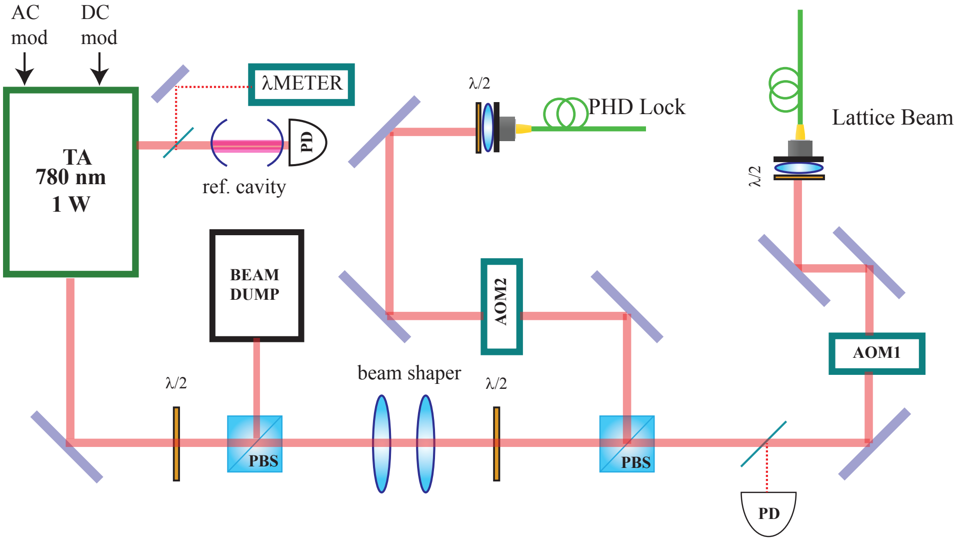

Figure 6.15: Laser system for cavity experiment. Both the laser beam for the PDH-Lock (see Sec. 6.5) and the lattice laser are provided by a diode-laser (DLPro) + TA system. The output of the TA is split by a polarizing beam splitter (PBS). The lattice beam path is fiber-coupled and guided to the atomic chamber as discussed in Sec. 5.1.2. It is intensity stabilized via the acousto-optic modulator (AOM1) and a PI feedback circuitry, as discussed in Sec. 5.1.2). The PDH beam is frequency shifted with AOM2 that is driven from the same source as the AOM1, coupled to a fiber and guided to the membrane module.

6.4.1 Laser System

The laser system that provides the lattice beam and another beam for the cavity interrogation via a Pound-Drever-Hall lock is shown schematically in Fig. 6.15. We use an integrated `DLPro` and a tapered amplifier system (Toptica `TA System`) operating around 780 nm (`LD-0780-0100-AR-1`). The output power of the TA is 1 W. The TA output beam is shaped with an elliptical lens pair and split with a $\lambda/2$-plate and a polarizing beam splitter (PBS) into the PDH locking path (cavity interrogation path) and the lattice laser path. A small part of the DLPro output is picked up for monitoring the wavelength (λ-METER) and for assuring that the laser is operating in a single mode (ref. cavity). The laser has a DC modulation input to modulate the grating of the DLPro (DC mod), which is used for locking the laser to the cavity (see Sec. 6.5). Additionally the laser has an AC mod input for fast modulation of the laser current. The AC mod can be configured (via the Bias tee) to respond up to 100 MHz and it has a measured modulation depth of maximally $\beta = 0.2$ corresponding to 1 % of power in the sidebands. The AC mod is useful for generating a sideband onto the laser at the membrane frequency, which allows us to calibrate the membrane amplitude.

The lattice beam path is built similar to the free-space setup using the existing module, as described in Sec. 5.1. The acousto-optic modulator AOM1 is used for the intensity stabilization of the lattice laser (Sec. 5.1.2). In order to avoid a beat note between the lattice beam and the PDH beam in the cavity, we add a second AOM into the PDH path, AOM2. The two AOMs are driven at the same frequency with a common rf-source. Both of the beam paths are fiber coupled and guided to a separate optical table, where the MOT and cavity vacuum chambers are built close to each other. The pick-up photodiode (PD) in Fig. 6.15 is used to monitor the backreflection of the lattice beam into the fiber during the alignment process. The lattice beam waist is chosen to be $w_0 = 350\,\mu\text{m}$ at the center of the MOT (same as before) and the lattice alignment follows the procedure described in Sec. 5.1.

6.4.2 Mode Matching of the MIM-Cavity

A successful procedure for aligning the MIM cavity starts by first mode matching the PDH (or alternatively the lattice) beam to the *empty* cavity. Thereafter, the membrane is carefully placed onto its holder and aligned with respect to the cavity mode. A perfectly aligned membrane should not distort the spatial mode. Next, the mode matching of the PDH beam to the empty cavity is described, and subsequently the alignment procedure of the membrane with respect to the cavity mode.

Mode Matching of the Empty Cavity

The goal is to mode match the laser beam to the fundamental TEM_{00} mode of the cavity. The cavity mirror substrates are plano-concave and act like diverging lenses, which means the input beam needs some effective beam waist w_{eff} at z_{eff} such that after going through the diverging lens its beam waist and focus coincide with the ones of the Gaussian mode of the cavity. If we take into account the refraction of the beam path due to the refractive index of the mirrors, n_{mirror}, the incoming Gaussian beam should have beam waist [136]

$$w_{0,\text{eff}} = \sqrt{\frac{\lambda}{\pi} \frac{R\sqrt{L_{\text{cav}}\left(2R - L_{\text{cav}}\right)}}{2R + L_{\text{cav}}\left(n_{\text{mirror}}^2 - 1\right)}}, \tag{6.27}$$

at the location

$$z_{0,\text{eff}} = \frac{L_{\text{cav}}}{2} - \frac{n_{\text{mirror}} L R}{2R - L_{\text{cav}}\left(n_{\text{mirror}}^2 - 1\right)}, \tag{6.28}$$

with respect to the cavity center. For our cavity with a length $L_{\text{cav}} = 26$ mm, $R = 30\,\text{mm}$, index of refraction for the fused silica substrate $n_{\text{mirror}} = 1.46$, and wavelength $\lambda = 780\,\text{nm}$, we obtain $w_{0,\text{eff}} = 50\,\mu\text{m}$ and $z_{0,\text{eff}} = -0.4\,\text{mm}$. The cavity mode waist is $w_0 = 60\,\mu\text{m}$. For perfect mode matching, the beam incident on the cavity must be in a single spatial mode. All other contributions

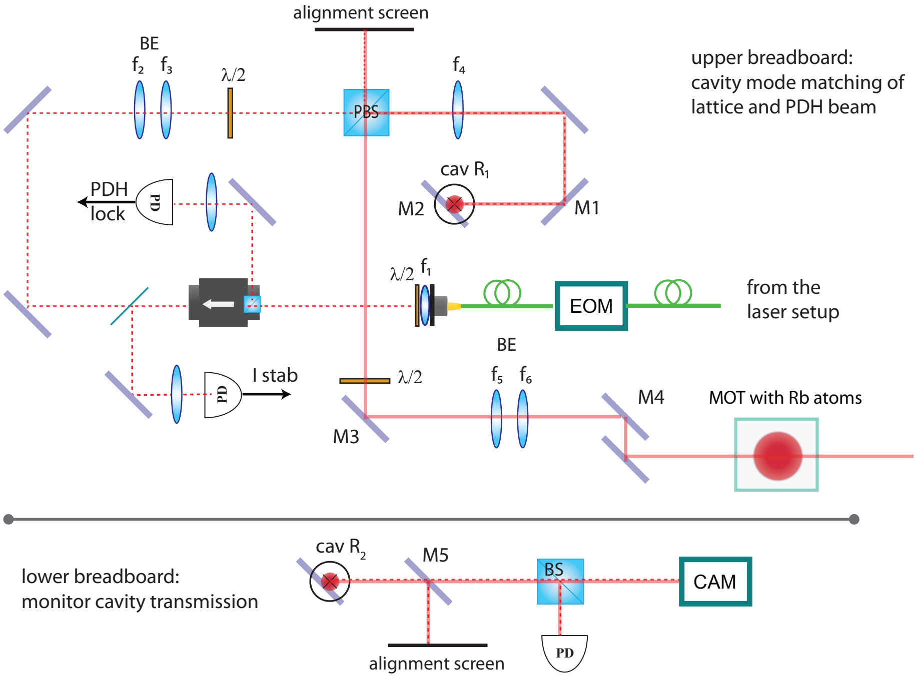

Figure 6.16: Upper part of the figure: The optics on the upper breadboard for mode matching both the PDH and the lattice beams into the cavity. The orthogonally polarized lattice beam and PDH beam are overlapped at the PBS, where they are adjusted to have the same, optimized beam waist, and focused to the cavity with a mode matching lens f_4. The mirrors M1 and M2 are used to couple the beams into the cavity. Lower part of the figure: Optics for monitoring the cavity transmission.

of the input beam will be reflected and lead to an imperfect mode matching and distortion of the lattice.

Both the lattice and the PDH beam are fiber coupled (Fig. 6.15) and therefore have a clean spatial mode before they are coupled into the cavity. Figure 6.16 shows a schematic of the mode matching optics that is clamped on the upper optical breadboard above the MIM-chamber. For mode matching both of the beams are collimated, adjusted in size (beam expander, BE) and finally focused by a properly chosen mode-matching lens such that the beams satisfy the Eqs. 6.27 and 6.28. For example, for the PDH path we collimate the fiber output (Thorlabs `PM780`) with $f_1 = 11\,\mathrm{mm}$ lens (`C220TME-B`, 0.25NA) resulting in a beam diameter of $D = 2.1\,\mathrm{mm}$. This beam is expanded by a factor of two with a BE consisting of $f_2 = -100\,\mathrm{mm}$ and $f_3 = 200\,\mathrm{mm}$ lenses, and finally focused down to the cavity with a $f_4 = 400\,\mathrm{mm}$ lens. The lenses used for the lattice beam path are chosen similarly and adjusted to match the lattice beam waist. An image of the laser setup on the top plate above the membrane vacuum chamber is shown in Fig. 6.17.

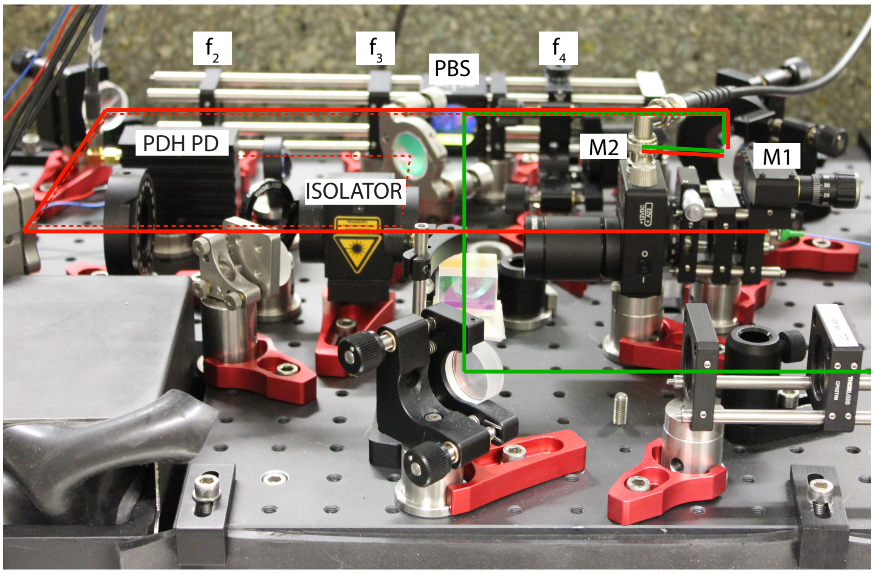

Figure 6.17: A photograph of the upper, optical breadboard, showing the Pound-Drever-Hall beam path (red and reflection dashed red) and the lattice beam path (green) that is overlapped at the PBS with the PDH. The mode-matching lenses are mounted on a rail-system to keep them on-axis while they are translated for optimal mode matching.

Finally, the wave vector of the incoming laser beam is made parallel to the cavity axis by adjusting the angular alignment of the planar mirrors M1 and M2. While adjusting M1 and M2, we simultaneously scan the cavity length with the high voltage piezo (Fig. 6.11) and monitor the cavity transmission at the lower optical breadboard below the MIM chamber (Fig. 6.16, bottom part). In the initial stage of the alignment, the cavity transmission is low, and the transmitted beam is likely off-axis with respect to the cavity. It is useful to monitor the transmitted light on a large fluorescent screen with an IR viewer (flipmirror M5). As some clear cavity modes appear on the fluorescent screen, we measure the cavity transmission on a photodiode (PD, Thorlabs, `DET10A/M`) and image the mode functions on a CCD camera (AlliedVision, `GUPPY`). The imaging is necessary during the alignment, especially when the membrane is placed inside the cavity, to assure that the cavity mode is the desired TEM_{00} one. To optimize the mode matching one seeks to eliminate all undesired higher-order modes by “beam walking” with M1 and M2. Simultaneously it is helpful to monitor the reflection from the cavity which should overlap with the incoming beam, and have the same size. The reflected beam is adjusted in an iterative manner by translating f_4.

Coarse Alignment of the MIM

After the mode matching to the empty cavity is optimized, the membrane is placed onto its holder. For this, the top breadboard is unmounted and the top flange of the vacuum chamber is opened (Fig. 6.13). During the unmounting and subsequent re-mounting of the top breadboard, the robust optical beam path does not experience significant misalignment. However, the membrane will be tilted with respect to the cavity mode which will distort the transmittance of the laser beam through the cavity. The first goal is to align the membrane with respect to the cavity mode.

A coarse alignment is done by tilting the membrane with the Θ and Φ piezo-stages (Fig. 6.12) until a transmission signal is detected. Thereafter one can carefully tweak the mirrors M1 and M2 to compensate for any spatial translation of the beam path with respect to the cavity axis. The membrane angle is simultaneously altered, until the transmittance of the fundamental mode is maximized. Figure 6.18 shows the theoretical intensity distributions for the spatial modes of a cavity (upper row) and the corresponding imaged MIM-cavity modes (lower row). A well aligned membrane does not distort the cavity modes compared to the experiments with empty cavity.

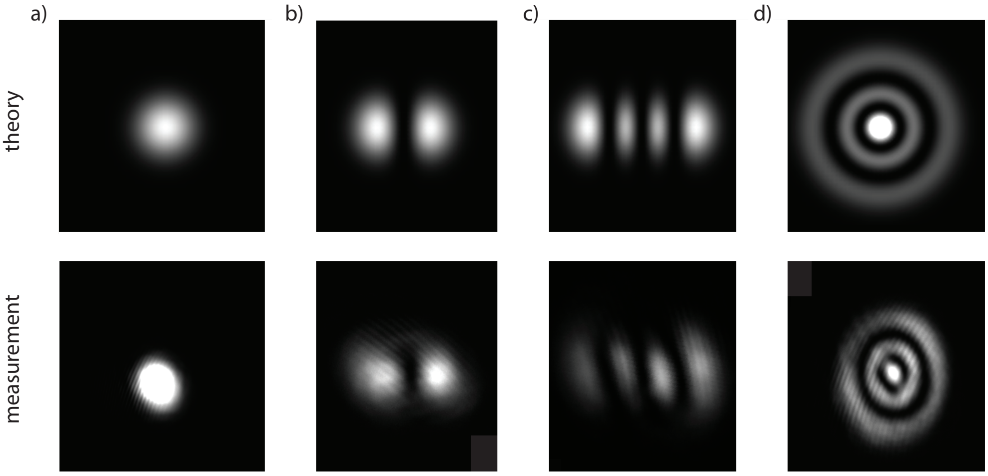

Figure 6.18: Spatial modes of the cavity. Top row shows the theoretical intensity profiles for Hermite-Gaussian modes a) (l=0, m=0), b) (l=1, m=0) c) (l=3, m=0). An example of a Laguerre-Gaussian mode is shown in d) for (p=2, m=0). The lower row shows the experimentally imaged cavity transmission for the corresponding modes when the membrane is properly aligned with respect to the cavity. In order to obtain the images, the cavity length is scanned and the axial in-coupling of the laser beam is slightly tilted. This measurement was done with a MIM-cavity that had $r_1 = r_2$ ($\mathfrak{F} = 80$). The behavior with an asymmetric set of mirrors ($r_1 < r_2$) is observed to be the same.

Fine Alignment of the MIM

The fine adjustment of the membrane tilt is done by monitoring the resonance frequency of the cavity as a function of the membrane position. For a perfectly aligned cavity, we would expect the cavity modes to shift according to Eq. 6.24. The cavity modes are measured by translating the membrane through a distance of $> \lambda/2$ along the cavity axis in small steps $\ll \lambda$, while monitoring the cavity resonance. In practice, after a single membrane step, we scan the laser over several FSR of the cavity and monitor the transmission signal of the cavity on a photodiode (PD in the bottom part of Fig. 6.16).

The alignment goal is to suppress any sort of mode anti-crossings that occur when the membrane is tilted with respect to the cavity axis [102]. Figure 6.19a shows an example of the recorded cavity spectra when the membrane has some angular tilt. By aligning the membrane with the angular Θ and Φ positioners, one can completely suppress the mode crossings. In this case the plane of the membrane is parallel to the wave fronts. Furthermore, the axial positioning

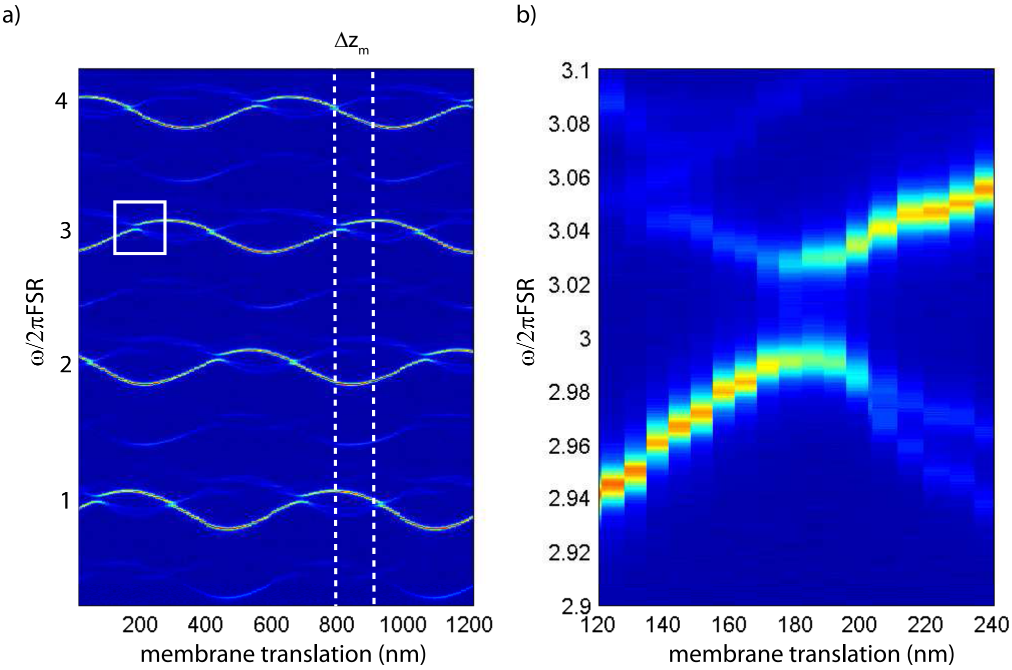

Figure 6.19: a) An example of a cavity spectrum as a function of the membrane position translation along the cavity axis, when the membrane has some angular tilt with respect to the cavity axis and is not positioned in the middle of the cavity. The angular tilt of the membrane leads to mode anti-crossings visible in the zoom of the white box in b). An offset in the cavity resonances separated by $2FSR$ with respect to membrane position, Δz_{m}, indicates that the membrane is not in the middle of the cavity. Note that the cavity used for this measurement was symmetric (i.e., $r_1 = r_2$), thus the variation in the finesse is absent (see Sec. 6.7.2).

of the membrane with respect to the cavity center can be done by comparing the cavity resonances separated by two FSRs. For a perfectly aligned cavity, the optomechanical coupling of these subsequent modes should be identical with respect to the membrane position. An offset Δz_{m}between the maximas of the two modes in Fig. 6.19a implies that the membrane is not in the middle of the cavity axis. An example of a well aligned cavity is shown in Fig. 6.26.

Mode Matching Further Beams into the Cavity

After one beam is mode-matched to the MIM cavity, any other beam can simply be adjusted in size and overlapped at the polarizing beam splitter (PBS) (Fig. 6.16) with the mode-matched PDH beam. The lattice beam is aligned with mirrors M3 and M4 by simultaneously overlapping it with the PDH beam on the alignment screen and in front of mirror M1. We have measured the mode-matching for a symmetric MIM-cavity ($\mathfrak{F} = 78$) as the fraction of the power incident on the cavity versus the transmitted power when the cavity is operated on-resonance. From this we estimate the mode-matching to be about 80% for both the lattice and the PDH beam. For our asymmetric science cavity the mode matching is difficult to determine in transmission, as the backmirror has very low transmittance. We expect to obtain similar mode matching efficiency for the asymmetric cavity than for the symmetric one, as only the back-mirror of the cavity is changed to another one which has the same radius of curvature. The optical beam path is kept the same. One quantitative way to estimate the mode matching, is to measure the optomechanical cavity cooling performance of the MIM-system for a given input power and compare this to theory. An example of such a cooling measurement and corresponding mode-matching determination is presented later in Sec. 6.7.3 and Fig. 6.33.

6.5 Pound-Drever-Hall Lock and the Membrane Read-Out

The stability of the MIM-cavity and the laser is required to be a lot better than the cavity resonance width $\Delta\omega \sim 2\pi \cdot 40\,\mathrm{MHz}$. If the cavity becomes detuned with respect to the lattice laser frequency, i.e., $\Delta_{\mathrm{c}} \neq 0$, the intensity inside the cavity will drop and the atom-membrane coupling is reduced. In addition, for $\Delta_{\mathrm{c}} \neq 0$ the optomechanical radiation pressure effects will start to take place. Blue-detuning ($\Delta_{\mathrm{c}} > 0$) will lead to amplification, and possible instability of the membrane motion, and red-detuning ($\Delta_{\mathrm{c}} < 0$) will result in cooling [137]. In Section 6.7.3 and in Fig. 6.31 we estimate the cooling performance for our cavity, and find that the cooling is largest, when $\Delta_{\mathrm{c}}/\Delta\omega \approx 0.2$. A detuning of $\Delta_{\mathrm{c}}/\Delta\omega = 0.2$ corresponds to cavity length change of 5 nm. A thermal drift of a 26 mm long cavity by 0.6 nm would require a temperature change of $\Delta T = 3\,\mathrm{mK}$ when the cavity is made of Titanium. The temperature in the laboratory is stabilized via a PI feedback system to 20 ± 0.1 Celsius. Consequently, a lock is needed to counteract long-term thermal drifts.

We lock the laser to the cavity using the Pound-Drever-Hall (PDH) technique [138]. This technique is simultaneously also used to detect the membrane motion, which acts to detune the cavity and is hence visible in the error signal of the PDH. The PDH technique relies on the interference of frequency sidebands with the main carrier laser to generate an error-signal for cavity stabilization. We use an electro-optic phase modulator (EOM) to create frequency sidebands at Ω with a modulation depth of β. The phase-modulated laser field can be written as:

$$E_{\text{inc}} = E_0 e^{i\omega t + i\beta \sin \Omega t}. \tag{6.29}$$

This expression is more obvious when it is expanded in terms of the Bessel functions. For the relevant case of small β we get

$$E_{\text{inc}} = E_0 e^{i\omega t} \left(J_0\left(\beta\right) + \sum_{n=1}^{\infty} J_n\left(\beta\right) e^{in\Omega t} + \sum_{n=1}^{\infty} \left(-1\right)^n J_n\left(\beta\right) e^{-in\Omega t} \right), \tag{6.30}$$

where the Bessel functions are defined as

$$J_a(x) = \sum_{n=1}^{\infty} \frac{(-1)^n}{n!(n+a)!} (\frac{x}{2})^{2n+a}. \tag{6.31}$$

The relative power in the carrier P_{c}, and in the sidebands P_{s}, is defined by the modulation depth β. If $P_0 = |E_0|^2$, then $P_{\text{c}} = {J_0}^2(\beta) P_0$, and the power in each first order sideband is $P_{\text{s}} = {J_1}^2(\beta) P_0$. When the modulation depth is small, the carrier and the first order sidebands carry almost all of the power; $P_{\text{c}} + 2P_{\text{s}} \approx P_0$.

The light reflected from the cavity can be expressed in terms of the reflection coefficient r_{cav} given by Eq. 6.7 as

$$E_{\text{ref}} = E_0 \left[r_{\text{cav}}\left(\omega\right) J_0\left(\omega\right) e^{i\omega t} + r_{\text{cav}}\left(\omega + \Omega\right) J_1 e^{i(\omega+\Omega)} - r_{\text{cav}}\left(\omega - \Omega\right) J_1\left(\beta\right) e^{i(\omega-\Omega)t} \right]. \tag{6.32}$$

The power of the reflected light field is measured on a photodiode, $P_{\text{ref}} = |E_{\text{ref}}|^2$

$$\begin{aligned} P_{\text{ref}} = {} & P_{\text{c}} \left| r_{\text{cav}}\left(\omega\right) \right|^2 + P_{\text{s}} \{ \left| r_{\text{cav}}\left(\omega + \Omega\right) \right|^2 + \left| r_{\text{cav}}(\omega - \Omega) \right|^2 \} + \\ & + 2\sqrt{P_{\text{c}} P_{\text{s}}} \{ \text{Re}\left[r_{\text{cav}}\left(\omega\right) r^*_{\text{cav}}\left(\omega + \Omega\right) - r^*_{\text{cav}}\left(\omega\right) r_{\text{cav}}\left(\omega - \Omega\right) \right] \cos \Omega t + \\ & + \text{Im}\left[r_{\text{cav}}\left(\omega\right) r^*_{\text{cav}}\left(\omega + \Omega\right) - r^*_{\text{cav}}\left(\omega\right) r_{\text{cav}}\left(\omega - \Omega\right) \right] \sin \Omega t \} + \\ & + \mathcal{O}\left(2\omega\right). \end{aligned} \tag{6.33}$$

The first term is a DC offset on the photodiode, but the second and third terms oscillating at Ω carry direct information about the phase of the reflected cavity field. In our experiment, we tune Ω to be a lot larger than $\Delta\omega$, such that the sidebands do not enter the cavity and interact with the membrane. In this regime only the carrier acquires a phase inside the cavity, and the expression

$$r_{\text{cav}}\left(\omega\right) r^*_{\text{cav}}\left(\omega + \Omega\right) - r^*_{\text{cav}}\left(\omega\right) r_{\text{cav}}\left(\omega - \Omega\right) \approx -i2\,\text{Im}\{ r_{\text{cav}}\left(\omega\right) \}, \tag{6.34}$$

is purely imaginary. Consequently the cos-term in Eq. 6.33 becomes negligible. These terms can be isolated from the PD signal with a mixer, and we arrive at an expression for the error signal

$$\epsilon_{\mathrm{PDH}} = -2\sqrt{P_{\mathrm{c}}P_{\mathrm{s}}}\,\mathrm{Im}\{r_{\mathrm{cav}}(\omega)\,r^{*}_{\mathrm{cav}}(\omega+\Omega) - r^{*}_{\mathrm{cav}}(\omega)\,r_{\mathrm{cav}}(\omega-\Omega)\}. \tag{6.35}$$

Figure 6.20 shows the PDH error signal of the single-sided MIM-cavity for the TEM_{00} mode. When the laser is resonant with the cavity, the error signal is zero, but has a maximal slope. From Eq. 6.35 we see that the error signal scales $\propto \sqrt{P_{\mathrm{c}}P_{\mathrm{s}}}$. In our lock, we want to minimize P_{c} to avoid optomechanical interaction between the membrane and the read-out beam, and at the same time maximize P_{s} to get higher signal-to-noise ratio as ϵ_{PDH} is used also for extracting the membrane motion. We choose the power level to be less than 1 mW, out of which 50% is carried in the sidebands.

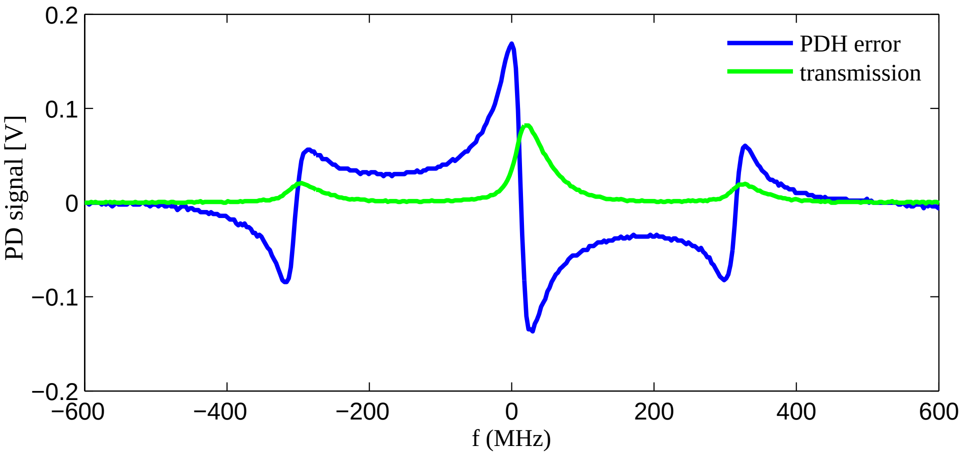

Figure 6.20: The PDH error signal of the MIM-cavity when the membrane is aligned to the fundamental mode (blue). The fundamental mode and the PDH-sidebands are visible in the cavity transmission (green). Information about the sideband frequency is used to calibrate the frequency axis. The limited bandwidth of the photodiode broadens the transmission response in this measurement.

A schematic of our PDH lock is shown in Fig. 6.21, and the corresponding component details are listed in Tab. 6.2. We use a fiber EOM to generate sidebands onto the laser. A voltage controlled oscillator (VCO) creates a rf-modulation signal at $\Omega = 350\,\mathrm{MHz}$. The rf-signal is split: one part of it drives the EOM and the other part goes to the mixer. An isolator is placed between the rf source and the EOM. The EOM has a half-wave voltage of only 2.3 V (at 1 GHz) and we set half of the power in the laser beam into the sidebands for optimal operation. Initially, we used a frequency generator to drive the EOM (SRS, 8 GHz) but it turned out that the generator has a higher background noise level than the VCO by

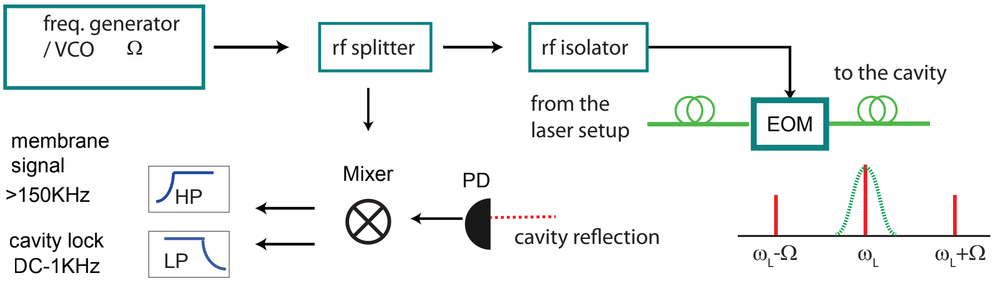

Figure 6.21: The Pound-Drever-Hall setup for locking the laser to the cavity. A voltage controlled oscillator (VCO) is used to generate sidebands onto the laser via an EOM. The VCO signal is split and part of it goes via an isolator to the EOM. A photodetector (PD) is used to detect the cavity reflection, which is mixed down with the split part of the VCO signal. The low-passed part of the signal is used for feedback via the piezo of the laser and the high-passed part is used for membrane read-out.

EOM	EOSPACE, `PM-0K5-10-PFA-780-UL`
VCO	MiniCircuits, `ZOS-400+`, 7dBm
rf splitter	MiniCircuits, `ZFSC-2-2+`
isolator	WENTEQ MICROWAVE, 250-500 MHz
rf- photodiode	MenloSystems `FPD310-FV`, 1 dB at 1 GHz
mixer	MiniCircuits, `ZFM-3+`

Table 6.2: The PDH electronics.

20 dB at $\Omega \sim 350$ MHz. The cavity reflection is measured with a high-sensitivity rf-photodiode (PD). The PD-signal is mixed down, and a low pass filter at the output of the mixer is used to isolate the low-frequency signal which serves as an input to a PI-servo-amplifier. We compensate for possible phase delays between the VCO signal and the PD signal by adjusting the Ω at the VCO. Alternatively one could add a phase-shifter into the PDH-circuitry. Finally, the correction signal acts on the piezo grating of the laser (via the "DC mod"-input in Fig. 6.15) locking the laser to the cavity frequency. The bandwidth of the PDH-feedback is limited by the piezo-response to 1 kHz.

Instead of modulating the laser light with an EOM, one can alternatively use the AC-modulation input of the TA, shown in Fig. 6.15, to produce the sidebands onto the laser via current modulation. The AC mod has a measured modulation depth of maximally $\beta = 0.2$ corresponding to 1 % of power in the sidebands. The PDH-locking via the AC mod resulted in a clean and stable lock-signal. However, we chose to use the EOM in the end as it provides more power in the sidebands and flexibility to tune the rf modulation frequency over one cavity FSR for additional purposes. We also experimented in locking the cavity to the laser, but observed the lock to be less stable that way as continuous correction displacements of the end mirror seemed to excite vibrations in the cavity body.

Read-Out of Membrane Motion

The membrane motion is extracted from the high-passed part ($> 150\,\mathrm{kHz}$) of the mixer signal, as shown in Fig. 6.21, and measured on a spectrum analyzer (Rohde and Schwarz, `FSVR30`). An example of the Brownian motion of a membrane in room temperature is shown in Fig. 6.22. In this measurement, the cavity is locked on resonance $\Delta_\mathrm{c} = 0$. The power spectral density is calibrated by assuming the area under the noise peak to be proportional to $\langle x^2 \rangle_\mathrm{th}$, according to Eq. 2.19. The calibration results in sensitivity on the order of $10^{-14}\,\mathrm{m}/\sqrt{\mathrm{Hz}}$. The resolution bandwidth of the spectrum analyzer is 1 Hz in this measurement. The width of the membrane noise peak is less than 1 Hz, implying $Q = \omega_\mathrm{m}/\gamma_\mathrm{m} > 3 \cdot 10^5$. In an auxiliary ringdown measurement we have indeed measured $Q = 3 \cdot 10^6$ for this membrane.

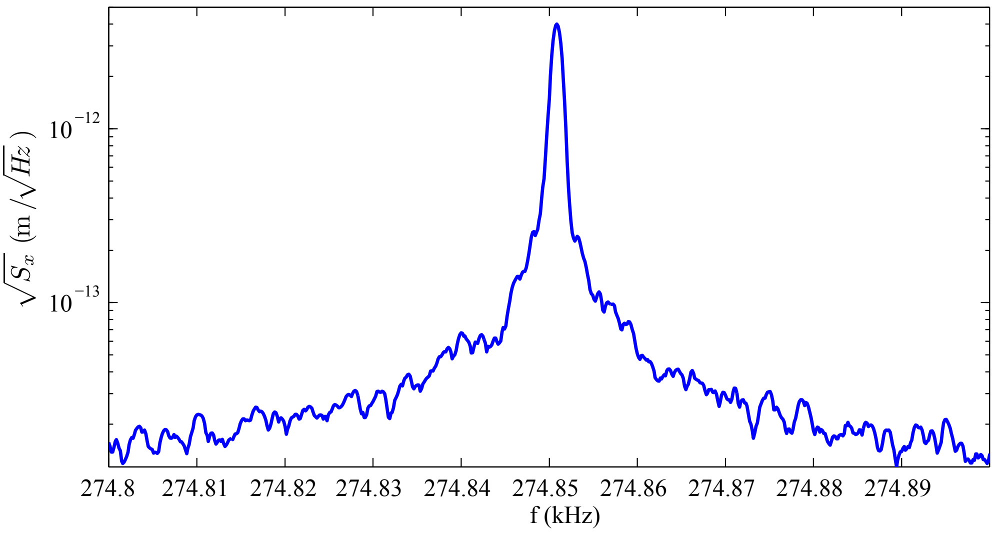

Figure 6.22: Membrane signal at the spectrum analyzer as derived from the PDH-lock signal. The power in the read-out beam was 1 mW of out which 50 % was in the sidebands. The sensitivity is $10^{-14}\,\mathrm{m}/\sqrt{\mathrm{Hz}}$. The resolution bandwidth of the spectrum analyzer is 1 Hz and the width of the noise peak is not resolved. This measurement was recorded with a symmetric cavity of $\mathfrak{F} = 78$.

Positioning the Membrane to the Slope of the Cavity Field

In order to position the membrane on the slope, half between the cavity field maxima and minima, we lock the laser to the cavity, and while changing the membrane position in small steps we monitor the signal to noise ratio (SNR) at the spectrum analyzer. The SNR is maximized when the membrane is on the middle of the cavity field slope, where the finesse is maximum (see Fig. 6.30).

6.6 Vibration Isolation

The MIM-module shown in Fig. 6.14 is built on top of a floating optical table (NewPort, `ST-UT2`). Without any vibration shield around the MIM-system, the seismic and acoustic noise ($< 1\,\mathrm{kHz}$) in the lab is strong enough to detune the MIM-cavity from on-resonance to off-resonance. The vibrations are larger in amplitude than the PDH locking capture range. This makes the on-resonance operation of the MIM-cavity difficult. On the other hand, the locking of an empty cavity is straightforward. Consequently, the vibrations couple to the MIM-cavity via the membrane holder and the piezo-positioning stack (see Fig. 6.12). The optomechanical coupling of the membrane to the cavity is measured to be $G_{\mathrm{opt}}^{\mathrm{max}} = 2\pi \cdot 11.9\,\mathrm{MHz/nm}$, when the membrane is placed on the slope of the cavity field (Sec. 6.7). If the cavity linewidth is $\Delta\omega \approx 2\pi \cdot 30\,\mathrm{MHz}$, a shift of the membrane position by more than a few nanometers is sufficient to detune the cavity out of resonance.

The vibrations in the MIM-setup are characterized with an accelerometer. By analyzing the accelerometer data together with the optical cavity transmission and reflection signal, one can distinguish electric noise in the setup from mechanical noise. Figure 6.23a shows a measurement of the acoustic vibrations on the lab floor and on the optical table. The optical table isolates the vibrations in the ground by more than 10 dB at frequencies above 10 Hz. The optical table has a characteristic resonance at 350 Hz. The distinct peaks in the spectra of the optical table are due to acoustic vibrations in the air, which excite the table. Even though the optical table is isolated from the ground, the airborne vibrations are transferred via the table to the MIM-setup, when it is placed directly on top of the optical table. Figure 6.23b shows the vibrations on the optical table (purple), and on the lower (green) and upper (black) breadboards of the MIM-module. In addition to being in direct contact with the lower bread-board, the acoustic waves in the air excite the MIM-chamber directly from all the sides. One can often identify and suppress most of the airborne noise sources. For example, the peak at 80 Hz in Fig. 6.23b is due to a fan of an oscilloscope close by and the peak around 180 Hz is due to a flow box located 6 m away from the setup. The strongest noise sources in the laboratory are shielded with sound absorbing materials when possible (described below).

For a proper vibration isolation we decouple the MIM-system from the optical table, suppress resonances within the vacuum chamber body, and shield the setup from sound-waves in the air. The MIM-setup is isolated from the vibrations on the optical table by placing the complete two-layer MIM-system on vibration damps. We use elastometric cone-shaped elements from NewPort (`M-ND50-A`). It is important to match the optimum load on each elastomer for optimal vibration isolation. The mass of the complete MIM-module (as in shown in the photograph in Fig. 6.14) is measured to be 69 kg, and the module is balanced on top of 6 damping feets.

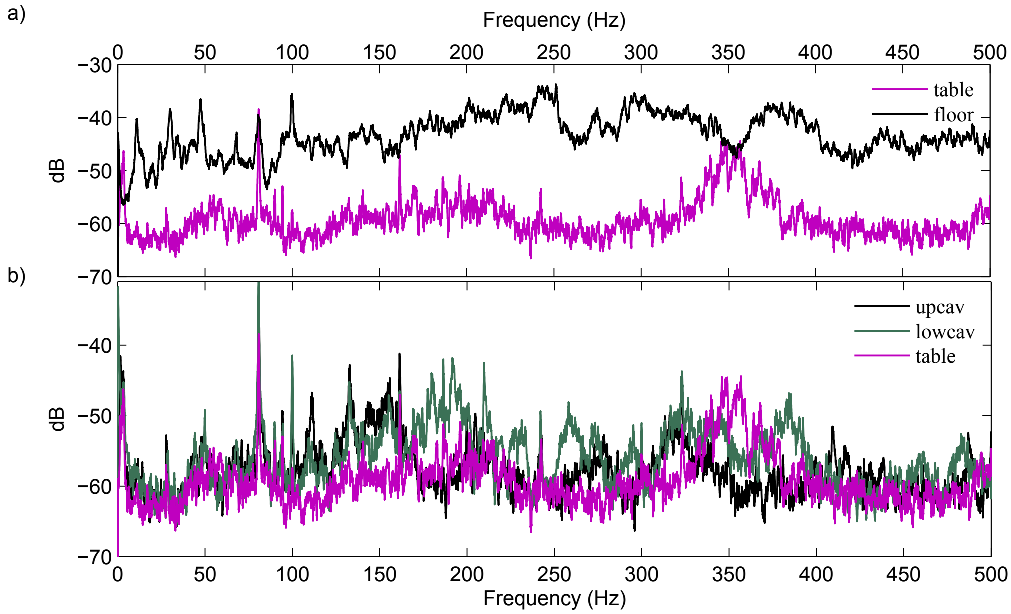

Figure 6.23: Compilation of the accelerometer data for a non-isolated MIM-setup showing the airborne vibrations in the optical table and the MIM-system. a) Black and purple traces correspond to the acceleration atop the laboratory floor and optical table. Above 500 Hz no significant peaks were visible on this particular measurement. The broad resonance around 350 Hz is characteristic to the table. b) Comparison of the low-frequency (< 200 Hz) vibrations in the MIM-system with respect to the optical table. The vibrations in the air excite the optical table (purple) and the MIM-chamber which via direct contact couple to the lower optical breadboard (green). The vibrations are less on the upper optical breadboard (back) than on the lower breadboard.

Heavy, elastic rubber is in general the optimal choice for damping resonances in bodies. We use Sorbothane sheets from Thorlabs (`SB12B`, 6.35 mm thick) to damp the resonances in the vacuum chamber body. These sheets absorbs up to 95.5% of impact energy and then reform to their original shape. The sheets are cut into shape and clamped with cable binders tightly around the vacuum chamber body. Furthermore all the aluminum posts (standard 1 inch optical posts) that support the vacuum chamber from below as well as the ion pump on the lower breadboard have the Sorbothane sheets in-between any metallic contact-surfaces.

The free space between the two optical breadboards is filled with profiled plastic foam (AixFOAM, Convoluted Foam, `SH0021`-Polyether anthracite). Part of this foam is seen in Fig. 6.14. The foam is used to hinder reflections of any sound waves that may leak into the system. Next, the Sorbothane sheets are used to close all the vertical sides between the two optical breadboards of the MIM-module. They are clamped at the edge of the higher optical breadboard (the clamps are shown at the edges of the top breadboard in Figure 6.14) and hang vertically around the setup. These are also advantageous to reduce the background level due to room light on the photodiode that monitors the cavity transmission. In the end, the whole MIM-module is enclosed inside a sound-isolation box consisting of 4 side walls and one top wall. The walls are made of a 40 mm heavy foam layer (AixFOAM, `SH 0071`) which is laminated with a 2.5 mm layer of heavy foil, as shown in Fig. 6.24. In addition to its sound isolation properties, the heavy foam is also an excellent temperature insulator having a heat conductivity of 0.033 W/mK. Two of the sound isolating walls are visible in the background of Fig.6.14.

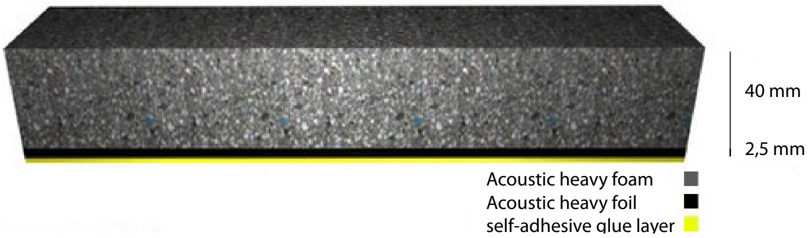

Figure 6.24: The vibration isolation walls built around the setup consist of a layer of heavy foam that is laminated with a heavy foil for optimal absorbance and damping of low frequencies. The heavy foam also acts as a passive thermal insulator.

Figure 6.25 shows a measured accelerometer spectra on the lab floor (black), on the optical table (purple), and inside the vibration isolation box (green). In this measurement, the setup is on another optical table as during the measurement in Fig. 6.23. During this measurement the large vibration isolation box is also open from the top. Yet, the vibrations inside the vacuum chamber body are considerably less from what is measured on the table. The most sensitive measure for the vibrations inside the cavity is the locking signal itself. When the vibration isolation was installed, the locking of the cavity to a desired point even in the presence of heavy noise sources in the background (e.g., turbo vacuum pump 1 m away) was a simple task.

Importantly, the MIM-cavity system is attached directly to the vacuum chamber wall by screws, as shown in Fig. 6.13. This direct contact couples vibrations in the cavity body to the membrane holder. In future designs, it would be advantageous to apply vibration isolation inside the vacuum and isolate the MIM-system from the vacuum chamber. This would most likely simplify the isolation requirements outside the vacuum chamber.

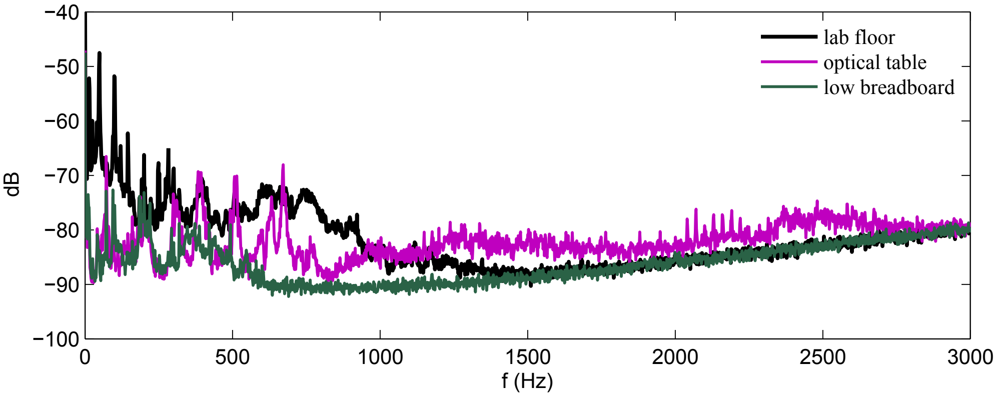

Figure 6.25: The noise characteristics on the lab floor (black), on the optical table (purple), and inside the vibration isolation box (green). The vibration isolation box was open from the top during this measurement.

6.7 MIM Characterization Measurements

In this Section I discuss optomechanical characteristic of the asymmetric MIM-setup. The calibration of the cavity parameters and optomechanical coupling are presented as well as the determination of the membrane reflectivity and thickness. In addition, preliminary optomechanical cavity cooling measurements are shown which give qualitative understanding of the role of the cavity cooling in our system. Such measurements are also useful for estimates of the mode-matching of the lattice laser into the cavity.

6.7.1 Optomechanical Coupling

An example of the optical cavity spectra as a function of the membrane position for a well-aligned, single-sided MIM-cavity is shown in Fig. 6.26. The measurement is done by recording the transmitted intensity as a function of membrane position and laser frequency. The membrane is translated along the cavity axis with the atto-cube piezo positioners and the wavelength scanning is done using the piezo-grating of the laser. The transmitted intensity for the single-sided cavity is only fraction of that for a symmetric cavity, thus the signal to noise is lower than that in the measurement in Fig. 6.19. Furthermore, in this figure the transmission is plotted on a logarithmic color scale to emphasize the higher order modes present in the system.

The analyzed measurement result in Figure 6.26 contains a number of important features that are required to calibrate the cavity finesse and the optomechanical coupling. These are explained below.

Calibration of the FSR and the Membrane Position

The frequency axis of the cavity transmission data can be calibrated to units of FSR since the TEM_{00} modes associated with either one of the subcavities are separated by 2FSR (see Fig. 6.6). For absolute calibration of the FSR, we use the PDH sidebands that are visible symmetrically around each transmission resonance at $\Omega = \pm 364\,\mathrm{MHz}$. In this way, we calibrate the FSR of the cavity to be $5.6\,\mathrm{GHz}$, corresponding to an effective cavity length of $L_{\mathrm{cav}} = 26.8\,\mathrm{mm}$. As an example, a zoom of a measured vertical cavity transmittance slice is shown in Fig. 6.27. The finesse can be calculated by fitting a Lorentzian distribution to the transmission lines.

Importantly, we observe that the laser piezo-response is non-linear and the non-linearity is more pronounced towards the edges of the scanning range. If high precision calibration of the frequency axis is required, information on the higher order modes and their relative separation can be used in addition. When the input power of the laser is not too low, these higher order transverse TEM_{mn} modes (with still small m and n), which are close in frequency to the driven TEM_{00} mode, are also populated and can be detected. The fine-precision calibration

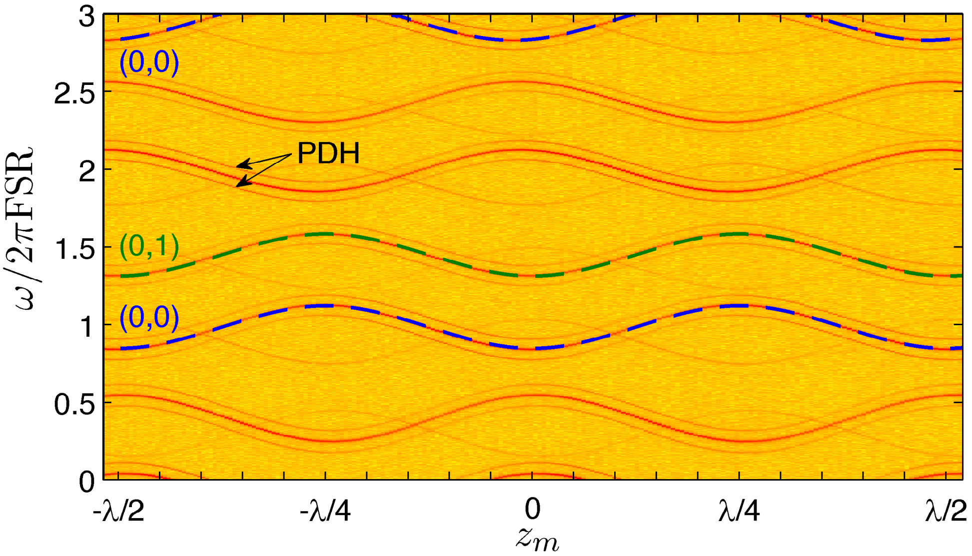

Figure 6.26: Cavity resonance spectra as a function of the membrane position z_m shown on a logarithmic color scale. The wavelength of the laser is expressed in terms of the cavity FSR, which is calibrated from the PDH sidebands that are visible symmetrically at $\Omega = \pm 364\,\mathrm{MHz}$ around each resonance. The green and blues dashed lines are theoretical curves for the TEM_{00} and TEM_{01}. The theory curves assume a membrane of thickness 42 nm, n=1.98, and reflectivity of $r_\mathrm{m} = 0.4163$.

using the higher order modes is discussed further below with a specific example, where the variation in the finesse is extracted over the whole scanning range as a function of membrane position.

We also observe the membrane positioners to have small non-linearities depending on the drive settings. The horizontal axis can be calibrated using Eq. 6.24.

Coupling Strength G_opt and Membrane Reflectivity

The optomechanical coupling strength depends on the membrane reflectivity r_m according to Eq. 6.24. We can estimate r_m, and consequently also the thickness of the membrane (Eq. 6.16), by fitting Eq. 6.24 to the experimental data. Using the mass density of the stoichiometric SiN membrane, we can then also compute the mass (see. 4.1). The green curve in Fig. 6.26 is a theoretical calculation for the TEM_{00} mode according to Eq. 6.24 that assumes $n_\mathrm{m} = 1.98$ and $d_\mathrm{m} = 42\,\mathrm{nm}$, resulting in $|r_\mathrm{m}| = 0.4163$. When the membrane is placed on the slope of the cavity field, the optomechanical coupling is maximum $G_\mathrm{opt}^\mathrm{max}/2\pi = 11.9\,\mathrm{MHz/nm}$. The blue curve in Fig. 6.26 is the theoretically calculated TEM_{01} mode, which is separated by $2\pi \cdot 2.6\,\mathrm{GHz}$ from the TEM_{00}.

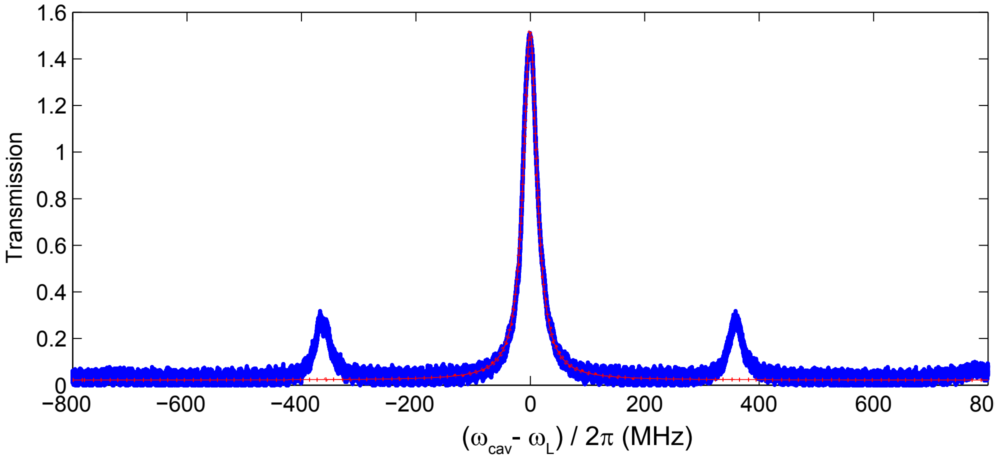

Figure 6.27: Cavity transmission signal measured by sweeping the laser frequency, while the laser has a carrier and two phase modulation sidebands. The sidebands are used as a ruler to calibrate the FSR. The cavity finesse is determined from the width of the transmission peak. For this measurement $\mathfrak{F}\,(z_\mathrm{m}) \sim 180$.

6.7.2 Cavity Finesse

The cavity finesse is a function of the membrane position, as discussed in Sec. 6.2.2 and in Fig. 6.10. To quantitatively analyze this, we perform a fine-resolution measurement of the cavity spectra. The measurement result is shown in Figure 6.28. The figure shows 4 TEM_{00} modes marked by dashed lines, corresponding to consecutive values of q in Eq. 6.15. Note that modes with even and odd q experience an opposite shift as function of membrane position (see also Fig. 6.6). In addition, higher order TEM_{lm} modes are visible, where each higher value of $l + m$ is shifted by an additional $\frac{\Delta\xi}{\pi}$FSR, as expected from equation 6.15.

Figure 6.29 shows a vertical slice through Fig. 6.28 and Lorentzian fits to each mode. Modes with the same q are grouped by color, and the modes are labeled by $(l+m)$. To correct for the non-linearity of the laser frequency sweep, we use these fitted peak positions to calibrate the frequency axis to units of FSR with a third-order polynomial. We fit the coefficients of the polynomial, while in addition having $\Delta\xi$, a global frequency offset, and an unknown shift between modes with even and odd q as free parameters. From the fit we obtain $\Delta\xi/\pi = 0.456\,\mathrm{FSR}$.

After the vertical frequency axis is calibrated, the finesse is calculated by extracting the width $\Delta\omega$ of the transmission peaks as function of z_m and using Eq. 6.10. The results for the TEM_{00} modes are shown in Fig. 6.30. The green data points have slightly lower values compared to the turquoise ones around $z_\mathrm{m} = \lambda/2$. This is probably due the fact that the frequency calibration is least accurate at this edge of the piezo scanning range. The theory developed in Sec. 6.2.2, accurately describes the measured variation in the finesse, as shown by the red curve in Fig. 6.30.

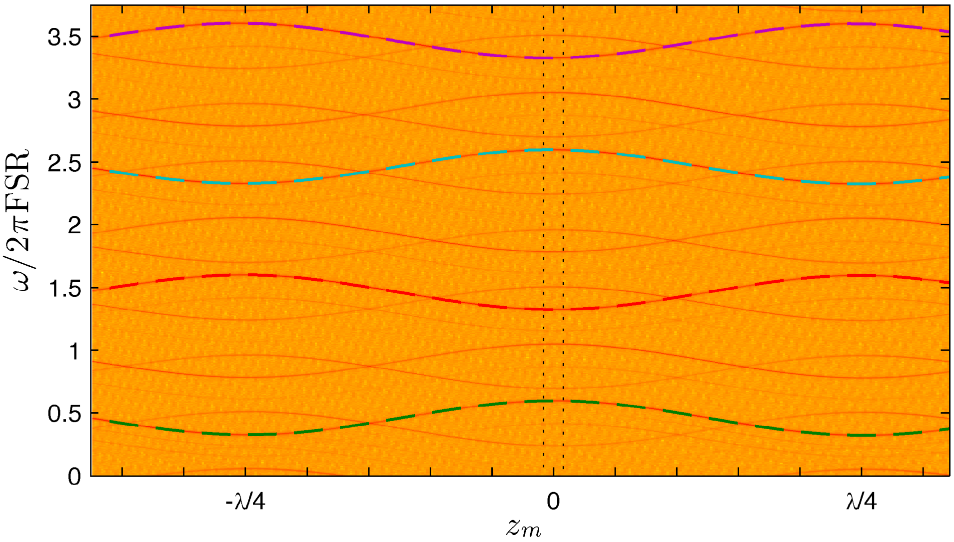

Figure 6.28: The cavity spectral data used to determine the variation in the finesse as a function of z_m. The colored dashed lines show the peak position of the cavity transmission along which the finesse is extracted in Fig. 6.30. A vertical slice averaged over the region between black dotted lines is shown in figure 6.29.

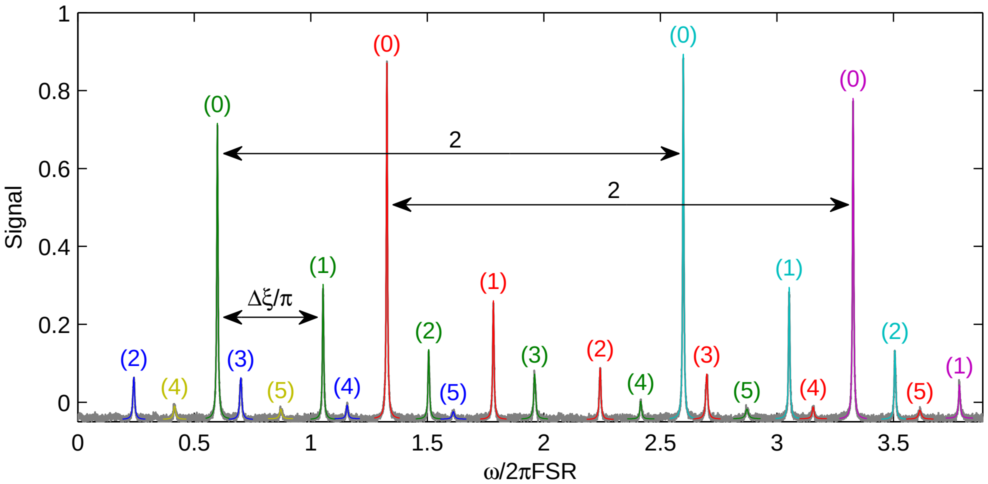

Figure 6.29: Average of 8 vertical slices of the transmission spectra in Fig. 6.28. Modes with the same mode number q are shown with the same color. For each value of q, different TEM$_{lm}$ modes can be seen, labeled by $(l+m)$. For identical $l+m$, the spacing between mode q, l, m and $q+2, l, m$ is constrained to $2\,$FSR.

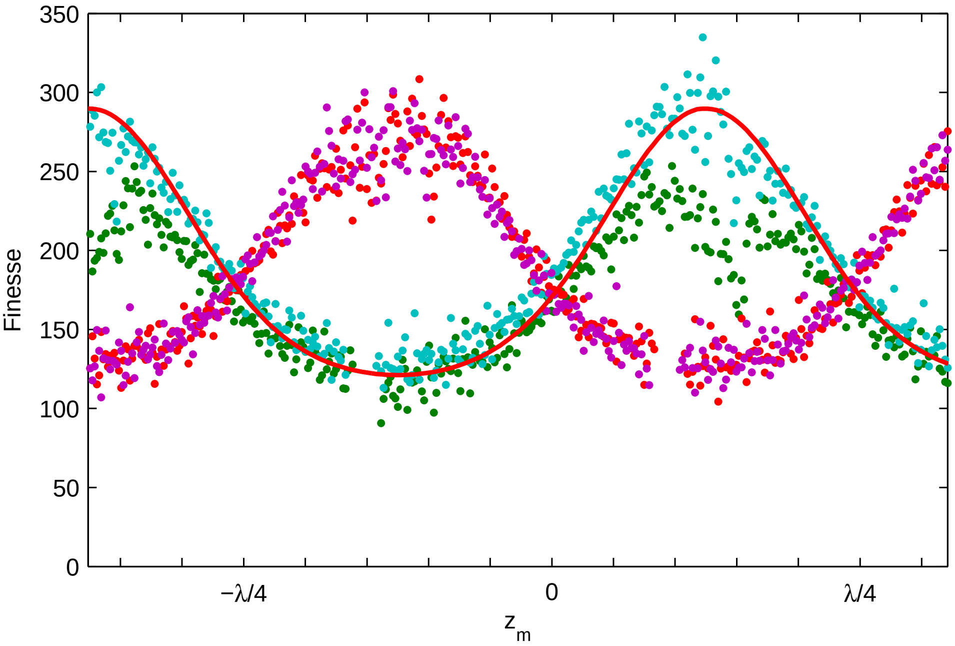

Figure 6.30: Cavity finesse as a function of membrane position for the TEM_{00}-modes in Fig. 6.28 (marked with respective colors). The red line is a simulation using the experimental MIM-parameters $r_2 = 0.99995$, $r_1 = 0.9818$, $\mathrm{Im}\,(n_\mathrm{m}) = 1 \cdot 10^{-5}$, $d_\mathrm{m} = 42\,\mathrm{nm}$, and $r_\mathrm{m} = 0.4163$.

6.7.3 Optomechanical Cavity Cooling

In the atom-membrane experiment we operate the cavity at the moment slightly red-detuned ($\Delta_\mathrm{c} \sim -2\pi \cdot 2\,\mathrm{MHz}$). We have observed that if we set the locking point to $\Delta_\mathrm{c} = 0$, it tends to drift slightly to the blue $\Delta_\mathrm{c} > 0$. In this case and for high lattice laser power incident on the cavity, we observe amplification and mechanical instability of the membrane motion. The operation of the lattice and PDH laser at $\Delta_\mathrm{c} < 0$ leads to optomechanical cavity cooling of the membrane.

It is important to be able to distinguish between the optomechanical cavity cooling of the membrane and the sympathetic cooling induced by the atoms. The optomechanical damping rate is given by [139]

$$\Gamma_\mathrm{opt} = G_\mathrm{opt}^2 \left[S_\mathrm{nn}\left(\omega_\mathrm{m}\right) - S_\mathrm{nn}\left(-\omega_\mathrm{m}\right)\right] x_\mathrm{zp}^2, \tag{6.36}$$

where the noise power spectrum is defined as

$$S_\mathrm{nn}\left(\omega\right) = \bar{n}_\mathrm{cav} \frac{\Delta\omega}{\left(\omega + \Delta_\mathrm{c}\right)^2 + \left(\Delta\omega/2\right)^2}. \tag{6.37}$$

The mean photon number in the cavity, $\bar{n}_\mathrm{cav}$, is proportional to the intracavity power, and thus to the power incident on the first cavity mirror P_inc as

$$\bar{n}_\mathrm{cav} = \frac{4P_\mathrm{inc}\eta}{\hbar\omega_\mathrm{L}\Delta\omega} \frac{1}{1 + \left(\frac{2\Delta_\mathrm{c}}{\Delta\omega}\right)^2}, \tag{6.38}$$

where η is the mode-matching efficiency of the P_inc to the TEM_{00} cavity mode. In the unresolved sideband regime ($\Delta\omega \gg \omega_\mathrm{m}$) the damping rate can be written as

$$\Gamma_\mathrm{opt} = G_\mathrm{opt}^2 x_\mathrm{zp}^2 \bar{n}_\mathrm{cav}\omega_\mathrm{m} \frac{-4\Delta_\mathrm{c}\Delta\omega}{\left(\frac{\Delta\omega^2}{4} + \Delta_\mathrm{c}^2\right)^2}. \tag{6.39}$$

In the absence of additional noise-sources the optomechanical cooling results in a mean steady-state phonon number

$$\bar{n}_\mathrm{ss} = \frac{\Gamma_\mathrm{opt}\bar{n}_0 + \gamma_m \bar{n}_\mathrm{th}}{\Gamma_\mathrm{opt} + \gamma_\mathrm{m}}, \tag{6.40}$$

where the minimum occupancy without mechanical damping is

$$\bar{n}_0 = -\frac{\left(\omega_\mathrm{m} + \Delta_\mathrm{c}\right)^2 + \left(\Delta\omega/2\right)^2}{4\omega_\mathrm{m}\Delta_\mathrm{c}}. \tag{6.41}$$

The optomechanical cooling is associated with a frequency shift of the mechanical mode. In the unresolved sideband regime this is given by [11]

$$\delta\omega_\mathrm{m}\left(\Delta_\mathrm{c}\right) = G_\mathrm{opt}^2 \bar{n}_\mathrm{cav} \frac{2\Delta_\mathrm{c}}{\Delta\omega^2/4 + \Delta_\mathrm{c}^2} x_\mathrm{zp}^2. \tag{6.42}$$

Figure 6.31a shows the optomechanical cavity-cooling in a MIM-setup as a function of P_{inc} for our parameter regime, when the membrane is placed on the middle of the slope of the cavity field and G_{opt} is given by Eq. 6.25. The optomechanical damping rate scales linearly with the intracavity power of the driving laser P_{inc} and is largest, when $\Delta_{\mathrm{c}}/\Delta\omega \approx -0.2$. The final phonon occupation will depend on the Q of the membrane as shown in Fig. 6.31b. The SiN membranes have demonstrated to have $Q > 10^7$ even in room temperature [104], and the Q has been observed to increase by an order of magnitude, when the bath temperature of the membrane is decreased from room temperature to 300 mK ($Q(300\,\mathrm{mK}) > 10^7$) [100].

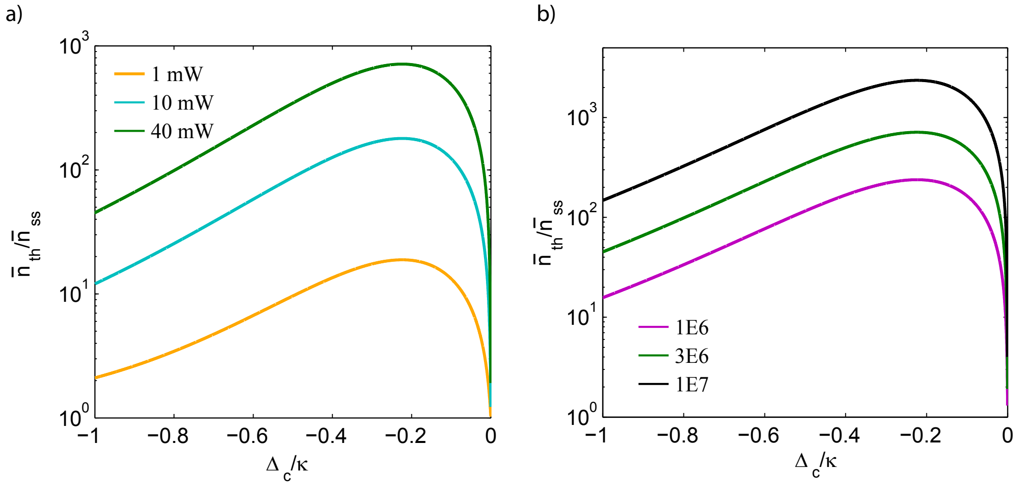

Figure 6.31: Optomechanical cavity cooling in the MIM-system. The parameters assumed in the calculation are $\Delta\omega = 2\pi{\cdot}60\,\mathrm{MHz}$, $\omega_{\mathrm{m}} = 2\pi{\cdot}274\,\mathrm{kHz}$, $r_{\mathrm{m}} = 0.416$, $M = 70\,\mathrm{ng}$, and $T_{\mathrm{bath}} = 293\,\mathrm{K}$. The plots show the cooling factor $\bar{n}_{\mathrm{th}}/\bar{n}_{\mathrm{ss}}$, when a) $Q = 3\cdot 10^6$ and $P_{\mathrm{inc}}\eta = (1, 10, 40)\,\mathrm{mW}$; and when b) $P_{\mathrm{inc}}\eta = 40\,\mathrm{mW}$ and $Q = 1\cdot 10^6, 3\cdot 10^6, 1\cdot 10^7$.

Preliminary Cavity Cooling Characteristics

We have performed a set of initial characterization measurements on the optomechanical cooling of the membrane inside the cavity. In particular, we observe optomechanical cooling and associated frequency shift of the membrane mode as a function of Δ_{c} and P_{inc}.

In order to measure cavity-optomechanical effects, we position the membrane on the slope of the cavity field. For this membrane position, we measure $G_{\mathrm{opt}} = 2\pi\cdot 9.2\,\mathrm{MHz/nm}$, $\Delta\omega \approx 2\pi\cdot 40\,\mathrm{MHz}$ (corresponding to $\mathfrak{F}(x_{\mathrm{m}}) = 140$). For cooling we use the lattice laser beam without the atoms being loaded into the lattice. We measure the membrane spectrum for two different cavity detunings $\Delta_{\mathrm{c}} = -2\pi\cdot 4\,\mathrm{MHz}$ and $\Delta_{\mathrm{c}} = -2\pi\cdot 6\,\mathrm{MHz}$ and for different power levels of the lattice beam, P. The power in the PDH beam is 0.2 mW out of which 0.14 mW is in the carrier. Thus, the total input power incident on the cavity is $P_{\text{inc}} = P + 0.14\,\text{mW}$. Figure 6.32 shows an example of the amplitude spectral density of the membrane for a few different power levels P_{inc}, when $\Delta_{\text{c}} = -2\pi \cdot 6\,\text{MHz}$. Both an increase in the optomechanical damping and an optomechanical frequency shift are observable as P_{inc} increases.

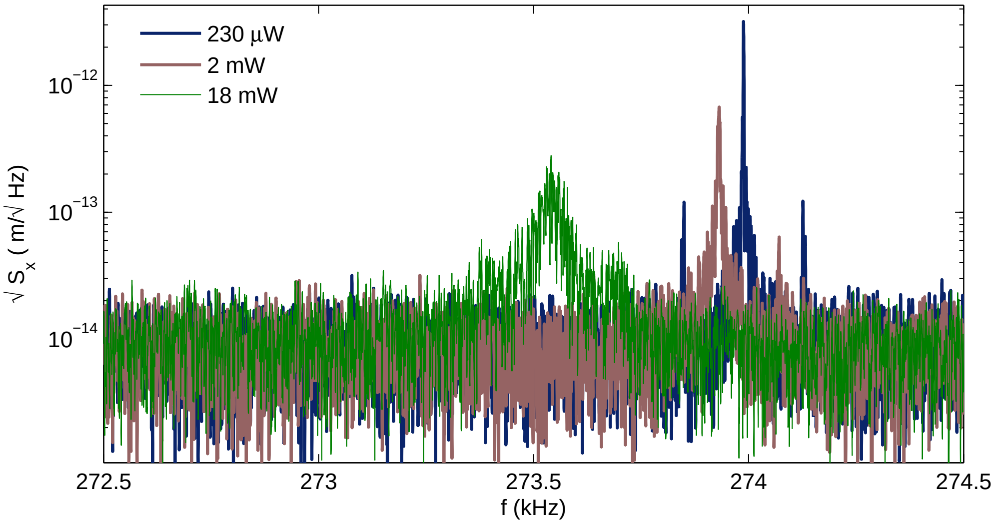

Figure 6.32: The amplitude spectrum of the membrane for red-detuned laser drive of $\Delta_{\text{c}} \sim -2\pi \cdot 6\,\text{MHz}$, and for input power P_{inc} of 230 µW, 2 mW, and 18 mW. The resolution bandwidth is 1 Hz. The amplitude spectral density is calibrated by assuming the noise peak at $P_{\text{inc}} = 230\,\mu\text{W}$ to correspond to the thermal motion of the membrane. The calibration obtained in Fig. 6.33 would anticipate a higher sensitivity level by a factor of ~ 2.

In order to extract the steady-state temperature T_{m} of the membrane mode for each power level, we determine the area under the noise peak, which is directly proportional to T_{m}, and compare this with the theory. The relative standard error for each data point is $< 1\,\%$. Figure 6.33 shows the resulting temperatures which are averaged over 20 experimental realizations, and the corresponding theory curves. We observe optomechanical cooling in our system by a factor of 30. The cooling is observed to be limited to $\sim 10\,\text{K}$ around P_{inc} of a few mW. We contribute this effect to laser noise. The effect of laser noise on the steady-state phonon occupation number has been theoretically discussed in Ref. [140]. We are currently working on quantitative analysis of the laser noise in our system.

In addition to optical damping, we also measure the associated optomechanical shift in the membrane frequency, as shown in Fig. 6.34. We observe a deterministic decrease in the membrane eigenfrequency with laser power. The thermal frequency shift of the membrane is negligible compared to the optomechanical shift according to the measurements in Sec. 4.2. The small discrepancy between

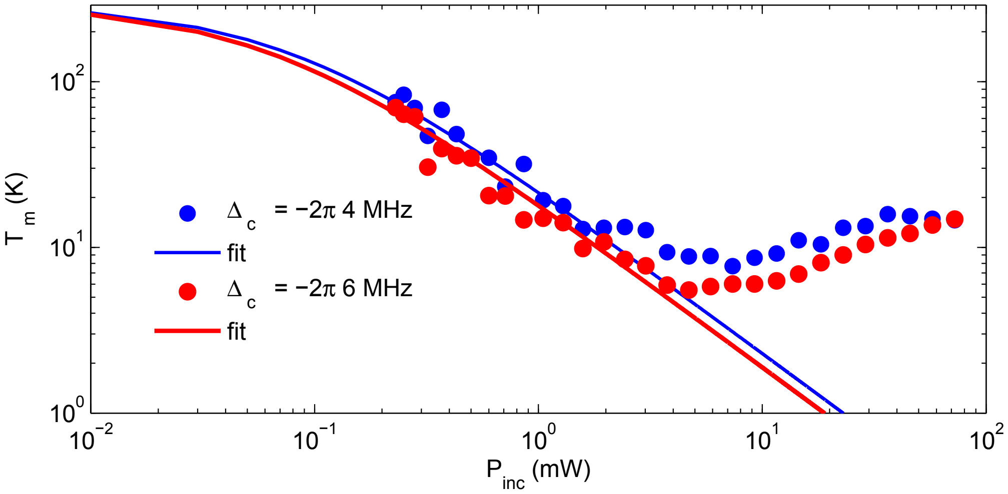

Figure 6.33: Preliminary measurement on optomechanical cavity cooling of the membrane for two different detunings $\Delta_\mathrm{c} = -2\pi \cdot 4\,\mathrm{MHz}$ and $\Delta_\mathrm{c} = -2\pi \cdot 6\,\mathrm{MHz}$. The theoretical curves are calculated using of Eq. 6.41. The theory assumes the measured values of $Q = 3.4 \cdot 10^6$, $\omega_\mathrm{m} = 2\pi \cdot 274\,\mathrm{kHz}$, $M = 70\,\mathrm{ng}$, and $T_\mathrm{bath} = 293\,\mathrm{K}$; and we obtain mode-matching of $\eta = 0.41$.

the measured and theoretical frequency suggests an offset in the calibration of Δ_c. In addition, the value of $\omega_\mathrm{m}\,(P_\mathrm{inc} = 0)$ is an estimate.

In conclusion, we observe optomechanical cavity cooling in our system, as well as an associated frequency shift. Such measurements can be used to determine the mode-matching η into the cavity. This is an essential factor as the atom-membrane coupling is reduced by η. Furthermore, this analysis shows that in the atom-membrane experiment, the optomechanical damping due to the lattice beam should be taken into account.

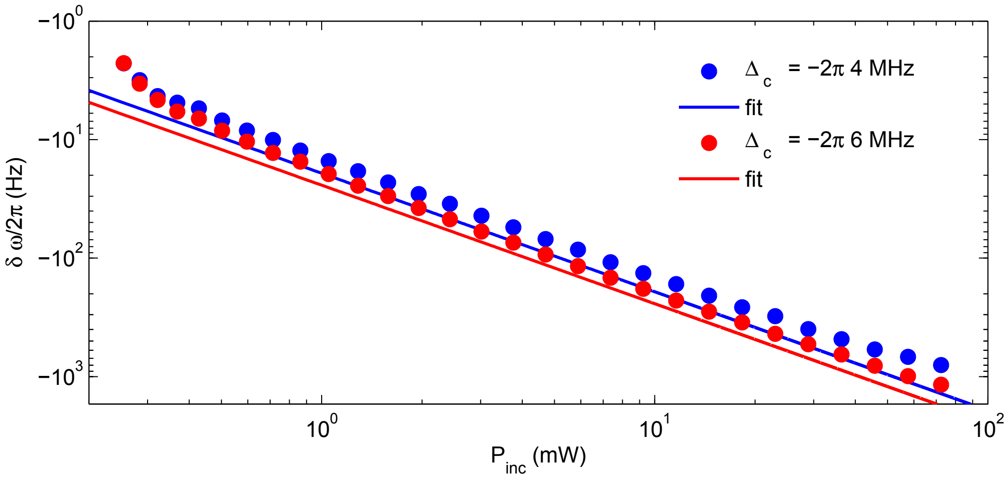

Figure 6.34: The shift of the membrane eigenfrequency with incident power for two different Δ_c. The theoretical curves are calculated using Eq. 6.42 and they assume the same parameters as in Fig. 6.33.

6.8 Outlook: Preliminary Measurement on Atom - Membrane Coupling

As an outlook to on-going work, we present preliminary measurements that demonstrate sympathetic cooling of the membrane via the atoms using the new MIM-setup. To measure the effect of the atoms onto the membrane, we excite the membrane motion from room temperature by 20 dB and perform a ringdown measurement. The excitation is done by modulating the intensity of the PDH beam at ω_{m}. During the ringdown we monitor the power spectral density of the membrane motion as a function of time and relate the area under the membrane noise peak to the effective mode temperature of the membrane. In order to distinguish the effect of the atoms onto the membrane from the optomechanical cavity cooling described in the previous Section, we perform a reference measurement with the lattice beam, but do not load the atoms into the lattice.

The preliminary sympathetic cooling result is shown in Fig. 6.35. After 100 ms of membrane ringdown the lattice laser power P is increased from 5.7 mW to the resonant power of 20 mW. The green curve shows sympathetic damping of the membrane when the atoms are continuously MOT-cooled in the lattice. The blue curve shows a similar measurement, where after an initial MOT cooling phase, the stronger molasses cooling is switched on, as indicated in the figure. During the molasses phase the atoms are colder, but over time they drift out of the lattice region. In both measurements, laser cooling is switched off after 0.6 s. The orange curve shows a reference measurement performed with the same lattice power (20 mW) in the absence of the atoms. By comparing the reference

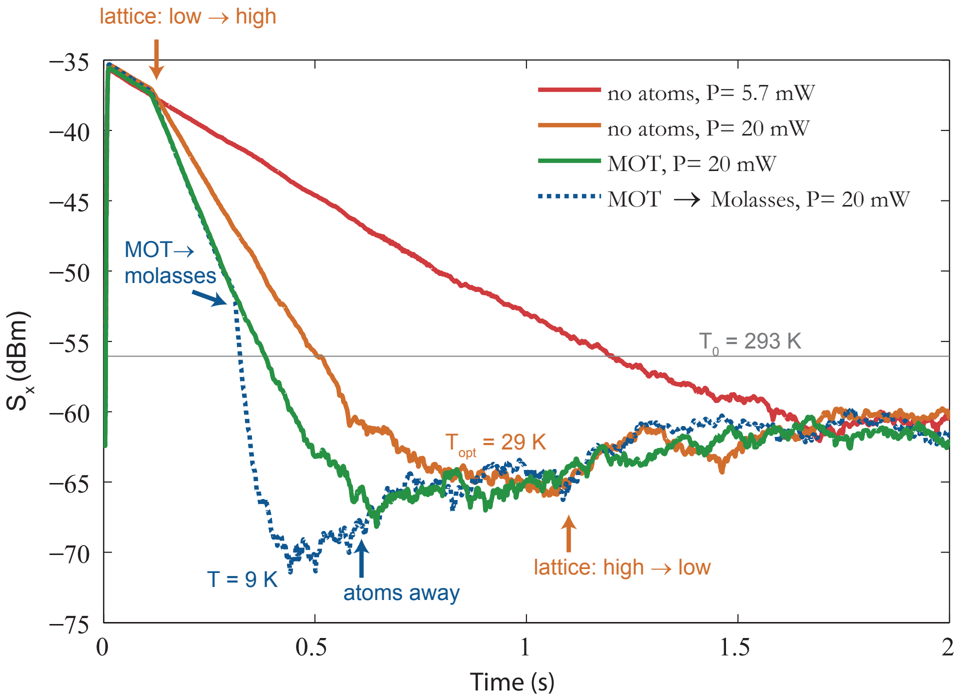

Figure 6.35: A preliminary result on sympathetic cooling of the membrane mode via the laser-cooled atoms. The plot shows the noise spectral density S_x of an initially excited membrane as a function of time for 4 different measurements. The green curve shows the membrane ringdown, while the atoms are MOT cooled in the resonant lattice (the lattice power is $P = 20\,\mathrm{mW}$). The blue, dashed curve shows a similar measurement, where molasses cooling is switched on during the membrane ringdown as indicated by the arrow. The orange and red curves are reference measurements for lattice laser powers of 20 mW and 5.7 mW, demonstrating the effects of cavity cooling only. The resolution bandwidth in this measurement is 200 Hz.

measurement with the two other decays using atoms, the effect of atoms is visible as a considerably faster decay of the membrane mode.

We measure the largest damping rate of the membrane in the presence of the resonant, molasses cooled atoms. By comparing the intrinsic damping rate of the membrane, $\gamma_\mathrm{m} = 0.5\,\mathrm{s}^{-1}$ to the observed damping rate with molasses cooling $\Gamma_\mathrm{c} = 72\,\mathrm{s}^{-1}$, we observe an increase in the damping of the membrane by a factor of $\Gamma_\mathrm{c}/\gamma_\mathrm{m} = 140$. The damping results in a minimum temperature of $T_\mathrm{min} = 9\,\mathrm{K}$ corresponding to a cooling factor of $T_\mathrm{bath}/T_\mathrm{min} = 32$ with respect to the room temperature bath. In the absence of the atoms, we observe cavity cooling of the membrane mode to a steady-state temperature of $T_\mathrm{min} = 29\,\mathrm{K}$, when $P = 20\,\mathrm{mW}$. The final occupation number in the membrane is most likely limited by the frequency noise in the lattice laser beam.

The faster decay of the membrane mode in the presence of molasses cooled atoms as compared to the MOT ones is most likely explained by the smaller

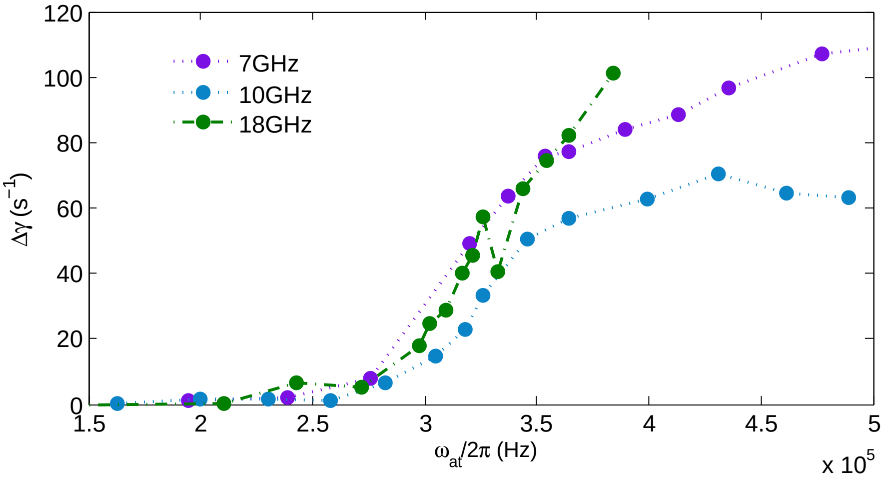

Figure 6.36: A change in the damping rate of the membrane due to the presence of the molasses-cooled atoms in the lattice as a function of ω_{at}. The measurement is done for three different detunings of the lattice beam: $\Delta_{\mathrm{L}} = -2\pi \cdot 7\,\mathrm{GHz}$, $\Delta_{\mathrm{L}} = -2\pi \cdot 10\,\mathrm{GHz}$ and $\Delta_{\mathrm{L}} = -2\pi \cdot 18\,\mathrm{GHz}$. The increase in the membrane damping starts to take place when $\omega_{\mathrm{at}} \sim \omega_{\mathrm{m}}$.

inhomogeneous broadening of the atomic resonance. A thorough quantitative understanding of the results requires further measurements and analysis. For example, we are currently characterizing the atomic module regarding e.g., the temperature and number of atoms in the lattice. As a rough parameter estimate, the total number of atoms in the lattice is around $\sim 7 \cdot 10^7$. The temperature of the MOT is around 100μK and the molasses temperature has been measured to be around 20μK.

In another measurement, we measure the change in the ringdown rate of the membrane with and without the presence of the atoms in the lattice. We do the measurement for three different lattice detunings of $\Delta_{\mathrm{L}} = -2\pi \cdot 7\,\mathrm{GHz}$, $\Delta_{\mathrm{L}} = -2\pi \cdot 10\,\mathrm{GHz}$ and $\Delta_{\mathrm{L}} = -2\pi \cdot 18\,\mathrm{GHhz}$, and change the trap frequency of the atoms by changing the power of the lattice beam. The trap frequency of the atoms scales as $\omega_{\mathrm{at}} \propto \sqrt{\frac{P}{\Delta_{\mathrm{L}}}}$. Figure 6.36 shows the resulting increase in the damping rate of the membrane due to the atoms, $\Delta\gamma$, as a function of ω_{at}. When the atoms are tuned on-resonance with the membrane, we observe an increase in the damping by a factor of 10^2. Note, that the onset of the mechanical damping starts at a different lattice power levels as Δ_{L} is changed, but at the same $\omega_{\mathrm{at}} \sim \omega_{\mathrm{m}}$.

We observe enhanced damping of the membrane in Fig. 6.36 over a broad range of ω_{at}. This maybe influenced by the strong membrane excitation together with the trap anharmonicity, the spatial spread in the trap frequencies, and the finite temperature of the atoms in the lattice, as discussed in Section. 5.5. A more quantitative analysis requires further trap characterization measurements that are underway. Nevertheless, these measurements demonstrate sympathetic cooling of the membrane motion via the atoms using the MIM-module. The measured increase in the damping of the membrane due to the atoms is remarkably 10^4 times larger than that observed in the first free-space experiments (Sec. 5.5). These measurements entail a promising start for exploring the atom-membrane coupling further using the cavity-enhanced setup, and are a successful continuation of the free-space experiments started in Munich.

7

Conclusions

In this thesis I have described a novel hybrid-optomechanical experiment, where a microscopic membrane oscillator is coupled via an optical lattice interface to the center of mass motion of a distant atomic ensemble. In the experimental realization, we trap 10^6 atoms in the optical lattice and observe bi-directional coupling between the atoms and the SiN membrane when the two systems are tuned to resonance at $2\pi \cdot 250\,\text{kHz}$. This is striking, as the atoms and the membrane have an enormous mass difference of a factor of 10^8. This experiment is also the first demonstration of backaction of ultra-cold atoms onto a mechanical oscillator.

We observe a resonant increase in the damping of the membrane motion on the order of a few percent in a ringdown measurement. The high Q-factor $\sim 10^6$ of the silicon nitride membrane allows us to precisely measure minute changes in its damping. Due to the high temperature of the atoms and the spatially inhomogeneous trapping potential, the coupling resonance is broadened. By including these effects into our theoretical model, we can accurately describe the shape and amplitude of the measured atom-membrane resonance. This suggests that the theory can be used for extrapolation to optimized parameters.

One route to considerably enhance the coupling is to enclose the membrane inside a cavity, which increases the radiation pressure on the membrane. As a part of this thesis, a successful extension of the membrane module was designed and implemented. In the new setup, the membrane is placed in the middle of an optical cavity and the atoms are trapped in an optical lattice formed by retroreflection from the cavity. When the membrane is positioned at the slope of a resonant cavity field the atom-membrane coupling is enhanced compared to the free-space coupling in proportion to the cavity finesse. At the same time, the modularity of the setup is preserved.

In preliminary measurements with the new cavity-enhanced setup we have observed an increase in the damping of the membrane due to the atoms that is a factor 10^4 stronger than with the previous setup. In addition, we have sympathetically cooled a 274 kHz membrane mode from room temperature to 9 K via continuous laser-cooling of the atoms. Furthermore, such an integrated membrane-cavity system provides a range of interesting physics on its own. We have theoretically analyzed the system, and found that the finesse of an asymmetric cavity can be increased beyond its free-space value by optimizing the membrane position inside the cavity with respect to the cavity field. This can be described by classical interference effects inside the cavity. The theory is in accurate agreement with our measurements.

Theoretical estimates show that both the free-space and cavity-enhanced setups should enable the ground-state cooling of a cryogenically pre-cooled membrane by making use of the tunable atomic dissipation [33, 41]. An interesting feature of the cavity setup is that unlike in cavity-optomechanical cooling [139], the sideband-resolved regime is not required to achieve ground state cooling of the membrane. This is advantageous since this regime is experimentally challenging to reach for low-frequency oscillators such as the membranes. The corresponding condition in our setup is that the atoms can be ground-state cooled, which is routinely achieved in experiments [77]. The proposed setup could also prove useful in the context of cooling other dielectric objects in a cavity such as levitated dielectric particles or molecules, which also have frequencies in the hundreds of kHz regime [83, 84]. Finally, coupling to the internal atomic degrees of freedom [30, 32] instead of the motional ones could open additional possibilities for manipulation and cooling, and might also enable even higher couplings.

Ultra cold atoms coupled to mechanical oscillators represents a novel type of hybrid mechanical system, where a long term prospect is to harness the atoms for read-out, cooling, and coherent manipulation of the mechanical oscillators [34]. The optical lattice demonstrated in this thesis provides a coherent, long-distance coupling between the the atoms and the membrane. Such a long-distance interface is beneficial, as it can link systems residing in very different environments. Furthermore, by functionalizing the membrane with magnetic moment or electric charge, it could serve as a transducer between otherwise incompatible quantum systems, thus providing an asset for versatile hybrid quantum networks.

Route Towards Coherent Coupling

The experiments presented in this thesis demonstrate the back-action of an ensemble of ultra cold atoms onto a membrane, which is a prerequisite for cooling and manipulating the membrane with the atoms. The next goal is to observe the normal-mode splitting in the current setup and thereafter explore sympathetic ground-state cooling of the membrane. In the following, some potential steps towards these goals are suggested.

Atomic Module

We expect the normal-mode splitting to be observable with current setup by increasing the number of atoms in the lattice and by ground-state cooling them. Ground-state cooling minimizes the effects of spatial inhomogeneities in the trapping potential and the finite temperature of the atoms on the coupling. Raman sideband cooling could be used to prepare up to 3×10^8 atoms in the ground state of a large volume 3D lattice [77]. In addition, a blue-detuned lattice could be used to couple the atoms to the membrane. This would suppress effects due to spontaneous emission of the atoms and thus allow for smaller laser detuning and power. In the transverse direction the atoms could be confined by a far-detuned 2D lattice.

Membrane Module

To access the quantum coherent coupling regime with currently available membrane and atom parameters requires a cryogenic membrane module to reduce the thermal decoherence rate of the membrane. In our experiment, we use a commercially available SiN membrane. At the moment, considerable effort is undertaken by various research groups to fabricate and develop membranes that are tailored for optomechanics experiments [108, 101, 36, 110, 111, 112]. By structuring the membranes and their clamping points to the environment, one can significantly reduce their damping [108]. Furthermore, sub-wavelength diffraction gratings patterned on the membrane surface have shown reflectivity of 99.8 % while simultaneously the membrane Q had an ultra-high value of 10^6 at room temperature [110, 111].

Noise Considerations

As the coherent coupling regime is approached, the setup becomes more vulnerable to various noise sources. In particular, the current detection sensitivity is $10^{-14}\,\mathrm{m}/\sqrt{\mathrm{Hz}}$, whereas the ground state amplitude of the membrane is $\sim 10^{-15}\,\mathrm{m}$. Careful analysis of the current sensitivity limits is therefore required. Furthermore, laser noise at the membrane frequency heats up the membrane, which is possibly limiting the current experiment. In the long term, we expect to require some aggressive filtering of the laser in order to reach the ground-state regime [141, 11, 140]. Finally, the vibrational noise in the system can be reduced further using a monolithic, rigid and small cavity design. [142].

Appendix A

Fundamental Constants and ^{87}Rubidium data

Fundamental Constants

Planck's constant	h	$6.62606876(52) \cdot 10^{-34}\,\mathrm{Js}$
	$\hbar = \frac{h}{2\pi}$	$1.054571596(82) \cdot 10-34\,\mathrm{Js}$
Boltzmann's constant	k_B	$1.3806503(24) \cdot 10^{-34}\,\mathrm{J/K}$
Speed of light	c	$2.99792458 \cdot 10^{8}\,\mathrm{m/s}$

^{87}Rb data

Atomic mass	m	$1.44316060(11) \cdot 10^{-25}\,\mathrm{kg}$
D_2 transition ($5^2\mathbf{S}_{1/2} \to 5^2\mathbf{P}_{3/2}$)		
Natural linewidth	γ_se	$2\pi \cdot 6.065(9)\,\mathrm{MHz}$
Saturation intensity	I_s	$1.669(2)\,\mathrm{mW/cm^2}$
for $\lvert F=2, m_\mathrm{F}=\pm 2\rangle \leftrightarrow \lvert F'=3, m'_\mathrm{F}=\pm 3\rangle$ ($\sigma^\pm$ pol.)		
Recoil energy	$E_\mathrm{r} = 2\pi^2\hbar^2/\lambda^2 m$	$h \cdot 3.7710\,\mathrm{kHz}$
$5^2\mathbf{S}_{1/2}$ Groundstate		
Hyperfine splitting	E_hfs	$h \cdot 6.835\,\mathrm{GHz}$

The data is taken from Ref. [75].

Appendix B

Intensity Stabilization: Circuit Diagram

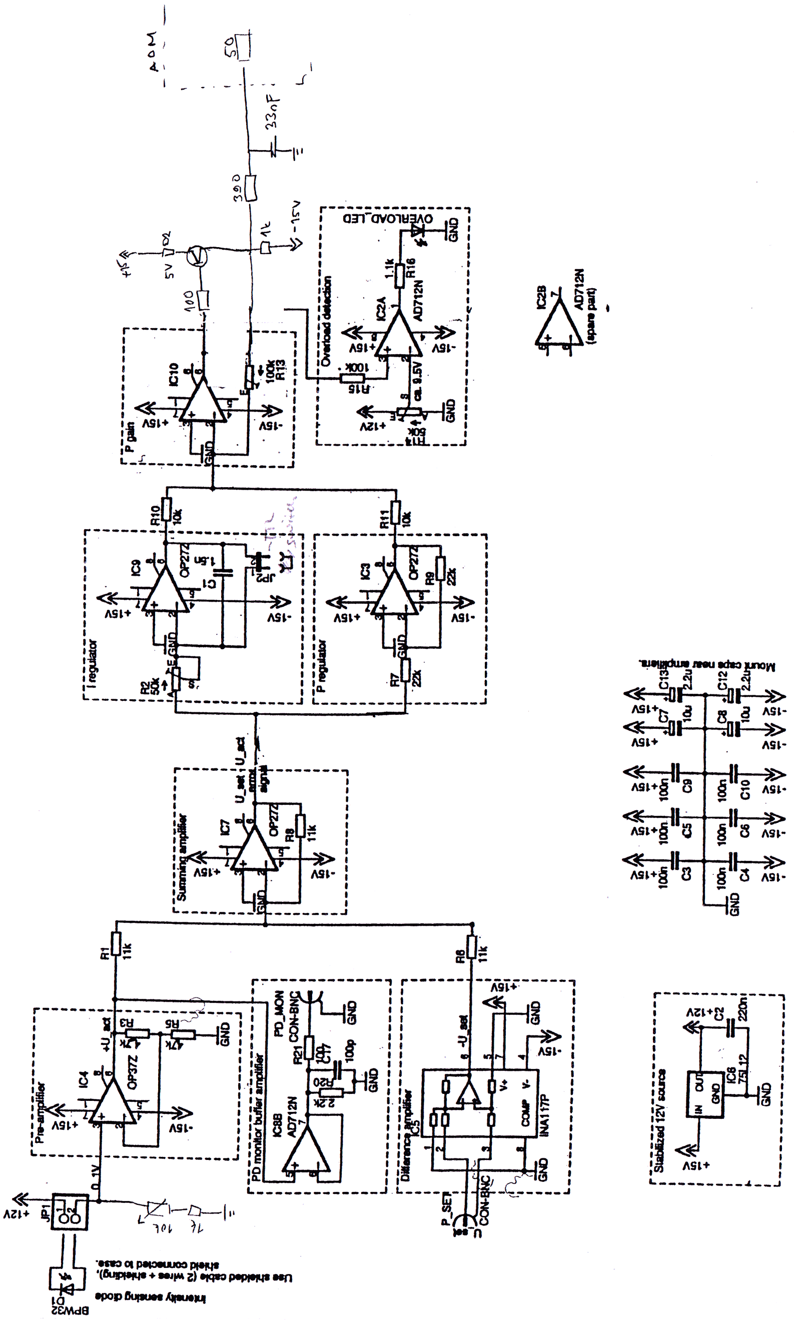

Figure B.1: Circuit diagram of the intensity stabilization for the lattice laser beam.

Appendix C

Impressions from Lab-Move

Some pictures taken in lab of Prof. T. W. Hänsch at LMU in Munich before and after the move from Munich to Basel are shown in Figs. C.1 and C.2.

The empty optical tables in Basel shown in Fig. C.3 were quickly taken over by the new atom-membrane experiment shown in Fig. C.4.

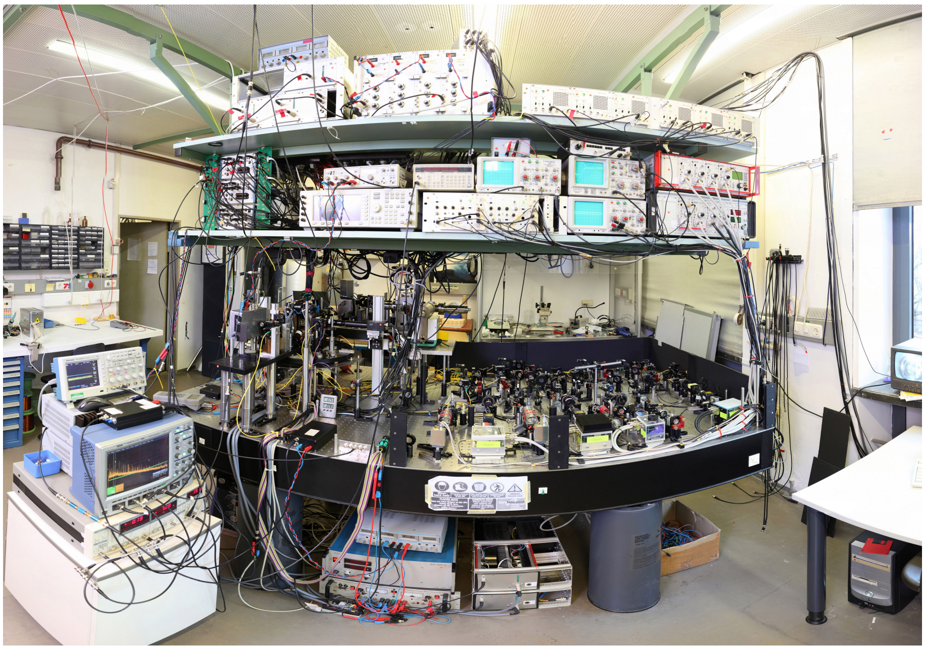

Figure C.1: One of the two experimental tables used for the atom-membrane laser setup. The experiments described in Chapter 5 were performed with this setup. Picture taken by T. W. Hänsch. August 2010.

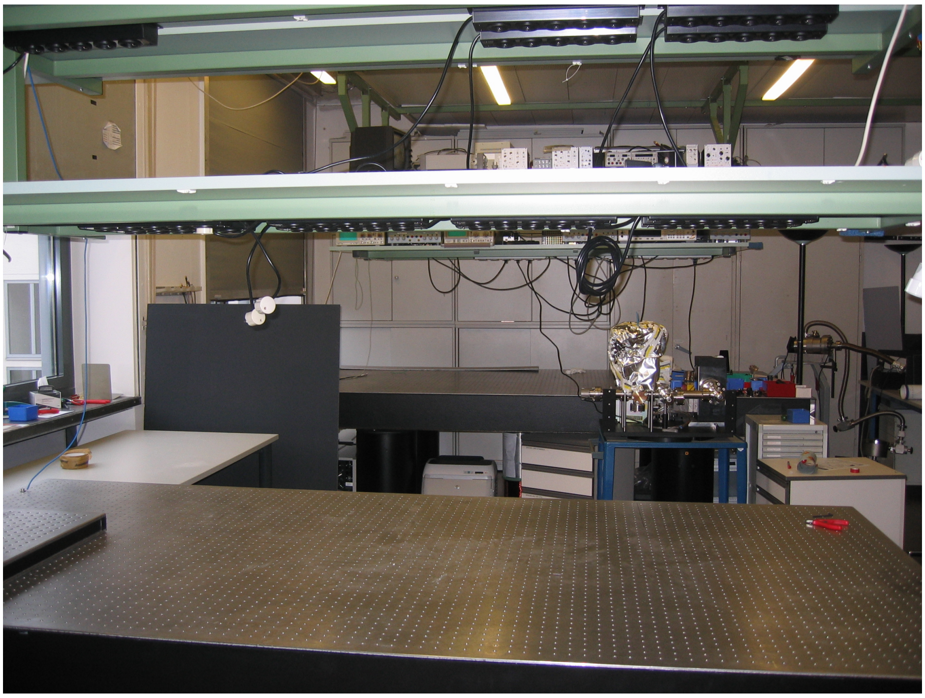

Figure C.2: Atom-membrane-lab in Munich taking off to Basel. November 2010.

Figure C.3: The new atom-membrane lab in Basel in October, 2010.

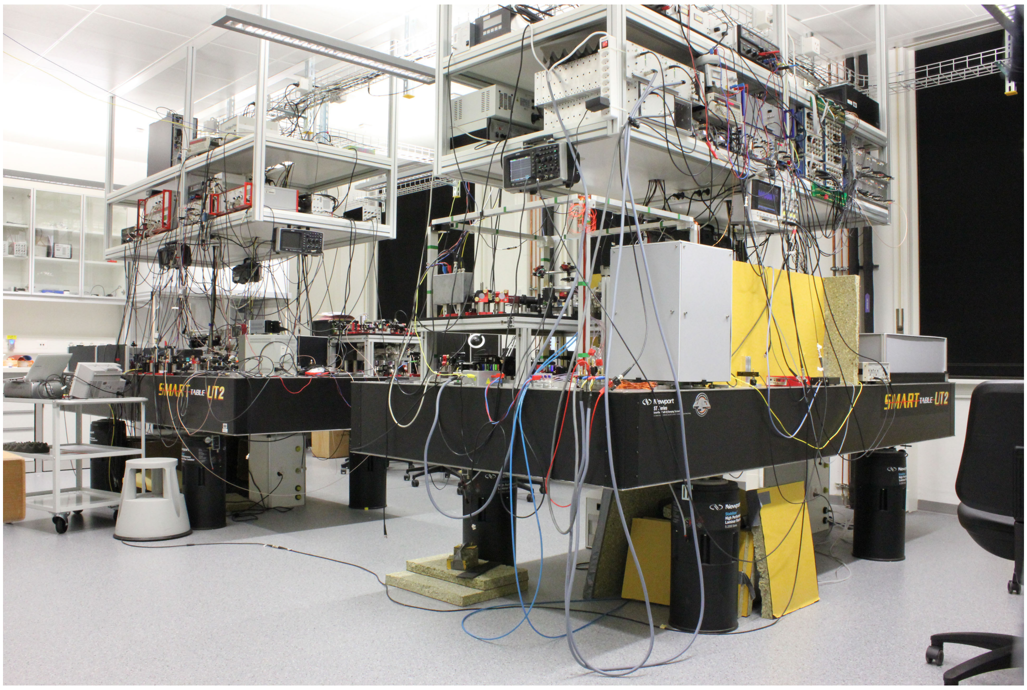

Figure C.4: The atom-membrane lab in Basel in August, 2013. The build-up of this experiment is described in Chapter. 6

Acronyms

AOM	Acousto-optical modulator
CCD	Charge coupled device
c.o.m	Center of mass mode
EOM	Electro-optic modulator
FSR	Cavity free spectral range
MI	Michelson Interferometer
MIM	Membrane in the middle
MOT	Magneto-optical trap
PBC	Polarizing beam cube
PD	Photodiode
PDH	Pound Drever Hall
Q	Mechanical quality factor
SiN	Silicon nitride
SNR	Signal-to-noise ratio
TA	Tapered amplifier
TOF	Time of flight

Symbols

Optical Field and Cavity

λ	Laser wavelength
$k = \frac{2\pi}{\lambda}$	Wave vector
P	Power in the laser beam
w_0	Beam waist
$A(\mathbf{r})$	Complex field amplitude
ω_{L}	Laser frequency
ω_{cav}	Cavity resonance frequency
$\Delta_{\mathrm{c}} = \omega_{\mathrm{L}} - \omega_{\mathrm{cav}}$	Detuning between cavity resonance and laser drive
κ	Cavity amplitude decay rate (HWHM of transmission resonance)
$\Delta\omega = 2\kappa$	Cavity decay rate (FWHM of transmission resonance)
$\bar{n}_{\mathrm{cav}}$	Mean photon number in the cavity
L_{cav}	Empty cavity length
FSR= $c/2L_{\mathrm{cav}}$	Free spectral range
r_i	Amplitude reflectivity of mirror i
$\mathfrak{F}$	Cavity finesse
G_{opt}	Optomechanical coupling strength
$\delta\omega_{\mathrm{m}}(\Delta_{\mathrm{c}})$	Optical spring
Γ_{opt}	Optomechanical damping rate

Mechanical Oscillator

M	Effective oscillator mass
l_{m}	Membrane side length
d_{m}	Membrane thickness
ω_{m}	Membrane frequency (angular units)
$Q = \omega_{\mathrm{m}}/\gamma_{\mathrm{m}}$	Mechanical quality factor
γ_{m}	Mechanical energy damping rate
x_{m}	Membrane displacement
x_{th}	r.m.s thermal amplitude of the oscillator
T_{bath}	Bath temperature
$x_{\mathrm{zp}} = \sqrt{\hbar/(2M\omega_{\mathrm{m}})}$	Zero-point amplitude
$\bar{n}_{\mathrm{th}}$	Mean thermal phonon number
$\gamma_{\mathrm{th}} = \gamma_{\mathrm{m}}\bar{n}_{\mathrm{th}}$	Thermal decoherence rate
$\bar{n}_{\mathrm{ss}}$	Steady-state occupation number
n_{m}	Refractive index of the membrane
r_{m}	Amplitude reflectivity of the membrane
$\mathfrak{r} = \lvert r_{\mathrm{m}}\rvert^2$	Intensity reflectivity of the membrane
$S_x(\omega)$	Single-sided power spectral density
Γ_{c}	Membrane damping rate in the presence of the atoms
$\Delta\gamma = \Gamma_{\mathrm{c}} - \gamma_{\mathrm{m}}$	Increase in the damping of the membrane due to the atoms
K_{th}	Thermal link
g	Atom-membrane coupling constant
$\delta = \omega_{\mathrm{m}} - \omega_{\mathrm{at}}$	Membrane-atom detuning

Optical Lattice

m	Atomic mass
Δ_{L}	Lattice detuning
x_{at}	Atomic displacement from equilibrium
V_0	Total depth of the dipole potential
V_{m}	Modulation of the dipole potential
$\mathfrak{t}$	Transmission losses
ω_{ax}	Atomic axial trap frequency (angular units)
ω_{rad}	Atomic radial trap frequency (angular units)
N	Number of atoms in the lattice
$T_{\mathrm{ax,rad}}$	Axial / radial temperature of the atoms
$\sigma_{\mathrm{ax,rad}}$	Axial / radial width of the atom cloud
$\Delta\omega_{\mathrm{at}}$	Spread in the atomic trap frequencies
γ_{c}	Cooling rate of the atoms
γ_{ϕ}	Atomic dephasing rate
$\gamma_{\mathrm{at}} = \gamma_{\mathrm{c}} + \gamma_{\phi}$	Total damping rate of the atoms

Bibliography

[1] S. Chu, *Cold Atoms and Quantum Control*, Nature **416**, 206 (2002).

[2] S. Chu, *Laser Manipulation of Atoms and Particles*, Science **253**, 861 (1991).

[3] D. Leibfried, R. Blatt, C. Monroe, and D. Wineland, *Quantum Dynamics of Single Trapped Ions*, Rev. Mod. Phys. **75**, 281 (2003).

[4] I. Bloch, *Ultracold Quantum Gases in Optical Lattices*, Nat. Phys. **1**, 23 (2005).

[5] R. Blatt and D. Wineland, *Entangled States of Trapped Atomic Ions*, Nature **453**, 1008 (2008).

[6] C. F. Ockeloen, R. Schmied, M. F. Riedel, and P. Treutlein, *Quantum Metrology with a Scanning Probe Atom Interferometer*, Phys. Rev. Lett. **111**, 143001 (2013).

[7] T. J. Kippenberg and K. J. Vahala, *Cavity Opto-Mechanics*, Opt. Express **15**, 17172 (2007).

[8] T. J. Kippenberg and K. J. Vahala, *Cavity Optomechanics: Back-Action at the Mesoscale*, Science **321**, 1172 (2008).

[9] F. Marquardt and S. M. Girvin, *Optomechanics*, Physics **2**, 40 (2009).

[10] I. Favero and K. Karrai, *Optomechanics of Deformable Optical Cavities*, Nat. Photon. **3**, 201 (2009).

[11] M. Aspelmeyer, T. J. Kippenberg, and F. Marquardt, *Cavity Optomechanics*, arXiv:1303.0733 (2013).

[12] J. Chan, T. P. M. Alegre, A. H. Safavi-Naeini, J. T. Hill, A. Krause, S. Gröblacher, M. Aspelmeyer, and O. Painter, *Laser Cooling of a Nanomechanical Oscillator into its Quantum Ground State*, Nature **478**, 89 (2011).

[13] S. Gröblacher, J. B. Hertzberg, M. R. Vanner, G. D. Cole, S. Gigan, K. C. Schwab, and M. Aspelmeyer, *Demonstration of an Ultracold Micro-Optomechanical Oscillator in a Cryogenic Cavity*, Nat. Phys. **5**, 485 (2009).

[14] E. Verhagen, S. Deleglise, S. Weis, A. Schliesser, and T. J. Kippenberg, *Quantum-Coherent Coupling of a Mechanical Oscillator to an Optical Cavity Mode*, Nature **482**, 63 (2012).

[15] A. D. O´Connell, M. Hofheinz, M. Ansmann, R. C. Bialczak, M. Lenander, E. Lucero, M. Neeley, D. Sank, H. Wang, M. Weides, J. Wenner, J. M. Martinis, and A. N. Cleland, *Quantum Ground State and Single-Phonon Control of a Mechanical Resonator*, Nature **464**, 697 (2010).

[16] J. D. Teufel, T. Donner, D. Li, J. W. Harlow, M. S. Allman, K. Cicak, A. J. Sirois, J. D. Whittaker, K. W. Lehnert, and R. W. Simmonds, *Sideband Cooling of Micromechanical Motion to the Quantum Ground State*, Nature **475**, 359 (2011).

[17] J. D. Teufel, D. Li, M. S. Allman, K. Cicak, A. J. Sirois, J. D. Whittaker, and R. W. Simmonds, *Circuit Cavity Electromechanics in the Strong-Coupling Regime*, Nature **471**, 204 (2011).

[18] M. Aspelmeyer, P. Meystre, and K. Schwab, *Quantum Optomechanics*, Phys. Today **65**, 29 (2012).

[19] W. Marshall, C. Simon, R. Penrose, and D. Bouwmeester, *Towards Quantum Superpositions of a Mirror*, Phys. Rev. Lett. **91**, 130401 (2003).

[20] I. Pikovski, M. R. Vanner, M. Aspelmeyer, M. S. Kim, and Brukner, Časlav, *Probing Planck-Scale Physics with Quantum Optics*, Nat. Phys. **8**, 393 (2012).

[21] O. Romero-Isart, *Quantum Superposition of Massive Objects and Collapse Models*, Phys. Rev. A **84**, 052121 (2011).

[22] O. R. Isart, A. C. Pflanzer, F. Blaser, R. Kaltenbaek, N. Kiesel, M. Aspelmeyer, and J. I. Cirac, *Large Quantum Superpositions and Interference of Massive Nanometer-Sized Objects*, Phys. Rev. Lett. **107**, 020405 (2011).

[23] D. McClelland, N. Mavalvala, Y. Chen, and R. Schnabel, *Advanced Interferometry, Quantum Optics and Optomechanics in Gravitational Wave Detectors*, Laser Photon. Rev. **5**, 677 (2011).

[24] D. Meiser and P. Meystre, *Coupled Dynamics of Atoms and Radiation-Pressure-Driven Interferometers*, Phys. Rev. A **73**, 033417 (2006).

[25] C. Genes, D. Vitali, and P. Tombesi, *Emergence of Atom-Light-Mirror Entanglement inside an Optical Cavity*, Phys. Rev. A **77**, 050307 (2008).

[26] H. Ian, Z. R. Gong, Y.-x. Liu, C. P. Sun, and F. Nori, *Cavity Optomechanical Coupling Assisted by an Atomic Gas*, Phys. Rev. A **78**, 013824 (2008).

[27] Y. Chang, T. Shi, Y.-x. Liu, C. P. Sun, and F. Nori, *Multistability of Electromagnetically Induced Transparency in Atom-Assisted Optomechanical Cavities*, Phys. Rev. A **83**, 063826 (2011).

[28] A. B. Bhattacherjee, *Cavity Quantum Optomechanics of Ultracold Atoms in an Optical Lattice: Normal-Mode Splitting*, Phys. Rev. A **80**, 043607 (2009).

[29] K. Zhang, W. Chen, M. Bhattacharya, and P. Meystre, *Hamiltonian Chaos in a Coupled BEC-Optomechanical-Cavity System*, Phys. Rev. A **81**, 013802 (2010).

[30] K. Hammerer, M. Aspelmeyer, E. S. Polzik, and P. Zoller, *Establishing Einstein-Poldosky-Rosen Channels between Nanomechanics and Atomic Ensembles*, Phys. Rev. Lett. **102**, 020501 (2009).

[31] K. Hammerer, M. Wallquist, C. Genes, M. Ludwig, F. Marquardt, P. Treutlein, P. Zoller, J. Ye, and H. J. Kimble, *Strong Coupling of a Mechanical Oscillator and a Single Atom*, Phys. Rev. Lett. **103**, 063005 (2009).

[32] M. Wallquist, K. Hammerer, P. Zoller, C. Genes, M. Ludwig, F. Marquardt, P. Treutlein, J. Ye, and H. J. Kimble, *Single-Atom Cavity QED and Optomicromechanics*, Phys. Rev. A **81**, 023816 (2010).

[33] K. Hammerer, K. Stannigel, C. Genes, P. Zoller, P. Treutlein, S. Camerer, D. Hunger, and T. W. Hänsch, *Optical Lattices with Micromechanical Mirrors*, Phys. Rev. A **82**, 021803 (2010).

[34] D. Hunger, S. Camerer, M. Korppi, A. Jöckel, T. Hänsch, and P. Treutlein, *Coupling Ultracold Atoms to Mechanical Oscillators*, Comptes Rendus Physique **12**, 871 (2011).

[35] M. Wallquist, K. Hammerer, P. Rabl, M. Lukin, and P. Zoller, *Hybrid Quantum Devices and Quantum Engineering*, Phys. Scripta **2009**, 014001 (2009).

[36] D. E. Chang, K.-K. Ni, O. Painter, and H. J. Kimble, *Ultrahigh-Q Mechanical Oscillators through Optical Trapping*, New J. Phys. **14**, 045002 (2012).

[37] P. Treutlein, D. Hunger, S. Camerer, T. W. Hänsch, and J. Reichel, *Bose-Einstein Condensate Coupled to a Nanomechanical Resonator on an Atom Chip*, Phys. Rev. Lett. **99**, 140403 (2007).

[38] D. Hunger, S. Camerer, T. W. Hänsch, D. König, J. P. Kotthaus, J. Reichel, and P. Treutlein, *Resonant Coupling of a Bose-Einstein Condensate to a Micromechanical Oscillator*, Phys. Rev. Lett. **104**, 143002 (2010).

[39] S. Camerer, M. Korppi, A. Jöckel, D. Hunger, T. W. Hänsch, and P. Treutlein, *Realization of an Optomechanical Interface Between Ultracold Atoms and a Membrane*, Phys. Rev. Lett. **107**, 223001 (2011).

[40] M. Korppi, A. Jöckel, M. T. Rakher, S. Camerer, D. Hunger, T. W. Hänsch, and P. Treutlein, *Hybrid Atom-Membrane Optomechanics*, EPJ Web of Conferences **57**, 03006 (2013).

[41] B. Vogell, K. Stannigel, P. Zoller, K. Hammerer, M. T. Rakher, M. Korppi, A. Jöckel, and P. Treutlein, *Cavity-Enhanced Long-Distance Coupling of an Atomic Ensemble to a Micromechanical Membrane*, Phys. Rev. A **87**, 023816 (2013).

[42] Y.-J. Wang, M. Eardley, S. Knappe, J. Moreland, L. Hollberg, and J. Kitching, *Magnetic Resonance in an Atomic Vapor Excited by a Mechanical Resonator*, Phys. Rev. Lett. **97**, 227602 (2006).

[43] S. Camerer, *Interfacing Ultracold Atoms and Mechanical Oscillators*, Ph.D. thesis, LMU München (2011).

[44] P. Treutlein, C. Genes, K. Hammerer, M. Poggio, and P. Rabl, *Hybrid Mechanical Systems*, arXiv:1210.4151 (2012), to appear in: "Cavity Optomechanics", ed. by M. Aspelmeyer, T. Kippenberg, F. Marquardt (Springer).

[45] I. Wilson-Rae, R. A. Barton, S. S. Verbridge, D. R. Southworth, B. Ilic, H. G. Craighead, and J. M. Parpia, *High-Q Nanomechanics via Destructive Interference of Elastic Waves*, Phys. Rev. Lett. **106**, 047205 (2011).

[46] A. Jöckel, M. T. Rakher, M. Korppi, S. Camerer, D. Hunger, M. Mader, and P. Treutlein, *Spectroscopy of Mechanical Dissipation in Micro-Mechanical Membranes*, Appl. Phys. Lett. **99**, 143109 (2011).

[47] A. N. Cleland, *Foundations of Nanomechanics* (Springer-Verlag Berlin Heidelberg New York) (2003).

[48] N. W. Ashcroft and D. N. Mermin, *Solid State Physics* (Thomson Learning, Stamford CT, Toronto), 1st edition (1976).

[49] L. D. Landau and E. M. Lifshitz, *Course on Theoretical Physics: Mechanics*, volume 1 (Elsevier Butterworth-Heinemann), 3rd edition (1982).

[50] P. R. Saulson, *Thermal Noise in Mechanical Experiments*, Phys. Rev. D **42**, 2437 (1990).

[51] A. A. Clerk, M. H. Devoret, S. M. Girvin, F. Marquardt, and R. J. Schoelkopf, *Introduction to Quantum Noise, Measurement and Amplification*, Rev. Mod. Phys. **82**, 1155 (2010).

[52] P. Meystre and M. Sargent, *Elements of Quantum Optics* (Springer-Verlag Berlin Heidelberg New York) (2007).

[53] P. Lambropoulos and D. Petrosyan, *Fundamentals of Quantum Optics and Quantum Information* (Springer-Verlag Berlin Heidelberg New York) (2007).

[54] M. Orszag, *Quantum Optics* (Springer-Verlag Berlin Heidelberg New York) (2008).

[55] M. Schlosshauer, *Decoherence and the Quantum-To-Classical Transition* (Springer-Verlag Berlin Heidelberg New York) (2007).

[56] A. H. Safavi-Naeini, J. Chan, J. T. Hill, T. P. M. Alegre, A. Krause, and O. Painter, *Observation of Quantum Motion of a Nanomechanical Resonator*, Phys. Rev. Lett. **108**, 033602 (2012).

[57] I. Favero, C. Metzger, S. Camerer, D. König, H. Lorenz, J. P. Kotthaus, and K. Karrai, *Optical Cooling of a Micromirror of Wavelength Size*, Appl. Phys. Lett. **90**, 104101 (2007).

[58] J. D. Thompson, B. M. Zwickl, A. M. Jayich, F. Marquardt, S. M. Girvin, and J. G. E. Harris, *Strong Dispersive Coupling of a High-Finesse Cavity to a Micromechanical Membrane*, Nature **452**, 72 (2008).

[59] J. Reichel, *Microchip Traps and Bose-Einstein Condensation*, Appl. Phys. B **74**, 469 (2002).

[60] R. Gehr, J. Volz, G. Dubois, T. Steinmetz, Y. Colombe, B. L. Lev, R. Long, J. Estève, and J. Reichel, *Cavity-Based Single Atom Preparation and High-Fidelity Hyperfine State Readout*, Phys. Rev. Lett. **104**, 203602 (2010).

[61] S. R. Jefferts, C. Monroe, E. W. Bell, and D. J. Wineland, *Coaxial-Resonator-Driven RF (Paul) Trap for Strong Confinement*, Phys. Rev. A **51**, 3112 (1995).

[62] H. Walther, B. T. H. Varcoe, B.-G. Englert, and T. Becker, *Cavity Quantum Electrodynamics*, Rep. Prog. Phys. **69**, 1325 (2006).

[63] T. Westphal, D. Friedrich, H. Kaufer, K. Yamamoto, S. Goßler, H. Müller-Ebhardt, S. L. Danilishin, F. Y. Khalili, K. Danzmann, and R. Schnabel, *Interferometer Readout Noise Below the Standard Quantum Limit of a Membrane*, Phys. Rev. A **85**, 063806 (2012).

[64] D. K. Armani, T. J. Kippenberg, S. M. Spillane, and K. J. Vahala, *Ultra-High-Q Toroid Microcavity on a Chip*, Nature **421**, 925 (2003).

[65] M. Li, W. H. P. Pernice, C. Xiong, T. Baehr-Jones, M. Hochberg, and H. X. Tang, *Harnessing Optical Forces in Integrated Photonic Circuits*, Nature **456**, 480 (2008).

[66] S. Gröblacher, K. Hammerer, M. R. Vanner, and M. Aspelmeyer, *Observation of Strong Coupling between a Micromechanical Resonator and an Optical Cavity Field*, Nature **460**, 724 (2009).

[67] P. F. Cohadon, A. Heidmann, and M. Pinard, *Cooling of a Mirror by Radiation Pressure*, Phys. Rev. Lett. **83**, 3174 (1999).

[68] D. Kleckner and D. Bouwmeester, *Sub-Kelvin Optical Cooling of a Micromechanical Resonator*, Nature **444**, 75 (2006).

[69] M. Poggio, C. L. Degen, H. J. Mamin, and D. Rugar, *Feedback Cooling of a Cantilever's Fundamental Mode below 5 mK*, Phys. Rev. Lett. **99**, 017201 (2007).

[70] C. Genes, D. Vitali, P. Tombesi, S. Gigan, and M. Aspelmeyer, *Ground-state Cooling of a Micromechanical Oscillator: Comparing Cold Damping and Cavity-Assisted Cooling Schemes*, Phys. Rev. A **77**, 033804 (2008).

[71] D. Jacks, *Optical Lattices, Ultracold Atoms and Quantum Information Processing*, Contemporary Physics **45**, 367 (2004).

[72] C. Orzel, *Searching for New Physics through Atomic, Molecular and Optical Precision Measurements*, Phys. Scripta **86**, 068101 (2012).

[73] R. Grimm, M. Weidemüller, and Y. B. Ovchinnikov, *Optical Dipole Traps for Neutral Atoms*, in B. Bederson and H. Walther (editors), *Advances In Atomic, Molecular, and Optical Physics*, volume 42, pp. 95 – 170 (Academic Press) (2000).

[74] B. E. A. Saleh and M. C. Teich, *Fundamentals of Photonics* (Wiley, New York, New York) (1991).

[75] D. A. Steck, *Rubidium 87 D Line Data*, URL http://steck.us/alkalidata/, revision 2.1.4 (2010).

[76] S. L. Winoto, M. T. Depue, N. E. Bramall, and D. S. Weiss, *Laser Cooling at High Density in Deep Far-Detuned Optical Lattices*, Phys. Rev. A **59**, 19 (1999).

[77] A. J. Kerman, V. Vuletic, C. Chin, and S. Chu, *Beyond Optical Molasses: 3D Raman Sideband Cooling of Atomic Cesium to High Phase-Space Density*, Phys. Rev. Lett. **84**, 439 (2000).

[78] H. J. Metcalf and P. van der Straten, *Laser Cooling And Trapping* (Springer-Verlag Berlin Heidelberg New York), 1st edition (1999).

[79] S. Friebel, C. D'Andrea, J. Walz, M. Weitz, and T. W. Hänsch, CO_2*-laser Optical Lattice with Cold Rubidium Atoms*, Phys. Rev. A **57**, R20 (1998).

[80] J. P. Gordon and A. Ashkin, *Motion of Atoms in a Radiation Trap*, Phys. Rev. A **21**, 1606 (1980).

[81] H. Ott, J. Fortágh, S. Kraft, A. Günther, D. Komma, and C. Zimmermann, *Nonlinear Dynamics of a Bose-Einstein Condensate in a Magnetic Waveguide*, Phys. Rev. Lett. **91**, 040402 (2003).

[82] J. Wu, R. Newell, M. Hausmann, D. J. Vieira, and X. Zhao, *Loading Dynamics of Optical Trap and Parametric Excitation Resonances of Trapped Atoms*, Appl. Phys. **100**, 054903 (2006).

[83] O. Romero-Isart, M. L. Juan, R. Quidant, and J. I. Cirac, *Toward Quantum Superposition of Living Organisms*, New J. Phys. **12**, 033015 (2010).

[84] D. E. Chang, C. A. Regal, S. B. Papp, D. J. Wilson, J. Ye, O. Painter, H. J. Kimble, and P. Zoller, *Cavity Opto-Mechanics using an Optically Levitated Nanosphere*, Proc. Natl. Acad. Sci. USA. **107**, 1005 (2010).

[85] A. Ashkin and J. M. Dziedzic, *Feedback Stabilization of Optically Levitated Particles*, Appl. Phys. Lett. **30**, 202 (1977).

[86] T. Li, S. Kheifets, and M. G. Raizen, *Millikelvin Cooling of an Optically Trapped Microsphere in Vacuum*, Nat. Phys. **7**, 527 (2011).

[87] J. Gieseler, B. Deutsch, R. Quidant, and L. Novotny, *Subkelvin Parametric Feedback Cooling of a Laser-Trapped Nanoparticle*, Phys. Rev. Lett. **109**, 103603 (2012).

[88] N. Kiesel, F. Blaser, U. Philć, D. Grass, R. Kaltenbaek, and M. Aspelmeyer, *Cavity Cooling of an Optically Levitated Submicron Particle*, Proc. Natl. Acad. Sci. USA. **110**, 14180 (2013).

[89] G. Raithel, W. D. Phillips, and S. L. Rolston, *Collapse and Revivals of Wave Packets in Optical Lattices*, Phys. Rev. Lett. **81**, 3615 (1998).

[90] A. Görlitz, M. Weidemüller, T. W. Hänsch, and A. Hemmerich, *Observing the Position Spread of Atomic Wave Packets*, Phys. Rev. Lett. **78**, 2096 (1997).

[91] N. V. Morrow, S. K. Dutta, and G. Raithel, *Feedback Control of Atomic Motion in an Optical Lattice*, Phys. Rev. Lett. **88**, 093003 (2002).

[92] G. Raithel, `http://cold-atoms.physics.lsa.umich.edu/projects/lattice/osc1.html`, [Online; accessed 05-Aug-2013].

[93] S. Gigan, H. R. Böhm, M. Paternostro, F. Blaser, G. Langer, J. B. Hertzberg, K. C. Schwab, D. Bäuerle, M. Aspelmeyer, and A. Zeilinger, *Self-cooling of a Micromirror by Radiation Pressure*, Nature **444**, 67 (2006).

[94] R. E. Sapiro, B. N. Slama, and G. Raithel, *Bragg Scattering and Brownian Motion Dynamics in Optically Induced Crystals of Submicron Particles*, Phys. Rev. E **87**, 052311 (2013).

[95] P. Zoller and C. W. Gardiner, *Quantum Noise* (Springer-Verlag Berlin Heidelberg New York) (2000).

[96] H. J. Carmichael, *Quantum Trajectory Theory for Cascaded Open Systems*, Phys. Rev. Lett. **70**, 2273 (1993).

[97] K. Karrai, I. Favero, and C. Metzger, *Doppler Optomechanics of a Photonic Crystal*, Phys. Rev. Lett. **100**, 240801 (2008).

[98] B. Zink, *Specific Heat and Thermal Conductivity of Low-Stress Amorphous SiN Membranes*, Solid State Commun. **129**, 199 (2004).

[99] M. T. Alam, M. P. Manoharan, M. A. Haque, C. Muratore, and A. Voevodin, *Influence of Strain on Thermal Conductivity of Silicon Nitride Thin Films*, Journal of Micromechanics and Microengineering **22**, 045001 (2012).

[100] B. M. Zwickl, W. E. Shanks, A. M. Jayich, C. Yang, A. C. B. Jayich, J. D. Thompson, and J. G. E. Harris, *High Quality Mechanical and Optical Properties of Commercial Silicon Nitride Membranes*, Appl. Phys. Lett. **92**, 103125 (2008).

[101] D. J. Wilson, C. A. Regal, S. B. Papp, and H. J. Kimble, *Cavity Optomechanics with Stoichiometric SiN Films*, Phys. Rev. Lett. **103**, 207204 (2009).

[102] J. C. Sankey, C. Yang, B. M. Zwickl, A. M. Jayich, and J. G. E. Harris, *Strong and Tunable Nonlinear Optomechanical Coupling in a Low-Loss System*, Nat. Phys. **6**, 707 (2010).

[103] M. Karuza, C. Biancofiore, M. Bawaj, C. Molinelli, M. Galassi, R. Natali, P. Tombesi, G. Di Giuseppe, and D. Vitali, *Optomechanically Induced Transparency in a Membrane-In-The-Middle Setup at Room Temperature*, Phys. Rev. A **88**, 013804 (2013).

[104] C. Reynolds, S. Chakram, B. Pang, K. Schwab, and M. Vengalattore, *Atom-Mediated Optical Cooling of a Mechanical Resonator*, in *Bulletin of the American Physical Society*, volume 58, American Physical Society (APS) (2013).

[105] A. M. Jayich, J. C. Sankey, B. M. Zwickl, C. Yang, J. D. Thompson, S. M. Girvin, A. A. Clerk, F. Marquardt, and J. G. E. Harris, *Dispersive Optomechanics: a Membrane Inside a Cavity*, New J. Phys. **10**, 095008 (2008).

[106] T. P. Purdy, R. W. Peterson, and C. A. Regal, *Observation of Radiation Pressure Shot Noise on a Macroscopic Object*, Science **339**, 801 (2013).

[107] Norcada Inc., `http://www.norcada.com`.

[108] P.-L. Yu, T. P. Purdy, and C. A. Regal, *Control of Material Damping in High-Q Membrane Microresonators*, Phys. Rev. Lett. **108**, 083603/1–5 (2012).

[109] D. J. Wilson, *Cavity optomechanics with high-stress silicon nitride films*, Ph.D. thesis, California Institute of Technology (2012).

[110] U. Kemiktarak, M. Durand, M. Metcalfe, and J. Lawall, *Cavity Optomechanics with Sub-Wavelength Grating Mirrors*, New J. Phys. **14**, 125010 (2012).

[111] U. Kemiktarak, M. Durand, C. Stambaugh, and J. Lawall, *High Contrast Grating Mirrors for Radiation-Pressure Optomechanics*, in *Proceedings of the SPIE*, volume 8633, pp. 86330N–86330N–11 (2013).

[112] K. Usami, A. Naesby, T. Bagci, B. Melholt Nielsen, J. Liu, S. Stobbe, P. Lodahl, and E. Polzik, *Optical Cavity Cooling of Mechanical Modes of a Semiconductor Nanomembrane*, Nat. Phys. **8**, 168 (2012).

[113] M. Mader, *Characterization of SiN-Membranes*, Bachelor thesis, Ludwig-Maximilians Universität, München (2010).

[114] Institute of Physics, *Avogadros Number and the Mass of an Air Molecule*, `http://www.nuffieldfoundation.org/practical-physics/avogadros-number-and-mass-air-molecule`.

[115] S. S. Verbridge, H. G. Craighead, and J. M. Parpia, *A Megahertz Nanomechanical Resonator with room Temperature Quality Factor over a Million*, Appl. Phys. Lett. **92**, 013112 (2008).

[116] S. Bianco, M. Cocuzza, S. Ferrero, E. Giuri, G. Piacenza, C. F. Pirri, A. Ricci, L. Scaltrito, D. Bich, A. Merialdo, P. Schina, and R. Correale, *Silicon Resonant Microcantilevers for Absolute Pressure Measurement*, Journal of Vacuum Science and Technology B: Microelectronics and Nanometer Structures **24**, 1803 (2006).

[117] H. O. Pierson, *Handbook of chemical vapor deposition (CVD): principles, technology, and applications* (Noyes Publications, Norwich NY), 2nd edition (1999).

[118] D. J. Wilson, *Cavity Optomechanics with High-Stress Silicon Nitride Films*, Ph.D. thesis, California Institue of Technology (2011).

[119] J. Reichel and V. Vuletić, *Atom Chips* (Wiley-VCH, Weinheim, Germany) (2011).

[120] P. Treutlein, *Coherent Manipulation of Ultracold Atoms on Atom Chips*, Ph.D. thesis, LMU München (2008).

[121] R. Folman, P. Krüger, J. Schmiedmayer, J. Denschlag, and C. Henkel, *Microscopic Atom Optics: From Wires to an Atom Chip*, in B. Bederson and H. Walther (editors), *Advances In Atomic, Molecular, and Optical Physics*, volume 48, pp. 263 – 356 (Academic Press) (2002).

[122] D. Hunger, *A Bose-Eisntein Condensate coupled to a Micromechanical Oscillator*, Ph.D. thesis, LMU München (2010).

[123] H. J. Metcalf and P. van der Straten, *Laser Cooling and Trapping of Atoms*, J. Opt. Soc. Am. B **20**, 887 (2003).

[124] J. Reichel, W. Hänsel, and T. W. Hänsch, *Atomic Micromanipulation with Magnetic Surface Traps*, Phys. Rev. Lett. **83**, 3398 (1999).

[125] T. W. Hänsch, M. D. Levenson, and A. L. Schawlow, *Complete Hyperfine Structure of a Molecular Iodine Line*, Phys. Rev. Lett. **26**, 946 (1971).

[126] J. Fortagh, G. A., T. W. Hänsch, and Z. C., *Fast Loading of a Magneto-Optical Trap from a Pulsed Thermal Source*, Appl. Phys. **84**, 3 (1998).

[127] P. Horowitz and W. Hill, *The Art of Electronics* (Cambridge University Press, Cambridge, New York, NY, USA) (1989).

[128] W. Ketterle, D. S. Durfee, and S. D. M. Kurn, *Making, Probing and Understanding Bose-Einstein Condensates*, in M. Inguscio, S. Stringari, and C. E. Wieman (editors), *Bose-Einstein Condensation in Atomic Gases (Proceedings of the International School of Physics "Enrico Fermi," Course CXL)* (IOS Press) (1999).

[129] T. Kwaaitaal, B. J. Luymes, and G. A. van der Pijll, *Noise Limitations of Michelson Laser Interferometers*, Journal of Physics D: Applied Physics **13**, 1005 (1980).

[130] M. Born and E. Wolf, *Principles of Optics* (Cambridge University Press, Cambridge) (1999).

[131] R. Jáuregui, N. Poli, G. Roati, and G. Modugno, *Anharmonic Parametric Excitation in Optical Lattices*, Phys. Rev. A **64**, 033403 (2001).

[132] N. Poli, R. J. Brecha, G. Roati, and G. Modugno, *Cooling Atoms in an Optical Trap by Selective Parametric Excitation*, Phys. Rev. A **65**, 021401 (2002).

[133] S. J. M. Kuppens, K. L. Corwin, K. W. Miller, T. E. Chupp, and C. E. Wieman, *Loading an Optical Dipole Trap*, Phys. Rev. A **62**, 013406 (2000).

[134] K. Dieckmann, R. J. C. Spreeuw, M. Weidemüller, and J. T. M. Walraven, *Two-Dimensional Magneto-Optical Trap as a Source of Slow Atoms*, Phys. Rev. A **58**, 3891 (1998).

[135] A. E. Siegman, *Lasers* (University Science Books, Mill Valley CA) (1986).

[136] H. Kogelnik and T. Li, *Laser Beams and Resonators*, Appl. Opt. **5**, 1550 (1966).

[137] O. Arcizet, P.-F. Cohadon, T. Briant, M. Pinard, and A. Heidmann, *Radiation-Pressure Cooling and Optomechanical Instability of a Micromirror*, Nature **444**, 71 (2006).

[138] R. Drever, J. Hall, F. Kowalski, J. Hough, G. Ford, A. Munley, and H. Ward, *Laser Phase and Frequency Stabilization using an Optical Resonator*, Appl. Phys. B **31**, 97 (1983).

[139] F. Marquardt, J. P. Chen, A. A. Clerk, and S. M. Girvin, *Quantum Theory of Cavity-Assisted Sideband Cooling of Mechanical Motion*, Phys. Rev. Lett. **99**, 093902 (2007).

[140] P. Rabl, C. Genes, K. Hammerer, and M. Aspelmeyer, *Phase-Noise Induced Limitations on Cooling and Coherent Evolution in Optomechanical Systems*, Phys. Rev. A **80**, 063819 (2009).

[141] A. M. Jayich, J. C. Sankey, K. Børkje, D. Lee, C. Yang, M. Underwood, L. Childress, A. Petrenko, S. M. Girvin, and J. G. E. Harris, *Cryogenic Optomechanics with a Si_3N_4 Membrane and Classical Laser Noise*, New J. Phys. **14**, 115018 (2012).

[142] T. P. Purdy, R. W. Peterson, P.-L. Yu, and C. A. Regal, *Cavity Optomechanics with Si_3N_4 Membranes at Cryogenic Temperatures*, New J. Phys. **14**, 115021 (2012).

Curriculum Vitae

Maria Korppi
Born: 6.4.1984, Espoo, Finland

Academic Background

PhD in Experimental Physics 2009 – 2013
group of Prof. P. Treutlein at University of Basel Basel, Switzerland
and Prof. T.W. Hänsch at LMU München München, Germany

MSc in Technology 2003 – 2009
Helsinki University of Technology Espoo, Finland

Erasmus Exchange Student 2008
Eidgenössische Technische Hochschule Zürich Zürich, Switzerland

Research Assistant at Helsinki University of Technology
(part time, incl. teaching)
group of Prof. M. Kaivola 2006 – 2009

group of Prof. H. Lipsanen 2005

Matriculation Examination 2000 – 2003
Kouvolan Lyseon Lukio, Upper Secondary School Kouvola, Finland

Acknowledgements

The work presented in this thesis is a result of team effort. During my PhD I have had the change to interact with a number of talented people who have contributed to the conceptual and practical realization of this work. A memorable counterbalance for the work in the lab has been provided by conference trips and sporty leisure activities in the Alpine region. I would like to thank with gratitude the people who have made my research time in Munich and Basel so meaningful:

- Prof. Theodor W. Hänsch and Prof. Philipp Treutlein for providing me the possibility to work in the field of optomechanics and ultra-cold atoms. The scientific environment in the Hänsch group / MPQ with the weekly group seminars, yearly Ringberg retreats and frequent international guests has been the most inspiring. On the other hand, building up an experiment in an initially empty lab in Basel and making it to work has been exciting and very rewarding.
- Philipp Treutlein for being a tireless and supporting mentor, teaching me a lot about experimental physics, and for having an ambitious and enthusiastic attitude towards research.
- The past and present team-members for full commitment in the membrane-lab and for encouraging, exciting atmosphere: Stephan Camerer, David Hunger, Andreas Jöckel, Matthias Mader, Matthew Rakher, Tobias Kampschulte and Aline Faber.
- Andreas Jöckel for being my trusted team mate in Basel from the beginning; building up the setup and carrying out measurements together, and for proofreading this thesis. For always being ready to help, sharing his technical expertise, and for sharing the thrills of PhD life with me.
- Stephan Camerer for introducing both the experiment and Munich to me; and the memorable cycling trips towards lake Starnberger and Kleis.

- Colleagues at the Microwave experiment for numerous helpful discussions and giving a hand when needed: Caspar Ockeloen, Roman Schmied, Max Riedel, Pascal Böhi, Andrew Horsley, Jad Halimeh, Baptiste Allard, Guan-Xiang Du.
- Matlab-wizard Caspar Ockeloen for generous and invaluable help with syntax. For careful proof-reading of my thesis and for numerous, perspective-broadening discussions about (meta-)physics.
- Antoni Scheich at LMU, who shared some of his secrets of circuit design with me and also supplied the experiment with high-end electronics.
- The exquisite electronics workshop in Basel. In particular Michael Steiner; the membrane-experiment relies on his ingenious electrical equipment.
- The mechanics workshop at Basel and leader Sascha Martin for manufacturing many essential parts - in particular the cavity - even at a short notice, but with refinement.
- Hannes Brachmann, Carolin Hahn, Louis Costa and the Weinfurter group for the humorous atmosphere at Schellingstrasse.
- Gabriele Gschwendtner at LMU for helping with all the official documents, but also for her dynamic and sparky personality that cheered up the corridor.
- Germaine Weaver for keeping track of all the official documents in Basel and helping out with any practical question.
- Barbara Kammermann and Astrid Kalt for supplying office equipment and helping out with administration in Basel.
- Audrey Fischer for the humour and attitude at the 4$^{\text{th}}$ floor in Klingelbergstrasse.
- Fruitful discussions with the theory collaborators, in particular with Klemens Hammerer, Kai Stanningel, and Berit Vogell.
- My family and friends for love and support that I every day enjoy for granted. My parents Riitta and Kyösti for emphasizing the core values of life.